Advanced Spectral Analysis Methods for Quantification of Coherent Ultrasound Scattering: Applications in the Breast

By

Ivan M. Rosado-Mendez

A dissertation submitted in partial fulfillment of

the requirements for the degree of

Doctor of Philosophy

(Medical Physics)

at the

UNIVERSITY OF WISCONSIN – MADISON

2014

Date of final oral examination: 6/02/2014

The dissertation is approved by the following members of the Final Oral Committee:

Timothy J. Hall, Professor, Medical Physics
James A. Zagzebski, Emeritus Professor, Medical Physics
Tomy Varghese, Professor, Medical Physics
Sean D. Fain, Professor, Medical Physics
Barry D. Vanveen, Professor, Electrical and Computer Engineering

Abstract

Quantitative Ultrasound (QUS) methods, in particular the creation of parametric images displaying the spatial variability of acoustic properties of tissue, aim at augmenting the basic echo amplitude information derived during an ultrasound examination. These methods are expected to increase the objectivity of tissue characterization and disease diagnosis. This is of particular importance for breast cancer detection where the use of conventional ultrasound improves the detection performance at the expense of a higher rate of misdiagnosed benign cases. Various techniques encompassed by QUS rely on Fourier-based spectral analysis to assess the power spectral density (PSD) of radiofrequency (RF) echo signals obtained from an ultrasound system.

Estimations of the PSD and of conventional QUS parameters derived from the power spectrum assume that backscattered echo signals are from a stationary random process within the PSD estimation window. Furthermore, these estimates apply to incoherent scattering, which can exist when the resolution cell contains a large number of randomly distributed scatterers. However, sources of coherent scattering, such as organized scatterers, often are present *in vivo*, violating these assumptions.

The goal of this dissertation was to improve the value of parametric images by identifying areas of the backscattered echo field exhibiting a significant source of coherent scattering. For this purpose, we designed a novel algorithm that empirically evaluates the statistical significance of optimized metrics with respect to their values estimated from a reference material that exhibits stationary, incoherent scattering. The algorithm describes the statistical nature of the scattering sources within a parameter estimation region regardless of whether scattering is dominated by incoherent or coherent scattering, stationary or non-stationary (random or non-random) processes.

The metrics that quantify these features were selected after simulation- and phantom-based optimizations centered on the task of creating parametric images, where tradeoffs exist between spatial resolution and detection performance. To analyze stationary features, we compared the performance of a Generalized Likelihood Ratio Test based on a Nakagami model of the statistics of the echo signal amplitude to other

model-based and model-free metrics. Regarding the analysis of non-stationary features, we advanced the use of the echo-signal generalized spectrum by comparing advanced estimators, such as the multitaper estimator, to the time-domain singular spectrum analysis method. Analyses of the stationary and the non-stationary features provided a way to estimate descriptors of the tissue organization scales below and above the resolution limit imposed by the size of the acoustic pulse.

In preliminary work, the algorithm was applied to echo data from human breast lesions scanned *in vivo*. Results supported the idea of a more homogenously random distribution of subresolution scatterers within invasive ductal carcinomas than within fibroadenomas. Results also supported the importance of the anisotropy of the scattering process to distinguish between different lesion types.

Our contribution to the field of Quantitative Ultrasound is a novel approach to the task of creating scattering-based parametric images that goes beyond the conventional assumptions of a stationary, diffuse scattering process. The approach tests for the validity of these assumptions and statistically decides which analysis is most appropriate for the particular data (coherent or incoherent scattering; stationary or non-stationary process). This approach is comprehensive because it considers a wide range of coherent and incoherent scattering scenarios, and transitions from the analysis of subresolution features (smaller than the acoustic pulse) to resolved features (larger than the acoustic pulse) that describe tissue organization. Future work will refine the tools developed here and explore the connections between the echo signal details they reveal and features of tissue microstructure studied through microscopy.

Acknowledgments

To my supervisors, James Zagzebski and Timothy Hall

Time, either *past*, *present*, or *future*, is the most valuable asset a person can ever have. It is also a treasured bequest when *past* is granted through knowledge and experience, *present* through constructive critique, help and support, and *future* through advice. You never hesitated in sharing with me your time through its three facets. For this, you will always have my most sincere, unending, and heartfelt gratitude.

To María Ester Brandan

In our field, Physics, we are always subjected to deal with variables, with time- or space-dependent entities. I am always grateful with you for going beyond Physics by offering constant support, unalterable guidance, ubiquitous advice, and most importantly, your friendship.

To my dear friends

Mariela, Horacio, Pao, Kibo, Dany, Mariajose, Francis, Misha,

Luis, Lindsey, Quincy, Larry, Hanna, and Lari

Life is not life if it is not lived intensely, if we do not laugh together, if we do not support each other, if we do not scream at unison, if it is lived without you. Thanks for always being there during the most strenuous challenges and during the brightest joys. You kept me, keep me, and will keep me going, regardless of time and distance.

A Mau

Eres mi luz y mi fuerza. Tu apoyo, tu paciencia, y tu amor son la única razón por la que hoy estoy en donde estoy. Cada palabra en esta tesis está dedicada a ti.

A mis padres, Iván and Ginny

Ustedes me han enseñado a sobrevolar los hombros de gigantes con el simple hecho de soñar, y que, al despertar del sueño, el trabajo duro y perseverante es la única forma de emprender vuelo seguro. Gracias por una vida llena de ustedes.

A mis hermanos, Andrés, Daniel y Esteban

Quien soy no lo soy sin ustedes. Gracias por enseñarme el valor de una vida acompañada, el calor de una sonrisa sincera y la avasalladora belleza de la inocencia.

A mi familia

Limitar la unión a la fuerza es pintar de blanco y negro el atardecer. Nosotros somos y seremos fuerza, impulso, base, apoyo, amortiguamiento, fulcro, energía, potencia, calor… Gracias por ser esperanza inquebrantable.

I would like to express my gratitude to

The members of the thesis committee, Dr. Tomy Varghese, Dr. Barry Vanveen, Dr. Sean Fain, Dr. James Zagzebski, and Dr. Timothy Hall for the time dedicated to reading this work and for their valuable input.

Dr. Ernest Madsen and Gary Frank, for their help with the construction of the tissue mimicking phantoms used in the experiments.

Dr. Kibo Nam, Sarah Kohn, and Haidy Gerges-Nasief, for the acquisition and management of the *in vivo* breast data.

Dr. Kibo Nam, Dr. Matthew McCormick, Dr. Ryan Dewall, Dr. Matthew Bayer, Dr. Nicholas Rubert, and Jannelle Anderson, for their help during the realization of the simulations and experiments.

The students of the ultrasound group (Lisa, Lindsey, Eric, Chi, Xiao, Atul, Eenas, Haiyan, Kayvan, Quincy, and Haidy) for all the experiences lived together at WIMR and beyond.

Dr. Gale Sisney, for the training in breast anatomy and pathologies.

Dr. Orhan Unal, Yacouba Traore, and Charles Rienke, for the computational support.

The staff of the Department of Medical Physics, Mary Wegner, JoAnn Kronberg, Beth Bierman, and Deb Torgerson, for their help and support during these past years.

Finally, I sincerely thank the following institutions for their support. Without it, this dissertation would not have been possible

Consejo Nacional de Ciencia y Tecnología de México

Becas en el extranjero, Registro 206414

National Institutes of Health

Grants R01CA111289, R21HD061896, R21HD063031, and R01HD072077

Department of Medical Physics, University of Wisconsin-Madison

Department of Radiology, University of Wisconsin-Madison

Institute of Electrical and Electronics Engineers

Table of Contents

List of Figures

List of Tables

1. Introduction

1.1 Breast Cancer

According to the American Cancer Society, breast cancer is the most commonly detected type of malignant tumor in women. For 2014, more than 230,000 new cases are expected to be diagnosed, amounting to 29% of the total number of new cancer cases in women. From these cases, about 40,000 will result in the patient's death. As a consequence, it is considered a major health problem.[1]

It is encouraging to note, since 1990, breast cancer mortality rates have declined as a consequence of the possibility of detecting the disease at an early stage and because of the improvement in treatment options. Early detection of breast cancer has been made possible by improved screening programs that aim at finding breast lesions before the diseases have spread to other parts of the body.[2]

1.2 X-ray mammography

X-ray mammography is the primary imaging modality for screening asymptomatic women. The American Cancer Society recommends an annual mammography study for women at or older than age 40.[2] This imaging modality is based on the detection of x-rays transmitted through the breast. The detection method can be radiographic film or, more commonly, a digital detection device.[3] Many studies have demonstrated that the early detection of breast cancer by means of screening programs based on mammography augment the treatment options and the possibility of their success.[2] Evidence shows that mammography screening studies reduce breast cancer mortality.[4]

X-ray mammography suffers from an important limitation: its projective nature. The cumulative absorption and scattering of the x-rays along their way to the detector by the volumetric structure of the breast is registered in a two dimensional image. Thus, the complicated internal structure of the breast reduces the conspicuity of any abnormality that might exist within it. As a result, an estimated 10% to 20% of malignant lesions in the breast go undetected using mammography. The sensitivity of

mammography is further reduced, to about 69% in one study,[5] in women with radiographically dense breasts, i.e., those that contain a high fraction of glandular tissue and ducts. This problem is particularly important in women under age 40 who tend to have radiographically denser breasts than older women, and who have a propensity to develop more aggressive types of cancers than other women, leading to a poorer prognosis than for women over 40.[2]

1.3 Pulse-echo ultrasound for breast cancer detection and diagnosis

In the context of breast cancer detection and diagnosis, the role of pulse-echo ultrasound scanning has been mainly as a supplemental examination for the differential diagnosis of suspicious findings. An example of a helpful finding is the anechoic appearance of cysts compared to the echogenic nature of solid masses.[6] Ultrasound is also used as a guiding tool during biopsy procedures that utilize minimum invasion. Recently, various studies have demonstrated that by performing conventional ultrasound sequentially after negative screening mammography (in those cases where screening mammography was negative) the rate of the detection of malignant lesions can be increased by 22%.[7] This increased detection power occurs mainly in women with breasts in which the fraction of glandular composition is above 50% (dense and highly dense breasts according to the categorization from the American College of Radiology). However, this comes at the expense of increasing the rate of false positive detections, i.e., cases deemed suspicious under imaging studies, but the pathological results indicate a benign lesion. In reviewing multiple studies about the advantage of performing bilateral ultrasound in cases where screening mammography revealed a suspicious finding, Nuthacker *et al.*[7] found that from cases in which ultrasound suggested a suspicious finding, only about 15% were cancers. Thus the number of biopsies in which the lesion was deemed benign was about 85%. This means that 85 out a hundred patients were subjected to the psychological stress that cancer suspicion and the biopsy procedure itself cause when they only had benign (or no) disease. Thus the overall consensus is that the emotional distress and the economic burden of additional benign biopsies that result from complementing x-ray mammography with

conventional ultrasound are not justified by the gain in detection power. In addition, it has not yet been demonstrated that sequential ultrasound screening leads to a reduction in cancer mortality.[6]

One of the main factors leading to the limited specificity of conventional B-mode ultrasound is that the appearance of a lesion in an ultrasound image depends on the skill of the operator, the scanner configuration, and the transmission path that the acoustic pulse traverses on its way to the lesion.[8] These factors lead to inter- and intra-observer variability in the evaluation of these images, that reduces the objectivity of the imaging modality. Aiming at standardizing the interpretation of sonographic features in ultrasound images as well as improving patient management, the ACR introduced in 2003 the Breast Imaging Reporting and Data System (BIRADS) for evaluation of breast lesions.[9-11] This system defines a common lexicon to describe various features related to the appearance of masses and their surrounding tissue in the ultrasound image. These features are presented in Table 1.1. Malignancy is usually associated with masses that have spiculated margins, an irregular shape, and a "nonparallel" orientation. The Positive Predictive Value of the margin, shape, and orientation features (the ratio of the number of detected cancers based on a particular feature to those classified as cancers) were 86%, 62%, and 69%, respectively. Lesions with circumscribed margins, oval shape and aligned parallel to the surrounding tissue layers tend to be benign. The Negative Predictive Values (ratio of the number of benign cases classified as benign using a particular feature to the total number of benign classifications) of these features were 98%, 84%, and 78%, respectively.[12] The BIRADS lexicon descriptors provide a final classification scheme which assigns the lesion to one of seven different groups, described in Table 1.2.

Table 1.1 Breast Imaging Reporting and Data System – Sonographic features. Reproduced from Refs. 9-11

Category	Feature	Value
Masses	Shape	Oval, round, or irregular
	Orientation	Parallel (long axis aligned with the skin line) Not parallel
	Margin	Circumscribed, indistinct, angular, microlobulated, spiculated
	Echo Pattern	An-, hypo-, iso- or hyperechoic
Posterior Acoustic Features	None, enhancement, shadowing, combined pattern.	
Surrounding Tissue	No effect. Abnormalities in the ducts or in the Cooper's ligaments, presence of edema, architectural distortion, skin thickening.	
Calcifications	None. Calcifications > 0.5mm, or <0.5mm but outside or within mass.	
Special Cases	Mass in or on the skin, presence of foreign body, intra-mammary or axillar nodes.	
Vascularity (based on Doppler exam)	Could not be assessed. None. Increased, same or decreased compared to normal tissue.	

Table 1.2 Breast Imaging Reporting and Data System – Final assessment categories. Reproduced from Refs. 9-11

Category	Description
0	Incomplete evaluation. Further imaging exams are required.
1	Negative – normal ultrasound. No suspicious finding was observed.
2	Benign findings, including simple cysts, typical intra-mammary lymph nodes, and fibroadenomas proven after biopsy. Recommended follow up for solid masses after 4 to 6 months.
3	Probably benign findings (probability of malignancy less than 2%).
4	Suspicious finding (probability of malignancy from 3% to 94%). Histological examination is required. 4a. Low probability of malignancy but tissue sampling needed 4b. Moderate probability of malignancy. 4c. Moderate to high probability of malignancy without features commonly associated with malignancy.
5	Findings highly suspicious of malignancy (>95%). Confirmation with image guided biopsy is required.
6	Proven malignancy.

In spite of the existence of this standardization scheme, studies evaluating the inter-observer variability of the use of this classification have reported limited agreement on both the use of the sonographic features and the final outcome classification. In 2009, Abdullah *et al.*[13] presented a retrospective evaluation of the assessments of 267 breast masses made by five radiologists who had been using the BIRADS terminology for at least 2 years. The authors used the Landis and Koch interpretation of the Aickin κ statistic to quantify inter-observer agreement in the following categories: poor agreement ($\kappa<0.2$), fair agreement ($0.21<\kappa<0.40$), moderate agreement ($0.41<\kappa<60$), substantial agreement ($0.61<\kappa<0.80$), and excellent agreement ($0.81<\kappa<1.00$). Results showed that the observers achieved only fair agreement in describing the margins of the lesion, which is the parameter with the highest positive predictive value for malignancy. Other descriptors showed moderate to substantial agreement. Less agreement was observed

in lesions with diameters smaller than 0.7mm, which limits the early detection and diagnostic power. More importantly, a greater disagreement was observed in the final outcome categorization (κ=0.30, fair disagreement), particularly among categories 4a, 4b, and 4c. The importance of this finding lies in the fact that these categories span a probability of malignancy from 3 to 94%, thus including a large variety of lesion features. Biopsy is recommended in all of them. In the case of the intra-observer variability, Calas *et al.*[14] reported moderate to substantial agreement among evaluations of BIRADS features separated by 3 and 6 months by each of 8 radiologists with 5 to 23 years of experience in evaluating ultrasound images of the breast. Other studies have found similar trends.[15,16] Thus, increasing the diagnostic power of pulse-echo ultrasound is expected to reduce the number of biopsies with negative results. This could ultimately reduce the emotional distress of patients and the amount of resources and time devoted to the detection and diagnosis of breast cancer.[17,18]

1.4 Quantitative Ultrasound

The development of a particular disease often affects the regional cellular microenvironment. As a consequence, tissue microstructure (glands, collagen bundles in connective tissue) suffers modifications in its acoustic properties.[19,20] Based on this premise, various research groups have explored methods to offer a quantitative assessment of these acoustic properties aiming at tracking how their values under healthy circumstances are affected by different pathological processes. These methods are commonly referred to as Quantitative Ultrasound (QUS). The goal of QUS is to estimate acoustic properties of tissue and use the values as system- and observer-independent diagnostic parameters. This would reduce the subjectivity of the sonographic analysis and, therefore, increase its specificity.[17,19]

QUS has greatly evolved in the sixty years since the seminal work by Wild and Reid,[21] which aimed at differentiating breast cancer from benign lesions based on simple characteristics of the radiofrequency (RF) echo signal such as the number of echoes and the average area beneath the demodulated RF (envelope, or "A-mode") echo signal trace. As of today, the various QUS techniques and methods can be

grouped into three general modalities: *backscatter-based QUS*, *flow-based QUS*, and *elasticity-based QUS*. The first modality aims at extracting information about the structural and physical properties of tissue microstructure from the statistical analysis of the scattering process. Some backscatter techniques are performed in the time domain, such as deriving envelope statistics or carrying out image texture analysis. Other backscatter techniques are performed in the frequency domain using spectral analysis of the RF signals. The second QUS modality encompasses Doppler-shift based techniques (color Doppler, power Doppler), widely used to study blood flow and the presence of new vascularity in tumors. Finally, the goal of elasticity-based techniques is to quantify the elastic and viscous properties of tissue.

The estimation of parameters in each of the QUS groups starts by the selection of a Region of Interest (ROI) over which the parameter will be analyzed. Within the ROI, a **Parameter Estimation Region** defines the minimum amount of data used for parameter estimation. An ROI may contain one or many parameter estimation regions depending on the task to be performed. This was succinctly defined by Lizzi *et al.*[22] as: bulk estimation or parametric imaging. Bulk estimation is a "large estimation region" task because the ROI includes usually one parameter estimation region. It aims at comprehensively gathering values of tissue properties to be used in tissue characterization or classification. This mode is often used for the analysis of *ex vivo* tissue samples, such as in D'Astous and Foster.[23]

In parametric imaging, the parameter estimation region is moved across the ROI in a raster scan fashion to estimate the parameter of interest in various spatial locations.[19] In this way, a 2D array of local values of the parameter of interest is obtained and then color-encoded to create a final image. Figure 1.1 illustrates the areas defined by the ROI and the parameter estimation region when creating a parametric image. The B-mode image on the right of Fig. 1.1 was created from backscattered echo data acquired *in vivo* from a human breast carcinoma. The ROI outlined in the image might include a lesion or a section of it and the surrounding tissue. Within the ROI, a parameter estimation region (PER) is defined and includes a set of adjacent segments of echo signal data, or the volume of tissue they represent, that is used to compute a QUS parameter. For the estimation of spectral-based QUS parameters, such as the attenuation coefficient or the backscatter coefficient in Fig. 1.1, the PER can include one or more power

spectral density (PSD) estimation windows indicated by each of the dashed-framed boxes in the diagram on the left. This is because the estimation of the attenuation coefficient $\alpha(f)$ requires the quantification of the power loss over the propagation length (α-estimation length) defined by the axial span of the centers of the PSD estimation windows.[24]

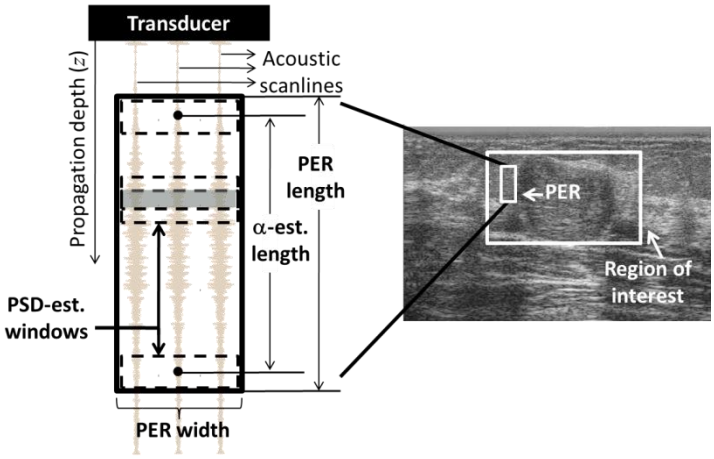

Figure 1.1 Description of a parameter estimation region (PER) from which one estimate of the attenuation coefficient is obtained. Each power spectral density (PSD) estimate is assigned to the center of the spectral estimation window, indicated by a dot. The PER width is defined by the number of adjacent scan lines it includes, and its length is defined by the α-estimation length plus one spectral estimation window length. The abbreviation "est." stands for estimation.[24]

The creation of parametric images is a "small parameter estimation region" task: the size of the PER will determine the spatial resolution of the parametric image. Ideally, the smaller the estimation region is, the finer the spatial resolution of the parametric image. This imposes a basic trade-off on the creation of parametric images because as the size of the estimation region is reduced the accuracy and precision of the estimates are compromised. The present work is focused on the creation of parametric images because:

1. The study of the spatial variability of the acoustic properties in the scanned anatomical section has important diagnostic value, as suggested by Kaffas *et al.*[25] and Gerges-Nasief *et al.*[26]

2. Each Parameter Estimation Region can be ultimately classified as corresponding to a region with healthy tissue or tumorous (benign or malignant) tissue by comparing the estimated values with collections of values of the estimated parameters for different lesions types.[19]

As an example of parametric images, Fig. 1.2(a) shows a conventional B-mode image as well as images corresponding to each one of the three QUS modalities: 1.2(b) a quasi-static elasticity strain image, 1.2(c) a color Doppler image showing the vascularity of the lesion, and 1.2(d) an attenuation-based parametric image computed by quantifying the spatial rate of acoustic energy loss in the backscatter spectrum.

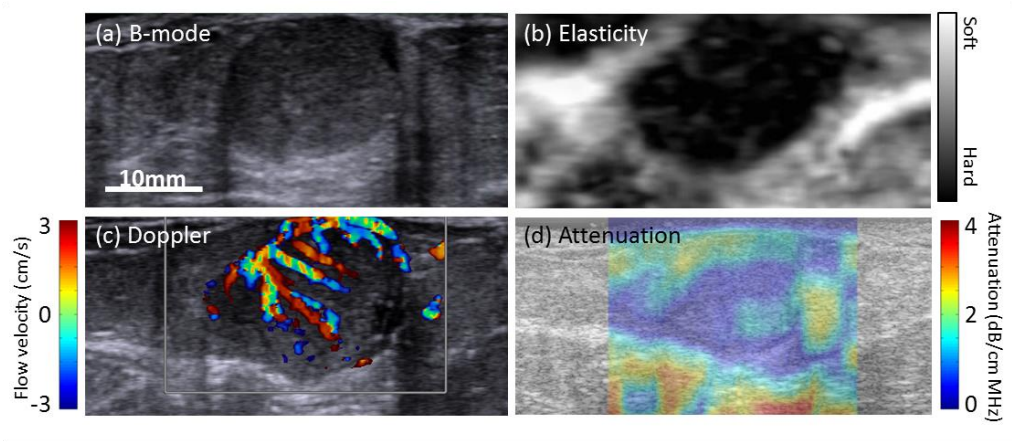

Figure 1.2 (a) Amplitude or B-mode image and (b) elasticity strain, (c) color Doppler and (d) attenuation parametric images of a human breast papillary carcinoma. Images correspond to the same lesion, but not necessarily to the same plane.

Our group has focused on backscatter-based QUS, and this is the focus of the research presented here. This modality relies on models describing the interaction of the acoustic pulse with the underlying tissue to solve the inverse problem of estimating a tissue property by comparing a quantity measured in the ultrasound signals with a model for the physical interaction. Conventional ultrasound works in a pulse-echo mode wherein a short acoustic pulse is emitted from the surface of an ultrasound probe. As the pulse travels through tissue, part of its energy will be absorbed as thermal energy.[20] This process affects both the amplitude and the frequency content of the acoustic pulse. When the pulse reaches a particular location within tissue, it will interact with a volume of tissue defined axially by the number of cycles and

the wavelength of the pulse and laterally and elevationally by the size and shape of the transducer's active aperture. This volume, referred to as the isochronous volume or the **resolution cell**, defines the elemental spatial sampling unit in the pulse-echo experiment.[27-29] Based on the characteristics of most clinically available ultrasound scanners, this volume spans approximately $0.25mm^3$.

An echo will be generated within the resolution cell if a change (heterogeneity) in acoustic impedance exists within it. If the size of the heterogeneity is larger than the resolution cell, it will act as a specular reflector and the pulse will be reflected and refracted. Thus, its frequency content will remain intact. If the resolution cell contains a number of small heterogeneities, each of them will elastically re-irradiate a scattered wave with frequency content that not only depends on that of the incident pulse, but also on the tissue microstructure. These tiny heterogeneities have been called "scatterers"[30] and the properties of each individual scattered wave depend on the physical and structural properties of each scatterer as well as on the incident pulse. The attenuation (the spatial rate of energy loss of the acoustic pulse) encompasses both absorption and scattering. The final echo signal containing the information of the echoes coming from structures at different locations along the path of the acoustic pulse is called the radiofrequency (RF) echo signal.

Two of the most commonly estimated acoustic properties related to these processes are the attenuation coefficient and the backscatter coefficient. The attenuation coefficient, α, quantifies the spatial rate at which the acoustic beam loses energy while traversing a particular tissue. The backscatter coefficient is defined as the differential scattering cross section per unit volume for a scattering angle of 180 degrees. These parameters and other ones derived from them, such as the effective scatterer size (which is estimated by fitting a scattering model to the estimated backscatter coefficient) or the acoustic concentration (product of the number of scatterers within the resolution cell and the square of their acoustic impedance difference compared to background) have been used to characterize as well as to classify healthy and diseased tissues in bone, liver, kidney, thyroid, and breast.[31-34]

Our laboratory has joined efforts with other laboratories to demonstrate the possibility of estimating the attenuation coefficient and the backscattered coefficient (or the effective scatterer size derived from it)

accurately regardless of the system architecture or the nuances of the estimation technique. This has been demonstrated in tissue mimicking phantoms as well in rodent models of breast tumors.[35-38]

The diagnostic value of these parameters has also been investigated. In Oelze *et al,*[39] statistically significant differences in the effective scatterer size and the acoustic concentration were found between rodent models of breast fibroadenoma and carcinoma. Results indicated a sparse distribution of large scatterers (~100 μm) in fibroadenomas, while a more homogenously random distribution of small scatterers (~30μm) was observed in carcinomas. Recently, Nam *et al.*[18] presented an *in vivo* study in human subjects aiming at correlating estimates of the attenuation coefficient and average backscatter coefficient within fibroadenomas and carcinomas to corresponding features in the BIRADS classification, i.e., posterior acoustic features and echogenicity. In general, lesions showing posterior enhancement or shadowing had correspondingly low (0.75±0.31 dB cm^{-1} MHz^{-1}) or high (1.56±0.18 dB cm^{-1} MHz^{-1}) attenuation. This study demonstrated a good correlation between the attenuation coefficient within the lesion and patterns of enhancement or shadowing below it. Although no correlation between the echogenicity pattern and the average backscatter coefficient was observed, estimates of the effective scatterer size derived from the backscatter coefficient and its spatial variation within the lesion suggested good discrimination properties. This work has been extended by Gerges-Nasief *et al.*[26] by feeding these values into a Bayesian classifier, which has also shown encouraging diagnostic results.

1.5 The reference phantom method and its underlying assumptions

The estimation of the frequency-dependent acoustic parameters within the Parameter Estimation Region is based on solving the inverse problem of relating the measured echo signal power spectral density to a scattering model that depends on the parameters of interest. One such estimation method is the Reference Phantom Method (RPM) derived by Yao *et al.*,[40] which is widely used to obtain estimates of the attenuation coefficient and the backscatter coefficient from data obtained with clinical ultrasound scanners. The importance of this method lies in its ability to account for variations of the echo intensity

caused by factors other than attenuation and scattering, such as the system/transducer transfer function and the diffraction field. In order to obtain accurate and precise estimates of the attenuation and backscatter coefficient estimates using the Reference Phantom Method, one must be aware on the conditions under which it can be applied.

The RPM is based on two important assumptions that, in fact, may limit the extent of its applicability. The first assumption is that the RF echo signal originates from a wide-sense stationary random process within the power spectral density estimation window, i.e., the co-variation between two time samples depends only on the separation between the samples, and not on their absolute occurrence with respect to the system's origin.[28] The second assumption is that the number of scatterers within the resolution cell is "large", which will be described later.

The co-variation is mathematically described by the autocovariance function $C(x_1,x_2)$, which for our purposes we write as:[28]

$$C(x_1, x_2) = \left\langle y(x_1) y^*(x_2) \right\rangle \tag{1.1}$$

where superscript * indicates the complex conjugate of the variable, y is the echo signal, x_1 and x_2 are the spatial locations of the resolution cell, related to different sampling times of the echo signal by means of the pulse-echo time-of-flight equation ($x=tc/2$, where t is the echo arrival time and c is the tissue sound speed). The echo signal is assumed to have zero mean. The brackets indicate the expectation value of the variable. Wagner *et al.*[28] demonstrated that in order for the echo signal to be stationary, two conditions must be met:

1. The point spread function of the system $h(x)$ must be shift invariant. As a consequence, the RF echo signal results from the convolution of the point spread function $h(x)$ describing the acoustic pulse with the scattering function $s(x)$ of the insonified tissue. The point spread function is related to the frequency and bandwidth of the acoustic pulse at a particular point in space, as well as to the diffraction pattern at that location.[19,41] The scattering function is defined by the spatial variations of the acoustic impedance within tissue. In the context of

parametric images using small estimation regions, the shift invariance can be assumed to be the case.

2. The second condition is that scattering function itself must be homogeneous, i.e., the same scattering process must dominate the volume occupied by the parameter estimation region. As a consequence the scattering function is stationary and its autocovariance function $R_s(x_1,x_2)$ depends only on the separation of x_1 and x_2.

The autocovariance function of the echo signal can thus be expressed as:[28]

$$C(x_1, x_2) = h(-\Delta x) * \left\langle R_s\left(\Delta x\right)\right\rangle * h^*(\Delta x) \tag{1.2}$$

where $\Delta x = x_2 - x_1$.The symbol * indicates convolution. For a continuous, infinite, and wide-sense stationary signal, vectors of the Fourier basis are eigenvectors of the autocovariance function, and therefore, the Fourier transform of the autocovariance function, the power spectral density, provides a full description of how the system distributes the acoustic energy among independent harmonic components of the echo signal.[42] The discrete homologue of the autocovariance function is the covariance matrix.[43,44] The covariance matrix of wide-sense stationary signals is diagonalized under Fourier transformation, and elements of its main diagonal correspond to the discrete power spectral density, which is the basic operational metric of the RPM.[42]

The second assumption behind the RPM is the scattering process results from randomly distributed scatterers. The backscatter coefficient is directly related to the scattering cross section of tissue. The scattering cross section describes the fraction of acoustic energy from the incident acoustic beam removed by scattering interactions.[20] Theoretical expressions for the scattering cross section are usually based on the solution of the wave equation for a medium containing scatterers smaller than the resolution cell. As described above, the total echo generated from that particular location of the resolution cell will result from the interference of the waves from individual scatterers. This is depicted in Fig. 1.3, where individual scattered waves $s(t,x_i)$ for N scatterers located at x_i $(i=1,\ldots,N)$ are represented as phasors of amplitude A_i and phase ϕ_i related to each scatterer location. Fig. 1.3(a) shows the phasor of the wave

scattered by the i^{th} scatterer, while Fig. 1.3(b) shows the net phasor corresponding to the sum of individual phasors. In this context, the RPM assumes a sufficiently large number (N>10) of scatterers uniformly and randomly located within the resolution cell. A direct result of this assumption is that multiple samples of the net phasor by independent resolution cells will not have a preferred orientation, i.e., the phase may be uniformly distributed between 0 and 2π. This condition is referred to as **diffuse or incoherent scattering.**[20] This is a consequence of the Central Limit Theorem applied to the real and imaginary parts of the net phasor.[28] This will be discussed in greater depth in Chapter 2.

As long as a linear relationship exists between the scattering process and the detected backscattered echo and the pulse/tissue spectrum has enough signal compared to the detection noise (for example, Chaturvedi and Insana[45] demonstrated that an SNR of at least 10dB is required to estimate the scatterer size within 5% of its true value), this method can provide precise estimates regardless on the system settings. This has been demonstrated by multiple cross-system studies using tissue-mimicking phantoms that were homogeneous in their composition and led to conditions of stationary echo signals and diffuse scattering.[35,36,46-48]

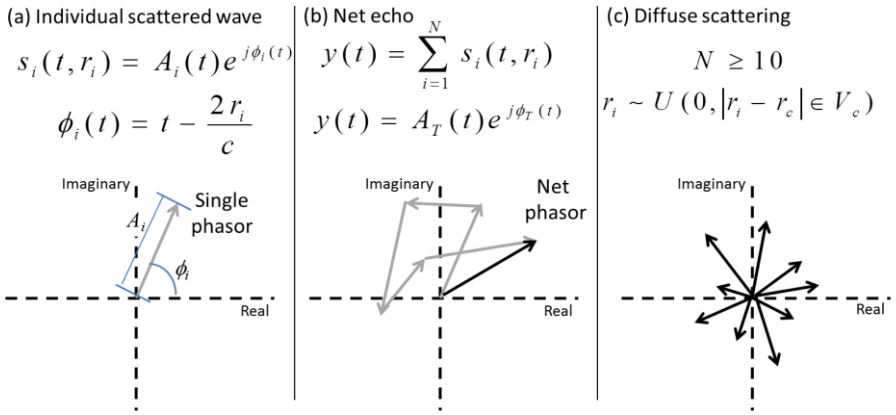

Figure 1.3 Sum of *N* individual scattered waves s*(t,x$_i$)* of amplitude *A$_i$* and phase *ϕ$_i$* related to each scatterer's position *x$_i$* with respect to the transducer. (a) Phasor representation of single scattered wave. (b) Phasor representation of net echo from sum of individual scattered waves. (c) Diffuse scattering condition, where *U(a,b)* indicates uniform distribution between *a* and *b*, *x$_c$* is the position of the center of the resolution cell with respect to the transducer. The notation indicates that the scatterers are uniformly randomly distributed within the volume *V$_c$* of the resolution cell.

1.6 Challenges for *in vivo* clinical application of QUS

As these techniques have been gradually expanded to clinical applications, some important obstacles have slowed this process. Initial *in vivo* studies in rodent models of breast tumors and human subjects have found that an important limitation is the inability to define an ROI in which the echo signals contained in all the estimation regions within it comply with the assumptions of stationarity and diffuse scattering. To illustrate this, Fig. 1.4(a)-(c) shows B-mode images of situations in which the assumptions are completely, partially, or not met, respectively. Figure 1.4(a) corresponds to a tissue-mimicking material in which the assumptions of stationarity and diffuse scattering are met (by visual inspection) in every possible estimation region. Figure 1.4(b) corresponds to the same breast carcinoma shown in Fig. 1.2. By visually comparing Figs. 1.4(b) and 1.4(a), only a limited region within the lesion seems to comply with the assumptions. Figure 1.4(c) corresponds to a fibroadenoma with a heterogeneous internal structure. As a consequence, no ROI can be defined within the lesion in which the assumptions are met and from which estimates of the attenuation and the backscatter could be obtained.

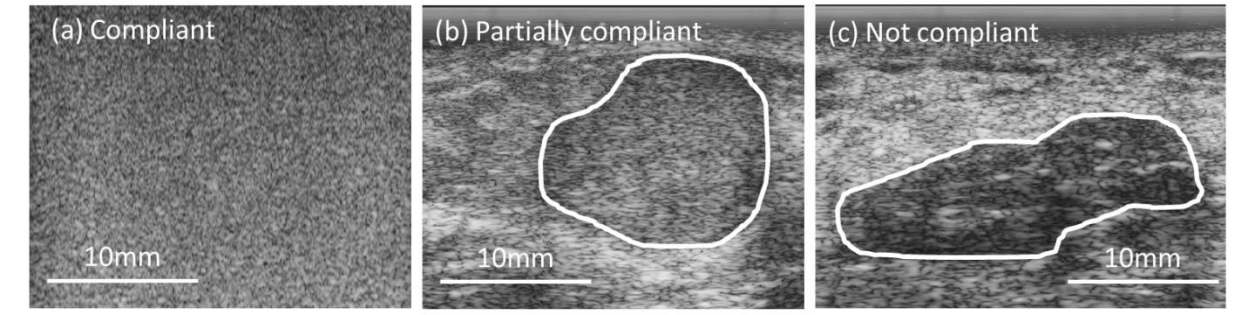

Figure 1.4 B-mode images of (a) a tissue mimicking phantom, (b) a human breast carcinoma, and (c) a human breast fibroadenoma. Labels suggest the degree to which the scattering statistics within the outlined ROI comply with the assumptions of stationarity and diffuse scattering. The curves in (b) and (c) follow the borders of the lesions.

In order to state the relevance of this problem, seventy-eight B-mode images of breast lesions from human subjects from an ongoing clinical protocol (described in Chapter 5) were visually analyzed to identify those cases in which an ROI could be defined in which the assumptions seemed to be fulfilled.

Table 1.3 shows the summary of this analysis: In more than half of the cases where the lesion was large enough to define at least one estimation region within it no such ROI could be identified.

Table 1.3 Results from visual analysis of B-mode images of breast lesions from human subjects when looking for regions in which the assumptions of stationarity and diffuse scattering seemed to be fulfilled.

Total number of images	78 cases
Fraction of images in which the assumptions are meet within ROI	42%
Fraction of images in which assumptions are not met within the lesion	49%
Fraction of images too small to analyze (largest dimension < 4mm)	9%

The problem of there being limited regions in which the assumptions are met have been addressed in three ways. The first one is just to ignore the fact that the assumptions are not met and apply the estimation methods over an arbitrary ROI framing the lesion. This is the strategy followed in Fig. 1.2(d). Estimates of the attenuation and the backscatter coefficient from PERs in which the assumptions are not met will be biased. Understanding the origin of this bias is essential for interpreting the resulting parametric images and to obtain information with diagnostic value from them. For example, high attenuation values close to the upper lesion boundary in Fig. 1.2(d) are mainly caused by underlying specular reflectors and contributions from the boundary itself.

The second strategy is to limit the ROI to the region where the assumptions are met. This will severely restrict the analysis to a reduced number of cases, as commented on above. In addition, this will depend on the ability of the observer to delineate margins between zones with different scattering properties. As was discussed before, the definition of lesion margins is one of the sonographic features with the largest inter-observer variability. Alternatively, one could try to estimate properties of tissue structure or parameters related to the physical process causing the assumptions of stationarity and diffuse scattering to fail. This is the strategy that this work follows.

This work addresses situations in which the assumptions of stationarity and large scatterer density are not met because of the presence of a source of deterministic phase in the echo signal, i.e., a non-random phasor added to the sum of random phasors described in Fig. 1.3(c). This can be represented by adding a phasor $\varepsilon(t)$ to the equation in Fig. 1.3(b).

$$y(t) = \varepsilon(t) + M(t)e^{j\varphi_T(t)} \tag{1.3}$$

The effect that $\varepsilon(t)$ has on the statistics of the echo signal will depend on how it originates from within the resolution cell. Figure 1.5 includes four different panels describing four different one-dimensional scattering scenarios with different $\varepsilon(t)$. A parameter estimation region, PER, defined by the upper bracketed line on top of Fig. 1.5 includes 10 uncorrelated adjacent resolution cells. Scatterers are depicted by either a vertical blue line if they have random locations or a red one if the scatterers belong to an organized structure. The height of these lines represents the magnitude of the scattering cross-section. These scatterers are distributed over the length of the parameter estimation region, shown at the bottom of each panel. Above the scatterer distribution in each of the four panels, the RF (blue) and echo amplitude (black) signals resulting from convolving the acoustic pulse shown on the top left part of Fig. 1.5 with each scatterer distribution are shown. Each of the four scenarios is now described:

- Figure 1.5(a): This scenario corresponds to diffuse scattering only, with an average concentration of 10 random scatterers per resolution cell. In this case the autocovariance function of the echo amplitude signal will depend only on the separation of the resolution cells. As a consequence, the echo amplitudes are stationary. The autocovariance function is represented in its discrete form, the autocovariance matrix, in Fig. 1.6(a). It was averaged over one thousand independent realizations of the scatterer distribution. As can be observed, the values along the diagonals are constant, indicating stationarity.
- Figure 1.5(b): In this case an organized (quasi-periodic) lattice of scatterers is present in the medium in addition to the randomly distributed scatterers. The mean spacing

among the organized scatterers is less than the size of the resolution cell. As a consequence, all the resolution cells within the parameter estimation region will have approximately the same underlying statistics, i.e., the coherent component $\mathcal{E}(t)$ is approximately invariant with the position of the resolution cell. Therefore, the echo signal amplitude will still be stationary. The autocovariance matrix of the echo amplitude shown in Fig. 1.6(b) reveals that this is a stationary process.

- Figure 1.5(c): This case is similar to the one described in Fig. 1.5(b). The difference is that the mean scatterer spacing is larger than the resolution cell. As a consequence, the periodically spaced scatterers are sampled by only those resolution cells separated by the mean scatterer spacing from each other. The presence of the coherent component $\mathcal{E}(t)$ within the signal from a resolution cell depends on the position of the resolution cell itself, and so do the scattering statistics. Thus, the autocovariance function of the echo amplitude depends on the absolute position of the scatterers. This is shown in Fig. 1.6(c) where the values of the autocovariance matrix vary along each of the diagonals and across diagonals.
- Figure 1.5(d): At particular locations within the parameter estimation region, the acoustic pulse "meets" a structure with significantly larger scattering cross section than that of the diffuse component, such as a microcalcification in the breast or a tissue interface acting as a specular reflector. These components are referred to as short-range specular components because of their sparse distribution within the analyzed volume.[41] Due to the small size of the parameter estimation region in the context of parametric imaging, only one of such structures might be included within it. The sparse nature of $\mathcal{E}(t)$ causes the autocovariance function of the echo amplitude to depend on the absolute position of the resolution cell, thereby making the signal non-stationary. Fig. 1.6(d) shows the autocovariance matrix under this situation. As

can be observed, the maximum covariance occurs at the location of the dominant scatterer (3mm).

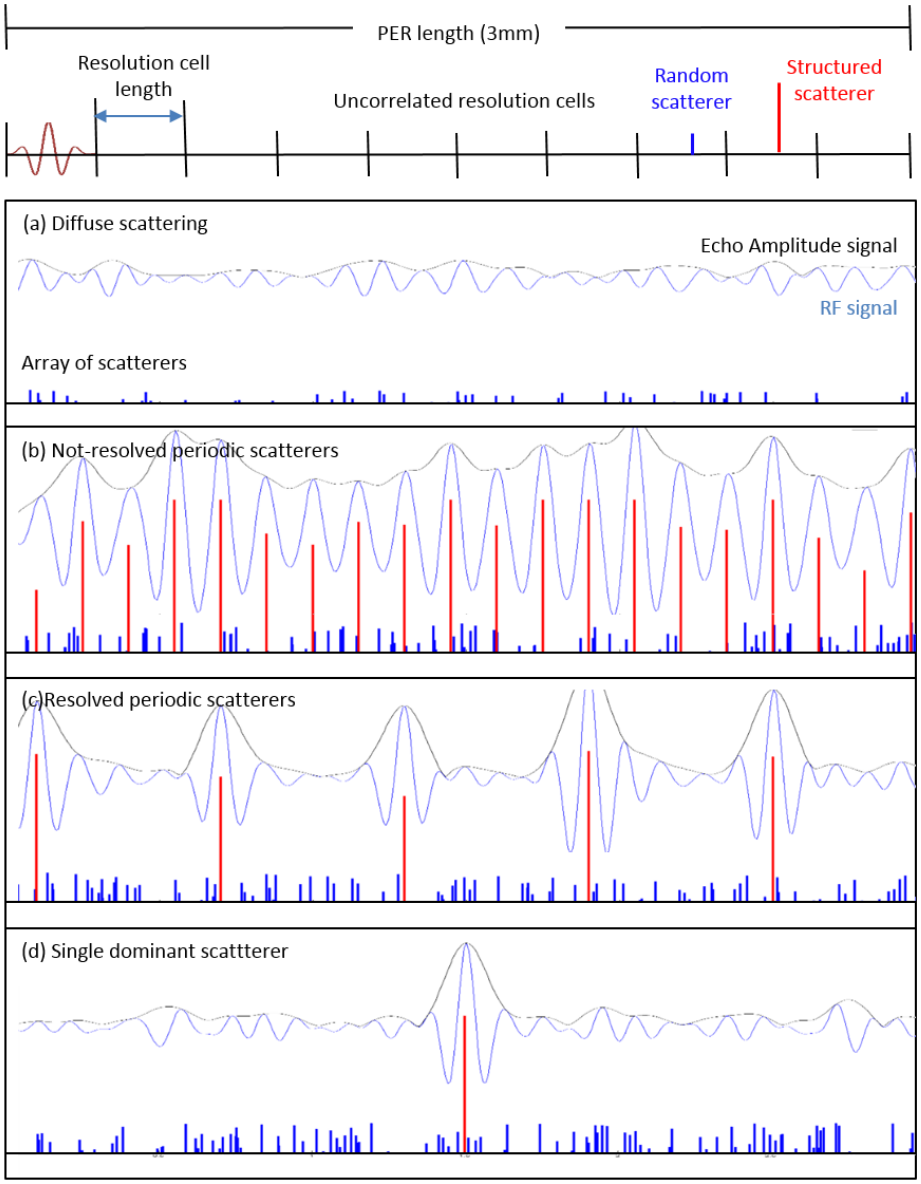

Figure 1.5 One-dimensional examples of various scattering scenarios. On the top part, the bracketed line indicates the length of a parameter estimation region, spanning 10 uncorrelated resolution cells. In each of the four panels, the array of vertical lines depicts the distribution of scatterers. Blue lines are random scatterers. Red lines are structured scatterers. Their heights are proportional to the scattering cross sections. Two echo signals are shown in each panel, the RF (blue) and the echo amplitude (black). (a) Diffuse scattering. (b) Not-resolved periodic scatterers. (c) Resolved periodic scatterers. (c) Dominant scatterer.

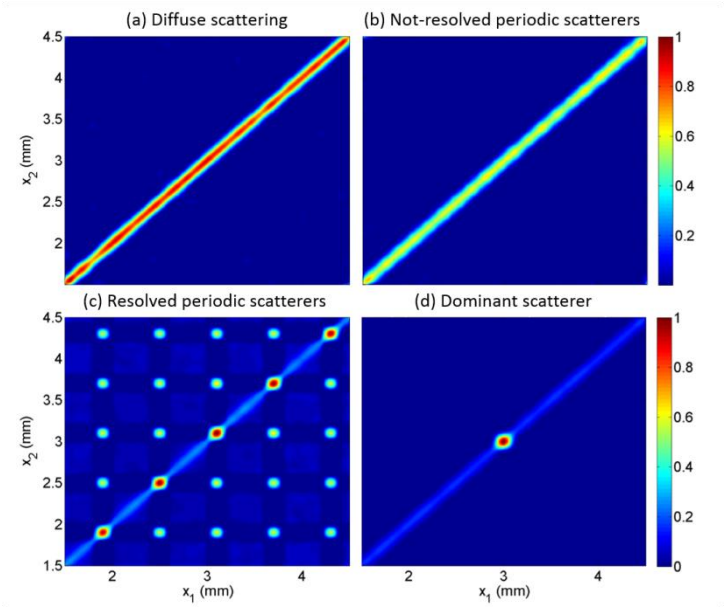

Figure 1.6 Autocovariance matrices of the four scattering scenarios described in Fig. 1.5. (a) Diffuse scattering, (b) not-resolved periodic scatterers, (c) resolved periodic scatterers, and (d) dominant scatterers.

Tissues are usually composed of both spatially structured and random distributions of heterogeneities in density and compressibility and, therefore, the backscattered echo signals contain different levels of coherent and incoherent scattering. In this context, there are three important questions when creating a parametric image. The first one is at a particular location of the parameter estimation region, is the coherent component sufficiently large so that the scattering process significantly departs from the situation of diffuse scattering? In case it is, various studies have demonstrated that properties of the structured field of scatterers, such as the mean scatterer spacing, can also be used to discriminate among different pathological processes among them and with respect to healthy tissue.[49-51]

The second important question is which of the cases from Fig. 1.5 best describes the scattering situation at that location of the resolution cell? A number of techniques have been proposed to quantify properties of the structured component. Most of these, such as the intensity spectrum method by Insana *et al.*,[52] the spectral correlation method by Varghese and Donohue,[50] the cepstrum analysis by Wear *et al.*,[49] or the singular spectrum analysis by Pereira *et al.*[53] have aimed at estimating parameters from situations in

which the coherent component is caused by a quasi-periodic array of scatterers with resolved spacing (Fig. 1.5(c)). Less attention has been paid to cases in which a quasi-periodic structure with subresolution periodicity is present.[54]

The third question is how can one estimate a parameter describing the underlying scattering situation? Clearly, the estimation method will depend on the nature of the echo signal and how it varies in each of the situations described in Fig. 1.5. Since the resolved periodicity case has been the center of most research efforts, one of the most frequently investigated parameters has been the mean scatterer spacing. Other researchers have investigated the ratio of the energy in the echo signal coming from the coherent component to the energy coming from the diffuse component.[29,52,55,56]

The goal of this work is to develop an automatic algorithm that allows us to decide whether at each location of the parameter estimation region there is a significant source of coherent scattering, and what is the nature of this source, i.e., which of the cases in Fig. 1.5 best describes the scattering scenario. Depending on the presence of absence of a source of coherent scattering, the algorithm will then quantify a parameter best describing the scattering situation. To achieve this goal, the following **specific aims** are pursued:

1. **To identify parameters that allows the classification of each parameter estimation region with respect to the nature of its source.**
2. **To evaluate the performance of these parameters as the size of the parameters estimation region is gradually constrained to improve the resolution of the parametric image. The parameters whose, sensitivity, accuracy and precision are more robust to reductions in the amount of data for the estimation will be used for further analysis.**
3. **To develop a method to make a statistical decision on whether the source of coherence causes the parameters selected in Aims 1 and 2 to be significantly different from the case of diffuse scattering.**

4. **To unify the results from Aims 1-3 to design an algorithm that automatically decides on the presence of coherent scattering, its source, and on the estimation of parameters describing the scattering situation.**

These aims can be put into perspective with the help of the diagram in Fig. 1.7. It describes the classification of a parameter estimation region into each of the cases described in Fig. 1.5. Also it includes an additional case in which the number of scatterers within the resolution cell is low. As a consequence, this situation will depart from diffuse scattering and violate the assumptions behind the Reference Phantom Method. Thus, identifying parameter estimation regions in which the scattering process belongs to this case is necessary. In order to move across this diagram, two main steps are necessary: the **Quantification** of parameters to discriminate among scattering scenarios (Aims 1 and 2), and a **Decision** (Aim 3) on the level of significance of that parameter to decide which direction of the diagram the classification algorithm (Aim 4) should follow.

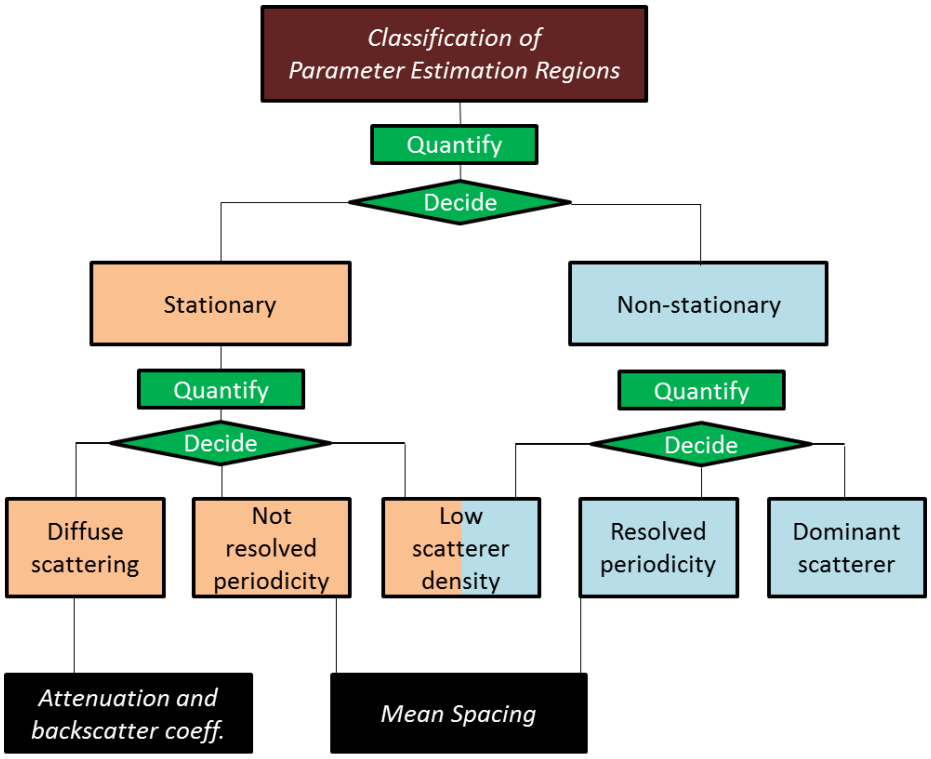

Figure 1.7 Diagram of the automated algorithm for the classification of a parameter estimation region into scattering scenarios with different sources of coherence.

This dissertation is organized as follows: Chapters 2 and 3 deal with each of the above **Quantification** steps, while Chapter 4 deals with the **Decision** step. Chapter 2 describes the situations in which the echo signals are stationary. This allows the use of techniques to analyze echo amplitude statistics to discriminate between scattering scenarios (subresolution periodicity, diffuse scattering, and low-scatterer density). Chapter 3 presents various methods to identify signals that are not stationary due to the presence of resolved periodicity or a dominant scatterer. A comparison of the performance of these parameters for detecting sources of coherent scattering and its variation as the size of the estimation region is reduced is presented. Chapter 4 describes a method to empirically decide on the level of significance of the difference between the values of parameters described in Chapters 3 and 4 when coherent scattering is present and when there is no coherent scattering, i.e., under diffuse scattering conditions. The **Quantification** and **Decision** steps are then put together to automatically decide on the scattering scenario best describing the detected echo signal. This is tested with a computational phantom that simulates regions with variations of the cases described in Fig. 1.5. Chapter 5 presents some initial application of this algorithm to echo data from human breast lesions scanned *in vivo*. This analysis aims at using parameters derived from the different scattering scenarios found in the frame of echo data to classify among different breast lesions. Chapter 5 also discusses these findings in the context of the previous chapters and presents a hypothesis about the sources of scattering in benign and malignant lesions. Finally, Chapter 6 closes this dissertation by proposing future lines of investigation.

2. Quantification of features from stationary signals

In Section 1.4 above, we defined a Parameter Estimation Region as the minimum amount of data used to obtain a reliable estimate of a parameter of interest. It usually comprises a set of adjacent segments of echo signal data, or the volume of tissue they represent, that is used to compute a QUS parameter, such as the attenuation coefficient, the backscatter coefficient, or the speed of sound. In general, many QUS parameter estimation strategies assume that a stationary random process underlies the generation of echo signals produced by a diffuse scattering process. In this and the following chapters, it will be demonstrated that these are not always valid assumptions. This chapter explores the effectiveness of various quantities to identify parameter estimation regions (PERs) that give rise to backscattered echo signals for which there are conditions other than diffuse scattering. The main assumption in this chapter is that the statistics of the backscattered echo signals are the same across all the samples of the resolution cell volume within the parameter estimation region. Two types of test quantities are explored: those based on the first order moments of the echo data, and those based on models of the probability density function of the echo data. Attention is paid to the effects of data size reductions on the sensitivity and precision of the estimates. This is motivated by the desire to have good spatial resolution (requiring small parameter estimation regions) of parametric images.

Section 2.1 presents the rationale to study echo signal statistics for the purpose of PER classification. This section also presents the necessary background for the quantities of interest. Section 2.2 states the aim of the analysis presented in this chapter. Section 2.3 describes the materials and methods of experiments that were performed to achieve the stated aim, while Section 2.4 presents the results of the analysis. Section 2.5 discusses the results and presents the conclusions of this chapter. A method to estimate a material's sound speed based on echo signal statistics is proposed in Appendix A at the end of this chapter.

2.1 Background

As discussed in the Introduction, the received echo signal is proportional to the total acoustic pressure incident on the transducer's face.[30,57] Due to the pulse-echo nature of the sonographic scan, the value of the echo signal at a particular time point is related to a particular location *z* of the acoustic pulse along the axis of propagation by means of the "time of flight" equation:

$$t = \frac{2z}{c} \tag{2.1}$$

where *c* is the sound speed of the medium. The total scattered acoustic pressure at that time point results from the interference of the individual acoustic waves scattered by each scatterer within the volume of tissue the acoustic pulse interacts with.[28,29,58] This volume, known as the **resolution cell**, is defined by the size of the point spread function of the imaging system.[28,29,56] Due to the random nature of the number and precise locations of scatterers within the resolution cell and the amplitude and phase of the scattered waves, this interference can be represented graphically by a random walk in a two-dimensional Euclidian space, as was described in Fig. 1.3.[58,59] Each step is represented by a vector whose magnitude is given by the amplitude of the scattered wave and its angle with the horizontal axis is given by the phase of the scattered wave. Mathematically, each vector is represented as a complex number, and the two dimensional space is the complex plane.[28,60] The general model for this scattering process is[58]

$$y(t) = \varepsilon(t) + r(t) \tag{2.2}$$

where $\varepsilon(t)$ represents a source of deterministic signal or the coherent component and *r(t)* is the signal from randomly positioned scatterers.[30,56-68] The detected radiofrequency (RF) signal is the real part of $y(t)$.[59,61] As described in Chapter 1, the random component *r(t)* will result from the interference of the waves from individual scatterers with random positions and scattering amplitudes located within the resolution cell.[30,57] Using the phasor representation described in Chapter 1,[54,61,62] *r(t)* can be represented mathematically as

$$r(t) = \sum_{i=1}^{N} A_i(t) e^{j2\pi f_0 (t - 2r_i/c)} = e^{j2\pi f_0 t} \sum_{i=1}^{N} A_i(t) e^{-j2\pi f_0 (2r_i/c)} = e^{j2\pi f_0 t} \sum_{i=1}^{N} A_i(t) e^{-j\varphi_i} \tag{2.3}$$

where $A_i(t)$ is the amplitude of each individual scattered wave which depends on the size, shape and orientation of each scatterer as well as on the properties of the pulse when it reaches that scatterer.[63] The sum is over N scattering sources in the pulse volume, each contributing independently to the scattered pressure. Also,

$$\varphi_i = 4\pi f_0 \frac{r_i}{c} \tag{2.4}$$

represents the phase of each echo signal from each individual scattered wave, which is proportional to the distance r_i from the scatterer to the transducer's active aperture. Let us express the coherent component $\varepsilon(t)$ as the product of a demodulated component $\varepsilon_d(t)$ and the carrier sinusoid of frequency f_0:

$$\varepsilon(t) = \varepsilon_d(t) e^{j2\pi f_0 t} . \tag{2.5}$$

Substituting Eq. (2.4) and Eq. (2.5) into Eq. (2.2), we obtain

$$y(t) = \varepsilon_d(t) e^{j2\pi f_0 t} + e^{j2\pi f_0 t} \sum_{i=1}^{N} A_i(t) e^{-j\varphi_i} . \tag{2.6}$$

Factoring out the carrier signal of frequency f_0, Eq. (2.6) can be expressed as:[64]

$$y(t) = \left[\varepsilon_d(t) + \sum_{i=1}^{N} A_i(t) e^{-j\varphi_i} \right] e^{i2\pi f_0 t} = \left[\varepsilon_d(t) + r_d(t) \right] e^{j2\pi f_0 t} \tag{2.7}$$

where $r_d(t)$ is the demodulated random component defined as

$$r_d(t) = \sum_{i=1}^{N} A_i(t) e^{-j\varphi_i} . \tag{2.8}$$

The sum of phasors in Eq. (2.8) results in a phasor of magnitude A_T and phase φ_T

$$r_d(t) = \sum_{i=1}^{N} A_i(t) e^{-j\varphi_i} = A_T e^{-j\varphi_T} \tag{2.9}$$

Let us focus on the demodulated signal $y_d(t)$, i.e., the signal from which the carrier sinusoid has been removed:

$$y_d(t) = y(t) e^{-j2\pi f_0 t} = \varepsilon_d(t) + A_T e^{-j\varphi_T} \tag{2.10}$$

The signal $y_d(t)$ can be expressed in terms of its amplitude $V(t)$ and phase $\xi(t)$ or decomposed into its real and imaginary components indicated by subscripts "Re" and "Im", respectively:[61]

$$y_d(t) = V(t)e^{j\xi(t)} = y_{d,\mathrm{Re}}(t) + jy_{d,\mathrm{Im}}(t) \tag{2.11}$$

where

$$\begin{aligned}
y_{d,\mathrm{Re}}(t) &= \varepsilon_{d,\mathrm{Re}}(t) + A_T\cos(\varphi_T),\\
y_{d,\mathrm{Im}}(t) &= \varepsilon_{d,\mathrm{Im}}(t) - A_T\sin(\varphi_T).\\
V(t) &= \sqrt{E^2(t) + A_T{}^2 + 2E_T(t)A_T\cos(\theta+\varphi_T)}\\
\xi(t) &= \arctan\left\{\frac{\varepsilon_{d,\mathrm{Im}}(t) - A_T\sin(\varphi_T)}{\varepsilon_{d,\mathrm{Re}}(t) + A_T\cos(\varphi_T)}\right\}
\end{aligned}$$

Note that the signal displayed in the conventional B-mode image is the echo amplitude $V(t)$ (after logarithmic compression). Here we expressed the demodulated coherent component $\varepsilon_d(t)$ in terms of its amplitude $E(t)$ and phase $\theta(t)$. The variables $y_d(t)$, $y_{d,\mathrm{Re}}(t)$, $y_{d,\mathrm{Im}}(t)$, $V(t)$ and $\xi(t)$ are random variables because of the random nature of the variables A_T and ϕ_T.[55] Their statistical properties depend on the statistics of the scattering process that define the values of A_T and ϕ_T. Therefore, the analysis of the statistical properties of $y_d(t)$ can, in principle, help us in our task of identifying parameter estimation regions with different scattering properties. The first logical step is to look at the first order statistical properties of $y_d(t)$ defined by its probability density function. The mathematical expression for the probability density function of $y_d(t)$ can be derived from the characteristic function $\Phi(\mathbf{u})$, which is the expected value of the Fourier kernel:[64]

$$\Phi(\mathbf{u}) = \int e^{j\mathbf{u}\cdot\mathbf{y_d}}\, p(\mathbf{y_d})\, d\mathbf{y_d} \tag{2.12}$$

The complex signal $y_d(t)$ is represented as a 2-dimensional phasor (vector) with components $\mathbf{y_d}=[y_{d,\mathrm{Re}}, y_{d,\mathrm{Im}}]$. $p(\mathbf{y_d})$ is the probability density function of $\mathbf{y_d}$. In order to move forward with the analysis, some assumptions have to be made about the scattering medium. The assumptions will be divided into two groups, general and circumstantial. The general assumptions will be ubiquitous in this work and will hold in all the analyzed scattering conditions:

I. The amplitudes and phases of the individual scattered waves in the random component, A_i and φ_i, are independent of each other.[58]

II. The scatterers are spatially randomly distributed within the resolution cell. As a consequence the individual phases φ_i are uniformly distributed between 0 and 2π.[58,65]

The circumstantial assumptions will depend on the particular scattering condition that is analyzed. The most common set of assumptions applied in Quantitative Ultrasound are those leading to diffuse scattering, which are:[55,65,66]

1. The number of scatterers within the resolution cell is constant and asymptotically large.
2. There is no coherent component within the resolution cell, i.e., $\varepsilon(t)=0$. As a consequence, $y_d(t)$ only contains the random component, and its amplitude $V(t)$ and phase $\xi(t)$ are equal to the amplitude $A_T(t)$ and phase $\phi_T(t)$ of the random component.

As a consequence of the general assumptions and these circumstantial assumptions, $p(\mathbf{y_d})$ can be expressed as the product of the probability density functions of the independent amplitude A_i and phase ϕ_i of the individual scattered waves:[59,67]

$$p(\mathbf{y}_\mathbf{d})d\mathbf{y}_\mathbf{d} = \prod_{i=1}^{N} p(A_i)p(\varphi_i)dA_i d\varphi_i \tag{2.13}$$

Substituting Eq. (2.13) into Eq. (2.12) and considering the uniform distribution of the phase we get

$$\Phi(\mathbf{u}) = \prod_{i=1}^{N}\left[\int_0^{2\pi}\frac{1}{2\pi}\int_0^{\infty} e^{j\mathbf{u}\bullet\mathbf{A_i}}\, p(A_i)dA_i d\varphi_i\right] \tag{2.14}$$

Expressing the vector $\mathbf{u}=Ue^{j\zeta}$,

$$\Phi(\mathbf{u}) = \left[\int_0^{\infty}\left\{\int_0^{2\pi}\frac{1}{2\pi}e^{jUA_i\cos(\zeta-\varphi_i)}d\varphi_i\right\}p(A_i)dA_i\right]^N \tag{2.15}$$

The expression within braces defines a Bessel function of the first kind and order zero $J_0(UA_i)$. Therefore, $\Phi(\mathbf{u})$ becomes the expected value over the probability density function of the individual amplitudes A_i of the Bessel function $J_0(UA_i)$ [59]

$$\Phi(\mathbf{u}) = \left[\int_0^{\infty} J_0(UA_i)\,p(A_i)dA_i\right]^N = \left\langle J_0(UA_i)\right\rangle^N$$

Normalizing the total signal by $N^{1/2}$ to keep the mean intensity constant,[58,68] we now consider the assumption of N being asymptotically large. This is a realization the Central Limit Theorem. Under this condition

$$\lim_{N\to\infty}\Phi(\mathbf{u})=\lim_{N\to\infty}\left\langle J_0(UA_i)\right\rangle^N=e^{-U^2<A_i^2>/4} \tag{2.16}$$

This is just the characteristic function of a zero-mean circular Gaussian distribution with variance $\sigma^2=<A_i^2>/2$:[28,62,65]

$$p(\mathbf{y_d})=p_{CG}(y_{d,\mathrm{Re}},y_{d,\mathrm{Im}})=\frac{1}{2\pi\sigma^2}\exp\left\{-\frac{{y_{d,RE}}^2+{y_{d,\mathrm{Im}}}^2}{2\sigma^2}\right\} \tag{2.17}$$

The value of σ^2 is related to the mean of the squared scattering cross sections of the scatterers within the resolution cell.[28,58,69] Thus, under the assumptions of the Central Limit Theorem, the real and imaginary parts of the demodulated signal $y_d(t)$ are zero-mean Gaussian distributed random variables with the same variance. Performing a transformation to polar coordinates, the probability density function of the amplitude $V(t)$ of $y_d(t)$ becomes a Rayleigh distributed random variable:[28,61]

$$P_{\mathrm{Rayleigh}}(V)=\frac{V}{\sigma^2}\exp\left\{-\frac{V^2}{2\sigma^2}\right\} \tag{2.18}$$

The mean μ_V and variance ${\sigma_V}^2$ of the Rayleigh distributed amplitude V are:[29]

$$\mu_V=\sqrt{\frac{\pi\sigma^2}{2}},\quad \sigma_V^2=\left(\frac{4-\pi}{2}\right)\sigma^2 \tag{2.19}$$

As a consequence, the signal-to-noise ratio SNR_V has a fixed value of [29,61]

$$\mathrm{SNR}_V=\frac{\mu_V}{\sigma_V}=\sqrt{\frac{\pi}{4-\pi}}=1.913 \tag{2.20}$$

The phase of $y_d(t)$, $\xi(t)$, is also uniformly distributed between 0 and 2π. The intensity of the backscattered echo is defined by the square of the amplitude:

$$I(t)=V^2(t) \tag{2.21}$$

Further transforming Eq. (2.16), the probability density function of $I(t)$ is exponential of the form

$$P_{Exp}(I) = \frac{I}{2\sigma^2}\exp\left\{-\frac{I}{2\sigma^2}\right\} \tag{2.22}$$

with mean μ_I, variance σ_I^2 and SNR_I

$$\mu_I = 2\sigma^2,\ \ \sigma_I^2 = 4\sigma^4,\ \ SNR_I = \frac{\mu_I}{\sigma_I} = 1 \tag{2.23}$$

This condition in which the real and imaginary parts of the demodulated echo signal are jointly zero-mean Gaussian random variables and the echo amplitude is Rayleigh distributed is referred to as **diffuse scattering** or **fully-developed speckle**.[29,61] Under this condition, tissue information such as the effective scatterer size can be obtained through the second order statistics of the echo signals. As discussed in Chapter 1, this condition is very difficult to be fulfilled in breast tissue.[55]

When a deterministic source of coherence is present in the backscattered echo signal ($\varepsilon(t)\neq 0$), the characteristic function becomes[55]

$$\Phi(\mathbf{u}) = e^{j\mathbf{u}\cdot\boldsymbol{\varepsilon}}\prod_{i=1}^{N}\left[\int_0^{2\pi}\frac{1}{2\pi}d\varphi_i\int_0^{\infty}e^{j\mathbf{u}\cdot\mathbf{A}_i}\,p(A_i)dA_i\right] \tag{2.24}$$

where the vector $\boldsymbol{\varepsilon}=[\varepsilon_{d,\mathrm{Re}},\ \varepsilon_{d,\mathrm{Im}}]$. Following the same derivation as for the case of diffuse scattering where N is sufficiently large,

$$\lim_{N\to\infty}\Phi(\mathbf{u}) = e^{j\mathbf{u}\cdot\boldsymbol{\varepsilon}}e^{-U^2<A_i^2>/4} \tag{2.25}$$

Applying Fourier inversion to the characteristic function, the probability density function for this scattering scenario is a Rician distribution:[28,58]

$$P_{\mathrm{Rice}}(V) = \frac{V}{\sigma^2}I_0\left(\frac{EV}{\sigma^2}\right)\exp\left\{-\frac{E^2+V^2}{2\sigma^2}\right\} \tag{2.26}$$

where I_0 denotes the modified Bessel function of the first kind and zero order. A quantity related to this distribution is the "structure parameter" k,[58] defined as ratio of the coherent power (E^2) to the incoherent power ($2\sigma^2$):

$$k = \frac{E^2}{2\sigma^2} \tag{2.27}$$

The mean and SNR of the intensity, μ_I and SNR_I, in this case are:[58]

$$\begin{aligned} \mu_I &= E^2 + 2\sigma^2 = 2\sigma^2(\mathrm{k}+1) \\ \mathrm{SNR}_I &= \frac{E^2 + 2\sigma^2}{2\sigma\sqrt{E^2 + \sigma^2}} = \frac{k+1}{\sqrt{2k+1}} \end{aligned} \tag{2.28}$$

The term, SNR_I only depends on the ratio of the echo signal's coherent power to its incoherent or diffuse power. Notice that in this case SNR_I is always greater than 1.

Finally, we consider the randomness in the number of scatterers within the resolution cell *N*. The random variable *N* is independent of the random variables A_i and φ_i. As a consequence of these fluctuations, the backscattered signal will have larger random fluctuations than the signal under circular Gaussian statistics. Various probability density functions have been proposed to model the randomness of this variable. The Negative-Binomial distribution has been empirically found to best represent the scattering conditions observed in various situations involving the interference of scattered waves.[64,66,67,70]

Under these circumstances, the characteristic function $\Phi(\mathbf{u})$ becomes

$$\Phi(\mathbf{u}) = e^{j\mathbf{u}\cdot\boldsymbol{\varepsilon}} \prod_{i=1}^{N} \left[\int_0^\infty p(N)dN \int_0^{2\pi} \frac{1}{2\pi} d\varphi_i \int_0^\infty e^{j\mathbf{u}\cdot\mathbf{A}_i} p(A_i)dA_i \right] \tag{2.29}$$

where *p(N)* is the Negative-Binomial distribution, with mean $\overline{N}$ and normalized variance (variance over squared mean) $\nu^{-1} + \overline{N}^{-1}$ [55,58,67]

$$p(N) = p_{NB}(N \mid \overline{N}, \nu) = \binom{N+\nu-1}{N} \frac{\left(\overline{N}/\nu\right)^{\nu}}{\left(1+\overline{N}/\nu\right)^{N+\nu}} \tag{2.30}$$

The parameter $\nu \in (0, \infty)$ quantifies the amount of clustering of the scatterers. Substituting Eq. (2.30) into Eq. (2.29), the characteristic function becomes

$$\Phi(\mathbf{u}) = e^{j\mathbf{u}\cdot\boldsymbol{\varepsilon}} \left[1 + \left(\frac{\overline{N}}{\alpha} \right) \left(1 - \left\langle J_0 \left(\frac{u\nu}{\sqrt{\overline{N}}} \right) \right\rangle \right) \right]^{-\nu} \tag{2.31}$$

The corresponding limit distribution for the amplitude $V(t)$ of the $y_d(t)$ is the homodyned-K distribution[58]

$$p_{HK}(V \mid \varepsilon, \sigma^2, \nu) = V \int u J_0(u\varepsilon) J_0(uV) \left(1 + \frac{u^2\sigma^2}{2}\right)^{-\nu} du \tag{2.32}$$

The mean and the SNR of the intensity of the homodyned-K distributed amplitude are:[58]

$$\begin{aligned} \mu_I &= E^2 + 2\sigma^2\nu = 2\sigma^2\nu(k+1) \\ \mathrm{SNR}_I &= \frac{E^2 + 2\sigma^2\nu}{2\sigma\sqrt{\nu\left(E^2 + \sigma^2(2+\nu)\right)}} = \frac{k+1}{\sqrt{2k+1+1/\nu}} \end{aligned} \tag{2.33}$$

where, as for the Rician distribution, k is the structure parameter quantifying the ratio of the coherent power E^2 to the diffuse power $2\sigma^2\nu$. An interesting property of the homodyned-K distribution is that it can be expressed in a compound form in which the diffuse power of a Rician-distributed random variable is modulated by a gamma-distributed random variable, w with mean and variance equal to the clustering parameter ν:[58]

$$p_{HK}(V \mid \varepsilon, \sigma^2, \nu) = \int p_{\mathrm{Rice}}(V \mid \varepsilon, w\sigma^2)\, p_{\Gamma}(w \mid \nu)\, dw \tag{2.34}$$

The homodyned-K distribution is the more general model for the probability density of the backscattered echo amplitude that will be discussed in this work. Other distributions, such as the generalized K distribution and the Rician inverse Gaussian distributions have been proposed to deal with spatial fluctuations of the coherent component.[58] However, the effectiveness of these distributions is restricted to how well the spatial variation is modeled and therefore, they have limited application. Since the echo signals that originate in these situations are non-stationary, they will be treated as such in Chapter 3.

It is important to understand the limiting cases of the homodyned-K distribution under the asymptotic behavior of its parameters:

1. When the coherent component tends to zero, the homodyned-K distribution becomes the K distribution with closed-form expression:[62,64,65,71]

$$p_K(V \mid \sigma^2, \nu) = \frac{4A^{\nu}}{\Gamma(\nu)\left(2\sigma^2/\nu\right)^{(\nu+1)/2}} K_{\nu-1}\left(\sqrt{\frac{2\nu}{\sigma^2}}A\right) \tag{2.35}$$

   where K_p is a modified Bessel function of the second kind and order p. The mean and SNR of the intensity of the K distribution are[58]

$$\mu_I = 2\sigma^2\nu$$
$$\mathrm{SNR}_I = \frac{2\sigma^2\nu}{2\sigma^2\sqrt{\nu(2+\nu)}} = \frac{\nu}{\sqrt{\nu(2+\nu)}} \tag{2.36}$$

It is easy to note that SNR_I is always less than 1.

2. When the clustering parameter ν goes to infinity, i.e., the scatterer density is fixed, the homodyned-K distribution tends to the Rician distribution. In particular, when the coherent component is zero and the clustering parameter tends to infinity, the distribution tends to the Rayleigh distribution.

A more physically-intuitive derivation of the homodyned-K distribution is offered by Shankar *et al.*[71] and Narayanan *et al*.[65] In this derivation, the number of scatterers N is fixed but finite, and the amplitudes of the individual scattered waves A_i are modelled as a K-distributed random variable with parameter ν_s. As for the case of the Negative-binomial distribution, the choice of the K distribution has been semi-empirical.[68] Following a derivation similar to those above but using a K distribution for $p(A)$ in the characteristic function in Eq. (2.14), the probability density function of the amplitude V becomes the homodyned-K distribution with parameters ε, σ^2 and $\nu=N\,\nu_s$.[68] This suggests that the parameter ν of the homodyned-K distribution can be interpreted as an effective number of random scatterers within the resolution cell.[59,65,72] As discussed before, as the parameter ν of the K distribution increases, the model approaches the Rayleigh distribution. A large ν occurs when both N and ν_s are large. A large ν_s indicates homogeneous individual scattering amplitudes or scattering cross-sections, i.e., very similar scatterers. However, as the effective scatterer number ν decreases, the K distribution departs from the Rayleigh distribution limit. A small ν can be caused by a limited number of scatterers within the resolution cell, regardless of how homogeneous their scattering cross sections are. This can also occur when, regardless of the number of scatterers, the scattering cross sections are very heterogeneous.[59] For example, when the distribution of scatterer sizes is very broad, the backscattered echo will be dominated by the individual echoes coming from the largest scatterers (with larger cross sections), thus leading to a low effective number of scatterers ν.[65]

Figure 2.1 illustrates examples of these conditions. Each of the subfigures shows a histogram of 250,000 independent and identically distributed homodyned-K random numbers generated in MATLAB (The MathWorks, Inc., Natick, MA) using the compound representation in Eq. (2.34), i.e., modulating the incoherent power of a Rician random variable with a gamma distributed random variable with mean and variance ν. In Fig. 2.1(a), the parameters of the homodyned-K distribution were ε=0 (no coherent component), ν=100, and σ=1. The red curve on top of the histogram corresponds to the theoretical Rayleigh probability density function with the same incoherent power as the data generator. The black curve is the theoretical homodyned-K probability density function, computed using Tadayon's Matlab algorithm.[73] The Rayleigh distribution is not visible because it matches the homodyned-K probability density function for these parameters. The data for Fig. 2.1(b) was generated with a nonzero coherent component ε=5. Fig. 2.1(c) corresponds to a situation of low value of the clustering parameter (ν=5) and ε=0. Similarly to Fig. 2.1(a), the Rician probability density function (red curve) describing the data in Fig. 2.1(b) and the K distribution (red curve) in Fig. 2.1(c) coincide with the corresponding theoretical homodyned-K probability density function. Theoretical Gaussian probability density functions constructed with the same mean and variance as the data histograms are also included for reference.

To offer a quantitative analysis of the agreement between a theoretical probability density function and a data histogram as well as between two theoretical probability density functions, two parameters are presented:

1. The chi-square test (χ^2): This parameter quantifies the agreement between a theoretical PDF p and the data histogram H. It is computed as:[54,72]

$$\chi^2 = \sum_{i=1}^{N} \frac{\left(H_i - p(x_i)\right)^2}{p(x_i)} \tag{2.37}$$

   where x_i is the center of the i^{th} bin of the data histogram. Its lowest value is zero for perfect agreement between H and p, and increases over zero as H and p diverge. To compute χ^2, the 250,000 random numbers were regrouped in 500 groups of 500 numbers. The value of χ^2

was computed for the histogram (20 bins) of each group. The average and standard deviation of χ^2 across the 500 groups were then computed.

2. Kullback-Lieber Divergence (KLD): This parameter quantifies the agreement between two probability distributions $p_0(x)$ and $p_1(x)$. It is defined as:[74]

$$D = \int \ln\left(p_0(x)/p_1(x)\right)p_0(x)dx \tag{2.38}$$

It equals zero when $p_0(x)$ and $p_1(x)$ are in perfect agreement, and differs from zero as $p_1(x)$ and $p_0(x)$ diverge. In this work, it was approximated as:

$$D = \sum_{j=1}^{M} \ln\left(\frac{p_0(x_j)}{p_1(x_j)}\right)p_0(x_j)\Delta x_i . \tag{2.39}$$

The theoretical values of p_0 and p_1 were sampled at points x_j, j=1,…,M=40.

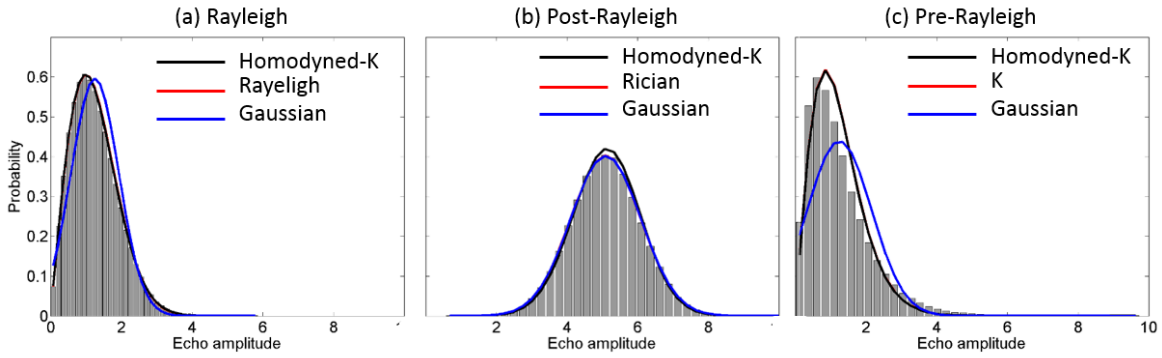

Figure 2.1 Histogram of 250,000 homodyned-K random numbers with parameters (a) ε=0, ν=100, σ=1 (approaching the Rayleigh limit), (b) ε=5, ν=100, σ=1 (approaching the Rician limit), and (c) ε=0, ν=5, σ=1 (K-limit). Continuous curves are theoretical probability density functions: homodyned-K with same parameters as the random variable generator (black), limiting distributions (red, either Rayleigh, Rician, or K), Gaussian with same mean and variance as data histogram (blue). The Rayleigh, Rician, and K distribution (red curves) in (a), (b), and (c), respectively, are not visible because they coincide with the theoretical homodyned-K distribution (black curve).

Table 2.1 presents the χ^2 and KLD values as well as the estimated SNR_V and of their squares (intensity) SNR_I. As can be observed, the values of χ^2 from the limit distributions (Rayleigh, Rician or K) are

comparable to those of the generating theoretical homodyned-K distribution. Thus, the limit probability density functions describe the statistics of the data. To put in perspective the KLD values, the KLD between the homodyned-K distribution in each of the cases in Table 1 and the Gaussian probability density function with the same mean and variance were computed. As can be observed, the KLD values between the homodyned-K distribution and the limit distributions are smaller than those between the homodyned-K and the Gaussian distribution. This indicates that the limit distributions are good theoretical descriptors of the corresponding homodyned-K distributed data.

Table 2.1 Values of χ^2 and the Kullback-Lieber divergence (KLD) between the limiting distributions and the homodyned-K (HK) distribution for the data shown in Fig. 2.1. Also included are the KLD values between the homodyned-K and a Gaussian fit using the average and standard deviation of the random numbers.

Limit	χ^2 (limit)	χ^2 HK	KLD HK-limit	KLD HK – Gaussian	SNR_V	SNR_I
Rayleigh	0.51±1.68	0.39 ±0.90	-0.0008	0.0578	1.87±0.06	0.96±0.05
Rician	0.20±0.18	0.27±0.30	0.0018	0.0022	5.14±0.18	2.63±0.09
K	$0.3\pm2.3\times10^3$	$0.3\pm2.3\times10^3$	-0.0037	0.1493	1.38±0.36	0.62±0.07

The background just presented suggests two possible ways to perform the quantitative classification of regions regarding whether they are populated with diffuse scatterers or whether other scattering conditions exist:

- **Data-based classification:** The classification is made based on quantitative parameters measured directly from the data, such as SNR_V or SNR_I.
- **Model-based classification:** This approach makes use of estimates of the parameters from models of the probability density functions of the backscattered echo amplitude to perform the classification.

2.1.1 Data-based classification

Variations in the computed SNR from the diffuse scattering limit values have been widely used as criteria for discriminating scattering situations departing from the diffuse scenario.[61,62,71] The SNR's for the echo amplitude (SNR_V) and the echo intensity (SNR_I) in Table 2.1 are in agreement with the limit distribution trends. For the case approaching diffuse scattering, SNR_V and SNR_I are 1.87±0.06 and 0.96±0.05, respectively, both close to the limit values of 1.91 and 1. For Rician statistics, SNR_V and SNR_I are larger than the diffuse scattering limit. For the case of a low effective number of scatterers they are lower than 1.91 and 1, respectively. When the values of SNR_V and SNR_I are above those of the diffuse scattering limits, the situation is referred to as "Post-Rayleigh" scattering.[61,55,75] Post-Rayleigh scattering is commonly associated with the presence of a source of coherent scattering within the resolution cell, such as when scatterers are spatially distributed with some degree of organization or when there is a dominant scatterer or specular reflector contributing to most of the total echo from a particular resolution cell. Under the assumption that the realizations of the resolution cell within the Parameter Estimation Region are populated with identically distributed samples of the scattering process, the coherent source $\varepsilon(t)$ would have to repeat itself within each of these samples. The only physically feasible phenomenon leading to this situation is the presence of periodically arrayed scatterers whose mean separation is smaller than the size of the resolution cell.[58,72] In this case, the demodulated amplitude and phase of the coherent component can be expressed as the sum of phasors representing the waves scattered by each of the periodic scatterers

$$\varepsilon_d(t) = E(t)e^{j\theta(t)} = \sum_{k=1}^{M} E_k(t)e^{j\theta_k(t)} \tag{2.40}$$

where $E_k(t)$ and $\theta_k(t)$ are the amplitude and phase of the wave scattered by the k^{th} periodic scatterer within the resolution cell. M is the total number of periodic scatterers within the resolution cell. Each phase $\theta_k(t)$ is related to the distance r_k from a particular scatterer to the face of the transducer:

$$\theta_k = 4\pi f_c \frac{r_k}{c}. \tag{2.41}$$

When the coherent component originates from the presence of an isolated, strong scatterer or specular reflector in addition to random scatterers within the resolution cell, this component would only be present in a limited number of resolution cells within the PER due to the short-range nature of this scattering scenario.[28,58] Therefore, as explained in the Introduction, the statistics of the signal will depend on the position of the resolution cell and the echo signal will be non-stationary. As a consequence, the spatial PER-based analysis of the echo signal's first order statistics is not the correct approach to analyze this situation. Alternative techniques are discussed in Chapters 3 and 4.

When the values of SNR_V and SNR_I are below the diffuse scattering limits, the scattering situation is referred to as 'Pre-Rayleigh" scattering.[61,55,75] This situation has been most frequently attributed to a low number of scatterers within the resolution cell or a large variance in the scattering cross sections.[55,59,65,76] As described above, both situations lead to a low effective scatterer number density. This property of SNR_V and SNR_I to vary across pre-Rayleigh, Rayleigh, and Post-Rayleigh conditions makes them possible candidates for the task of discriminating PERs with statistics other than Rayleigh.

2.1.2 Model-based parameters

The homodyned-K distribution is the most general model for stationary backscatter echo signals. Its parameters k and ν provide a direct quantification of structural properties of the array of scatterers. However, the lack of a closed-form expression for its mathematical representation complicates the estimation of k and ν.[63,77] Since its introduction in the ultrasound field in 1994 by Dutt and Greenleaf,[55] methods for estimating the parameters k and ν have been improving in terms of the accuracy and precision. One of the most recent methods proposed by Hruska and Oelze[56] relies on the closed-form expression of fractional moments of the homodyned-K distribution. In the algorithm, theoretical expressions for the SNR, skewness, and kurtosis of fractional powers of the echo amplitudes are obtained for a range of values of k and ν. Then, the SNR, skewness and kurtosis are measured from echo data from the material or tissue of interest. The measured and theoretical values of these parameters are compared.

This method has been proven to provide accurate and precise estimates of the parameters. However, when the value of *k* decreases below 0.2, the bias and standard deviation of the estimates can be as large as a factor of 6 and a factor of 3 from the expected value, respectively.[56] This is an important limitation when trying to estimate a value close to zero if trying to identify a PER with diffuse scattering. Another complication that was found in the implementation of this method in this work was the difficulty in computing the theoretical values of the SNR, skewness, and kurtosis.

An alternative to the general homodyned-K distribution is the Nakagami distribution, which has been proposed as a good approximation to the homodyned-K.[58,63,68,76] Its advantages over the homodyned-K distribution are that its probability density function has a closed-form expression, thus making it mathematically tractable. Furthermore, the estimation of its parameter is relatively easy compared to those of the homodyned-K distribution.[78] The probability density function was proposed by Nakagami *et al.*[78] for dealing with fading radar echoes.[78,80] It has the following form:

$$p_{Nakagami}(A \mid m,\Omega) = \frac{2m^m}{\Gamma(m)\Omega^m} A^{2m-1} \exp\left\{-\frac{mA^2}{\Omega}\right\} \tag{2.42}$$

where *m* is the "shape parameter" and Ω is a "scaling parameter". [77,63,76] The intensity corresponding to the Nakagami distributed amplitude follows a gamma distribution of the form: [77,63,76]

$$p_{\Gamma}(I \mid m,\Omega) = \frac{m^m}{\Gamma(m)\Omega^m} I^{m-1} \exp\left\{-\frac{mI}{\Omega}\right\} \tag{2.43}$$

Various works have demonstrated the effectiveness of the Nakagami parameter *m* to distinguish zones with Post-Rayleigh and Pre-Rayleigh statistics from those with Rayleigh.[77,63,76] When the shape parameter *m* is equal to 1, Eq. (2.42) reduces to the Rayleigh distribution in Eq. (2.18) with $\Omega=2\sigma^2$. Regions where $m>1$ are associated with Post-Rayleigh statistics, while zones where $m<1$ are identified as having Pre-Rayleigh statistics. Shankar *et al.*[77] demonstrated that the parameter *m* has the ability to distinguish zones with different scatterer concentrations as long as the Rayleigh limit has not been reached. It has been suggested that the parameter *m* could be interpreted as an effective number of scatterers, analogous to ν, but with a limited dynamic range (while ν tends to infinity in the Rayleigh limit, *m* tends to 1).[68,77]

Most of the applications of the Nakagami distribution in ultrasound estimate the Nakagami parameter *m* as the squared signal-to-noise ratio of the echo signal intensity.[63,76,77,79] Alternatively, the relative simplicity of the Nakagami probability density function makes it possible to define the maximum likelihood estimator (MLE) for both parameters *m* and Ω.[68] The joint probability density function for a vector **V** composed of a set of K independent and identically distributed (i.i.d.) samples of the amplitude *V* is:

$$\mathbf{V}=\{V_k\}_{k=1}^{K} \overset{iid}{\sim} p(\mathbf{V}\mid m,\Omega)=\prod_{k=1}^{K}\frac{2m^m}{\Gamma(m)\Omega^m}V_k^{\,2m-1}\exp\left\{-\frac{mV_k^{\,2}}{\Omega}\right\} \tag{2.44}$$

The MLE estimators are obtained by finding the values of *m* and Ω that maximize $p(\mathbf{V}|m,\Omega)$. After taking the logarithm of $p(\mathbf{V}|m,\Omega)$ (a monotonic transformation that does not affect the maximization process), the derivative with respect to Ω becomes:

$$\begin{aligned}\frac{\partial}{\partial\hat{\Omega}}\ln\left[p(\mathbf{V}\mid\hat{m},\hat{\Omega})\right]&=\frac{\partial}{\partial\hat{\Omega}}\left\{\sum_{i=1}^{K}\left[\ln 2+\hat{m}\ln\hat{m}-\ln\Gamma(\hat{m})-\hat{m}\ln\hat{\Omega}+(2\hat{m}-1)\ln V_k-\frac{\hat{m}}{\hat{\Omega}}V_k^{\,2}\right]\right\}=0\\ -\frac{K\hat{m}}{\hat{\Omega}}+\frac{K\hat{m}}{\hat{\Omega}^2}\overline{V^2}&=0\\ \hat{\Omega}&=\overline{V^2}\end{aligned} \tag{2.45}$$

where the overbar indicates the sample average and the hat ^ indicates an estimate. Following the same procedure for the parameter *m*

$$\begin{aligned}\frac{\partial}{\partial\hat{m}}\ln\left[p(\mathbf{V}\mid\hat{m},\hat{\Omega})\right]&=\frac{\partial}{\partial\hat{m}}\left\{\sum_{i=1}^{K}\left[\ln 2+\hat{m}\ln\hat{m}-\ln\Gamma(\hat{m})-\hat{m}\ln\hat{\Omega}+(2\hat{m}-1)\ln V_k-\frac{\hat{m}}{\hat{\Omega}}V_k^{\,2}\right]\right\}=0\\ \ln\hat{m}+1-\frac{\partial\ln\Gamma(\hat{m})}{\partial\hat{m}}-\ln\hat{\Omega}+\overline{\ln V^2}-\frac{\overline{V^2}}{\hat{\Omega}}&=0\\ \ln\hat{m}-\psi(\hat{m})&=\ln\overline{V^2}-\overline{\ln V^2}\end{aligned} \tag{2.46}$$

where $\psi(x)$ is the digamma function of *x*. The MLE estimator is obtained by minimizing the difference between the expression on the left and the expression on the right of the equal sign.[68] The function in the left is plotted in Fig. 2.2.

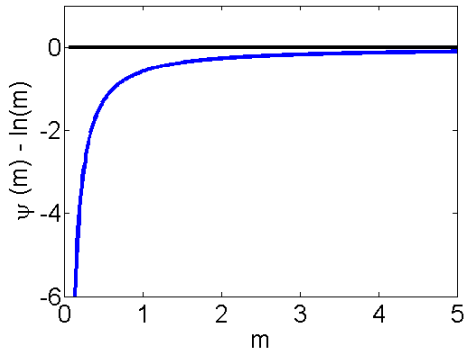

Figure 2.2 Dependence on the Nakagami shape parameter *m* of the left term in Eq. (2.46).

Since this function increases monotonically with *m*, a simple binary search algorithm can be used to obtain the value of *m*.[68] The MLE estimator of *m* has been shown to provide the least minimum squared error when compared to other estimators, such as one based on the squared SNR of the intensity.[68] Thus, the MLE estimator of the Nakagami parameter *m* will be used in our analysis as a discriminating parameter.

Figure 2.3 and Table 2.2 replicate Fig. 2.1 and Table 2.1, respectively, but with the Nakagami distribution instead of the limiting distributions. The MLE estimators of the two Nakagami parameters *m* and Ω were obtained from each of the 500 realizations of 500 numbers generated using the compound expression for the homodyned-K distribution. The inter-group average and standard deviation of the parameters are reported in Table 2.2. As expected, the *m* parameter approaches 1 for the Rayleigh distribution, increases above 1 for the Post-Rayleigh case, and decreases below 1 for the Pre-Rayleigh case. The inter-group average of the parameters were used to construct the Nakagami probability density function (red). The low KLD and χ^2 values, relative to those of the homodyned-K distribution in the case of the Rayleigh and Post-Rayleigh scenarios, indicate that the Nakagami distribution is a good model for these situations. The agreement between the Nakagami distribution and the homodyned-K distribution and data histogram in the pre-Rayleigh case is not as good as in the other two cases, but it still is a good representation of the data.

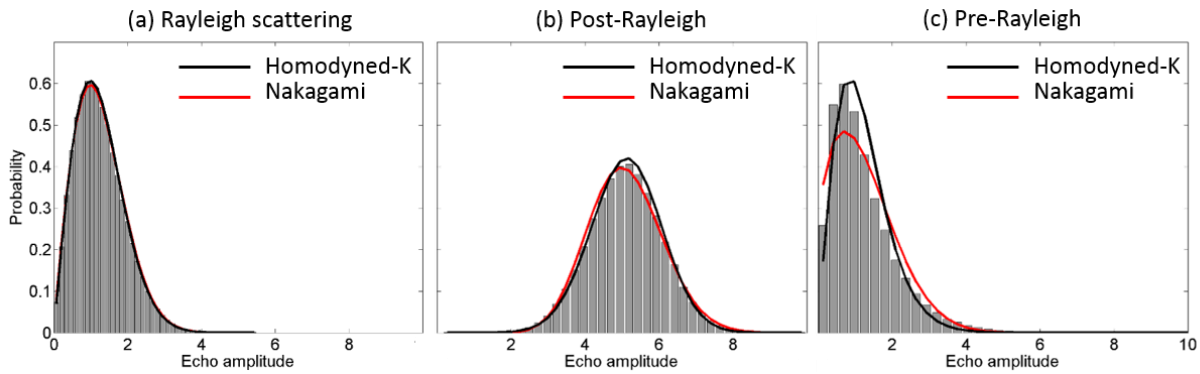

Figure 2.3 Histogram of 250,000 homodyned-K random numbers with parameters (a) ε=0, ν=100, σ=1 (approaching the Rayleigh limit), (b) ε=5, ν=100, σ=1 (approaching the Rician limit), and (c) ε=0, ν=5, σ=1 (Pre-Rayleigh domain). Continuous curves are theoretical probability density functions: homodyned-K with same parameters as the random variable generator (black), and Nakagami approximation (red).

Table 2.2 Values of χ^2 and the Kullback-Lieber divergence (KLD) between the limiting the Nakagami distribution and the homodyned-K distribution for the data shown in Fig. 2.3.

Limit	χ^2 (Nakagami)	KLD HK-Nakagami	Shape parameter M	Scale parameter Ω
Rayleigh	0.33±0.43	-2.341×10^{-4}	0.98±0.05	2.02±0.09
Rician	2±26	0.0072	6.60±0.43	27.00±0.46
K	$5\pm67\times10^{4}$	0.0521	0.64±0.03	2.40±0.17

2.1.3 Nakagami T statistic

In this section we use statistical decision theory to define an optimum statistic to decide whether the scattering properties of the medium correspond to diffuse scattering or not. This analysis makes use of the good properties of the Nakagami distribution to approximate the homodyned-K distribution. Let us start by defining our two hypothesis:

- **Null Hypothesis – H_0:** The medium contains a large number of randomly distributed weak scatterers leading to diffuse scattering. Under this condition, the amplitude of the backscattered

echo follows a Rayleigh distribution, while the intensity (squared amplitude) follows an exponential distribution.

- **Alternative Hypothesis – H_1**: The medium contains a scattering field that leads to conditions other than diffuse scattering. The amplitude distribution of the backscattered echo signals can be approximated in this case by a Nakagami distribution, while the intensity follows a Gamma distribution.

In the following analysis the intensity will be the random variable of interest due to better tractability of the expressions.[52] To define the statistic, K independent and identically distributed samples of the intensity $\{I_k\}$, k=1,…,K are drawn from a particular PER location. These samples are represented by a vector **I**. It is important to remind the reader that we are assuming the backscattered echo signals are stationary. Therefore, axial intensity trends caused by attenuation and diffraction are considered negligible for small PERs or have to be corrected for by means of time-gain compensation. The hypotheses presented above can be expressed mathematically as follows:

$$\begin{aligned} \mathrm{H}_0\text{:}\quad & \mathbf{I}=\{I_k\}_{k=1}^{K} \overset{i.i.d.}{\sim} p(\mathbf{I}\,|\,\mathrm{H}_0)=\prod_{k=1}^{K}\frac{1}{\Omega_0}\exp\left\{-\frac{I}{\Omega_0}\right\} \\ \mathrm{H}_1\text{:}\quad & \mathbf{I}=\{I_k\}_{k=1}^{K} \overset{i.i.d.}{\sim} p(\mathbf{I}\,|\,\mathrm{H}_1)=\prod_{k=1}^{K}\frac{m^m}{\Gamma(m)\Omega_1{}^m}I_k{}^{m-1}\exp\left\{-\frac{mI_k}{\Omega_1}\right\} \end{aligned} \tag{2.47}$$

Note that the exponential distribution under H_0 was expressed in terms of $\Omega_0=2\sigma^2$ to make clear that this distribution can be obtained from the gamma distribution under H_1 when m=1. The parameters m, Ω_1 and Ω_0 are unknown. According to the Neyman-Pearson criterion, the Generalized Likelihood Ratio Test (GLRT) offers optimum performance for the detection of H_1 from H_0.[74] The GLRT is given by the ratio of the probability density functions under H_1 over H_0 using the maximum likelihood estimators $\hat{m}$, $\hat{\Omega}_1$, and $\hat{\Omega}_0$ for the parameters m, Ω_1 and Ω_0, which were presented in the previous sections. The Generalized Likelihood Ratio is therefore

$$\hat{\Lambda} = \frac{p(\mathbf{I} \mid \mathrm{H}_1)}{p(\mathbf{I} \mid \mathrm{H}_0)} = \frac{\prod_{k=1}^{K} \frac{\hat{m}^{\hat{m}}}{\Gamma(\hat{m})\hat{\Omega}_1^{\hat{m}}} I_k^{\hat{m}-1} \exp\left\{-\frac{\hat{m} I_k}{\hat{\Omega}_1}\right\}}{\prod_{k=1}^{K} \frac{1}{\hat{\Omega}_0} \exp\left\{-\frac{I_k}{\hat{\Omega}_0}\right\}} \tag{2.48}$$

$$\hat{\Lambda} = \prod_{k=1}^{K} \frac{\hat{m}^{\hat{m}} \hat{\Omega}_0}{\Gamma(\hat{m})\hat{\Omega}_1^{\hat{m}}} I_k^{\hat{m}-1} \exp\left\{-\left(\frac{\hat{m}}{\hat{\Omega}_1} - \frac{1}{\hat{\Omega}_0}\right) I_k\right\}$$

Applying a monotonic logarithmic transformation to Eq. (2.48),

$$\ln \hat{\Lambda} = K \ln\left(\frac{\hat{m}^{\hat{m}} \hat{\Omega}_0}{\Gamma(\hat{m})\hat{\Omega}_1^{\hat{m}}}\right) + (\hat{m}-1)\sum_{k=1}^{K} \ln I_k - \left(\frac{\hat{m}}{\hat{\Omega}_1} - \frac{1}{\hat{\Omega}_0}\right)\sum_{k=1}^{K} I_k \tag{2.49}$$

The MLE estimators of Ω_0 and Ω_1 are the same, i.e., the average intensity within the PER. We rename it $\hat{\Omega}$. Therefore the statistic $T=2\ln\hat{\Lambda}_1$ can be expressed as

$$T = 2K\left\{\hat{m}\ln\hat{m} + (\hat{m}-1)\left[\overline{\ln I} - \ln \bar{I} - 1\right] - \ln\Gamma(\hat{m})\right\} \tag{2.50}$$

The advantage of this statistic relies on the fact that, for a large number of samples, its probability density function approaches a χ^2 distribution. This is a consequence of Wilks theorem[81] that states that under H_1 the T statistic is well behaved and under H_0 it follows a χ^2 distribution with one degree of freedom if the following assumptions are met:[81,82]

1. The probability density functions under H_1 and H_0 are functionally the same.
2. The composite hypothesis is nested (the number of unknown parameters of $p(I,H_1)$ is larger than the number of unknown parameter of $p(I,H_0)$).
3. The probability density function satisfies the "regularity conditions" of continuous derivatives.
4. The expected value of the derivative of the logarithmic transform of the probability density function with respect to each parameter is zero:

$$\left\langle \frac{\partial \ln p(I)}{dm} \right\rangle = \left\langle \frac{\partial \ln p(I)}{d\Omega} \right\rangle = 0$$

The first assumption is met because, as explained before, the exponential distribution or $p(I|H_0)$ is the same as $p(I|H_1)$ when the shape parameter m=1. The second assumption is met because under H_1 there are two unknown parameters m and Ω_1, while under H_0 the only unknown parameter is Ω_0. The third assumption dealing with the differentiability of the Gamma distribution holds as this distribution is a member of the exponential family.[83] Finally, assumption 4 can be easily verified

$$\begin{aligned}\left\langle \frac{\partial \ln p(I)}{dm} \right\rangle &= \left\langle \ln m + 1 - \psi(m) - \ln \Omega + \ln I - \frac{I}{\Omega} \right\rangle \\ \left\langle \frac{\partial \ln p(I)}{dm} \right\rangle &= \ln m + 1 - \psi(m) - \ln \Omega + \langle \ln I \rangle - \frac{1}{\Omega} \langle I \rangle\end{aligned} \tag{2.51}$$

For the gamma distributed I, the expectation values above are

$$\langle \ln I \rangle = \psi(m) + \ln \Omega - \ln m$$
$$\langle I \rangle = \Omega$$

Therefore

$$\left\langle \frac{\partial \ln p(I)}{dm} \right\rangle = \ln m + 1 - \psi(m) - \ln \Omega + \psi(m) + \ln \Omega - \ln m - 1$$
$$\left\langle \frac{\partial \ln p(I)}{dm} \right\rangle = 0$$

Similarly, for Ω

$$\left\langle \frac{\partial \ln p(I)}{d\Omega} \right\rangle = \left\langle -\frac{m}{\Omega} + \frac{mI}{\Omega^2} \right\rangle$$
$$\left\langle \frac{\partial \ln p(I)}{d\Omega} \right\rangle = -\frac{m}{\Omega} + \frac{m\langle I \rangle}{\Omega^2}$$
$$\left\langle \frac{\partial \ln p(I)}{d\Omega} \right\rangle = 0$$

Therefore, Wilks theorem works for the composite hypothesis studied here, and our statistic T follows a χ^2 distribution with one degree of freedom:

$$p(T \mid H_0) = \chi_1^2 \tag{2.52}$$

Knowing the distribution of the statistic T under H_0 allows us to define a threshold for the decision between H_0 and H_1 based on a particular probability of false detection β, i.e., a value T_0 for which $P(T>T_0|H_0)=\beta$. If the computed value of T is larger than T_0, the alternative hypothesis H_1 is accepted in lieu of H_0. In case it is smaller than T, H_1 is rejected and H_0 is accepted. If H_0 is accepted, the scattering conditions correspond to those in which the intensity is distributed according to an exponential distribution and, therefore, to diffuse scattering.

2.2 Aim

Most of the research about the use of data-based and model-based quantities (referred from this point forward to as parameters) to characterize the statistical properties of echo signals has been centered at using them for tissue characterization. The advantage of model-based parameters, such as the Nakagami m value, over data-based parameters, such as the SNR_I, is that a physical interpretation can be given to them.[58] Thus a more direct understanding of the properties of tissue microstructure can be achieved. Furthermore, some of these parameters, such as the effective number of diffuse scatterers ν, have been shown to provide better contrast (larger change in the mean value of the quantity) between regions with different scattering properties.[77] However, the goal here is to classify regions with different scattering properties when creating parametric images. In this context, not only the contrast but also spatial resolution and variance are important. As discussed in Chapter 1, the ability of a parametric image to display the spatial variations of a parameter depends on its spatial resolution. Spatial resolution is improved by reducing the size of the PER. However, this limits the number of samples of the backscattered echo from which the QUS parameters are estimated. As a consequence, the accuracy and precision of the estimates is compromised.[56] Some investigators have addressed effects on the accuracy of QUS parameters as the size of the PER is reduced.[63] The ability to statistically discriminate between zones of different scattering properties will depend also on the statistical variation of the estimated

parameters about their means. Therefore, the variance needs to be included in any analysis of the discriminative properties of a given parameter.

The aim of the following analysis is to identify the parameter that has the best statistical discrimination power to identify PERs in which the underlying scattering process leads to statistics other than Rayleigh or diffuse scattering. Data-based parameters and model-based parameters will be studied. In particular, attention will be paid to the effect of reductions of the PER size on the discrimination power of each of the analyzed parameters. The analysis will be done on backscattered echoes generated from a simulation tool and from tissue mimicking phantoms scanned with a clinical ultrasound scanner.

2.3 Methods

2.3.1 Experimental Design

In order to analyze the effectiveness of each of the proposed parameters to identify a parameter estimation region with scattering properties other than diffuse scattering, three topics need to be addressed:

1. How sensitive is the parameter to departures from diffuse scattering? In other words, it is necessary to quantify how much each parameter changes when the scattering statistics are other than Rayleigh statistics. This is achieved by quantifying the normalized contrast C_q of the parameter q defined as:

$$C_q = \frac{\bar{q} - \bar{q}_{\text{Rayleigh}}}{\bar{q}} \tag{2.53}$$

   where q_{Rayleigh} is the value of the parameter estimated from data known to have Rayleigh statistics. The overbar indicates the average over a set of independent estimates.

2. How large is the variation of each parameter compared to the random fluctuations of the values of the parameter? This will be quantified by means of the Contrast to Noise Ratio CNR_q of parameter q, defined as:

$$\mathrm{CNR}_q = \frac{\bar{q} - \bar{q}_{\mathrm{Rayleigh}}}{\sqrt{\sigma_q{}^2 + \sigma_{q,\mathrm{Rayleigh}}{}^2}} \tag{2.54}$$

where σ_q^2 is the variance of the estimate of parameter q, and $\sigma_{q,\mathrm{Rayleigh}}{}^2$ is the variance of the estimate of the same parameter among data known to have Rayleigh statistics.

3. How much are the discrimination properties of each parameter affected by reductions in the amount of data used in their estimation?

These three topics are addressed in the context of parametric image formation, i.e., by using Parameter Estimation Regions. The general procedure for this study is the following:

1. Two sets of radiofrequency echo data are obtained:
    a. A reference data set, generated under scattering conditions leading to Rayleigh statistics.
    b. A sample data set that is to be compared to the reference data to measure the contrast and the CNR of each of the proposed parameters.

    Each of these data sets is composed of uncorrelated echo data frames. Each frame is made up of a set of adjacent acoustic scan line signals, acquired while imaging the scattering medium with an array transducer. The amplitude and intensity of the backscattered echo signals are obtained by means of the Hilbert transform.[61]
2. A group of N_{PER} uncorrelated Parameter Estimation Regions is defined at the same depth in all of the data frames from both the sample and the reference. They are located at the same depth to limit the effects of the variation of the point spread function over the scanning depth.
3. Data-based parameters (SNR_V and SNR_I) and model-based parameters (m and T) are estimated within each parameter estimation region using the methods described above. For this purpose, only uncorrelated samples within each parameter estimation region are used.
4. The average and variance of each of the estimated parameters from the pool of N_{PER} estimates are computed and used to quantify C_q and CNR_q.

5. Steps 1-4 are repeated after reducing the size of the PERs to analyze the effect of limiting the amount of data used in the estimation of the parameters on C_q and CNR_q.

The diagram in Fig. 2.4 describes graphically this procedure. The procedure was applied for two general scenarios.

- **Scenario A**: Identification of PERs that exhibit signals with pre-Rayleigh statistics from zones of Rayleigh statistics. In this experiment, the sample data frames were obtained from scattering conditions in which the number of scatterers within the resolution cell were reduced over those necessary to achieve Rayleigh statistics (see descriptions of simulated and physical phantoms below).
- **Scenario B**: Identification of PERs exhibiting with post-Rayleigh statistics from zones of Rayleigh statistics. In this experiment, the sample data frames contained a source of coherent scattering introduced by a lattice of periodically arranged scatterers. Different configurations of the periodic lattice of scatterers were studied to analyze how these variations affected the performance of the parameters.

Scenarios A and B were set up both using simulated backscattered echo data and experimental data acquired from tissue mimicking phantoms scanned with a clinical system. We proceed to describe the generation of backscattered echo data from the simulation tool and the data acquisition in the phantom experiment.

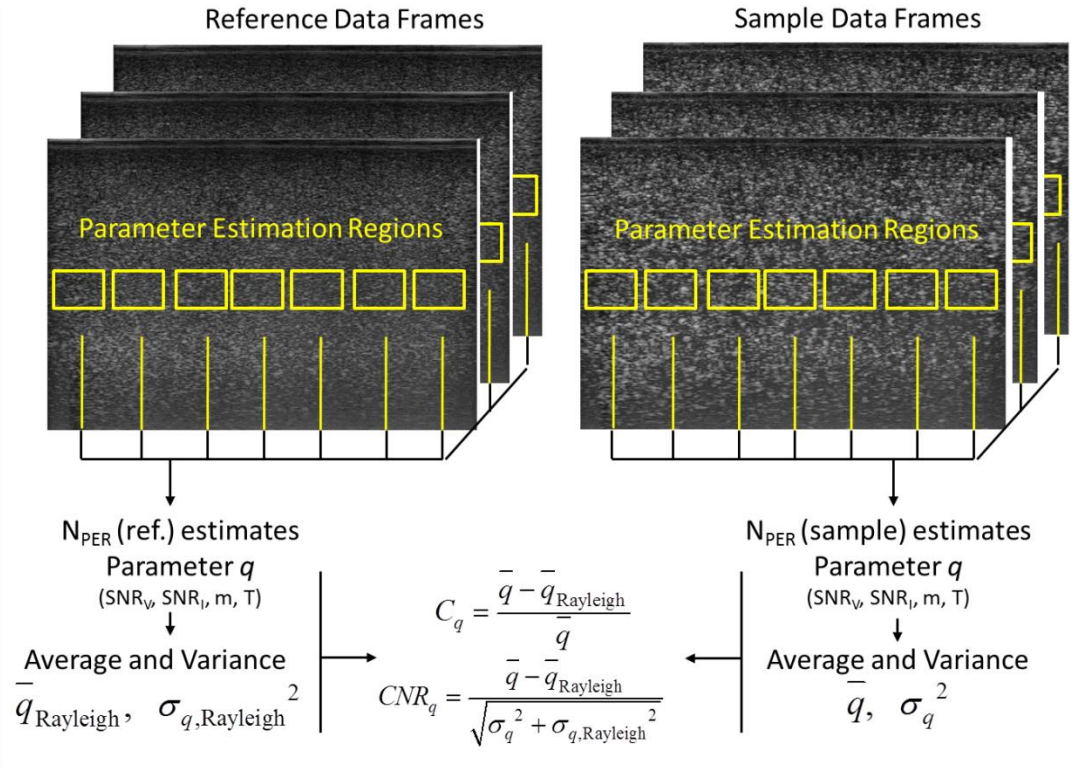

Figure 2.4 Diagram of the general procedure followed to study the discrimination properties of SNR_V, SNR_I, *m* and T from zones with Rayleigh statistics by means of the quantification of the contrast C_q and CNR_q of each parameter *q*. There were several independent parameter estimation regions in each frame of echo data, and there were several independent frames of echo data from which parameter estimates were combined to estimate statistical properties.

2.3.2 Simulations

A simulation tool was implemented that mimicked the formation of backscattered echo signals as a random walk, following methods proposed elsewhere.[61] This was achieved by convolving a mathematical acoustic pulse $h(t,z)$ with a one-dimensional array of scatterers $s(z)$:[61]

$$y(t) = h(t,z) * s(z) \tag{2.55}$$

The simulated pulse was formed by modulating a sine function of frequency f_0 with a Gaussian envelope

$$h(t) = e^{j2\pi f_0 t} e^{-t^2/2D^2} \tag{2.56}$$

The parameter D controls the duration of the modulation function and is directly related to the effective pulse duration τ. Both D and τ are also related to the pulse bandwidth. We arbitrarily define τ as the full width of the modulation function at 0.1 of the maximum. This allows us to express D in terms of τ:

$$D^2 = \frac{\tau^2}{8\ln 10} \tag{2.57}$$

The center frequency (6 MHz), -6dB fractional bandwidth (72%) were set to mimic the properties of the ultrasound transducer used in the clinic. This led to an effective pulse duration of 0.38μs, or a pulse length of 0.29mm. The propagation speed of the acoustic pulse was assumed to be 1540m/s. Thus, the wavelength of the pulse was 0.26mm.

The scattering function $s(t)$ consisted of a one-dimensional array of scatterers with a scattering function of the form:[61]

$$s(t) = \sum_{i=1}^{N_T} a_i \delta(t - 2r_i / c) \tag{2.58}$$

where a_i is the square root of the scattering cross section and r_i is the location of the i^{th} scatterer from the position of the acoustic pulse at t=0. N_T is the total number of scatterers within the simulation length. Only the amplitude and phase of the pulse was affected by the scatterer but not its frequency content. Scenarios A and B were created as follows:

- **Scenario A:** Scatterers were randomly distributed within the resolution cell according to a uniform distribution. The scattering amplitudes a_i of the scatterers were normally distributed between 0 and 1. The number of scatterers within the resolution cell was a Poisson-distributed random variable, with mean density varying from 2 to 48 scatterers within the resolution cell. As shown in Fig. 2.5, the SNR asymptotically tends to the Rayleigh limit of 1.91 as the scatterer concentration is increased. The change in SNR_V from increasing the random scatterer concentration above 48 scatterers per resolution cell is negligible. Therefore, 48 scatterers per resolution cell will be used as the concentration under which the Rayleigh statistics limit has been practically achieved.

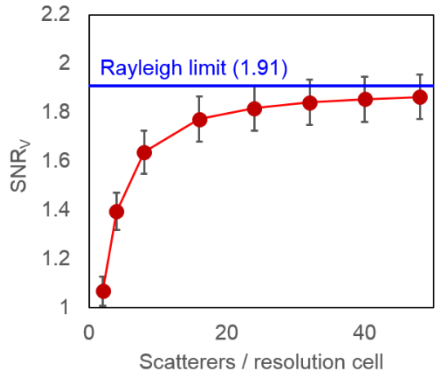

Figure 2.5 Asymptotic trend of the amplitude SNR of simulated backscattered echoes towards the Rayleigh statistics limit of 1.91.

- **Scenario B:** The scatterer distributions in this scenario included a random component with mean density of 48 scatterers per resolution cell and a set of periodically spaced scatterers with spacing ranging from 0.2 λ to 2 λ, where λ is the wavelength (0.26mm). The scattering amplitudes of the periodic scatterers were varied from a factor of 2 to a factor of 24 times the mean scattering amplitude of the random scatterers. Finally, Gaussian distributed fluctuations in the spacing of the periodic scatterers were considered, with variance equal to 5% to 200% of the mean spacing.

The reference data set included only randomly positioned scatterers with a mean density of 48 scatterers per resolution cell. Backscattered echo signals were sampled at 40MHz. The simulation was implemented in Matlab.

2.3.3 Tissue-mimicking phantoms

Four tissue mimicking phantoms were used for the purpose of evaluating the discriminating properties of the data-based and model-based parameters. Three phantoms (A, B, and, C) consisted of 15 cm × 5 cm × 15 cm homogeneous blocks of a uniform mixture of agarose gel media with glass beads acting as scattering agents. The diameter of the glass beads in phantom A ranged between 5 and 40μm (3000E, Potter Industries, Malvern, PA) with a mean concentration of 236 scatterers/mm^3. This phantom has been

used before as a reference to provide diffuse scattering.[84,85] The glass bead diameter range and bead concentration in phantom B were 75-90μm and 9 scatterers/mm^3.[85] The glass bead diameter range and bead concentration in phantom C were 126-151μm and 3 scatterers/mm^3.[85] The speed of sound and attenuation coefficient of the phantoms A, B, and C were measured using a narrowband substitution method from test samples of the background material prepared at the time of phantom fabrication. These values are reported in Table 2.3.[85] A fourth phantom, phantom D, consisted of mix of gel with glass beads with a diameter distribution of 5-40μm. It also included two perpendicular planes of 100μm-diameter nylon fibers spaced 400μm apart in a "T" arrangement: a horizontal plane (perpendicular to the direction of propagation of the acoustic beam) at a depth of 2.6cm, and a vertical plane starting at 2.6cm and spanning 1cm in depth. These fibers acted as a source of coherent scattering due to their periodic spacing. Because no test sample was prepared for this phantom at the time of its fabrication, its attenuation was estimated using a reference phantom method by acquiring backscattered echo data only from the background.[40] The reported speed of sound in Table 2.3 was provided by the expert who prepared the phantom.

Table 2.3 Physical properties of the tissue mimicking phantoms

Phantom	Diameter of random scatterers (μm)	Random scatterer concentration (mm^{-3})[85]	Spacing of periodic scatterers (μm)	Speed of sound (at 22°C) (m/s)	Slope of attenuation coefficient at 7.5MHz (dB/cm-MHz)
A	5-40	236	--	1543	0.64
B	75-90	9	--	1543	0.67
C	126-151	3	--	1543	0.79
D	5-40	236	400	1530	0.16

Phantoms A-D were used to address Scenarios A and B in the following way:

- **Scenario A:** Phantoms A, B, and C were scanned with a Siemens Acuson S2000 (Siemens Medical Solutions USA, Inc, Malvern, PA) using an 18L6 linear array transducer operated at 10MHz excitation frequency. This transducer is identical to the one used in our clinical protocol. The transmit focus was placed at 3cm. Radiofrequency (RF) data frames were acquired from the system's Axius Direct Research Interface.[86] RF data frames from 10 independent planes were obtained by shifting the transducer elevationally at least by one aperture. Reference data consisted of 10 RF data frames from 10 independent planes of phantom A. Figure 2.6 shows B-mode (amplitude) images of phantoms A, B, and C acquired with these parameters.

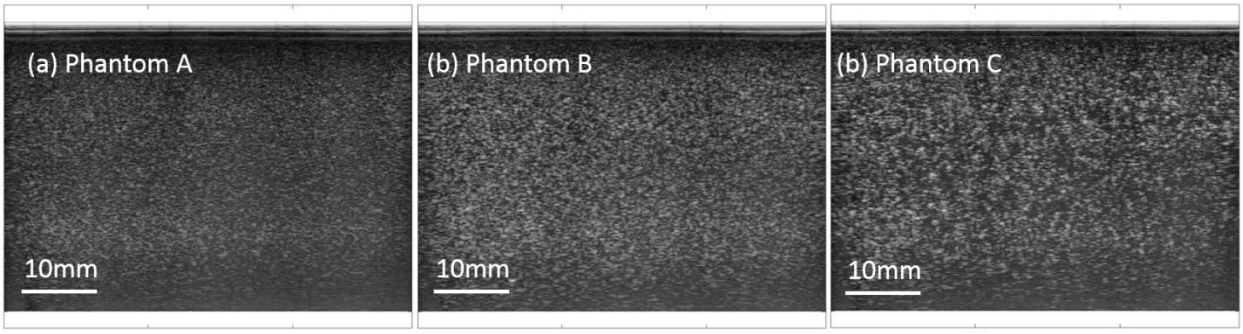

Figure 2.6 B-mode (amplitude) images of phantoms A, B, and C, scanned with the Siemens S2000 scanner using the 18L6 linear array transducer operated at 10MHz.

- **Scenario B:** In this experiment phantom D was sample data and Phantom A was used as a reference. The maximum axial size of the correlation length achieved with the transducer used in the clinical protocol is still smaller than the spacing among the fibers in this phantom. To overcome this limitation, the lower-frequency 9L4 linear array transducer available on the Siemens Acuson S2000 was used to scan the phantoms. The probe was operated at 4MHz. As discussed below, the axial size of the resolution cell in this case was larger than the 400μm spacing of the fibers in phantom D. B-mode images of phantoms A and D scanned with the 9L4 transducer and these parameters are shown in Fig. 2.7. Only three independent data frames of the fiber plane could be obtained.

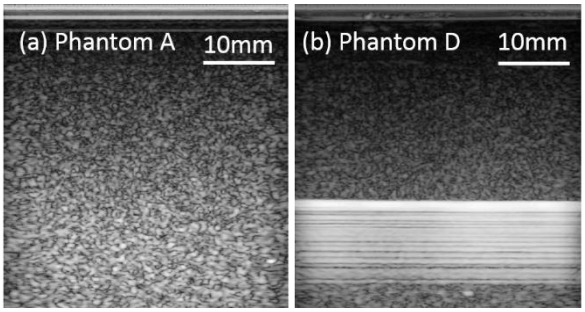

Figure 2.7 B-mode (amplitude) images of phantoms A and D, scanned with the Siemens S2000 scanner using the 9L4 linear array transducer operated at 4MHz.

2.3.4 Parameter Estimation

The data-based parameters (SNR_V and SNR_I) and the model-based parameters (m and T) were estimated using a PER approach. In the case of the simulations, each of the 3000 echo signals for each scatterer configuration were grouped in sets of 10 frames of 300 simulated scan lines. Each frame of radiofrequency data, either simulated or obtained from the clinical system, was transformed into envelope data by means of the Matlab's Hilbert transform function.

Parameters were estimated as described above using only uncorrelated echo data. Because adjacent acoustic scan lines for both the 18L6 and 9L4 transducers are spaced less than a beam width apart, it was necessary to estimate the separation among uncorrelated samples of the experimental backscattered echo signals. According to Wagner *et al.*[28] the intensity correlation area can be used as a measure of the smallest independent sampling area of the backscattered echo signal. The size of the correlation area is given by the pulse length in the axial direction and the beam width in the lateral direction. Thus, in the case of the simulations, only samples separated by one pulse length within the PER were used for parameter estimation. All scan lines were used since they were formed independently.

In the case of the experiments, the correlation area was quantified by measuring the lateral and axial correlation lengths. These were defined as the range of spatial lags (samples in the axial direction, acoustic lines in the lateral direction) over which the one-sided correlation coefficient of the echo intensity remained above 0.2. The lateral correlation coefficient was defined as: [87-92]

$$\rho_L(\Delta) = \frac{1}{N_j}\sum_{j=1}^{N_j}\frac{\sum_{i=1}^{N_i}\left[\left(X_{j,i}-\overline{X_j}\right)\left(X_{j+\Delta,i}-\overline{X_{j+\Delta}}\right)\right]}{\sqrt{\sum_{i=1}^{N_i}\left[\left(X_{j,i}-\overline{X_j}\right)^2\left(X_{j+\Delta,i}-\overline{X_{j+\Delta}}\right)^2\right]}} \tag{2.59}$$

where $X_{j,i}$ is the intensity value of the i^{th} axial sample of the segment of the j^{th} acoustic scan line included in a selected correlation region spanning N_i samples axially (5mm) and N_j adjacent scan lines (15 mm laterally) in the reference data frame. The upper bar indicates the axial sample average. Under this criterion the axial and lateral correlation lengths when scanning with the 18L6 transducer at 10MHz (Scenario A) were 0.13mm and four adjacent acoustic scan lines, respectively. In the axial direction, we define the "pulse echo correlation length" as the full width of the two-sided correlation curve at a 0.2 level, i.e., twice the one-sided axial correlation length or 0.26mm. This is an estimate of the pulse length.[28] The corresponding correlation lengths when scanning with the 9L4 transducer at 4MHz were a pulse-echo correlation length of 0.51mm (larger than the fiber spacing in phantom D) and a lateral correlation length spanning five adjacent scan lines.

The PER sizes ranged axially from 5 to 30 pulse lengths and from 5 to 30 uncorrelated scan lines in the case of the simulations. In the case of the phantom experiments with the 18L6 transducer, they ranged from 5 to 30 axial correlation lengths (1.3mm to 7.8mm) and 5 to 30 lateral correlation lengths (2.5mm to 14.9mm). For the 9L4 experiment, a single PER size of 12 axial × 12 lateral correlation lengths (6.1mm × 5.3mm) was used. A total of 100 uncorrelated PERs from each simulated scenario were obtained. A total of 36 uncorrelated PERs were obtained for the phantom-based analysis in Scenario A. A total of 9 uncorrelated PERs could be obtained from the three independent data frames in Scenario B.

2.4 Results

Results will be presented in four sections: Scenario A (Rayleigh vs pre-Rayleigh) with simulated backscattered echoes, Scenario A with phantom-based results, Scenario B (Rayleigh vs post-Rayleigh) with simulated data, and Scenario B with phantom-based results.

2.4.1 Scenario A-Simulations

Figure 2.8(a) shows the normalized contrast C_q for a simulated tissue mimicking phantom with a random scatterer concentration of 2 scatterers per resolution length, as a function of the size of the Parameter Estimation Region (PER) expressed as multiples of the pulse length and number of uncorrelated scan lines. Each color curve corresponds to a different parameter: SNR_V (blue), SNR_I (green), Nakagami shape parameter *m* (cyan) and Nakagami *T* statistic (black). Since the first three parameters are expected to decrease as the random scatterer concentration decreases below that necessary to achieve the diffuse scattering limit, C_q and CNR_q are expected to be negative. In order to compare with the positive C_q and CNR_q from the statistic *T*, the negative values are shown here as positive. The model-based parameters led to about 60% higher contrast than the data-based parameters. This is one of the main reasons behind the interest in model based parameters for tissue characterization.[62] In general, the contrast remains constant when the PER size included at least 10 pulse lengths × 10 uncorrelated scan lines. This means that if there is any dependence of the parameter value on the amount of data used for its estimation, the same effect is presented in the estimation of the value from the reference, so the difference is not affected. Figure 2.8(b) shows the contrast-to-noise ratio CNR_q in the same format as Fig. 2.8(a). Negative values of CNR_q from SNR_V, SNR_I and *m* are shown as positive for comparison with *T*. In general, CNR_q increases as the PER size increases. This is expected as the variance of the estimates is reduced as the amount of data used for the estimation increases. The CNR_q from SNR_V and the Nakagami *m* are comparable and start to be significantly larger than the CNR_q from the Nakagami *T* statistic for a PER size larger than 15 axial × 15 lateral correlation lengths.

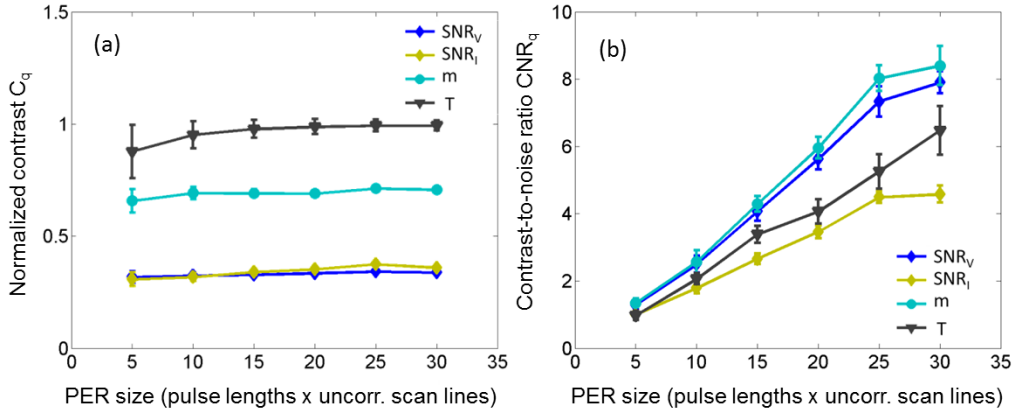

Figure 2.8 (a) Normalized contrast C_q and (b) Contrast-to-Noise CNR_q of the investigated parameters as a function of the PER size (pulse lengths × uncorrelated scan lines) from simulated echo signals. The simulated sample had a random scatterer concentration of 2 scatterers per resolution cell. The simulated reference had a random scatterer concentration of 48 scatterers per resolution length. C_q and CNR_q based on SNR_I, SNR_V, and Nakagami parameter m were negated.

Figure 2.9 shows CNR_q as a function of the random scatterer concentration for a PER size of 15 pulse lenghts × 15 uncorrelated scan lines. CNR_q increases as the simulated scatterer concentration decreases, as expected. Differences among the different parameters were, in general, not significant for concentrations larger than 8 scatterers per resolution cell. Additionally, the CNR_q was practically zero for concentrations larger than 24 scatterers per resolution cell.

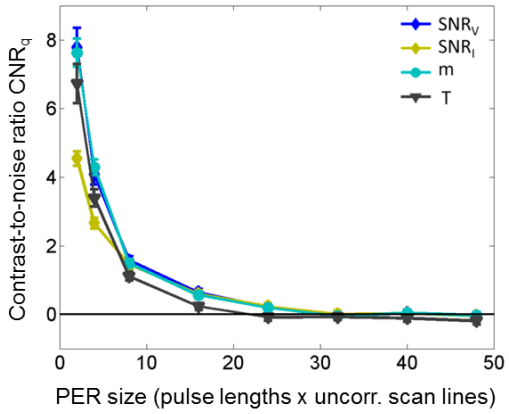

Figure 2.9 CNR$_q$ of the investigated parameters as a function of the random scatterer concentration for a PER size of 15 pulse lengths × 15 uncorrelated scan lines from simulated echo signals. The simulated reference had a random scatterer concentration of 48 scatterers per resolution length. Values from SNR$_V$, SNR$_I$ and *m* were negated.

2.4.2 Scenario A – Phantom experiment

Figure 2.10(a) shows the normalized contrast C_q obtained experimentally from tissue mimicking phantom C (lowest random scatterer concentration of 3 scatterers/mm) as a function of the size of the Parameter Estimation Region (PER), expressed as multiples of the axial and lateral correlation lengths. As before, negative C_q values from SNR_V, SNR_I and *m* are presented as positive. C_q from SNR_V, *m* and *T* were approximately independent of the size of the Parameter Estimation Region. SNR_I slightly decreases with PER size. The large error bars of the Nakagami *T* statistic depict the large variance in the estimation of the parameters. This fact shows in Fig. 2.10(b) displaying CNR_q as a function of the PER size. The large variance of the Nakagami *T* statistic estimates significantly reduces the CNR_q compared to the values from other parameters. As in the case of the simulations, CNR_q increases with PER size. As in simulations in Fig. 2.8(b), SNR_V and the Nakagami parameter *m* were found to provide the largest CNR_q in zones with pre-Rayleigh statistics.

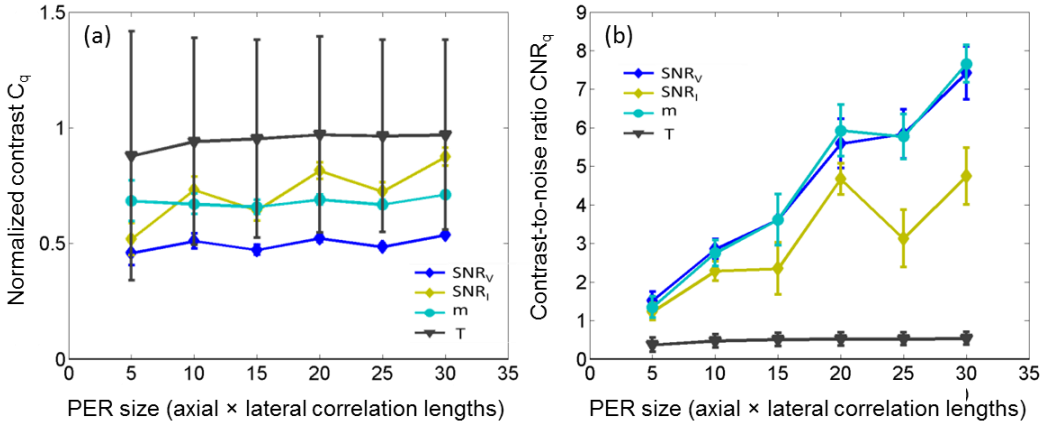

Figure 2.10 (a) Normalized contrast C_q and (b) Contrast-to-Noise CNR_q of the investigated parameters as a function of the PER size (axial × lateral correlation lengths) obtained from the phantom-based experiment. The phantom with pre-Rayleigh statistics is phantom C (3 scatterers/mm³). The reference data came from phantom A (236 scatterers/mm³). C_q and CNR_q based on SNR_V, SNR_I, and the Nakagami parameter m were negated.

Figure 2.11 shows CNR_q as a function of the random scatterer concentration for a PER size of 15 axial × 15 lateral correlation lengths corresponding to 4mm axially × 5.2mm laterally with the 18L6 transducer. Scatterer concentrations are classified as "Low" (phantom C, 3 scatterers/mm^3), "Medium" (phantom B, 9 scatterers/mm^3) and "High" (phantom A, 236 scatterers/mm^3). As for C_q, the CNR_q values from SNR_V, SNR_I, and *m* are shown as positive. As in the case of the simulations, CNR_q increases as the scatterer concentration decreases. As commented before, the large variance of the Nakagami *T* statistic significantly reduces its CNR_q and reduces its discrimination power. SNR_V and the Nakagami parameter *m* offered the largest CNR_q values.

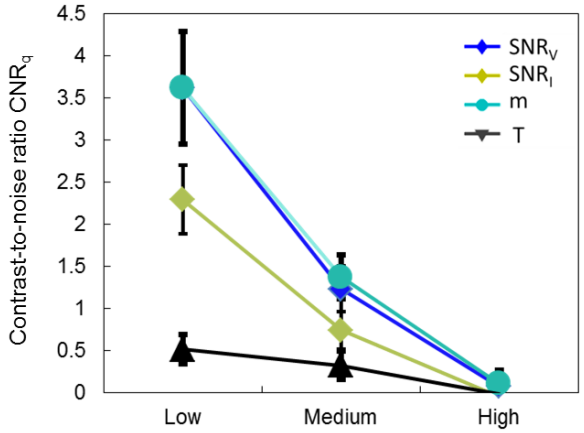

Figure 2.11 CNR$_q$ of the investigated parameters as a function of the random scatterer concentration for a PER size of 15 axial × 15 lateral correlation lengths from phantom-based experiment. Low concentration (phantom C, 3 scatterers/mm^3), Medium concentration (phantom B, 9 scatterers/mm^3), and High concentration (phantom A, 236 scatterers/mm^3). The simulated reference data were uncorrelated data frames from phantom A. Values from SNR$_V$, SNR$_I$ and *m* were negated.

2.4.3 Scenario B – Simulations

Now the effectiveness of each of the parameters to identify PERs with Post-Rayleigh statistics is explored. Figure 2.12(a) shows C_q for each of the four studied parameters as a function of the PER size for a simulated sample having, in addition to a random component of 48 scatterers per resolution length, a periodic array of scatterers separated by 0.5λ (the choice of this particular spacing will be discussed below). The periodically spaced scatterers had scattering amplitude 12 times that of the randomly positioned scatterers. As in the case of Scenario A, reductions in the amount of data used for the estimation of the parameter do not seem to affect the contrast of the parameters. This trend was not changed by variations in the ratio of the coherent power to incoherent power or by the introduction of variance in the scatterer spacing. The largest contrast is obtained with the Nakagami *T* statistic, followed by the Nakagami shape parameter *m*. As mentioned before, this is one of the reasons why model-based parameters have been selected by researches in applications of tissue characterization. As in the case of Scenario A, the variance of the estimates affects their discrimination power. Figure 2.12(b) shows CNR$_q$

as a function of the PER size under the same simulated conditions as in Figure 2.12(a). The highest CNR is achieved with SNR_V, although the advantage over SNR_I and the Nakagami *T* statistic is small. The lowest value is obtained with the Nakagami shape parameter *m*.

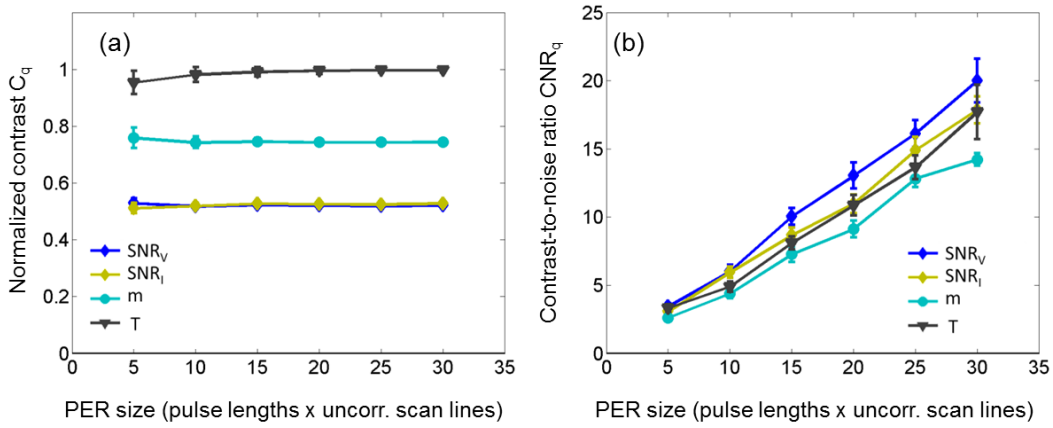

Figure 2.12 (a) Contrast C_q and (b) CNR_q of the investigated parameters as a function of the PER size (pulse lengths × uncorrelated scan lines). The simulated sample had a diffuse scatterer concentration of 48 scatterers per resolution cell and a coherent component of periodically spaced scatterers (0.5λ spacing). The periodically spaced scatterers had scattering amplitude 12 times that of the randomly positioned scatterers. The simulated reference had a random scatterer concentration of 48 scatterers per resolution cell.

Figure 2.13 shows the contrast-to-noise ratio CNR_q of the four parameters explored as a function of the scatterer spacing. The CNR_q values of the four parameters follow the same trend as observed with the scatterer spacing: the maximum CNR_q value occurs at a spacing equal to 0.5λ. As the spacing is reduced below this value, CNR_q decreases until it becomes practically zero at a value of 0.3λ. As the spacing is increased above 0.5λ, CNR_q starts decreasing down to a minimum at a 0.78λ spacing. Above this scatterer spacing CNR_q increases again and reaches a maximum at a spacing of about 0.90λ, although of smaller value than the peak at 0.5λ. Then CNR_q values from SNR_V, SNR_I and *m* decrease as the spacing is further increased. The values are zero at about 1.3λ for SNR_V and *m*, and are zero at about 1.5λ for SNR_I. Then, the CNR_q values of these parameters become negative. In the case of the Nakagami *T*

statistic, its CNR_q values decrease beyond 0.90λ, reach a minimum at about 1.15λ and start increasing again. This complicated trend will be explained in the Discussion section of this chapter. From this point forward, results will be presented for a spacing of 0.5λ.

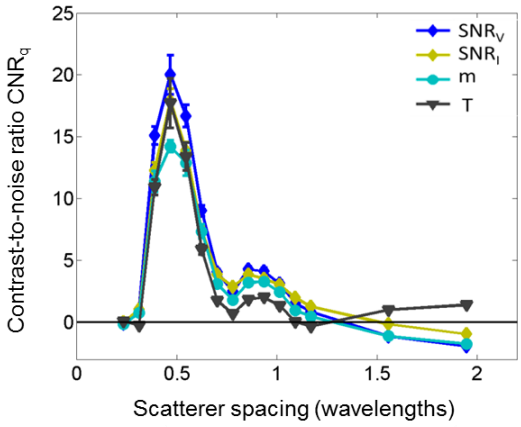

Figure 2.13 CNR_q of the investigated parameters as a function of the scatterer spacing expressed in multiples of the pulse wavelength (λ=0.26mm). The scattering cross section of the periodic scatterers was 12 times larger the scattering cross section of the random scatterers. The PER size was 30 pulse lengths × 30 uncorrelated scan lines. The simulated reference had a random scatterer concentration of 48 scatterers per resolution cell.

Figure 2.14 shows the effect of varying the scattering cross section of the periodic scatterers on CNR_q. The scattering cross section is expressed in terms of the ratio of the total scattering power of the periodic scatterers to that of the randomly located scatterers per periodic scatterer, as defined by Varghese and Donohue:[93]

$$R = 10\log_{10}\left[\frac{\frac{1}{N_{\text{Per}}}\int_{t_0}^{t_0+\Delta t} y_{\text{Periodic}}{}^2(t)dt}{\int_{t_0}^{t_0+\Delta t} y_{\text{Random}}{}^2(t)dt}\right] \tag{2.60}$$

where N_{Per} is the number of scatterers within the resolution cell, $y_{\text{Periodic}}(t)$ is the RF signal only from the backscattered echoes from periodic scatterers, and $y_{\text{Random}}(t)$ is the RF signal only from the backscattered echoes from random scatterers.[93] The N_{per} normalization guarantees that R does not depend on the number

of periodic scatterers within the integrated interval. Also, note that *R* corresponds to an empirical definition of the structure parameter *k* defined in Eq. (2.27) when normalized by the number of periodic scatterers within the resolution cell. The scatterer spacing was 0.5λ and the PER size was 15 pulse lengths × 15 uncorrelated scan lines. As can be observed, CNR_q values for all parameters increase more steeply from values close to zero when the coherent to incoherent power ratio becomes larger than a value of *R* of -5dB.

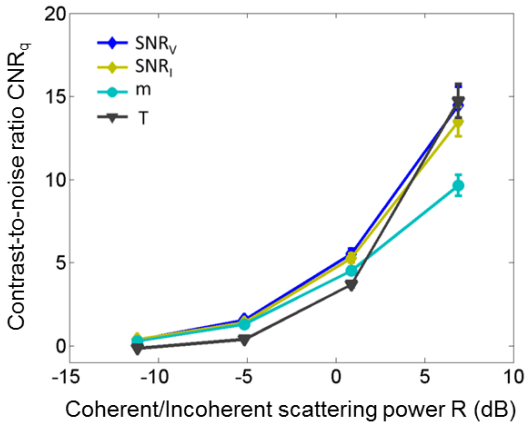

Figure 2.14 CNR_q of the investigated parameters as a function of the ratio of coherent to incoherent power ratio *R* in dB. The simulated sample had a diffuse scatterer concentration of 48 scatterers per resolution cell and a coherent component of periodically spaced scatterers (0.5λ spacing). The PER size was 15 pulse lengths × 15 uncorrelated scan lines. The simulated reference had a random scatterer concentration of 48 scatterers per resolution cell.

Figure 2.15 shows the effect of introducing random variations in the spacing between periodic scatterers on the CNR_q of the investigated parameters. As previously described, the spacing was modeled as a Gaussian distributed random variable with mean equal to 0.5λ and standard deviation varying from 0.05 to 2 times the mean spacing. In general, CNR_q decreases as the standard deviations of the spacing increases above 0.1 times the mean spacing. The Nakagami *T* statistic presented the largest reduction in its CNR_q values caused by the random variations of the periodic scatterer spacing. Both data-based parameters (SNR_V and SNR_I) had the largest CNR_q values for all range of values of the standard deviation of the spacing that were explored. When the standard deviation of the spacing is equal to the mean

spacing, the scattering statistics become Pre-Rayleigh. This is because the periodic component (now more random than periodic) has a higher scattering cross section than the incoherent component and, therefore, dominates the backscattered echo signal. Since the concentration of the periodic scatterers is lower than the concentration of scatterers in the reference, the values of SNR_V, SNR_I and *m* are smaller than in the diffuse scattering limit, and therefore, their CNR_q values are negative. As the standard deviation of the mean spacing is further increased, the spreading among the initially perfectly periodic scatterers increases. This effectively reduces the periodic scatterer concentration and makes the CNR_q values of SNR_V, SNR_I and *m* more negative. Similarly, the CNR_q values of the Nakagami *T* statistic increase after reaching a minimum when the spacing standard deviation is equal to the main spacing.

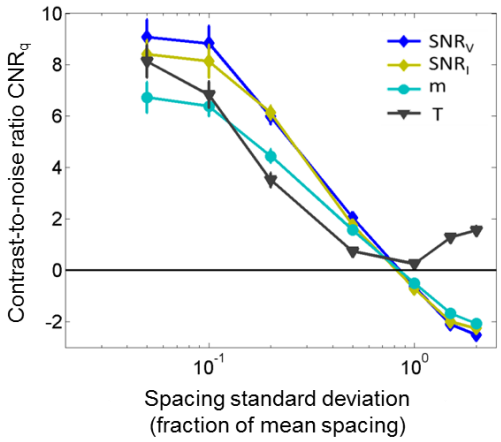

Figure 2.15 CNR_q of the investigated parameters as a function of the standard deviation of the periodic scatterer spacing expressed as a fraction of the mean spacing. The simulated sample had a diffuse scatterer concentration of 48 scatterers per resolution cell and a coherent component of periodically spaced scatterers (0.5λ spacing). The PER size was 15 pulse lengths × 15 uncorrelated scan lines. The simulated reference had a random scatterer concentration of 48 scatterers per resolution cell.

2.4.4 Scenario B – Phantom Experiment

Figure 2.16 shows the contrast to noise ratio C_q for each of the four parameters evaluated from a region with periodic scatterers for (a) simulations and (b) phantom-based results. As a reminder, the coherent component in the phantom experiment was generated by the vertical plane of nylon fibers, with fibers

separated by 0.4mm or 1.1λ. The simulations include results from a simulated periodic array of scatterers with spacing equal to 1.1λ (0.28mm). The PER size was 12 pulse lengths × 12 uncorrelated scan lines in the simulation case, and 12 axial × 12 lateral correlation lengths in the case of the phantom experiment. Although the absolute CNR_q values differ between the simulations and the experiments, the trend among the different parameters is very similar. The highest CNR_q values are achieved with SNR_V and SNR_I. The larger variance of the estimates in the phantom experiment than in simulations can be attributed to the difficulty in achieving perfect perpendicularity between the fibers and to a limited number of uncorrelated planes of backscattered echo data in the phantom experiments.

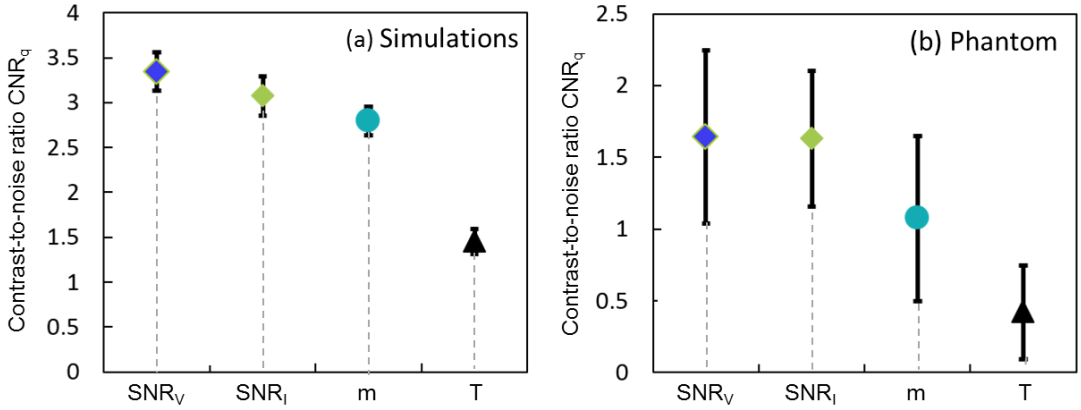

Figure 2.16 CNR_q values of the four investigated parameters for (a) simulated data and (b) the phantom-based experiment. In both situations the coherent component was generated by periodically arranged structures with spacing equal to 1.1λ (0.28mm in the simulations, and 0.4mm in the phantom experiment). The PER size was 12 pulse lengths × 12 uncorrelated scan lines in the simulations, and 12 axial × 12 lateral correlation lengths in the case of the phantom experiment.

2.5 Discussion

In this chapter, four parameters were investigated for use in identifying Parameter Estimation Regions that might have scattering statistics other than Rayleigh statistics, i.e., diffuse scattering. The estimation of all of the proposed parameters makes use of independent and identically distributed samples of the backscattered echo signal. Two different scenarios were explored: departure from Rayleigh statistics due

to a low concentration of randomly positioned scatterers within the resolution cell, i.e., pre-Rayleigh statistics, and departure from Rayleigh statistics due to the presence of a source of coherent scattering, i.e., post-Rayleigh statistics. Two of the parameters, the SNR of the echo amplitude (SNR_V) and the SNR of the echo intensity (SNR_I) are simple measurements of the first-order statistics of the echo data. The other two parameters are derived from modeling the first-order statistics with a particular probability density function, the Nakagami distribution. The effectiveness for the classification was quantified in terms of both the contrast and the contrast-to-noise ratio of the parameters with respect to their values under Rayleigh statistics. Two important results were that the contrast of the parameters was not affected by reductions in the PER size. This indicates that if any bias is introduced by reducing the amount of data for the estimation, a similar bias would occur in the reference data, and the contrast would be the same. Also, this suggests the idea that a possible way to make a statistical decision about the significance of the difference of a parameter value with the value that would be obtained under Rayleigh conditions would be to compare that value with values obtained from a reference material and estimated with the same procedure. This idea is expanded in Chapter 4. The second result is that that the simple SNR_V offered the highest power to quantitatively discern both the Pre-Rayleigh and the Post-Rayleigh scenarios from Rayleigh statistics. The advantage of SNR_V over SNR_I in terms of the CNR_q can be attributed to the larger variance of estimates of higher order moments under the same number of samples.[72] The advantage of the SNR_V over the model-based parameters can be attributed to the fact that the Nakagami model is only an approximation to the real probability density function of the echo data.

An interesting result was the complicated dependence of the CNR_q values from all the parameters as the spacing of the periodic scatterers is varied. To understand this trend, it is necessary to understand the process of constructive and destructive interference among the echoes backscattered from the array of periodic scatterers. Consider again the coherent component introduced from a periodic array of scatterers in Eq. (2.40)

$$\varepsilon_d(t) = E(t)e^{j\theta(t)} = \sum_{k=1}^{M} E_k(t)e^{j\theta_k(t)} \tag{2.61}$$

where

$$\theta_k = 4\pi f_c \frac{r_k}{c}$$

Consider an array of N scatterers with a constant spacing Δ. If the first scatterer is assumed to be arbitrarily at location r_1=0, then Eq. (2.61) can be expressed as

$$\varepsilon_d(t) = \sum_{k=1}^{M} E_k(t)e^{4\pi f_0 k\Delta/c} \tag{2.62}$$

When the spacing Δ is an integer multiple *n* of half wavelengths,

$$\varepsilon_{\mathrm{d}}(t) = \sum_{i=1}^{N} E_i(t)\exp\left\{\left(-j2\pi\frac{nif_0\lambda}{c}\right)\right\} \tag{2.63}$$

Since λf_0=*c*, Eq. (2.63) reduces to

$$\varepsilon_{\mathrm{d}}(t) = \sum_{i=1}^{N} E_i(t)e^{-j2\pi ni} \tag{2.64}$$

The last factor is equal to 1 for every integer value of *n* or *i*. Therefore, it further reduces to:

$$\varepsilon_{\mathrm{d}}(t) = \sum_{i=1}^{N} E_i(t) \tag{2.65}$$

Therefore, all scattered waves add up in phase, leading to perfect constructive interference. When the spacing is an odd integer multiple *l* of one-fourth of the wavelength, Eq. (2.63) reduces to:

$$\begin{aligned} \varepsilon_{\mathrm{d}}(t) &= \sum_{i=1}^{N} E_i(t)e^{-j\pi li} \\ \varepsilon_{\mathrm{d}}(t) &= \sum_{i=1}^{N} E_i(t)(-1)^i \end{aligned} \tag{2.66}$$

If the scatterers are identical (same scattering cross section) and the number of periodic scatterers within the resolution cell *N* is even, then the sum in Eq. (2.66) will have an equal number of 1 and -1 values, causing perfect destructive interference and the signal from the periodic scatterers is zero. If *N* is odd, the

signal will effectively be equivalent to that from one scatterer. Even if the scatterers are not identical, a minimum in the signal from the periodic scatterers would be achieved.

A similar explanation was developed by Molthen *et al.*[54] to explain the lack of uniformity in the phase of the backscattered echoes when an array of periodic scatterers with subresolution spacing is present. This modulation of the coherent component $\varepsilon_d(t)$ also modulates the signal to noise ratio, as can be seen in Eq. (2.33) through E, the magnitude of $\varepsilon_d(t)$. Since $\varepsilon_d(t)$ is expected to have maxima at 0.5λ and 1.0λ and minima at 0.25λ and 0.75λ, the SNR_V is expected to have maxima and minima at these values. Since the SNR_V from the reference is constant, then contrast C_q and the CNR_q of SNR_V are expected to have the same maxima and minima.

The Nakagami parameter m is monotonically related to SNR_V through the equation[94]

$$SNR_V = \frac{1}{\sqrt{m\left(\frac{\Gamma(m)}{\Gamma(m+0.5)}\right)^2 - 1}} \tag{2.67}$$

Figure 2.17 shows the comparison of the estimates of the SNR_V and the Nakagami parameter obtained from the simulations and theory. Each pair of SNR_V and m estimates obtained from simulations was obtained from a different scattering scenario generating pre-Rayleigh statistics (variations in scatterer concentration) in (a) and post-Rayleigh statistics (variation of the periodic scatterer spacing) in (b). The values estimated from simulations are in good agreement with theory. Thus, the Nakagami parameter m is expected to show the same trends with variations in the spacing of the periodic scatterers as SNR_V. This agrees with Fig. 2.13. Variations from the expected locations of the maxima and minima can be attributed to the finite bandwidth of the acoustic pulse.

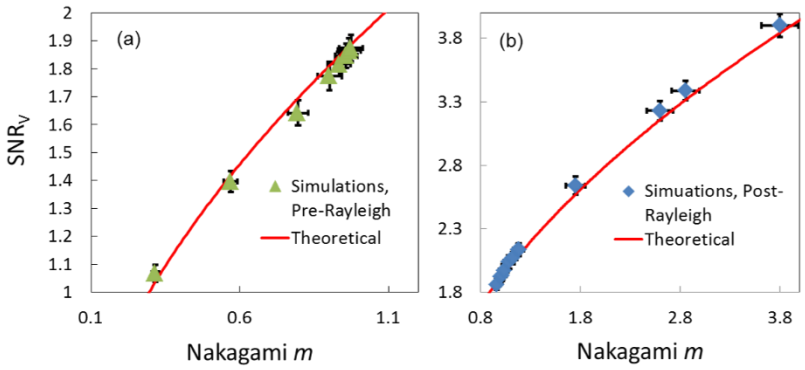

Figure 2.17 Estimates of SNR$_V$ vs estimates of the Nakagami parameter *m* under (a) pre-Rayleigh statistics conditions and (b) post-Rayleigh statistics conditions. Estimates were obtained from simulated echo data using a PER size of 30 pulse lengths × 30 uncorrelated scan lines. The red curve indicates the theoretical relationship.

Ideally, this alternate maxima and minima would keep occurring as the spacing is increased. However, this is limited by the finite length of the acoustic pulse. As the spacing is increased above one resolution cell or 1.13λ, some resolution cells may contain one of the periodic scatterers and some may not. As a consequence, the statistics of the scattering process as sampled by the resolution cell become dependent on the location of the resolution cell. Therefore, as explained by Tuthill *et al.*,[61] the spatial variations of the signal amplitude outgrow the mean value of the echo signal which is now mostly defined by the incoherent component. Thus, SNR_V decreases below the diffuse scattering limit and the statistics become apparently Pre-Rayleigh, even if a coherent component is present. As a consequence, the contrast C_q and CNR_q of SNR_V, SNR_I and *m* become progressively negative, and those of the *T* statistic gradually increase. This ambiguity between a true pre-Rayleigh condition originating from a low random scatterer number density and the apparent pre-Rayleigh condition of a periodic array of scatterers with a resolved spacing suggests the necessity of a method to differentiate the latter case from the former. These are the topics of Chapters 3 and 4.

When comparing the phantom-based results to the simulation results, the Nakagmi *T* statistics was found to perform significantly more poorly in the phantom case. This can be attributed to various factors. First, the estimation of this parameter depends on the prior estimation of the shape parameter *m*. Therefore, its

accuracy and precision will depend on the accuracy and precision of the estimate of the parameter *m*. Furthermore, the estimation of the *T* statistic depends on scaling terms such the sample average of the echo intensity (which is just the MLE estimate of the scaling parameter Ω) and its logarithm. These terms, i.e., Ω, describe the overall echo level, while *m* is more related to the shape of the probability density function. As a consequence, Ω is more susceptible to spatial variations in the echo level caused by the diffraction field and by attenuation. This was also acknowledged by Shankar *et al.*[94] Diffraction can also alter the value of the SNR and the Nakagami parameter *m* by introducing spatial variations in the size of the resolution cell within the PER. This phenomenon is exploited in Appendix A to investigate a method based on severely deforming the diffraction field to estimate the propagation sound speed using pulse-echo data. In addition, the estimation of Ω and *m* can be affected by spatial variations statistics of the backscattered echoes.[95] Further refinement of the estimation methods of Ω and *m* as those presented in Ref. 95 will remain a topic of future research interest.

The departure of SNR_V and SNR_I from the diffuse scattering limits is usually associated with a low random scatterer number density or with the presence of a source of coherence. However, combinations of these cases can also occur. It is therefore important to understand how SNR_V and SNR_I vary in these scenarios. Equation (2.29) relates SNR_I to parameters of the homodyned-K distribution. From this expression, it is possible to derive an expression for the relationship between the ratio of the coherent power to the incoherent power *k* in terms of the effective number of random scatters ν when the Rayleigh statistics limit is reached:

$$\begin{aligned} SNR_I &= \frac{k+1}{\sqrt{2k+1+1/\nu}} = 1 \\ (k+1)^2 &= 2k+1+1/\nu \\ k^2 &= 1/\nu \\ k &= \sqrt{1/\nu} \end{aligned} \tag{2.68}$$

Figure 2.18 shows a contour curve of SNR_I=1 (diffuse scattering) separating the regions where SNR_I>1 (Post-Rayleigh) and where SNR_I<1 (pre-Rayleigh). The importance of Eq. (2.68) relies on the fact that

even for finite ν and the presence of a coherent component, it is possible to obtain an SNR_I=1 when a sufficiently large source of coherent scattering is present. Clearly this does not represent an ideal diffuse scattering condition. In this sense using the parameters of the homodyned-K distribution as discriminators can resolve this ambiguity. However, as mentioned before, the high complexity of the estimation methods and the large bias when estimating low *k* values are important constraints. Thus, the development of more accurate methods to estimate the values of the homodyned-K distribution will be a topic of further investigation.

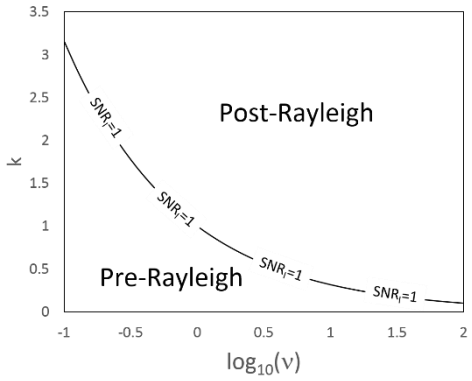

Figure 2.18 Separation of scattering domains where the statistics are pre-Rayleigh (SNR_I<1) or post-Rayleigh (SNR_I>1) for different values of the parameters *k* (ratio of the powers of the coherent component to the incoherent component) and ν (effective number of scatterers) of the homodyned-K distribution.

In conclusion, a parameter that is effective at identifying PERs with stationary backscattered echo signals that exhibit scattering statistics other than Rayleigh has been identified (the envelope SNR). The lack of any trends of the contrast of this parameter as the PER size was reduced led to the idea of comparing the values of this parameter to those in a reference material obtained with the same estimation procedure to make a statistical decision about the departure from Rayleigh statistics. The next chapter will explore situations in which the methods proposed here result ambiguous because the coherent component spatially varies within the PER, and, therefore, signals are not stationary.

Appendix A. Sound speed estimation based on backscattered echo statistics

A.1 Background

Image sharpness in diagnostic ultrasound is improved by "beam forming" the echo signals detected by individual elements within the receive aperture of an ultrasound transducer array. This process involves the coherent addition of individual channel signals. Phase differences among these signals are reduced by dynamic focusing, achieved by time-shifting each element's signal in proportion to its distance to the echo origin.[96] Conventionally time shift values are computed assuming a sound speed value c_{bf} =1540 m/s.[96-101]

However, variations in compressibility and density among different soft tissues cause their sound speed c_s to range from about 1450 m/s for fatty tissue to about 1710 m/s for muscle.[98-100] Differences between c_s and c_{bf} effectively increase the size of the three-dimensional point spread function, resulting in phase-aberration effects and image sharpness degradation.[98] The sharpest image will correspond to the case where $c_{bf} \approx c_s$.[97] These effects can be used to estimate c_s by systematically creating ultrasound images with different c_{bf} values. Various methods have been proposed to exploit this idea. Some of them rely on the presence of suitable features, such as point reflectors or tissue boundaries, to evaluate image sharpness.[99] Other methods require pre-beamformed or individual channel data, which might not be available from many ultrasound systems.[101]

The motivation behind c_s estimation is its use for real-time image quality corrections as well as a potential quantitative diagnostic parameter.[97,98] In addition, the accuracy and precision of the parameters of Quantitative Ultrasound can be compromised if previous quantifications of the mean speed of sound in tissue are not available. Nam *et al.*[84] measured the bias and variance of estimates of the attenuation coefficient obtained by means of the Reference Phantom Method. Their analysis showed that differences in the sound speed of the reference phantom and the tissue under characterization lead to an incorrect

compensation of the diffraction pattern in the power spectrum, introducing bias of up to 60% at the location of the transmit focus. This further motivates the quantification of an average sound speed value to guide in the selection of a correct reference material.

The hypothesis of the analysis presented in this Appendix can be drawn from the ability to differentiate materials with different random scatterer densities with echo statistics as observed in the simulations and phantom results of Scenario A in Chapter 2. As discussed by Narayanan *et al.*[65], changes in the number of scatterers within the resolution cell volume can also be attributed to changes in the pulse frequency and shape, and to the characteristics of the transducer. The alteration of the volume of the resolution cell that occurs during "flawed focusing" when the system's beam former sound speed c_{bf} is different from the sound speed of the medium c_s, effectively varies the number of scatterers per resolution cell. As a result, the Nakagami parameter m could be used to track this variation in the scatterer number density. The goal of the proposed method is to detect the case when the beam former sound speed matches that of the medium by finding the value of c_{bf} at which the resolution cell, and consequently, the number of scatterers it contains, are minimized. Under this condition, an estimate of the scatterer number density or of a metric related to it, such as m, will be minimized. The aim of this Appendix is to present a first exploration of this method. Because it remains a side topic of this dissertation, deeper details, such as sources of bias in c_s estimates, will be explored in the future.

A.2 Materials and Methods

The proposed sound speed estimation method is tested on a tissue mimicking phantom consisting of a homogeneous rectangular parallelepiped of tissue mimicking material with a scanning area of $10\times10\text{cm}^2$ and 16cm deep. The phantom was enclosed in an acrylic box, covered by a 25μm thick Saran-Wrap® (Dow Chemical, Midland MI, USA) scanning window. It was composed of a mixture of water-based agarose-propylene glycol mix and filtered milk. Glass beads ranging between 5 and 40μm in diameter (3000E, Potters Industries, Inc., Valley Forge, PA) were added to the phantom with a concentration of 4

mg/cm^3 to mimic subresolution incoherent scattering. Laboratory estimates of the frequency-dependent acoustic attenuation $\alpha(f)$ and sound speed c_s were obtained using 2.5cm thick test samples composed of the phantom's materials. The estimation methods consisted of a narrowband substitution technique applied to test samples. The frequency-dependence of α is represented by a power-law fit $\alpha=\alpha_0 f^n$.[102] The measured values were c_s=1544±1 m/s, $\alpha(f)=0.35f^{1.24}$ (R^2=0.99).

The phantom was scanned with a 9L4 linear array transducer on a Siemens Acuson S2000 system clinical imaging system (Siemens Medical Solutions USA, Inc, Malvern, PA). The transducer was operated in a linear scan fashion driving each element within the active aperture with a 1-cycle single burst. The driving frequency was 6.15MHz, and the pulse amplitude led to a mechanical index of MI~1.2 (as shown in the system). The system was equipped with the Axius Direct Ultrasound Research Interface (URI) that allows acquisition of beam formed RF echo signals after time-gain compensation (TGC), as well as with an engineering interface software that grants the user control over c_{bf}.

Keeping the transducer fixed on the scanning window of each phantom, 21 RF data frames of the same phantom plane were acquired. Each of these frames applied a different value of c_{bf}, ranging from 1450m/s to 1650m/s, in steps of 10m/s. This process was repeated for five image planes, spaced at least 1cm apart. Assuming a sound speed of 1540 m/s for depth calculations, the transmit (lateral) focus was kept fixed and placed about the transducer's elevational focus during data acquisition.

Two feature-independent image sharpness metrics were explored: a direct metric and an indirect metric. The direct metric is based on Wagner *et al.*'s[28] analysis of speckle statistics. Under conditions of fully developed speckle, the 2D autocovariance of the intensity data is proportional to the auto-convolution of the point spread function. Thus, image sharpness can be assessed by measuring the size of the resolution cell from the 2D autocovariance matrix. The autocovariance matrix was computed as suggested by Anderson *et al.*[98] obtaining the inverse Fourier transform of the product of the Fourier transformed intensity data $I_f(f_z,f_x)$ within the ROI:

$$C(\Delta z,\Delta y)=\frac{1}{L_z-|\Delta z|}\frac{1}{L_x-|\Delta x|}\Im^{-1}\left\{I_f(f_z,f_x)*I_f(f_z,f_x)\right\},$$
$$I_f(f_z,f_x)=\Im\left\{I(x,z)\right\}. \tag{A.1}$$

where Δz and Δx are the axial and lateral shifts, L_z and L_x are the axial and lateral dimensions of the ROI, and f_z and f_x are frequency components in the axial and lateral directions. Figure A.1 shows images of $C(\Delta z,\Delta x)$ when (a) $c_{bf}=0.95c_s$ and when (b) $c_{bf}\approx c_s$. The area over which $C(\Delta z,\Delta x)$ is significantly different than 0 increases as c_{bf} is shifted from c_s.

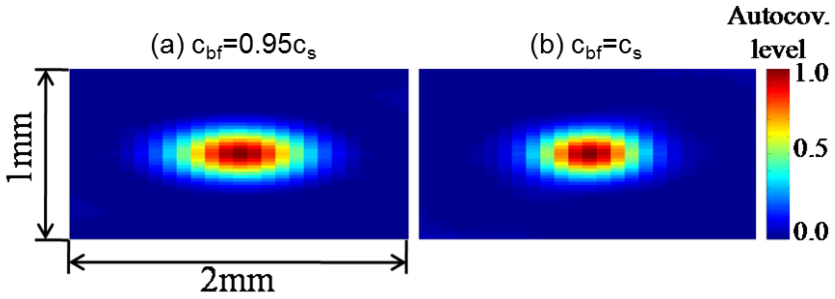

Figure A.1 2D Autocovariance when (a) $c_{bf}\approx 0.95c_s$ and (b) $c_{bf}\approx c_s$ at the location of the transmit focus. Values have been normalized to the variance, so that the autocovariance at zero shift is 1.

RF echo signals were envelope-detected and squared to obtain intensity data. A 7 mm axial × 9 mm lateral parameter estimation region was swept across the image data over a 1 cm range aligned with the transmit focus position (5 cm). Then the correlation cell size S_c was computed as the 2D integral of the autocovariance matrix including values larger than 0.5.

The indirect sharpness metric was the Nakagami shape parameter *m*. As previously discussed, the number of scatterers within the resolution cell is also expected to increase as the size of the resolution cell increases. Therefore, the Nakagami parameter *m* will approach the Rayleigh limit. This parameter was computed using its maximum likelihood estimator as described in Chapter 2. The data for the estimation was acquired over the same Parameter Estimation Region used to estimate the correlation cell size. Each variable (S_c and *m*) was independently tracked as c_{bf} was varied. The c_{bf} values at which each parameter was optimized were chosen as c_s estimates. This optimization means minimization of S_c and *m*. The c_s

estimate error was computed as an inter-plane average of the percentage difference from laboratory measurements.

A.3 Results

Figure A.2 shows the variation of (a) the Nakagami parameter *m* and (b) the correlation cell size S_c as a function of the beam former speed of sound c_{bf}. For the sake of comparison, both variables were normalized with respect to the minimum value. The most important result is that both variables follow the same trend as c_{bf} is changed and are minimized at ~1520m/s. After averaging the c_s estimates from all frames, the mean ± standard deviation were 1520±6m/s based on the Nakagami parameter *m* and 1519±3m/s based on the correlation cell size S_c. This represents a bias of 1.6% form the expected value of 1544m/s.

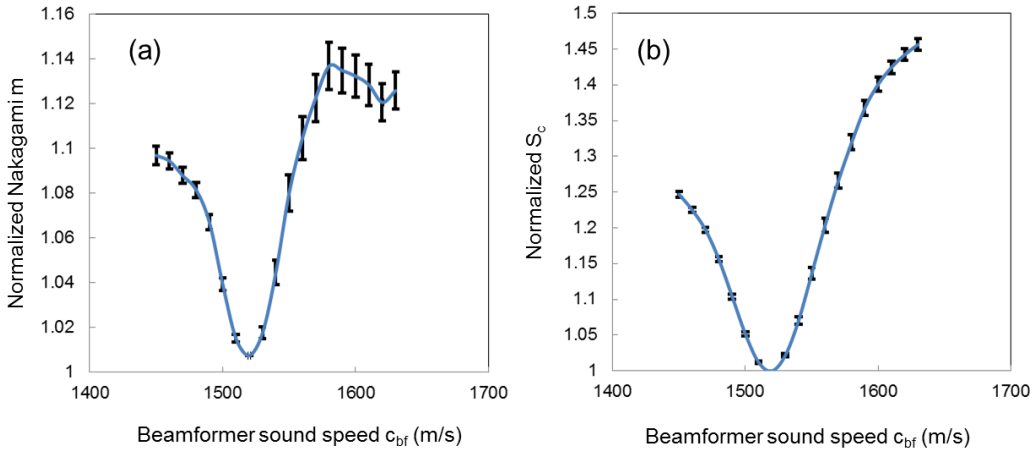

Figure A.2 Values of the (a) Nakagami parameter *m* and (b) the correlation cell size S_c as a function of the beam former sound speed. The values have been normalized to the minimum over the explored range.

Note that while S_c keeps increasing as c_{bf} departs from 1520m/s, the Nakagami parameter seems to reach a plateau. This plateau can be attributed to the resolution cell becoming large enough to achieve the Rayleigh limit. Figure A.3 shows a plot of the Nakagami parameter values as a function of the correlation cell area. The values of the Nakagami parameter increase linearly until the value of *m*=1 is achieved for

S_c= 0.84mm^2. Beyond this limit the Nakagami parameter estimates stay at m=1 regardless of the larger values of the resolution cell area.

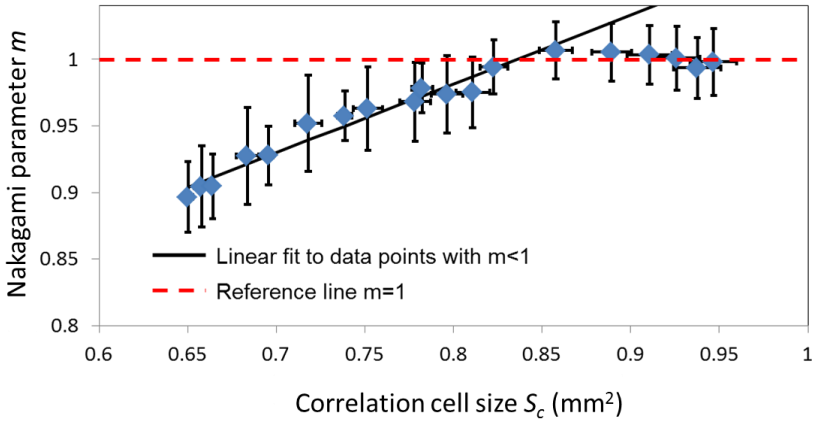

Figure A.3 Scatter plot of the estimates of the Nakagami parameter *m* and the correlation cell S_c. The black line shows a linear fit was applied to the Nakagami parameter *m* vs S_c when *m*<1. The red dashed line shows the diffuse scattering limit of *m*=1.

A.4 Discussion and conclusion

Pulse-echo estimates of the sound speed in tissue-mimicking phantoms based on the Nakagami parameter *m* estimated from backscattered echo data were comparable to laboratory measured values. An underestimation of -1.6% was observed and its cause is still been investigated. It is worth noting that the laboratory values of c_s were measured three times by two different investigators, and one year apart. The values were consistent among measurements. A similar bias from the speckle statistics based method was observed when testing the method at higher frequencies and lower beam intensities.[103] This suggests that this bias may not be due to attenuation or nonlinear propagation effects. This bias is large compared to the maximum bias suggested by Robinson *et al.*[104] for c_s to be of value as a diagnostic parameter itself. However, the estimates can be used for first order adjustments of the beam former sound speed to improve image sharpness as well as to reduce possible bias introduced in QUS estimates. Changes in the values of the Nakagami parameter *m* were correlated with variations of the resolution cell size, measured

with the techniques proposed by Wagner *et al.*,[29] as long as the Rayleigh limit (m=1) is not achieved. This suggests that materials with low scatterer concentrations could lead to a larger range of m values as c_{bf} is changed and, therefore, a better estimation of c_s.

An important advantage of the current method using the Nakagami parameter m is its relatively simplicity compared to other more complicated methods such as those in Napolitano *et al*.[99] and Yoon *et al.*[101] requiring individual channel data, the presence of sharp structures, or Fourier-domain analysis. The current implementation of the proposed method is limited by the significant amount of time (approx. 1.5 minutes) for the acquisition of multiple RF data frames with different beam former sound speed values. However, if incorporated as a real-time tool in the system, it is not expected to be more time consuming than current methods that involve multiple frame acquisition, such as multi-foci imaging. This experiment is currently being validated with simulations. The method is being applied to *in vivo* characterization of diffuse liver diseases.

3. Quantification of features from non-stationary signals

In the previous chapter, the performance of various parameters to detect the presence of a quasi-periodic lattice of scatterers was presented. The parameter that was most robust to variations in the amplitude of the scatterers, to the introduction of variance in the scatterer spacing, and to the reduction of the amount of data for the estimation of the parameter itself was the amplitude signal-to-noise ratio of the backscatter echo signal, designated SNR_V. An important limitation of this parameter is that its values became ambiguous once the spacing was larger than the size of the resolution cell. In this chapter we explore the use of the generalized spectrum of the radiofrequency signal for the detection of quasi-periodic scatterers, focusing on situations in which the mean spacing is larger than the resolution cell. The aim is to find an optimum estimator of the generalized spectrum for the detection of this source of coherent scattering. In addition, we study the influence of reducing the size of the parameter estimation region on the estimate of the generalized spectrum as well as when features in the generalized spectrum related to coherent scattering become less conspicuous because of the reduction of the scattering amplitude of the periodic scatterers and the introduction of variance in their spacing.

This chapter is divided into the following sections. Section 3.1 presents background that motivates the use of the generalized spectrum to characterize non-stationary signals and discusses previous applications in the field of ultrasound tissue characterization. Section 3.2 presents a theoretical analysis on the effects of the gating/windowing operation on the estimation of the generalized spectrum. Section 3.3 presents a simulation- and phantom-based quantitative analysis on the conspicuity of periodicity-based features of the generalized spectrum and how various estimators of the generalized spectrum affect this conspicuity. Section 3.4 presents a simulation- and phantom-based statistical analysis on the ability of the generalized spectrum to provide the expected frequency component corresponding to the spacing of the periodic scatterers. These results are correlated with the results from the conspicuity analysis in Section 3.3. Section 3.5 discusses the results from this chapter and summarizes the most important observations. The

chapter is extended in Appendix B which explores the formation of false coherence that can be detected when the phase from incoherently scattered waves is significantly different from zero due to insufficient averaging.

3.1 Background

3.1.1 Motivation

In this work, we make use of tools of statistical spectral analysis of backscattered echo signals to detect their non-stationary features. The goal of statistical spectral analysis is to estimate the spectral properties of a random process from a finite discrete time series $y(t)$ that is drawn from it.[105] To be able to use these tools, the backscattered echo signals are assumed to be harmonizable, i.e., the single realization $y(t)$ can be represented as an infinite sum of sine waves of frequency f within the Nyquist limits (-1/2 to 1/2, where the sampling frequency f_s is assumed to be 1), each one of them with amplitude and phase given by the complex number $dZ(f)$:[105-107]

$$y(t) = \int_{-1/2}^{1/2} \mathrm{e}^{i2\pi ft}\, dZ(f) \quad . \tag{3.1}$$

The complex quantity $dZ(f)$ quantifies how the amplitude and the phase of each harmonic component contributes to the signal $y(t)$ at time t. To illustrate this, let us look at a very simplified example when the signal $y(t)$ is the result of the sum of $2L+1$ sinusoids of frequency f_l, $l=-L,\ldots,0,\ldots,L$:[108]

$$y(t) = \sum_{l=-L}^{L} D_l e^{-j2\pi t f_l} \quad . \tag{3.2}$$

where each of the $2L+1$ coefficients D_l has constant magnitude and random phase uniformly distributed between $-\pi$ and π. Under these assumptions, the coefficients D_l are uncorrelated, and $D_l = D_{-l}$. In this case, $Z(f)$ becomes the sum of the coefficients D_l from l=l to the value of l corresponding to the frequency f_l immediately smaller than f:[108]

$$Z(f)=\sum_{l=1}^{l'} D_l, \quad f_{l'} < f \le f_{l'+1},\ l'=1,\ldots,\ L \tag{3.3}$$

and the differential $dZ(f)$ can be interpreted as[108]

$$dZ(f)=\begin{cases} D_l, & f = f_l \\ 0, & f \neq f_l \end{cases}. \tag{3.4}$$

This is illustrated in Fig. 3.1, which shows the line components D_l (the height of each vertical line is the magnitude of D_l for each of the $2L+1=9$ components), and how $Z(f)$ builds up from them. $Z(f)$ is also stochastic and is referred to as the *increments random process*.[108]

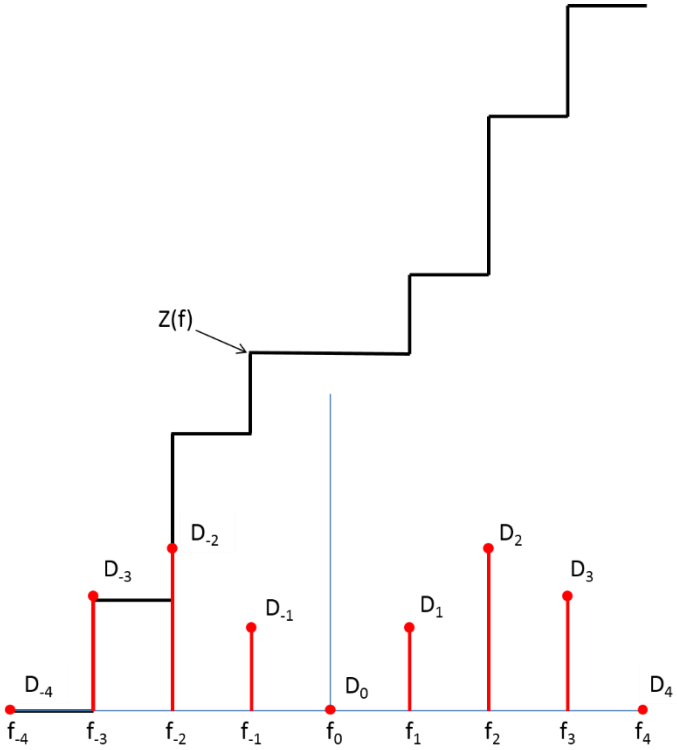

Figure 3.1 Diagram illustrating the role of the increments random measure $Z(f)$ when the signal is composed of the sum of a finite set of sinusoids. Red dots indicate the amplitude D_l of a particular harmonic component of frequency f_l.

Continuing with the overall motivation, the finite-length signal $y(t)$ can be used to obtain an estimate $C_r(t_1,t_2)$ of the autocovariance function $C(t_1,t_2)$, of the underlying random process:

$$C_r(t_1,t_2) = y(t_1)\, y^*(t_2), \tag{3.5}$$

where the subscript *r* indicates that it is obtained from a single realization of the signal. The estimate $C_r(t_1,t_2)$ is also harmonizable and can be expressed in terms of the integrated bispectrum $\gamma(f_1,f_2)$[106]

$$C_r(t_1,t_2) = \iint e^{i2\pi(f_1t_1 - f_2t_2)} d\gamma(f_1, f_2). \tag{3.6}$$

which is related to the increments random measure $Z(f)$ by:

$$d\gamma(f_1, f_2) = dZ(f_1)\, dZ(f_2). \tag{3.7}$$

The expected value of $C_r(t_1,t_2)$ is the autocovariance function[107,109]

$$C(t_1,t_2) = E\left[C_r(t_1,t_2)\right] = \iint e^{i2\pi(f_1t_1 - f_2t_2)} E\left[d\gamma(f_1, f_2)\right]. \tag{3.8}$$

In the same way, the expected value of the integrated bispectrum $\gamma(f_1,f_2)$ is the generalized spectral distribution $S^I(f_1,f_2)$ of the underlying random process[107,109,110]

$$dS^I(f_1, f_2) = E\left[d\gamma(f_1, f_2)\right] = E\left[dZ(f_1)dZ^*(f_2)\right]. \tag{3.9}$$

When $dS^I(f_1,f_2)=0$ for $f_1 \neq f_2$ Eq. (3.9) can be expressed as

$$dS^I(f_1, f_2) = \delta(f_1 - f_2)\,\mathrm{E}\left[\left|dZ(f_1)\right|^2\right]. \tag{3.10}$$

Substituting into Eq. (3.8),

$$C(t_1,t_2) = \int e^{j2\pi f(t_1 - t_2)} E\left[\left|dZ(f)\right|^2\right]. \tag{3.11}$$

This shows that, when $dS^I(f_1,f_2)=0$ for $f_1 \neq f_2$, the autocovariance function $C(t_1,t_2)$ depends only on the difference t_1-t_2.[107,109] Therefore, by definition, the random process from which $y(t)$ is drawn is stationary, and we can re-express $C(t_1,t_2)$ it in terms of $\tau = t_1 - t_2$:

$$C(\tau) = \int e^{i2\pi f\tau} E\left[\left|dZ(f)\right|^2\right]. \tag{3.12}$$

The fact that $E[dZ(f_1)\, dZ^*(f_2)]=0$ indicates that the values of $dZ(f)$ are orthogonal.[105] Thus, under stationary conditions, $Z(f)$ is referred to as a random orthogonal increments measure. The expectation value in the right side of Eq. (3.12) is, by definition, the differential of the integrated spectrum $P^I(f)$[105]

$$E\left[\left|dZ(f)\right|^2\right] = dP^I(f) \quad . \tag{3.13}$$

The integrated spectrum quantifies the cumulative energy in the stationary signal within the bandwidth from -1/2 to f.[108] If $P^I(f)$ is continuous, it can be expressed in terms of the well-known **power spectral density or power spectrum** $P(f)$

$$dP^I(f) = E\left[\left|dZ(f)\right|^2\right] = P(f)df \tag{3.14}$$

which leads to the well known Wiener-Khinchin theorem that relates the autocovariance function and the power spectral density as a Fourier pair when the random process they describe is stationary:[108]

$$C(\tau) = \int e^{i2\pi f\tau} P(f)df \quad . \tag{3.15}$$

If $dS^I(f_1,f_2)\neq 0$ for $f_1\neq f_2$, then the values of the increment random measure $Z(f)$ at different frequencies are correlated. As a consequence, the autocovariance function depends on t_1 and t_2, and not only on their difference. Thus, the signal is non-stationary.[111] This motivates the quantification of the correlation between different frequency components of the stochastic signal to detect the presence of non-stationary features in the backscattered echo signal. If the generalized spectral distribution $S^I(f_1,f_2)$ is continuous, then it can be expressed in terms of the **generalized spectral density or generalized spectrum** $S(f_1,f_2)$:[109,112]

$$dS^I(f_1, f_2) = S(f_1, f_2)\, df_1\, df_2 \quad . \tag{3.16}$$

The generalized spectrum is complex and quantifies the correlation between different frequency components of the echo signal.[107,108,111,112,113] This is illustrated in Fig. 3.2, where the spectrum Y^T of a signal $y(t)$ and its conjugate Y^{T*} at frequencies f_1 and f_2 are shown in perpendicular directions (the meaning of the superscript T will be explained below). The red lines take the values of the spectra and its conjugate at f_1 and f_2 and place their color-coded correlation in the bifrequency plane, i.e., $S(f_1,f_2)$. The values have been normalized as described below, so a value of 1 indicates maximum correlation, while a value of 0 indicates no correlation.[113] In the case shown in Fig. 3.2(a), the values off the main diagonal are close to zero, indicating that the underlying random process is stationary. In the case of Fig. 3.2(b), some of the

values of the off diagonal elements differ from zero, thus suggesting a non-stationary signal. Therefore, the detection of nonzero values in the off diagonal elements motivates the use of the generalized spectrum to detect the presence of non-stationary trends in the backscattered echo signal.[107,108,111,112,113]

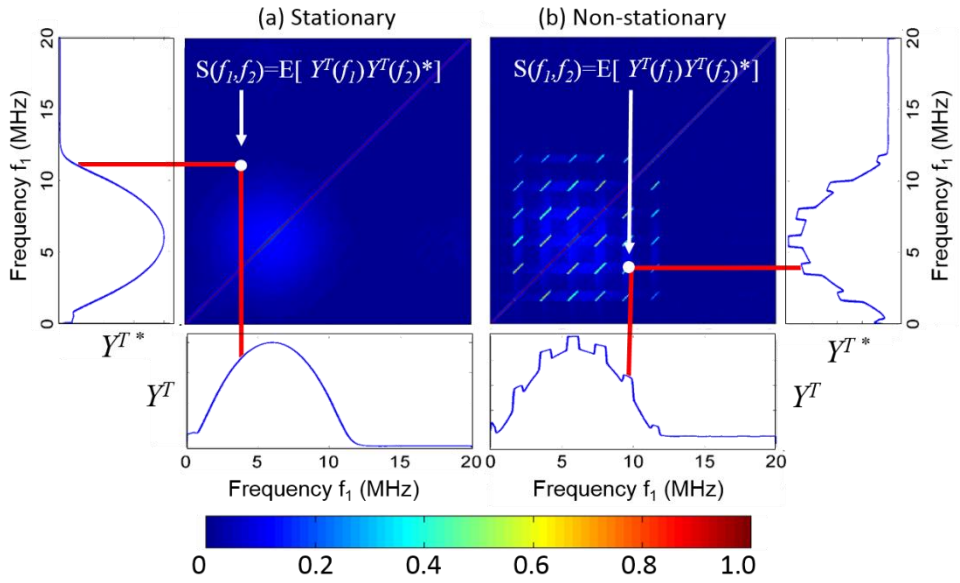

Figure 3.2 Diagram illustrating the relationship between the echo signal spectrum $Y^T(f)$ and the generalized spectrum $S(f_1,f_2)$ for two cases: (a) a stationary signal and (b) a non-stationary signal obtained from convolving a simulated acoustic pulse with an array of periodic scatterers.

3.1.2 Applications to ultrasound tissue characterization

In the field of quantitative ultrasound, applications of the generalized spectrum have been focused on situations when the signal is periodically correlated due to the presence of resolved periodicity in the scatterer distribution.[50,93.110] Under these circumstances $dZ(f_1)$ and $dZ(f_2)$ are correlated when $\Delta f=f_1-f_2$ is an integer multiple m of $1/T$, where T is the period of the periodic feature in the echo signal. From this it follows that the generalized spectrum can be represented as[50,109,111,112]

$$S(f_1, f_2) = \sum_m \delta\left(f_1 - f_2 - \frac{m}{T}\right) P_m(f) \qquad (3.17)$$

where $P_m(f)$ is a diagonal spectral density. This corresponds to the scenario shown in Fig. 3.2(b). In particular, $P_0(f)$ is usually referred to as the power spectral density.[93,114] However, this should be avoided because the power spectral density is defined under the assumption of stationarity. Other methods have been proposed to quantify the effect that a quasi-periodic array of scatterers has in the spectral properties of the backscatter echo signals. Initial attempts were done by Insana *et al.*[52] using the spectrum of the intensity signal. Based on this technique, the use of the cepstrum (Fourier transform of the logarithm of the power spectral density) was proposed as a way to reduce the system effects by applying a high pass filter after the logarithmic transformation. This is based on the transformation of the multiplicative relationship between the pulse/system spectrum and the scattering function into an additive one.[50,112-118] In addition, the additional Fourier transform aims at concentrating the periodicity signal from the fundamental component and its harmonics into a single peak.[119] Its main limitation is that the diffuse component also contributes to the regular scatterer cepstrum in a nonlinear way. Wear *et al.*[49] proposed the use of autoregressive models as an alternative to the nonparametric Fourier approach for spectral analysis. The main drawback of this technique was the dependence of the results on the selection of the autoregressive model order.[49,120] The generalized spectrum has been demonstrated to perform better than the cepstral techniques when analyzing echo signals with coherent scattering from periodic scatterers embedded in a diffuse component, particularly when variance in the spacing is present.[50,119] The main reason for this is that, since these techniques are based on properties of the power spectral density, they do not take advantage of the phase information that results from the interference of the waves scattered by individual scatterers.[50] In this sense, the advantage of using the generalized spectrum relies on the use of the phase information in addition to the magnitude information.[93,121] The generalized spectrum has been suggested to be robust to the presence of diffuse components. [93,121] Now we proceed to describe how $S(f_1,f_2)$ is estimated from the finite-length signal $y(t)$.

3.1.3 Estimation

The estimation of the generalized spectrum from data within a single parameter estimation region is done in three steps:

Step A: Spectrum estimation

First, the complex frequency spectrum of each individual scan line segment within the parameter estimation region, or PER, is obtained using the discrete Fourier transform:[105,109]

$$Y_i^T(f) = \sum_{t=0}^{N-1} g(t) y_i(t) e^{-j2\pi ft} \tag{3.18}$$

where $y(t)$, t=0,…,N-1 is a set of continuous samples of the backscatter echo signal, and $g(t)$ is a set of coefficients that define the tapering function. The superscript T indicates that the Fourier transform is obtained from a tapered version of the signal segment. The multiplication of the echo signal by a tapering function $g(t)$ results in the convolution of the Fourier transform of the signal with the Fourier transform of the tapering function in the Fourier domain. Figures 3.3(a) and 3.3(b) show a boxcar weighting function that has constant values over the span of the echo signal segment and the magnitude of its discrete Fourier transform $G(f)$[122]

$$G(f) = \sum_{t=0}^{N-1} g(t) e^{-j2\pi ft} \tag{3.19}$$

Note that this is equivalent to not using a tapering function. As seen in Fig. 3.3(b) the Fourier transform of the tapering function $G(f)$ is characterized by a main lobe bracketed by lower amplitude side lobes. The width of the main lobe is inversely proportional to the time duration (or length by means of the time-space correspondence) of the signal segment (designated by the number of samples, N). It defines the **frequency resolution** of the spectrum estimate, i.e., the separation between two independent frequency bins in the spectrum.[122] As $G(f)$ is convolved with $Y(t)$ (the non-tapered estimate of the spectrum of an infinite length $y(t)$), the presence of the side lobes causes the value of Y^T at a particular frequency f to have contributions from other frequencies. This effect, known as spectral leakage or broad band bias, biases the estimate $Y^T(f)$.[105,107,122,123]

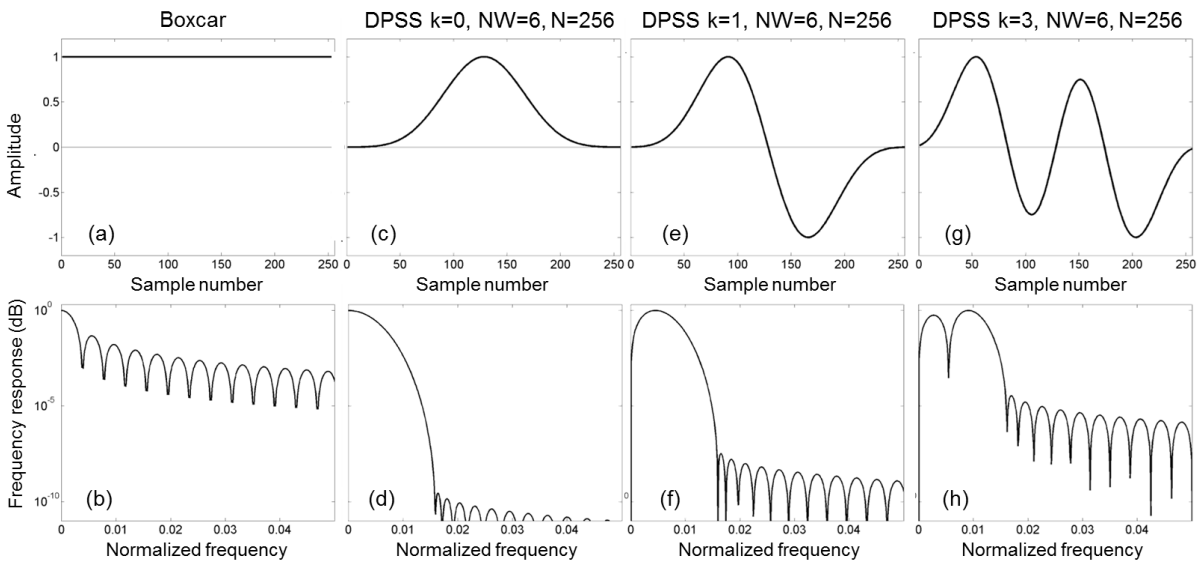

Figure 3.3 Tapering functions (top) and their discrete Fourier transforms (bottom). (a,b) Boxcar function (no taper), (c,d) first (k=0) discrete prolate spheroidal sequence (DPSS) for a "time-half bandwidth product," NW=6. (e,f) second (k=1) DPSS for NW=6, (g,h) fourth (k=3) DPSS for NW=6. The signal segment contained 256 samples.

To reduce spectral leakage, tapering functions with various shapes have been designed.[105,122,123] Ideally we would like to concentrate the energy of $G(f)$ within a main lobe to minimize the energy leaked to the side lobes and limit the spectral leakage.[108,122] The fraction of the total energy of $G(f)$ that is within a main lobe of arbitrary bandwidth $2W$ is expressed as:

$$\lambda(N,W) = \frac{\int_{-W}^{W} |G(f)|^2 \, df}{\int_{-1/2}^{1/2} |G(f)|^2 \, df} \tag{3.20}$$

where the parameters N and W denote the dependence of λ on the duration (length) of the signal segment and the arbitrary bandwidth $2W$.[108,122] Note that λ will be less than 1 because a finite length signal cannot be perfectly band limited.[109] Substituting Eq. (3.19) into Eq. (3.20), we obtain

$$\lambda(N,W) = \frac{\sum_{t'=0}^{N-1}\sum_{t=0}^{N-1} g(t)\dfrac{\sin\left[2\pi W(t'-t)\right]}{\pi W(t'-t)}g(t')}{\sum_{t=0}^{N-1}\left|g(t)\right|^2} \quad (3.21)$$

Expressing the values $g(t)$ as a vector **g** and the mid factor in the numerator of the equation above as a matrix operator **C**, this results in the eigenvalue equation:[122]

$$\mathbf{Cg - \lambda g = 0} \quad (3.22)$$

The solution to this equation is the set of orthogonal vectors $v_k(t)$, k=0,…,N-1 known as the discrete prolate spheroidal sequences (DPSS), also known as Slepian sequences after their proponent David Slepian.[122,124] The eigenvalues $\lambda_0>\lambda_1>\ldots>\lambda_{N-1}$ quantify the energy within the frequency band $2W$ of each of the eigenvectors $v_k(t)$, in decreasing order.[105] In particular, the first eigenvector is the finite-length taper with the smallest energy leaked to the side lobes of its Fourier transform.[107] Thus it can be used as an optimum taper to reduce spectral leakage.[105] Its frequency resolution is dictated by the value of W.[107,125] Figure 3.3(c) and 3.3(d) show the first eigenvector for N=256 and the time-half bandwidth product, NW=6. In addition, only the first $2NW$ eigenvectors have a significant fraction of the energy within the main lobe.[105] The rest of them have very poor leakage properties. Figures 3.3(e) and (f) show the second eigenvector and its Fourier transform, while figures 3.3(g) and (h) show the fourth eigenvector and its Fourier transform. As the eigenvector index k increases, the side lobe level increases.[105,122]

Once the spectrum Y_i^T is estimated, an estimate of the generalized spectrum from the i^{th} scan line within the PER is obtained by computing the product of the spectrum with its conjugate at frequencies f_1 and f_2, respectively:[50,93,110,114,115,126]

$$S_i(f_1, f_2) = Y_{T,i}(f_1)Y_{T,i}(f_2)^* \quad (3.23)$$

Note that the values of $S_i(f_1,f_2)$ are complex, except along the diagonal where $f_1=f_2$, where the values are real and positive.[112]

Step B. Averaging of individual estimates

The use of tapers to reduce spectral leakage comes at the cost of increasing the variance of the spectral estimate. This results from the effective reduction of the duration of the signal segment by preferentially weighting samples in the center of the segment.[107,122] Different tapers, such as the Hann taper or the first Slepian sequence, differ from each other in their bias-variance tradeoff.[122] In addition, all estimates based on Eq. (3.18), referred to as **Single-Taper (ST)** estimates**,** are inconsistent, i.e., the variance is not reduced by increasing the number of samples within the signal segment.[108] In order to reduce the variance of the estimates, two methods have been investigated and are further explored in this work for the task of detection of coherent features in the backscatter echo signals.

The first method is the **Weighted Overlapped Segment Average (WOSA)** estimate, initially proposed by Welch[127] for power spectrum estimation.[50,110] In this method each signal segment within the PER is subdivided into overlapped subsegments. This subdivision is parameterized in terms of the subsegment length ratio (the length of the subsegments with respect to the original segment) and the overlap ratio (the amount of overlap between consecutive subsegments expressed as a fraction of their length), with a common value of 50% for both.[51,110, 128-130] Then the estimate from each signal segment is obtained as:

$$S_i(f_1, f_2) = \frac{1}{N_{SS}} \sum_{n=1}^{N_{SS}} Y_{T,i}(f_1; t_n)\, Y_{T,i}^{*}(f_2; t_n) \tag{3.24}$$

where N_{SS} is the number of subsegments each segment is divided into, and t_n refers to the center of the n^{th} subsegment.[50,114,110,52,129] Assuming an underlying white Gaussian noise stationary random process, the 50%-overlap (N_{SS}=3), the WOSA estimate using a Hann taper is expected to reduce the variance of the power spectrum $P(f)$ by a factor $18N_{SS}^2/(19N_{SS}-1)= 2.89$.[108] The drawback of this estimate is that the frequency resolution of the estimate is worsened compared to the single taper estimates by using smaller signal segments.[125] This estimator has been widely used in many quantitative ultrasound applications due to the focus on obtaining estimates over large regions of interest instead of forming parametric images.[50,51,93,110,114]

The second method, referred to as the **Multitaper (MT)** estimate, exploits the orthogonality of the Slepian vectors $v_k(t)$ to reduce the variance of the spectral estimate. This method was suggested as useful when dealing with short signal segments such as when creating parametric images.[105,112,122] The multitaper approach originates from the relationship between the value of the discrete Fourier transform of $Y^T(f)$ from Eq. (18) and the increments measure $Z(f)$[105,109]

$$Y^T(f) = \int_{-1/2}^{1/2} \frac{\sin\left(N\pi(f-f')\right)}{\sin\left(\pi(f-f')\right)}\, dZ(f') \qquad (3.25)$$

This is the basic equation of spectral estimation and establishes the relationship between an observable quantity $Y^T(f)$ and a non-observable quantity $Z(f)$.[105] The ratio of sinusoids in Eq. (3.25) is known as the Dirichlet Kernel.[105,109] This equation is not invertible, and as a consequence, we cannot directly obtain *Z(f)* from the discrete and finite *Y(f)*. This also forbids obtaining $S(f_1, f_2)$. Thomson[105] proposed a statistically tractable solution that reduces spectral leakage. This approach involves the eigenfunction expansion of the Dirichlet Kernel combined with a local least squares error criterion between the estimate and the expected spectrum within a frequency interval *(-W,W]*:[105]

$$\int_{-Wf_s}^{Wf_s} \frac{\sin N\pi(f-f')}{\sin \pi(f-f')}\, U_k(N,W,f')\, df = \lambda_k(N,W)\, U_k(N,W,f') \qquad (3.26)$$

where U_k and λ_k are the k^{th} eigenfunction and the k^{th} eigenvalue resulting from the problem. Notice the similarity of this problem with the energy concentration problem described in Eq. (3.21).[105] The eigenfunctions of the Dirichlet kernel are the Discrete Prolate Spheroidal Wave Functions (DPSWFs) $U_k(N,W,f)$ and are the Fourier pairs of the Slepian sequences found in the concentration problem.[105] The process of tapering the signal $y(t)$ by one of the Slepian sequences can be interpreted as the projection of the $Z(f)$ onto the frequency range *(f-W, f+W)* using the k^{th} sequence.[107] Since only the first $2NW$ eigenvectors have a significant fraction of their energy within the main lobe, the multitaper method estimates the generalized spectrum by obtaining the weighted average of the products of the Fourier

transform $Y^{T}_{i,k}$ estimates obtained from the signal segment $y_i(t)$ tapered by each of the first k=1,…,K<2NW Slepian sequences for a particular value of the time-half bandwidth product NW:[105,107,111,113,122]

$$S_i(f_1, f_2) = \frac{\Lambda}{K} \frac{\sum_{k=0}^{K-1} \lambda_k \, d_k(f_1) \, Y^{T}_{i,k}(f_1) \, d_k(f_2) \, Y^{T\,*}_{i,k}(f_2)}{\left[\sum_{k=0}^{K-1} d_k(f_1)^2\right]^{1/2} \left[\sum_{k=0}^{K-1} d_k(f_2)^2\right]^{1/2}} \tag{3.27}$$

where the subindex k refers to each of the K tapers, and

$$\Lambda = \sum_{k=0}^{K-1} \lambda_k^{-1} \, . \tag{3.28}$$

As previously discussed, higher order eigenvectors have progressively poorer spectral leakage properties.[122] Figure 3.4 shows the effective frequency response of the multitaper estimator when used for power spectrum estimation, i.e., when computing Eq. (3.27) when f_1=f_2. The parameters used were NW=6 and the different curves correspond to a variable number of tapers K, and the weighting factors $d_k(f)$=1.[125] Note that the effective frequency response acts as a band pass filter with bandwidth 2W.[105] Increasing the number of tapers results in a reduction of variance due to the averaging of approximately uncorrelated spectral estimates.[105,122] Figure 4.4 shows that increasing the number of tapers also increases the amount of bias beyond the main lobe because of the use of higher order tapers. The weights $d_k(f)$ are designed to reduce the contribution of high order tapers in regions of the spectrum more susceptible to bias from spectral leakage, such as regions with low power or rapid changes over frequency.[107,122] Since the computation of the weights requires previous knowledge of the spectrum, they are computed iteratively. The estimation of these weights is described in detail in Thomson[105] and Park *et al.*[122] Under the assumption of a white Gaussian stationary random process, the multitaper method would reduce the spectral variance by K. For colored spectra the variance reduction efficiency will also depend on the dynamic range of the spectrum.[108] Initial applications of the multitaper estimator in the context of Quantitative Ultrasound were reported by Rubert and Vargese.[131] The authors evaluated the gain in accuracy and precision of estimates of the mean scatterer spacing obtained with the multitaper estimator

of the generalized spectrum compared to other estimators for the purpose of monitoring changes in the structure of liver (~1mm scatterer spacing from portal triads) during thermal ablation. Here we present a more general approach to this analysis by presenting a theoretical analysis of the use of different tapering functions to detect coherent scattering from periodic structures and also by expanding the range of spacing values and factors that complicate the detection of the coherent scattering component, such as the reduction of the PER size.

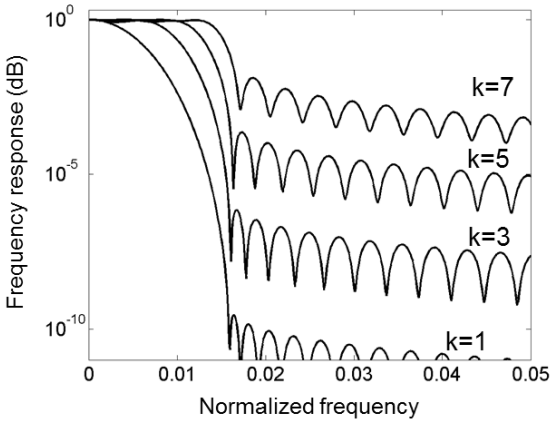

Figure 3.4 Effective frequency response of the multitaper estimator (*NW*=6) when used to estimate the power spectrum, i.e., S(f_1,f_2) for f_1=f_2, for a stationary random process. Each curve corresponds to a different number of averaged tapers.

After obtaining the generalized spectrum estimates from the individual echo signal segments within the PER, these are then averaged[51,110]

$$S_{\mathrm{AV}}(f_1, f_2) = \sum_{i=1}^{N_{AL}} S_i(f_1, f_2) \quad . \tag{3.29}$$

where N_{AL} is the number of acoustic scan lines within the PER. This averaging step follows two objectives. First, it further reduces the estimation variance of the generalized spectrum estimator. Second, it acts as a statistical filter that reduces the contribution from the diffuse, stationary component, while reinforcing the contribution of any coherent scattering components.[119] When averaging various echo signal segments with a quasiperiodic array of scatterers, it is important to synchronize the periodic components of the different echo signal segments with respect to their center. This is done to improve the

convergence of the phase summation in the off diagonal elements.[50,114,119,126] This synchronization is performed by applying a phase correction factor $F(f_1,f_2,\tau)$ to the estimate of the generalized spectrum from each segment.[119] $F(f_1,f_2,\tau)$ is defined as

$$F(f_1, f_2, \tau) = \exp\left(j2\pi\left[f_1 - f_2\right]\tau\right). \tag{3.30}$$

where τ is a synchronization parameter usually estimated as the difference between the location of the maximum value within each echo segment and its center.[114,126] This assumes that the stronger echo within the signal segment would be caused by one of the periodic scatterers.[110] The use of this factor is particularly important when there are only a few of the ordered scatterers within each signal segment. In the case where only diffuse scatterers are present, the phase factor will not affect the estimate of the generalized spectrum because its phase would be uniformly distributed and be reduced during averaging.[110] Note that when the WOSA estimator is used, the phase factor is applied to the estimate from each subsegment.

Step 3. Normalization

The final step in the estimation is to normalize $S_{AV}(f_1,f_2)$ to transform it to an overall measure of coherence. This is done by dividing $S_{AV}(f_1,f_2)$ over the values of its main diagonal at f_1 and f_2:[107,109,111,113,132]

$$S_{Norm}(f_1, f_2) = \frac{S_{AV}(f_1, f_2)}{\sqrt{S_{AV}(f_1, f_1)\, S_{AV}(f_2, f_2)}}. \tag{3.31}$$

The elements off the main diagonal of the bifrequency plane depend on various factors, including the relative power of the coherent component to that of the incoherent component, and the pulse spectrum and how it is modified while it propagates through tissue. This normalization reduces these effects. The magnitude of $S_{Norm}(f_1,f_2)$ is bounded to values between 0 and 1.[112] In addition, the values along the main diagonal are equal to 1, i.e., $S_{Norm}(f,f)=1$.[50,51,93,112,119]

The finite bandwidth of the acoustic pulse imposes a limit on the information that can be obtained from the generalized spectrum.[115] The normalization step must be performed after selecting a bandwidth with sufficient energy along the main diagonal to avoid amplifying noisy regions that could lead to false detection.[50,93] In this work, the useful bandwidth was selected to be the region where the power spectral density was larger than 10dB above the spectral noise floor.[24]

3.1.4 Analysis of the generalized spectrum

To simplify the analysis of the generalized spectrum, a collapsed average representation (CAGS) is obtained from the bifrequency plane by averaging the complex values of $S_{Norm}(f_1, f_2)$ along its diagonals, i.e., points with equal $\Delta f = f_1 - f_2$:[51,93,112,119,133]

$$\mathrm{CAGS}(\Delta f) = \frac{1}{M(\Delta f)} \left| \sum S_{\mathrm{Norm}}(f_1, f_2 \mid f_1 - f_2 = \Delta f) \right| . \tag{3.32}$$

where M(Δf) is the number of elements along a secondary diagonal of the bifrequency plane with the same Δf. The computation of the CAGS is illustrated in Fig. 3.5. It exploits the coherent sum of phases along the secondary diagonals of the generalized spectrum when quasi-periodic scatterers are present, as well as the incoherent sum in the off-diagonal elements resulting from diffuse scatterers, to improve the detection of coherence features.[51,112,133] This is particularly useful when dealing with limited amounts of data.[119] The collapsed average is an estimate of the autocorrelation function of the signal spectrum when no normalization is applied to the generalized spectrum.[119,110,126] Note that as Δf increases, there is a smaller number of bifrequency plane elements that are averaged to obtain the collapsed average value at that Δf. Thus, the variance of the CA value increases with Δf, and the detection performance will vary depending on the frequency corresponding to the periodic spacing.[112]

When only diffuse scatterers are present in the medium, the frequency components of the contribution of these scatterers to the total echo signal are uncorrelated.[50] Thus, the expected value of the diffuse scatterer component does not contribute significantly to the off-diagonal values of the generalized spectrum.[50,112]

As a result, the values of the CAGS at $\Delta f \neq 0$ are close to zero. [50,112] When the scattering function is nonrandom and has spatial dependence, the echo signal becomes non-stationary and different frequency components of the signal spectrum become correlated.[51] This will cause a characteristic structure in the off-diagonal elements of the CAGS determined by the structure of the periodic array of scatterers.[50,51,115,121] Thus the shape of the CAGS can be analyzed to gain knowledge about the structural properties of tissue.[51] In particular, we are interested in the task of detecting scattering scenarios when a periodic array of scatterers is present with spacing of the order or larger than the resolution cell. In these cases, the CAGS values will peak at frequencies which are integer multiples of the fundamental frequency $f=c/2\Delta$, where Δ is the mean scatterer spacing.

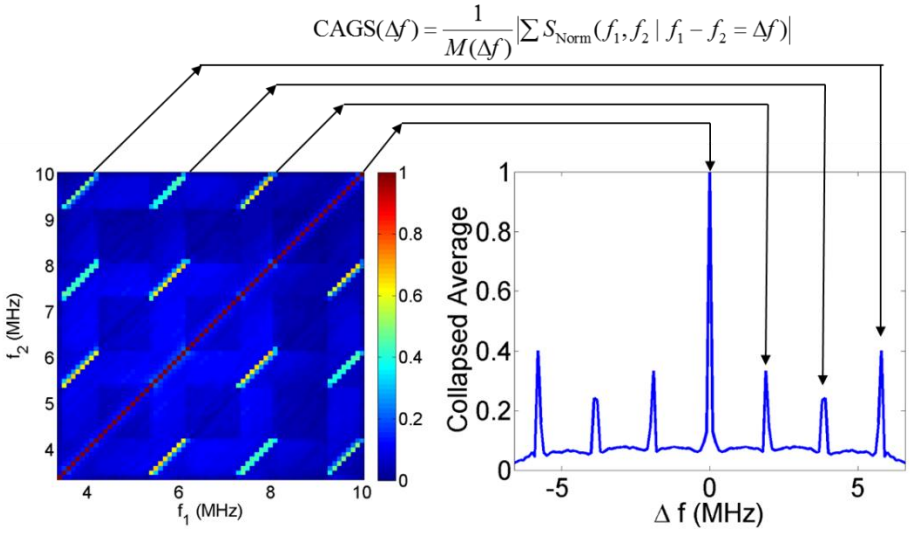

Figure 3.5 Computation of the Collapsed Average from the bifrequency plane of the generalized spectrum.

Initial applications of the generalized spectrum in the field of Quantitative Ultrasound were performed by the group of Kevin Donohue.[50,51,93,110,114-116,119,128,130] These initial applications were focused on the characterization of breast lesions using parameters extracted from the generalized spectrum itself (such as templates based on the difference between the generalized spectra estimated from benign and malignant breast lesions)[110] or its collapsed average representation (such as the integrated collapsed average or mean scatterer spacing estimates obtained from particular frequency bands).[115,119,128,130] Recently, mean

scatterer spacing estimates obtained from the generalized spectrum were used by Rubert and Varghese[131] to monitor liver tissue undergoing thermal ablation. The authors found that the multitaper estimator of the generalized spectrum provided more accurate and precise estimates of the 1mm spacing between portal triads in the liver when performing bulk parameter estimation (long estimation regions) compared to estimates obtained from single taper or WOSA estimators of the generalized spectrum.[131]

Another method that has been used for the detection and characterization of periodic scatterers in tissue is the Singular Spectrum Analysis method (SSA).[53,134-139] This technique aims at separating periodic and non-periodic components of the echo signals by obtaining an empirical basis from the eigenvectors of the time-domain covariance matrix of the echo signal. Ultrasound applications of SSA, particularly the works by Machado *et al*.[134, 138, 139] and Pereira and Maciel,[53,137] have focused on estimating the mean separation among regularly spaced scatterers in liver and cancellous bone by exploiting the fact that oscillatory components in the signal generate similar eigenvalues of the covariance matrix. SSA was used by these authors to identify oscillatory eigenvectors and then the center frequency of their spectral density was used to estimate the mean scatterer spacing distance. SSA was found to perform similarly to the WOSA-estimated generalized spectrum.[53,134,139]

In this chapter, we advance the use of the generalized spectrum and SSA over previous work by Donohue *et al*.,[51,110,114-116,119,128,130] Varghese *et al*.,[50,93] Rubert and Varghese[131], Machado *et al*.[133, 138,139] and Pereira and Maciel,[53,137] by comparing advanced estimators of the generalized spectrum, i.e., the multitaper estimator to SSA, for the task of detecting coherent scattering from organized tissue structures producing non-stationary echo signals. The intended task is to create parametric images with good spatial resolution. We emphasize the focus on the detection task under data size constraints (small PERs) rather than just focusing on the estimation of the mean scatterer spacing as in previous papers.[50,93,128,131,139] When dealing with the small estimation regions required to create parametric images with good spatial resolution, the final estimate of the generalized spectrum will depart from the expected value, and the off-diagonal values of the generalized spectrum may have contributions from the diffuse component, affecting the

detection performance. In addition, conventional estimators of the generalized spectrum, such as the single taper estimator and the WOSA estimator, are also included in the analysis for completeness.

To extend the applicability of the analysis, the performance of the different generalized spectrum estimators and the SSA is studied over an ample range of scatterer spacing values. As the scatterer spacing increases, the separation among the fundamental frequency and the harmonics that appear in the CAGS when periodic scatterers are present decreases and becomes more difficult to resolve. Thus, the different frequency resolution characteristics of each generalized spectrum estimator will result in different detection performance for different spacing values. It is important to note that the scatterer spacing range that will be explored in this chapter overlaps with the range explored in the analysis of parameters extracted from stationary echo signals presented in Chapter 2. This is done to identify the transition between the stationary signal analysis and the non-stationary signal analysis. Furthermore, regular lattices of scatterers in tissues are not perfectly periodic, and fluctuations in the scatterer spacing about a mean value are expected (thus the use of the term "quasi-periodicity"). These fluctuations reduce the amplitude of the maxima in the CAGS corresponding to periodic features, as observed by Donohue *et al*.[50,92] In addition, the energy of the coherent scattering component with respect to the incoherent scattering component will also affect the detection performance.[93] As a consequence, there is a need to perform a comprehensive study of the performance of the SSA and the various estimators of the generalized spectrum, including the multitaper estimator, under all these scenarios that hinder the detection of the coherent scattering component of the backscattered echo signals. Based on these ideas, the aim of this chapter is now formally defined.

3.2 Aims

The following analysis studies the conspicuity of parameters indicating the presence of sources of coherent scattering leading to non-stationary signals from different estimators of the generalized spectrum for the task of creating parametric images with the implicit constraints in data availability for parameter

estimation. The aim is to identify the estimator of the generalized spectrum, in particular the tapering function that maximizes the detection of coherent scattering from non-stationary signals. This estimator must maintain good performance over a wide range of different scatterer spacing values and should be robust to the introduction of variance in the spacing and to reductions of the contribution of the coherent component to the total echo power. In addition, by continuously varying the periodic scatterer spacing from values smaller (not resolved) to values larger (resolved) than the size of the resolution cell, we aim at identifying the transition from the analysis of stationary signals to that of non-stationary ones. These aims will be investigated in three steps:

1. A theoretical analysis of the influence of the time-gating/tapering operation on the estimate of the generalized spectrum is developed. The theoretical findings are compared to results from simulated RF signals obtained using the simulation tool described in Chapter 2.
2. A quantitative analysis of the conspicuity of coherence-related features in the generalized spectrum is presented. This analysis quantifies the contrast and contrast to noise ratio of the value of the collapsed average of the generalized spectrum corresponding to a peak caused by an array of periodic scatterers. The values of these quantities are compared for the different estimators of the generalized spectrum studied in Step 1. The influence of various factors on the contrast and CNR, such as the PER size, the scatterer spacing, the scattering amplitude of the periodic scatterers, and the introduction of variance in the scatterer spacing, is also studied. Results from both simulations and phantom experiments are presented.
3. A statistical analysis of the process of detection of coherent scattering by looking at the maximum value of the collapsed average of the generalized spectrum is presented. This analysis is focused on two specific questions:
    a. Does the maximum value of the collapsed average of the generalized spectrum occur at the expected frequency corresponding to the scatterer spacing?
    b. How much does the reduction of the PER size affect the detection of the correct frequency by means of finding the maximum value of the collapsed average?

Step 3 also compares the detection performance of the generalized spectrum to the singular spectrum analysis (SSA) approach.

3.3 Theoretical Analysis

This section extends the derivations of the theoretical expressions of the generalized spectrum by Donohue *et al.*,[114] in which no explicit expression for the tapering functions were included. Consider an infinite distribution of scatterers along the propagation path of the acoustic pulse. The scattering function of such array is represented by:[114]

$$s(t) = \sum_{n=1}^{\infty} a_n \delta(t - \tau_n) \quad . \tag{3.33}$$

where a_n is the scattering cross section of the n^{th} scatterer. For now, we assume that each scatterer does not modify the frequency content of the acoustic pulse so that a_n is assumed to be frequency independent. The delay $\tau_n = 2r_n/c$, where r_n is the location of the n^{th} scatterer arbitrarily referenced to the face of the transducer.[114] The radiofrequency (RF) signal is given by the convolution ($*$) of $s(t)$ with the point spread function $h(t)$[93,110,119,140]

$$y(t) = h(t) * s(t) \quad . \tag{3.34}$$

The point spread function includes the effects of the system transfer function, diffraction and attenuation.[93,110,119,140] To analyze the frequency content of the RF signal, we gate it with a window of duration T and a tapering function $g(t)$. Then the gated signal becomes

$$y^T(t) = \left[h(t) * s(t)\right] \, g\left(t\right) \quad . \tag{3.35}$$

The Fourier transform of $y^T(t)$ is

$$Y^T(f) = \left[H(f) \, S(f)\right] * G\left(f\right) \quad . \tag{3.36}$$

where $H(f)$, $S(f)$ and $G(f)$ are the Fourier transforms of $h(t)$, $s(t)$, and $g(t)$, respectively. The Fourier transform of the scattering function $S(f)$ takes the functional form[114]

$$S(f) = \sum_{n=1}^{\infty} a_n \; e^{-j2\pi f \tau_n} \quad . \tag{3.37}$$

Substituting Eq. (3.37) into Eq. (3.36) and considering that the convolution is a linear operation

$$Y^T(f) = \sum_{n=1}^{\infty} a_n \; \left[\left\{ H(f) \; e^{-j2\pi f \tau_n} \right\} * G(f) \right] \quad . \tag{3.38}$$

where the sum is over the individual scatterers, as defined in Eq. (3.33). Taking the expression within the square parentheses in Eq. (3.38) for each individual scatterer and expanding the convolution operation, we obtain

$$\left\{ H(f) \; e^{-j2\pi f \tau_n} \right\} * G(f) = \int_{-\infty}^{\infty} H(f') \; e^{-j2\pi f' \tau_n} \; G(f - f') \; df' \quad . \tag{3.39}$$

Notice that the expression on the right is just the inverse Fourier transform of the function $H(f')\; G(f-f')$ evaluated at $t=-\tau_n$. The inverse Fourier transform of $G(f-f')$ is obtained as follows:

$$\begin{gathered} \int_{-\infty}^{\infty} G(f - f') \; e^{j2\pi f' t} \; df' = \int_{-\infty}^{\infty} G(f'') \; e^{j2\pi f t} \; e^{j2\pi f''(-t)} \; df'' \\ \int_{-\infty}^{\infty} G(f - f') \; e^{j2\pi f' t} \; df' = g(-t) \; e^{j2\pi f t}. \end{gathered} \tag{3.40}$$

Therefore:

$$\left\{ H(f) \; e^{-j2\pi f \tau_n} \right\} * G(f) = \left\{ h(t) * \left[g(-t) \; e^{j2\pi f t} \right] \right\} (-\tau_n) \quad . \tag{3.41}$$

We can express $h(t)$ in 1D as the product of a sinusoid and an "envelope function" $\zeta(t)$:

$$h(t) = e^{i2\pi f_0 t} \; \zeta(t) \quad . \tag{3.42}$$

Therefore

$$h(t) * \left[g(-t)\, e^{j2\pi ft} \right] = \int_{-\infty}^{\infty} e^{j2\pi f_0 t'}\, \zeta(t')\, g(t'-t)\, e^{j2\pi f(t-t')}\, dt'$$

$$h(t) * \left[g(-t)\, e^{j2\pi ft} \right] = e^{j2\pi ft} \int_{-\infty}^{\infty} \zeta(t')\, g(t'-t)\, e^{-j2\pi(f-f_0)t'} dt' \tag{3.43}$$

$$h(t) * \left[g(-t)\, e^{j2\pi ft} \right] = e^{j2\pi ft}\, \xi(t; f, f_0)$$

.

We have defined $\xi(t;f,f_0)$ as

$$\xi(t; f, f_0) = \int_{-\infty}^{\infty} \zeta(t')\, g(t'-t)\, e^{-j2\pi(f-f_0)t'}\, dt'$$

$$\xi(t; f, f_0) = \zeta_f(f - f_0) * \left[G(f - f_0)\, e^{-j2\pi(f-f_0)t} \right] \tag{3.44}$$

.

where $\zeta_f(f)$ is the Fourier transform of the pulse envelope function $\zeta(t)$. Finally, substituting Eq. (3.43) and Eq. (3.44) into Eq. (3.38) we obtain

$$Y^T(f) = \sum_{n=1}^{\infty} a_n\, e^{-j2\pi f\tau_n}\, \xi(-\tau_n; f, f_0) \tag{3.45}$$

.

The estimate of the Generalized Spectrum from a single scan line is computed as the product of $Y^T(f)$ at frequency f_1 times its conjugate (*) at frequency f_2

$$S(f_1, f_2) = Y^T(f_1)\, Y^{T*}(f_2)$$

$$S(f_1, f_2) = \sum_{n'=1}^{N} \sum_{n=1}^{N} a_n\, a_{n'}\, e^{-j2\pi f_1\tau_n}\, e^{j2\pi f_2\tau_{n'}}\, \xi(-\tau_n; f_1, f_0)\, \xi^*(-\tau_{n'}; f_2, f_0) \tag{3.46}$$

.

In order to simplify the analysis and the visualization of the different tapering functions on the generalized spectrum, we will assume that the point spread function is very small compared to the windowing function so that

$$h(t) * \left[g(-t)\, e^{j2\pi ft} \right] \approx g(-t)\, e^{j2\pi ft} \tag{3.47}$$

.

In incoming Sections 3.4 and 3.5 this assumption will be challenged when considered small echo signal durations. Therefore, Eq. (3.45) reduces to

$$Y^T(f) = \sum_{n=1}^{\infty} a_n \, e^{-j2\pi f \tau_n} \, g(\tau_n) \quad . \tag{3.48}$$

and

$$S(f_1, f_2) = \sum_{n'=1}^{N} \sum_{n=1}^{N} a_n \, a_{n'} \, e^{-j2\pi f_1 \tau_n} \, e^{j2\pi f_2 \tau_{n'}} \, g(\tau_n) \, g(\tau_{n'}) \quad . \tag{3.49}$$

Separating the sum of equal indices, we obtain

$$S(f_1, f_2) = \sum_{n=1}^{N} a_n{}^2 \, g^2(\tau_n) \, e^{-j2\pi (f_1 - f)_2 \tau_n} + \sum_{n'=1}^{N} \sum_{n=1, n\neq n'}^{N} a_n \, a_{n'} \, e^{-j2\pi f_1 \tau_n} \, e^{j2\pi f_2 \tau_{n'}} \, g(\tau_n) \, g(\tau_{n'}) \quad . \tag{3.50}$$

We now investigate the functional form of the expected value of $S(f_1,f_2)$ under two ideal conditions, when the scattering function includes only randomly located scatterers, and when it is composed of a perfect lattice of identical scatterers with a fixed spacing.

3.3.1 Case A. Random scatterers

We consider first the case where both a_n and τ_n are independent random variables and their values for each scatterer are independent from the other scatterers. We assume that the scatterers are uniformly distributed within any segment of arbitrary length, such as the gating window.[93,114] Then, the expected value of $S(f_1,f_2)$ becomes

$$\begin{aligned} E\left[S(f_1, f_2)\right] = {} & E\left[\sum_{n=1}^{N} a_n{}^2 \, g^2(\tau_n) \, e^{-j2\pi (f_1 - f)_2 \tau_n}\right] + \ldots \\ & E\left[\sum_{n'=1}^{N} \sum_{n=1, n\neq n'}^{N} a_n \, a_{n'} \, e^{-j2\pi f_1 \tau_n} \, e^{j2\pi f_2 \tau_{n'}} \, g(\tau_n) \, g(\tau_{n'})\right]. \end{aligned} \tag{3.51}$$

Since a_n and τ_n are independent[114]

$$\begin{aligned} E\left[S(f_1, f_2)\right] = {} & \sum_{n=1}^{N} E\left[a_n{}^2\right] \, E\left[g^2(\tau_n) \, e^{-j2\pi (f_1 - f)_2 \tau_n}\right] + \ldots \\ & \sum_{n'=1}^{N} E\left[a_n\right] \, E\left[e^{-j2\pi f_1 \tau_n} \, g(\tau_n)\right] \sum_{n=1, n\neq n'}^{N} E\left[a_n\right] E\left[e^{j2\pi f_2 \tau_{n'}} \, g(\tau_{n'})\right]. \end{aligned} \tag{3.52}$$

As mentioned before, the sums are over the individual discrete scatterers. The time delay τ_n associated to the n^{th} scatterer is a continuous random variable uniformly distributed between 0 and T.[115] From this, the expected value in the second factor in the argument of the first sum to the right of the equal sign in Eq. (3.52) is evaluated over the probability density function of each scatterer's τ_n and becomes

$$E\left[g^2(\tau_n)\, e^{-j2\pi(f_1-f)_2\tau_n} \right] = \frac{1}{T}\int_0^T g^2(\tau_n)\, e^{-j2\pi(f_1-f_2)\tau_n}\, d\tau_n \quad . \tag{3.53}$$

The tapering function is zero outside the interval [0, T]. Thus, we can extend the integration limits

$$E\left[g^2(\tau_n)\, e^{-j2\pi(f_1-f)_2\tau_n} \right] = \frac{1}{T}\int_{-\infty}^{\infty} g^2(\tau_n)\, e^{-j2\pi(f_1-f_2)\tau_n}\, d\tau_n \quad . \tag{3.54}$$

The integral is the Fourier transform of $g(\tau_n)^2$. Therefore

$$E\left[g^2(\tau_n)\, e^{-j2\pi(f_1-f)_2\tau_n} \right] = \frac{1}{T}\left[G * G^* \right](f_1 - f_2) \quad . \tag{3.55}$$

Following the same procedure,

$$E\left[g(\tau_n)\, e^{-j2\pi f\tau_n} \right] = \frac{1}{T}\, G(f) \quad . \tag{3.56}$$

Therefore,

$$E\left[S(f_1, f_2)\right] = \frac{1}{T}\left[G * G^* \right](f_1 - f_2) \sum_{n=0}^{N} E\left[a_n{}^2 \right] + \frac{1}{T^2} G(f_1)\, G^*(f_2) \sum_{n=0}^{N} E\left[a_n\right] \sum_{n'=0}^{N} E\left[a_{n'}\right] \quad . \tag{3.57}$$

Note that subscript * indicates complex conjugate, while in-line * indicates convolution. The components of the generalized spectrum that are off the main diagonal are dominated by the term including the convolution of $G(f)$ with its conjugate (first term to the right of the equal sign) because the term with the product $G(f_1)G^*(f_2)$ will be significantly smaller for $f_1, f_2 > 1/T$.[114] Thus, Eq. (3.57) reduces to:

$$E\left[S(f_1, f_2)\right] \approx \frac{N\overline{a^2}}{T}\, \left[G * G^* \right](f_1 - f_2) \, . \tag{3.58}$$

Note that this term depends only $\Delta f=f_1-f_2$, i.e., it is constant along the diagonals of the bifrequency plane. Therefore, the collapsed average of the generalized spectrum under these conditions has the same functional form as the generalized spectrum.

Figure 3.6 shows the comparison between Eq. (3.58) and the collapsed average obtained from simulated RF data with the simulation tool described in Chapter 2. The simulation conditions were a 6MHz pulse, with a 72% -6dB bandwidth, leading to a pulse length of 0.296mm. The random scatterers were uniformly distributed with a concentration of 48 scatterers per resolution cell. Figures 3.6(a) and (b) were constructed using the single-taper estimator with the boxcar taper and the first Slepian sequence for a time-half bandwidth product NW=4. Figure 3.6(c) was obtained with the multitaper estimator with NW=4 (7 tapers). The figures show the average of 3000 independent realizations of the collapsed average of the generalized spectrum. The gating window had a length of 2mm. The agreement between theory and simulations is excellent. In all cases, the values outside the main lobe at Δf=0MHz are very small.[115] In particular, notice that the shape of the collapsed average for the multitaper estimator is different from the ideal bandpass shape expected for the multitaper power spectrum estimator shown in Fig. 3.3. The reason for this is that on the estimation of the collapsed average, the phases of the different tapers contribute to its final shape, while in the case of power spectrum estimations only the square magnitude of the tapers come into play.[105]

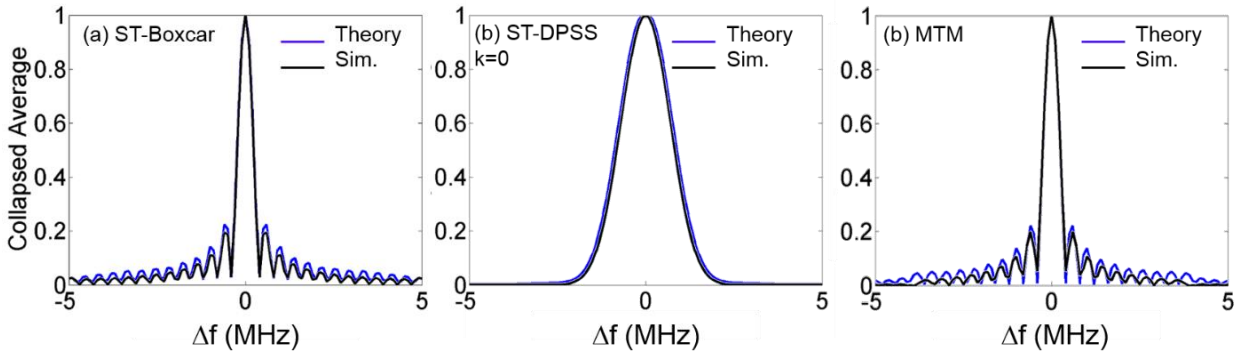

Figure 3.6 Collapsed average of the generalized spectrum obtained from a distribution of random scatterers. (blue) theory and (black) simulations (48 scatterers/resolution length). (a) Single-taper estimator with boxcar taper, (b) Single-taper estimator with first (k=0) DPSS taper for NW=4. (c) Multitaper estimator for NW=4 and K=7. Segment length: 2mm.

3.3.2 Case B. Lattice of periodic scatterers

Now we consider the case of an assortment of periodically spaced scatterers. To simplify the analysis, we express each scatterer position as a multiple of a fixed spacing Δ[50]

$$\tau_n = n\,\Delta\,. \tag{3.59}$$

Therefore, Eq. (3.48) becomes

$$Y^T(f) = \sum_{n=1}^{N} a_n\; e^{-j2\pi fn\Delta}\; g(n\Delta)\,, \tag{3.60}$$

and

$$E\left[S(f_1, f_2)\right] = \left\{\sum_{n=1}^{N} E[a_n]\; e^{-j2\pi f_1 n\Delta}\; g(n\Delta)\right\}\;\left\{\sum_{n'=1}^{N} E[a_{n'}]\; e^{-j2\pi f_2 n'\Delta}\; g(n'\Delta)\right\}. \tag{3.61}$$

Define a function $G_{\text{per}}(f)$ which is related to the tapering function by its Fourier series expansion:

$$G_{per}(f) = \sum_{n=0}^{N} g(n\Delta)\; e^{-j2\pi fn\Delta}\,. \tag{3.62}$$

Therefore

$$g(n\Delta) = \frac{1}{\phi}\int_{-\phi/2}^{\phi/2} G_{per}(f)\; e^{-2\pi fn\Delta}\; df\;. \tag{3.63}$$

The inverse Fourier transform of $G_{per}(f)$ becomes

$$\tilde{g}(t) = \int_{-\infty}^{\infty} G_{per}(f)\; e^{j2\pi ft}\; df \tag{3.64}$$

.

Substituting Eq. (3.62) in (3.64)

$$\tilde{g}(t) = \int_{-\infty}^{\infty} \sum_{n=0}^{N} g(n\Delta)\, e^{-j2\pi f n\Delta}\, e^{j2\pi ft}\, df$$

$$\tilde{g}(t) = \sum_{n=0}^{N} g(n\Delta) \int_{-\infty}^{\infty} e^{-j2\pi f(n\Delta - t)}\, df \quad . \tag{3.65}$$

$$\tilde{g}(t) = \sum_{n=0}^{N} g(n\Delta)\, \delta(t - n\Delta)$$

$$\tilde{g}(t) = g(t)\ \mathrm{comb}(t, \Delta)$$

where comb(t,Δ) is the train of Dirac delta functions separated by Δ. $G_{\mathrm{per}}(f)$ is the Fourier transform of the equation above:

$$G_{per}(f) = \Im\{g(t)\ \mathrm{comb}(t, \Delta)\}$$

$$G_{per}(f) = G(f) * \frac{1}{\Delta}\mathrm{comb}\left(f, \frac{1}{\Delta}\right) \tag{3.66}$$

Substituting the definition of the comb function in the equation for G_{per} yields

$$G_{per}(f) = \frac{1}{\Delta} \sum_{k=-\infty}^{\infty} G\left(f - \frac{k}{\Delta}\right). \tag{3.67}$$

Finally

$$E\left[S(f_1, f_2)\right] = \frac{\bar{a}^2}{\Delta^2} \sum_{k=-\infty}^{\infty} G\left(f_1 - \frac{k}{\Delta}\right) \sum_{k'=-\infty}^{\infty} G^*\left(f_2 - \frac{k'}{\Delta}\right). \tag{3.68}$$

Note that when either f_1, f_2, or both are a multiple integers of 1/Δ, the terms within each of the summations are in phase.[114,121] Therefore, the shape of the generalized spectrum in this case is a 2D grid of "periodicity cells". This can be seen in Figs. 3.7(a), (c), and (e), which show the generalized spectrum (before normalizing by the values in the main diagonal) obtained for a simulated combination of random scatterers (48 scatterers/resolution cell) and periodic scatterers with Δ=0.40mm (c/2Δ=1.93MHz). The expected value was approximated by averaging 3000 realizations of the generalized spectrum obtained from signal segments of 208 samples sampled at 40MHz, spanning a 4mm range. Figures 3.7(a) and (c) were obtained with the single taper estimator with a boxcar and the first DPSS (W=1MHz) taper,

respectively. Fig. 3.7(e) was obtained with the multitaper method with W=1MHz and K=9 tapers. The centers of these cells are located at ($f_1=kc/2\Delta$, $f_2=k'c/2\Delta$) where k and k' are integers.[115] The "effective" size of each of those cells is given by the span of the function given by the 2D product of the Fourier transform of the tapering function $G(f)$ with its conjugate. The theoretical appearance of the function $G(f_1)G^*(f_2)$ that is repeated in every periodicity cell indicated by a white square in Figs. 3.7(a), (c), and (e) is shown in Figs. 3.7(b), (d), and (f) for the boxcar and DPSS single taper estimators and the multitaper estimator, respectively. The agreement between theory and simulations is excellent. In the case of the multitaper method, the half bandwidth W of its band pass response was set to 1MHz. The values were normalized to the maximum to facilitate the comparison. Note that since the pulse was very small compared to the window length, the shape of the pulse spectrum did not appear in the theoretical expressions of the generalized spectrum. In the simulated results from Figs. 3.7(a), (c) and (d) the pulse spectrum modulates the values of the generalized spectrum from the point of the center frequency (6MHz, 6MHz).

An interesting property of the multitaper estimator is that the periodicity cell has square shape of width $2W$, and that within it the energy concentrates along its diagonal. This property is beneficial for the detection of periodicity based on the collapsed average compared with the other two estimators in which the energy is blurred about the center of the periodicity cell. In the latter cases, the contribution of these nodes to the corresponding value of the collapsed average will be small. In the following section we proceed to quantify the conspicuity of features related to scatterer quasi-periodicity that appear in the collapsed average. The analysis will be focused on identifying the estimator that leads to the best detectability of these features.

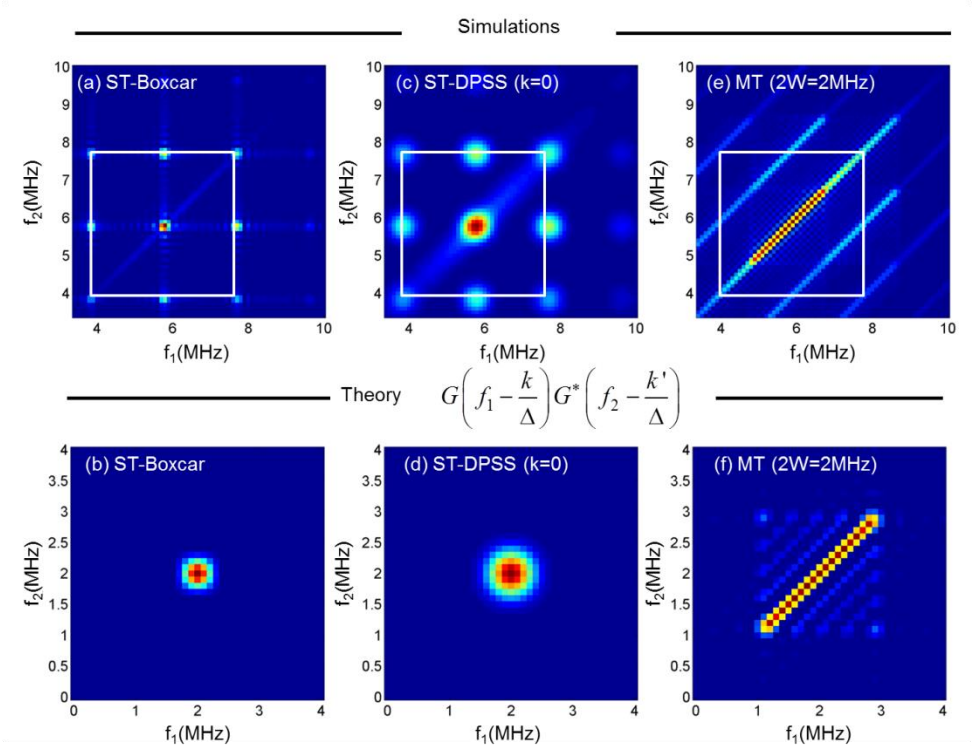

Figure 3.7 Generalized spectrum obtained with (a,b) single-taper with boxcar taper, (c,d) single-taper with first (k=0) DPSS for *W*=1MHz, and (e,f) multitaper for *W*=1MHz from (top) simulated backscatter echo data from a periodic array of scatterers separated by 0.4mm within a cloud of 48 random scatterers/resolution cell and (bottom) theory.

3.4 Analysis of conspicuity

3.4.1 Methods

In this section, the aim is to quantify the conspicuity of the value of the collapsed average at the frequency corresponding to the spacing among scatterers arranged in a periodic or quasi-periodic lattice. To do this, we follow a similar procedure to the one described in Chapter 2 to evaluate the discrimination power of parameters from echo statistics. As in Chapter 2, there are three different questions to answer:

1. How different is the parameter with respect to its value when only random scatterers are present? For this purpose we quantify the contrast of the parameter, i.e., the magnitude of the periodicity peak with respect to a reference value. The normalized contrast C_q is defined as:

$$\mathrm{C}_q = \frac{\bar{q} - \bar{q}_{\mathrm{Ref}}}{\bar{q}_{\mathrm{Ref}}} . \tag{3.69}$$

where q is the value of the magnitude of the periodicity peak in the collapsed average of the generalized spectrum estimated from echo signals from a medium with periodic scatterers. q_{Ref} is the magnitude of the collapsed average from the generalized spectrum from a medium with diffuse scattering, evaluated at the frequency of the periodicity peak. The overbar indicates averaging over multiple realizations.

2. How large is the difference in values of the parameter in the sample and in the reference with respect to their statistical variations? For this purpose we quantify the Contrast to Noise Ratio, defined as:

$$\mathrm{CNR}_q = \frac{\bar{q} - \bar{q}_{\mathrm{Ref}}}{\sqrt{\sigma_q{}^2 + \sigma_{q_{\mathrm{Ref}}}{}^2}} . \tag{3.70}$$

where the denominator is the sum of the variances of q and q_{ref}.

3. How much do these properties of the parameters change when the amount of data for their estimation is reduced? As discussed in Chapters 1 and 2, good spatial resolution in parametric images is achieved by reducing the size of the Parameter Estimation Regions. This will come at the expense of affecting the accuracy and precision of the parameters and, therefore, the ability to detect the scattering scenario these parameters are aimed to identify.

The diagram in Fig. 3.8 depicts the procedure to quantify the contrast and the CNR described in Eqs. (3.69) and (3.70). Two data sets are obtained: a sample data set and a reference data set. The sample data set includes frames of echo data from a material with a periodic array of scatterers within a cloud of randomly positioned scatterers. As defined in Chapter 2, a frame of data comprises the RF echo signal segments from the acoustic scan lines forming a single ultrasound image. The reference data are obtained from a material with only randomly distributed scatterers. A set of parameter estimation regions, or PERs, including uncorrelated data and located at the same depth range are defined in the sample and the reference frames of echo data. An estimate of the collapsed average of the generalized spectrum is

obtained from each PER. The magnitude q of the collapsed average of the generalized spectrum at the frequency corresponding to the periodic scatterer spacing is measured in each of the estimates from the sample data. The value of the reference collapsed average q_{Ref} is measured at the same frequency in all of the estimated reference collapsed averages. The mean and variance of q and q_{Ref} are estimated from the estimates in the sample and the reference. Finally, the normalized contrast C_q and CNRq are computed according to Eqs. (3.69) and (3.70).

This procedure was applied to simulated echo signals and signals obtained from tissue mimicking phantoms using a commercial ultrasound system. The simulated echo signals were obtained using the simulation tool described in Chapter 2. The scatterer distribution in this experiment included a random component with mean density of 48 scatterers per resolution cell and a set of periodically spaced scatterers with spacing ranging from 0.5λ to 7.8λ (λ=0.26mm, as described below). Note that this range overlaps with the one used in the analysis of the statistics of stationary signals. This was done to identify regions in which the two methods are able to detect the presence of coherence. The scattering cross section of the periodic scatterers was varied from a factor of 2 to a factor of 24 times the mean scattering cross section of the random scatterers. Finally, following Ref. 92, gamma distributed fluctuations in the spacing of the periodic scatterers were considered, with variance equal to 5% to 100% of the mean spacing. The gamma distribution has been widely used in other evaluations of scatterer periodicity for quantitative ultrasound purposes.[50,118,121,131] The reference data set included only randomly positioned scatterers with a mean density of 48 scatterers per resolution cell. Backscattered echo signals were sampled at 40MHz. The center frequency (6 MHz) and -6dB fractional bandwidth (72%) were set to mimic the properties of the ultrasound transducer used in the experiment. This led to an effective pulse duration of 0.38μs, or a pulse length of 0.29mm. The propagation speed of the acoustic pulse was assumed to be 1540m/s. Thus, the wavelength within the pulse was 0.26mm.

The tissue mimicking phantoms used in the experimental part were phantoms C and D from Chapter 2. Phantom C contains a homogeneous distribution of randomly positioned scatterers, with a concentration

of 236 scatterers/mm^3. Phantom D had, in addition to a cloud of random scatterers with a concentration of 236 scatterers/mm^3, an array of 0.4mm spaced, 0.1mm diameter nylon fibers arranged in a single plane and spanning 1cm axially. For more detail about the phantoms' properties, refer to Chapter 2. The phantoms were scanned with a Siemens Acuson S2000 (Siemens Medical Solutions USA, Inc, Malvern, PA) using an 18L6 linear array transducer operated at 10MHz excitation frequency. This transducer is the one used in our clinical protocol described in Chapter 5 of this thesis. The transmit focus was placed at the center of the 1cm span of the fiber plane in phantom D. Radiofrequency (RF) data frames were acquired from the system's Axius Direct Research Interface.[86] RF data frames from 10 independent planes in phantom C and from 1 plane (fiber plane) from phantom D were obtained by shifting the transducer elevationally at least by one aperture.

The generalized spectrum was estimated using the single taper estimator (boxcar and first DPSS (k=0) for NW=6), the WOSA estimator (50% subsegment length, 50% overlap), and the multitaper estimator. In the latter case, the time-half bandwidth NW product was varied from 2 to 12, within the range suggested by Haykin *et al.*[109] In addition, we explored using fixed half bandwidth W values (0.5MHz and 1MHz). Notice that in these two cases the number of tapers is reduced as the signal segment length is shortened. The PER sizes ranged axially from 5 to 30 pulse lengths, and laterally from 5 to 30 uncorrelated scan lines in the case of the simulations. A total of 100 uncorrelated PERs from each simulated scenario were obtained. In the case of the phantom experiments with the 18L6 transducer, the PER ranged from 4 to 16 axial correlation lengths (1.3mm to 7.8mm) and 4 to 16 lateral correlation lengths (2.5mm to 14.9mm). This resulted in a total of 9 uncorrelated PERs within the frame of sample echo signals.

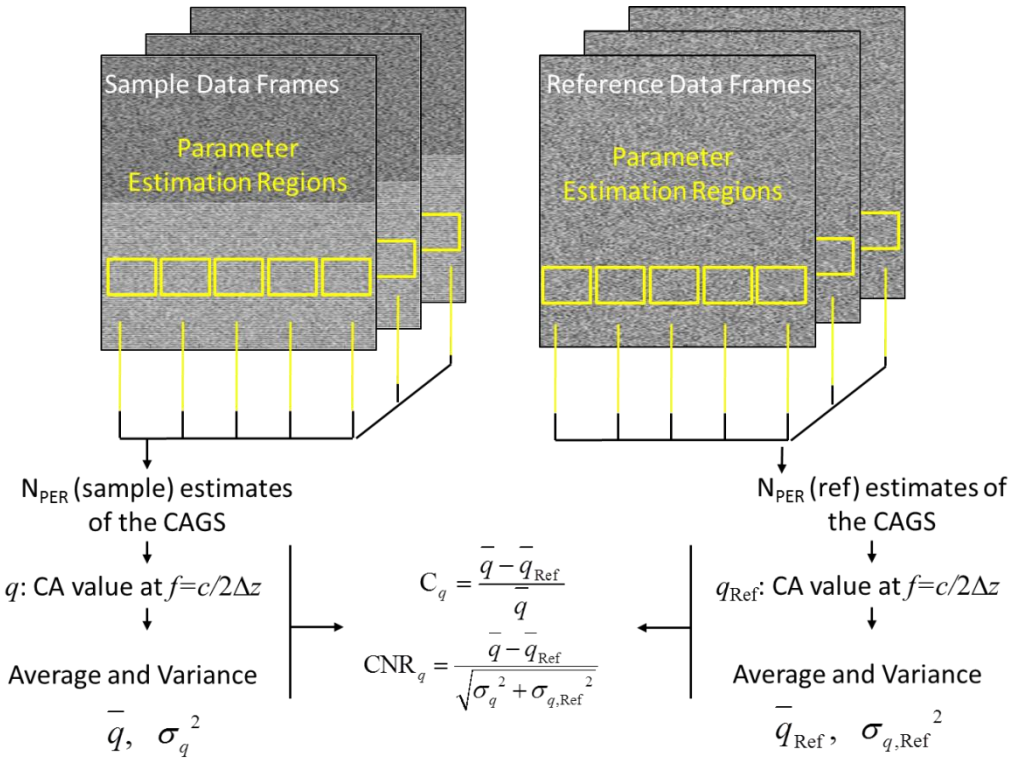

Figure 3.8 Diagram of the general procedure followed to quantify the conspicuity of the periodicity peak in the collapsed average of the generalized spectrum by means of the normalized contrast C_q and the contrast to noise ratio CNR_q.

3.4.2 Results - Simulations

Figure 3.9 shows the normalized contrast C_q in panel (a) and the contrast to noise ratio CNR_q in panel (b) of the periodicity peak in the collapsed average of the generalized spectrum (CAGS) as a function of the size of the parameter estimation region (PER) expressed in pulse lengths times the number of uncorrelated scan lines included in the PER. Each color curve corresponds to a different GS estimator: Single-taper with boxcar (blue) or the first (k=0) DPSS taper for NW=6 (red), WOSA (green), and multitaper, MTM, NW=6 (black). The coherent component in the sample was a periodic array of scatterers separated by 0.4mm and a scattering amplitude 12 times the mean scattering amplitude of the random scatterers. Note that contrast from all the estimators approaches zero for PER sizes smaller than 5 pulse lengths × 5 uncorrelated scan lines. When using larger PERs, the multitaper method offers the

highest contrast of the periodicity peak in the CAGS. At a PER size of 15 pulse lengths × 15 uncorrelated scan lines, the contrast from the multitaper estimator is about 3 times higher than those from the other methods.

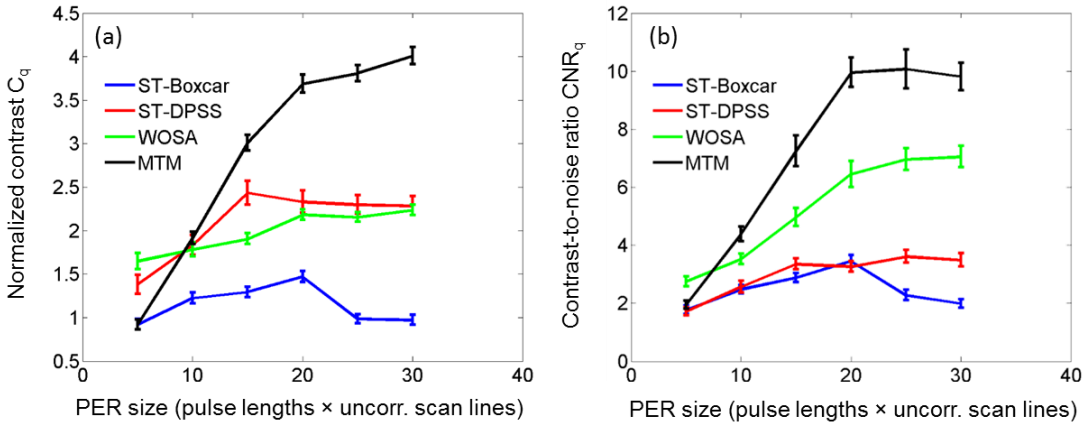

Figure 3.9 (a) Normalized contrast C_q and (b) contrast-to-noise ratio CNR_q of the periodicity peak in the Collapsed Average of the Generalized Spectrum as a function of the PER size. Curves correspond to different estimators: Single taper estimator with boxcar (blue) or first DPSS (k=0) for NW=6 (red) tapers, Weighted Overlapped Segment Average estimator (WOSA, green) and multitaper estimator (MTM, black). The simulated sample phantom consisted of a random scatterer concentration of 48 scatterers per resolution cell and a periodic array of scatterers with spacing equal to 1.6λ and having 12 times the scattering cross section of each of the randomly positioned scatterers. The simulated reference had a random scatterer concentration of 48 scatterers per resolution cell.

In Fig. 3.9(b), the CNR_q of the periodicity peak of the CAGS from the multitaper estimator is greater than the values from other estimators. At a PER size of 15 pulse lengths × 15 uncorrelated scan lines, the CNR_q from the multitaper estimator is about 3.3 times higher than that of the single taper estimators, which is the same gain observed in terms of contrast for this particular PER size. This suggests that the advantage of the multitaper method for small PERs is caused by the morphological features of the periodicity cell rather than the variance reduction. In addition, the gain obtained when using a low leakage taper in the single taper estimator is lost due to its poorer variance properties. As a consequence, the boxcar and the DPSS taper performed similarly in terms of CNR_q. In the case of the WOSA estimator,

the gain in CNR_q with respect to the single-taper boxcar estimator is slightly larger than the gain in contrast, indicating its advantage in terms of variance reduction.

Figure 3.10(a) shows the CNR_q of the periodicity peak in the CAGS as a function of the spacing between consecutive scatterers in the simulated data. The CNR_q from all the estimators drops to zero drastically when the scatterer spacing is smaller than 0.7λ. The reduction of CNR_q from the WOSA and the multitaper estimators is more severe because, as the spacing increases, the separation among adjacent periodicity cells decreases and their overlap increases.

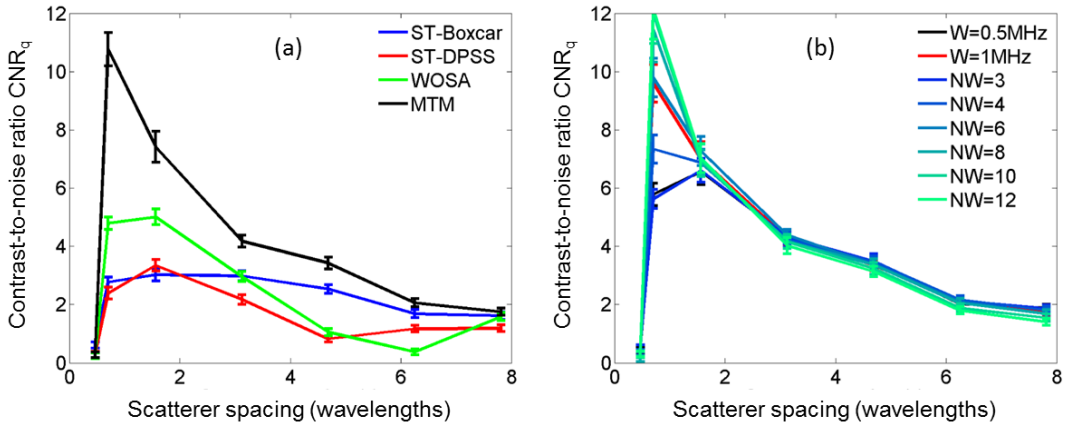

Figure 3.10 Contrast-to-noise ratio CNR_q of the periodicity peak in the Collapsed Average of the Generalized Spectrum as a function of the scatterer spacing in units of wavelengths (λ=0.256mm). Curves in (a) correspond to a different estimator: Single taper estimator with boxcar (blue) or first DPSS (k=0) for NW=6 (red) tapers, Weighted Overlapped Segment Average estimator (WOSA, green) and multitaper estimator (MTM, black). Curves in (b) correspond to different versions of the multitaper method. The simulated sample phantom consisted of a random scatterer concentration of 48 scatterers per resolution cell and a periodic array of scatterers with 12 times the scattering cross section of each of the randomly positioned scatterers. The simulated reference had a random scatterer concentration of 48 scatterers per resolution cell. The PER size was 15 pulse lengths (axially) × 15 uncorrelated scan lines (laterally).

Figure 3.10(b) presents the dependence of the CNR_q of the periodicity peak as the time-half bandwidth product *NW* of the multitaper method, and hence the number of tapers (2*NW*-1), is varied. Each blue-

green shade corresponds to a different *NW* value. The black and red curves correspond to fixed bandwidths $2Wf_s$ (0.5MHz and 1MHz, respectively). A significant difference among the different *NW* values occurs only for very small scatterer spacing's. The reason for this is that as the *NW* value is reduced for a particular PER length (fixed *N*), *W* and the size of the periodicity cells are reduced and become smaller than the spacing among the periodicity cells. As a consequence, the zero values between adjacent periodicity cells along each secondary diagonal reduce the average value in the collapsed average representation. As the spacing among scatterers is increased the periodicity cells come closer and overlap, regardless of the size of the periodicity cell. As a consequence, for these larger spacing values, varying *NW* becomes inconsequential. As stated before, the fact that equivalent CNR_q values are obtained with different *NW* values indicates that it mainly depends on the morphological features of the generalized spectrum and not on the variance reduction efficiency.

Figure 3.11 shows contour curves (dashed lines) of the amplitude of the periodicity peak in the CAGS from 0.4mm spaced periodic scatterers as the scattering amplitude of the periodic scatterers (expressed as a multiple of the average scattering strength of the random scatterers) and the concentration of the diffuse scatterers is varied. The numbers next to the curves indicate the value for that particular contour. It can be observed that the amplitude of the periodicity peak in the CAGS increases as the scattering amplitude of the periodic scatterers increases and as the concentration of the diffuse scatterers decreases. On top of the contour curves of the peak of the CAGS are contour curves of the ratio of the average signal intensity per periodic scatterer to that of the random scatterers:[50]

$$R = 10\log_{10}\left[\frac{\frac{1}{N_{\text{Per}}}\int_{t_0}^{t_0+\Delta t} {y_{\text{Periodic}}}^2(t)dt}{\int_{t_0}^{t_0+\Delta t} {y_{\text{Random}}}^2(t)dt}\right] \tag{3.71}$$

where N_{Per} is the number of scatterers within the resolution cell, $y_{\text{Periodic}}(t)$ is the RF signal only from the backscattered echoes form the periodic scatterers, and $y_{\text{Random}}(t)$ is the RF signal only from the backscattered echoes from random scatterers.[50] To get the contour curves based on *R*, the average of the *R*

values for different combinations of the scattering amplitude of the periodic scatterers and concentrations (number of scatterers per resolution cell) of the randomly positioned scatterers yielding the same amplitude of the periodicity peak in the CAGS were computed. Then contour curves for those average values were created and plotted on top of contour plots based on the amplitude of the peak of the CAGS. This figure shows that the amplitude of the peak of the collapsed average follows the same dependence on the periodic scattering amplitude and diffuse scatterer concentration as *R*. This suggests a relationship between the amplitude of the periodic feature and the ratio of the power of the coherent signal per periodic scatterer to the power of the diffuse component.

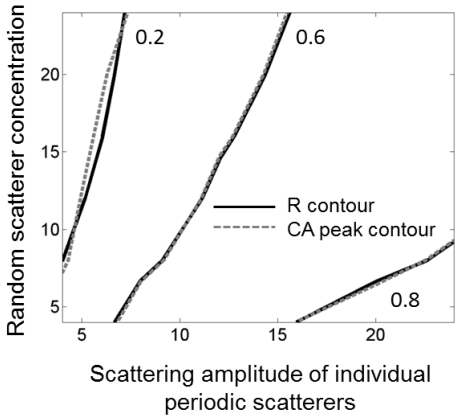

Figure 3.11 Contour curves (dashed) of the maximum value of the collapsed average (CA) of the generalized spectrum as a function of the individual periodic scatterer's scattering amplitude and the random scatterer concentration (number of scatterers per resolution cell). Contour curves (solid) of the ratio of the energy of the coherent component of the backscatter echo signal per periodic scatterer to that of the incoherent component.

Figure 3.12(a) shows the CNR_q of the periodicity peak from a periodic array of scatterers with spacing equal to 1.6λ as a function of *R*, the ratio of coherent to incoherent power per periodic scatterer. The PER size was 15 pulse lengths × 15 uncorrelated scan lines. Over the range of explored scattering cross sections of the coherent component, the multitaper method offered the largest CNR_q of the periodicity peak. The CNR_q becomes significantly different from zero for values of *R* larger than about -7dB. Figure 3.12(b) analyzes the effects of introducing variance in the spacing among the "regularly spaced"

scatterers. It shows the CNR_q of the periodicity peak of the CAGS corresponding to a periodic spacing of 1.6λ as a function of the SNR of the scatterer spacing (mean / standard deviation). As expected, CNR_q of the periodicity peak decreases as the spacing among the regular scatterers becomes less regular (lower SNR). In terms of the contrast, no significant difference among the various estimators exists when the spacing SNR is smaller than 2, i.e., the mean is twice the standard deviation. In addition, no significant difference was found between the WOSA and the multitaper estimator for SNR smaller than 10.

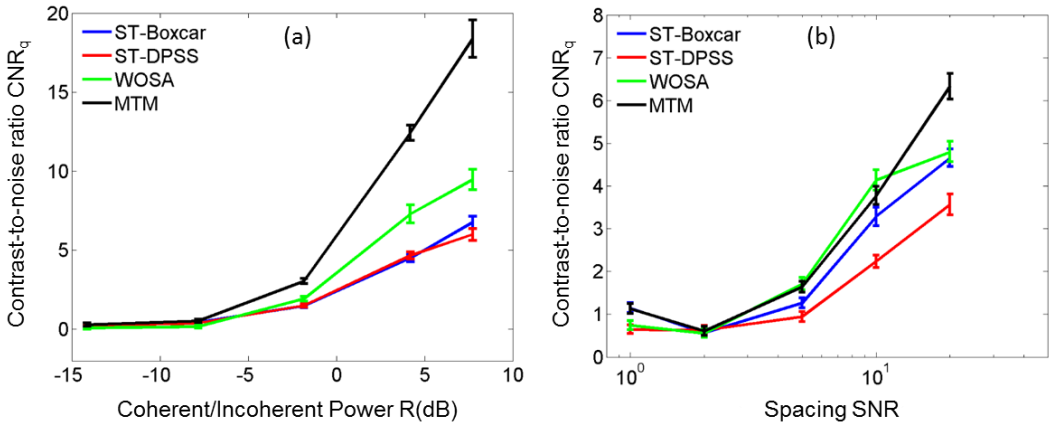

Figure 3.12 Contrast-to-noise CNR_q of the periodicity peak in the Collapsed Average of the Generalized Spectrum as a function of (a) *R*, the ratio of the total scattering power of the coherent component to that of the incoherent component, and (b) the SNR of the scatterer spacing. Curves correspond to different estimators: Single taper estimator with boxcar (blue) or first DPSS (k=0) for NW=6 (red) tapers, Weighted Overlapped Segment Average estimator (WOSA, green) and multitaper estimator (MTM, black). The simulated phantom consisted of a random scatterer concentration of 48 scatterers per resolution cell and a periodic array of scatterers with 1.6λ spacing. The simulated reference had a random scatterer concentration of 48 scatterers per resolution cell. The PER size was 15 pulse lengths (axially) × 15 uncorrelated scan lines (laterally).

3.4.3 Results – Tissue mimicking phantom

Figure 3.13 shows the CNR_q of the fundamental frequency detected by means of the collapsed average of the generalized spectrum (CAGS) for the expected 0.4mm fiber spacing as a function of the size of the parameter estimation region in units of axial × lateral correlation lengths as defined in Chapter 2. Each

curve corresponds to a different estimator of the generalized spectrum. As expected, the CNR increases as the PER size increases for all estimator methods. However, no significant difference was observed among the different estimators, with the exception of the single-taper estimator with the DPSS taper, which offered the lowest CNR over most of the analyzed PER sizes.

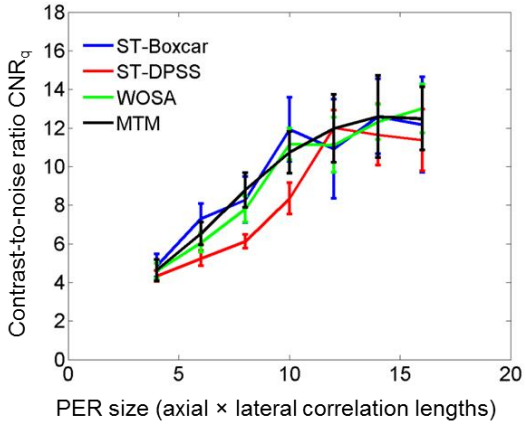

Figure 3.13 Contrast-to-noise ratio CNR_q of the periodicity peak in the Collapsed Average of the Generalized Spectrum corresponding to the 0.4mm spacing of the fibers in the tissue-mimicking phantom, plotted as a function of the PER size. Curves correspond to different estimators: Single taper estimator with boxcar (blue) or first DPSS (k=0) for NW=6 (red) tapers, Weighted Overlapped Segment Average estimator (WOSA, green) and multitaper estimator (MTM, black).

3.5 Accuracy of detection performance

3.5.1 Methods

In this section, we investigate the relationship between the conspicuity of the scatterer-periodicity feature (maximum value of the collapsed average of the generalized spectrum) and the accuracy of the detected frequency component. Ideally the maximum value of the collapsed average of the generalized spectrum (CAGS) outside the 0MHz main lobe (corresponding to the main diagonal of the generalized spectrum) would be located at $f=c/2\Delta$, where Δ is the mean scatterer spacing. However, the different signal processing steps involved in the estimation of the generalized spectrum can cause the maximum to occur at a harmonic of this frequency instead of the fundamental. In addition, the reduction of the size of the

parameter estimation region reduces the number of scattering volumes containing random scatterers, thus causing insufficient averaging of the contribution from random scatterers to the total phase. These maxima are referred to as "spurious" or "false coherence" peaks in the CAGS. Thus the following analysis explores the performance of the generalized spectrum and the Signal Spectrum Analysis to produce a maximum at the expected frequency and discusses the observations in light of the results from the previous section.

There are two main questions to answer in this section:

1. Does the maximum value of the collapsed average of the generalized spectrum occur at the expected frequency corresponding to the scatterer spacing? To answer this question, two parameters were quantified:
    - **Fractional occurrence of the fundamental frequency FO_{Fund}**: Number of estimates of the collapsed average of the generalized spectrum in which the maximum value occurred at the frequency corresponding to the mean spacing of the periodic scatterers $f=c/2\Delta$, expressed as a fraction of the total number of realizations
    - **Fractional occurrence of the fundamental frequency plus its harmonics FO_{All}**: Number of estimates of the collapsed average of the generalized spectrum in which the maximum value occurred at the frequency corresponding to the mean spacing of the periodic scatterers $f=c/2\Delta$ or one of its harmonics, expressed as a fraction of the total number of realizations.
2. How much does the reduction of the PER size affect the detection of the expected frequency by means of finding the maximum value of the collapsed average? To answer this question, the variations of FO_{Fund} and FO_{All} were determined as the PER size was reduced.

The importance of the evaluation of both FO_{Fund} and FO_{All} relies on the fact that, when working with real tissue, there is no previous knowledge about the presence of periodic scatterers or of their spacing. Therefore, it is not possible to know beforehand if the detected maximum value of the collapsed average is a fundamental or a harmonic. If the mean scatterer spacing is estimated by only using the maximum value of the collapsed average, the estimate will be biased if the maximum collapsed average value occurs at a harmonic. Therefore, it is important to understand how the estimation of the generalized spectrum affects the detection of the fundamental and its harmonics.

The analysis of the accuracy of the detected frequency component corresponding to a periodic scatterer array has been previously and independently studied and discussed by Huang *et al.*[119] and Donohue *et al.*[51] using single-taper and WOSA estimators of the generalized spectrum, and by Machado *et al.*[134,139] using singular spectrum analysis. Here, we advance these previous studies by comparing the performance of these techniques with the multitaper estimator of the generalized spectrum and by providing a broader study that considers a wide range of scatterer spacing values (from not-resolved to resolved scales), spacing variance, coherent-to-incoherent scattering power ratios, and PER sizes (of great importance in the context of parametric image formation). The evaluation of FO_{Fund} and FO_{All} was done using the same estimates of the generalized spectrum from simulated and phantom-based echo data from Step 2, which allows us to discuss the observations in terms of the conspicuity analysis presented in the previous section. The maxima were selected within a search region bounded by a low frequency limit corresponding to 90% of the gate length as suggested by Huang *et al.*,[119] and by a high frequency limit equal to half the highest frequency within the +10dB useful bandwidth (5MHz) (see Discussion).

3.5.2 Singular Spectrum Analysis

In addition to the generalized spectrum, we explored the use of the singular spectrum analysis method to decompose the echo signal into its periodic and its diffuse components to detect the presence of a periodic array of scatterers. Singular Spectrum Analysis (SSA) provides a data-adaptive, orthonormal basis to describe the stochastic properties of a signal.[43,134,135,136] It is applied in two stages: *Decomposition* and

Reconstruction. The *Decomposition* stage involves two steps. First, a set of *M* lagged vectors is obtained by running an *L*-length window along each envelope segment one sample at a time. Each of the *M* lagged vectors is arranged into a matrix **X** known as the *trajectory matrix*. Second, singular value decomposition is applied to the autocovariance matrix $\mathbf{C}=\mathbf{X}\mathbf{X}^{\dagger}$ (where † indicates a matrix adjoint) as well as to $\mathbf{C}^{\dagger}$ by solving the eigen-equations:[141]

$$\mathbf{C}\mathbf{v}_l = \lambda_l \mathbf{v}_l, \quad \mathbf{C}^{\dagger}\mathbf{u}_l = \lambda_l \mathbf{u}_l, \tag{3.72}$$

where each set $\{\mathbf{u}_l, \mathbf{v}_l, \lambda_l\}$, with $l=1,\ldots,L$ is referred to as an *eigentriplet*. Both eigenvector sets $\mathbf{u}_l$ and $\mathbf{v}_l$ have the same eigenvalues λ_l, which are zero or positive, are sorted in decreasing order, and their sum equals the total signal variance. The set of all eigenvalues is called the *eigenspectrum*. Figure 3.14(a) shows the eigenspectrum of an envelope signal segment spanning 16 pulse lengths along Phantom D's fiber plane. Periodic components in the envelope signal generate pairs of closely-valued eigenvalues. These were identified by means of a four-step selection process proposed by Machado *et al.*[134] First, noise-related eigentriplets were ruled out by keeping only those contributing to 98% of the total variance. Second, eigenvalues differing less than 2.5% were identified as periodic pairs (Fig. 3.14(a)). Third, the cross-correlation between the eigenvectors corresponding to the eigenvalues of each periodic pair was computed. Pairs with maximum cross-correlation smaller than 0.95 were excluded from the analysis. Finally, frequency spectra from the remaining eigenvector pairs were compared. Those pairs whose spectra had maximum values at frequencies differing less than half a frequency bin were selected as the final periodic pairs from which the periodic component $y_p(t)$ of the envelope signal segment was reconstructed.

In the *Reconstruction* stage, a time-series $y_p(t)$ including only contributions from periodic components is formed. This stage involves three steps. First, trajectory matrices from the $i=1,\ldots,p$ eigentriples of the periodic pairs are reconstructed as follows:[141]

$$\mathbf{X}_i = \sqrt{\lambda_i}\,\mathbf{u}_i \mathbf{v}_i{}'. \tag{3.73}$$

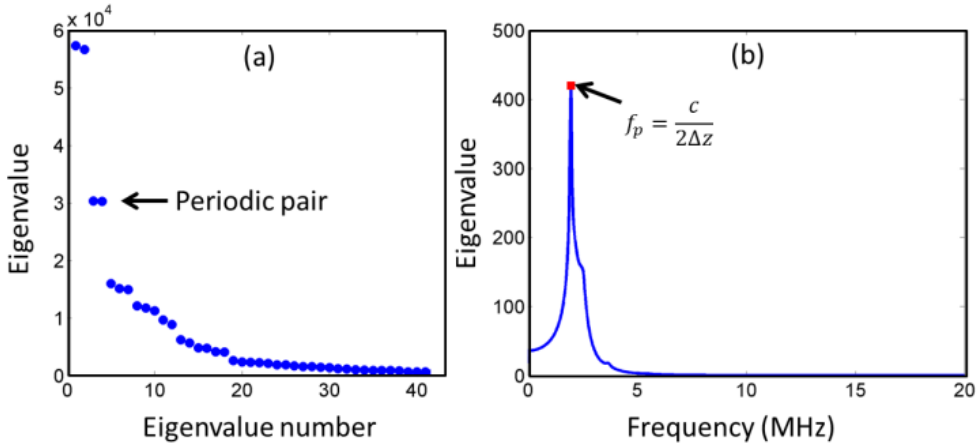

Figure 3.14 (a) Singular Spectrum of a single envelope signal segment of length 16 pulse lengths. The arrow indicates the presence of closely-valued eigenvalues corresponding to a periodic component. (b) Average power spectrum from the reconstructed periodic components from 16 uncorrelated scan lines. The arrow indicates the presence of a maximum a frequency corresponding to the periodic scatterer spacing.

Second, a total periodic trajectory matrix **P** is composed by summing the reconstructed $\mathbf{X}_i$, $i=1,\ldots,p$. Third, **P** is transformed into a time series $y_p(t)$ by averaging along its diagonals. The procedure was applied to the envelope segment of each of the N_{AL} acoustic scan lines within the PER, resulting in N_{AL} periodic components. Finally, the power spectrum was obtained from each periodic component and averaged across the N_{avg} estimates. The frequency of the maximum value of the average spectrum was selected as the frequency f_p associated to the periodicity of the signal ($f_p=c/2\Delta$). Figure 3.14(b) shows the average power spectrum of the reconstructed periodic components as well as the f_p=1.9MHz corresponding to the 0.4mm spacing between fibers in Phantom D. It is important to mention that this procedure is based on the recommendations by Pereira *et al.*,[53] and no further optimization was performed. The purpose of its inclusion was only to compare the detection performance of one of the currently applied techniques (SSA) to the one optimized in this work (the generalized spectrum).

3.5.2 Results - Simulations

Figure 3.15 shows scatter plots of the maximum values of the 100 estimates of the collapsed average of the Generalized Spectrum and their frequencies for the three estimators of the generalized spectrum: (a) single taper with boxcar taper, (b) WOSA estimator, and (c) multitaper estimator. Fig. 3.15(d) shows a scatter plot of the maximum values of the power spectrum of the 100 estimates of the reconstructed periodic component using SSA and the corresponding frequency. The simulated conditions are 100 independent realizations of a periodic array of scatterers with 0.4mm spacing, each with a scattering amplitude 12 times that of the surrounding random scatterers. Randomly positioned scatterers have a concentration of 48 scatterers/resolution cell. The PER size was 30 pulse lengths × 30 uncorrelated scan lines (largest). The expected periodicity frequency for the 0.4mm spacing is 1.93MHz. The ideal case would be to have all 100 estimates concentrated at the same collapsed average value and at 1.93MHz. This is most closely arrived at with the multitaper estimator of the generalized spectrum. In the case of the single taper estimate (Fig. 3.15(a)), the presence of spurious peaks (frequencies different from the expected 1.93MHz or its harmonics) is evident. The additional averaging performed in the WOSA (Fig. 3.15(b)) and MTM (Fig. 3.15(c)) estimates of the generalized spectrum reduces the presence of spurious components over the single taper estimate. In particular, the WOSA estimate is sensitive to both the fundamental 1.93MHz component and its first harmonic (3.86MHz). Under the simulated conditions, the MTM estimate and the SSA method led to perfect detection of the fundamental component.

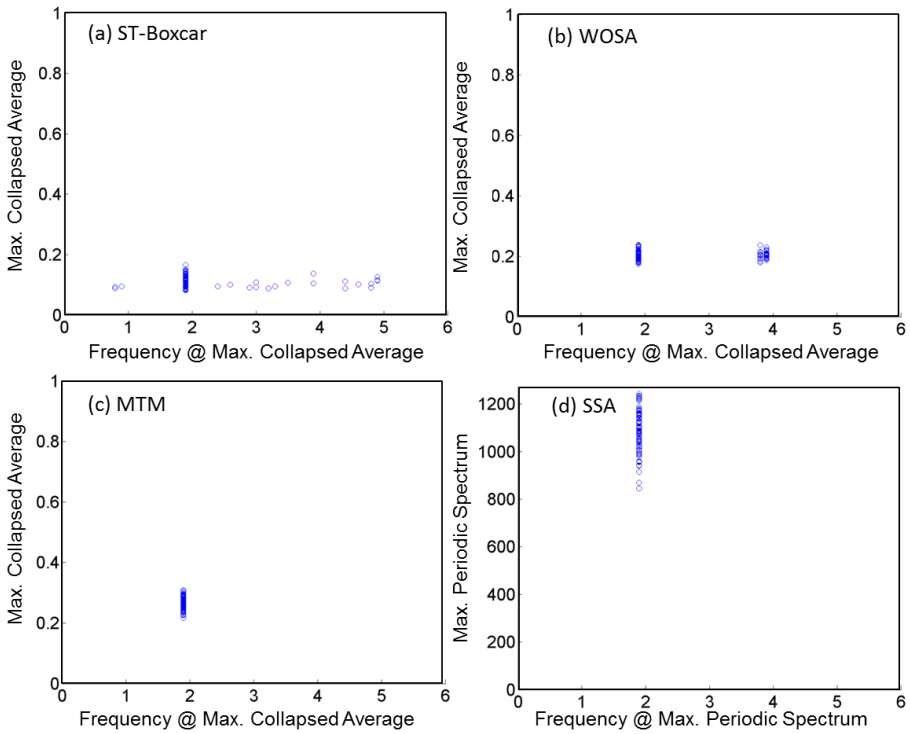

Figure 3.15 Scatter plots of the value of the periodicity feature and its frequency from 100 independent realizations of the detection methods: (a) single taper generalized spectrum (ST-Boxcar), (b) Weighted Overlapped Segment Average (WOSA) generalized spectrum, (c) multi-taper generalized spectrum (MTM) and (d) Singular spectrum analysis (SSA). Simulated conditions were a perfect lattice of 0.4mm spaced periodic scatterers with scattering amplitude 12 times that of the surrounding random scatterers (48 scatterers/resolution cell). The PER size was 30 pulse lengths × 30 uncorrelated scan lines.

Figure 3.16 presents the variation of the fractional occurrence of the periodicity-related maxima in the CAGS on the size of the parameter estimation region. The simulated conditions are the same as in Fig. 3.16. Figure 3.16(a) shows the fractional occurrence of the fundamental frequency (FO_{Fund}) and Figure 3.16(b) shows the cumulative fractional occurrence (FO_{All}) of the fundamental frequency plus its first harmonic (3.86MHz). Each curve corresponds to a different GS estimation method (single taper in blue, WOSA in green, multitaper in black) or the singular spectrum analysis (magenta). The fractional occurrence of the fundamental peak as well as that of all the periodicity related peaks have the largest

values when using the multitaper estimate of the generalized spectrum. When the presence of the second harmonic is also taken into account, the fractional occurrence of all periodicity related maxima increases for the generalized spectrum based methods. The exception is the fractional occurrence of the SSA, which remains practically unchanged after the inclusion of the harmonics. The cumulative fractional occurrence of most methods starts decreasing significantly when the PER size is reduced below 20 pulse lengths × 20 uncorrelated scan lines. The fractional occurrence of the multitaper method remains at the highest value of 1 even when the PER size was reduced down to 10 pulse lengths × 10 uncorrelated scan lines. The cumulative fractional occurrence of the single taper estimate decreases for PER sizes larger than 20 pulse lengths × 20 uncorrelated scan lines due to the smaller size of the periodicity cell as the PER gated RF signal segment is reduced. Note that this correlates to the lower CNR of the periodicity peak for this estimator shown in Fig. 3.9(b).

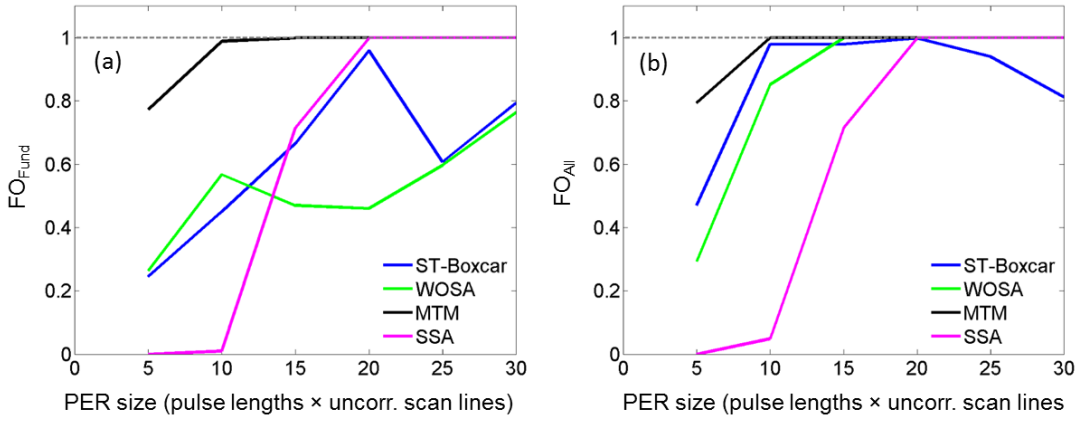

Figure 3.16 PER size dependence of the fractional occurrence of (a) the fundamental frequency FO_{Fund} and (b) the fundamental plus its harmonics FO_{All} related to the spacing of the periodic scatterers and detected as the maximum value of the collapsed average of the generalized spectrum (CAGS). Values shown were obtained using the single taper with a boxcar taper (blue), Weighted Overlapped Segment Average (WOSA, green) and multitaper (MTM, black) estimates of the generalized spectrum, or the maximum value of the power spectral density of the reconstructed periodic component using singular spectrum analysis (SSA). The gray dashed line indicates perfect detection (fractional occurrence equal to unity). Simulated conditions were a perfect lattice of 0.4mm spaced periodic scatterers, with scattering amplitude 12 times that of each of the surrounding random scatterers (48 scatterers/resolution cell).

In Fig. 3.17(a) and 3.17(b) the fractional occurrence of the fundamental frequency and the fundamental plus its harmonics are plotted as a function of the scatterer spacing expressed in wavelengths. As in Fig. 3.16, each curve corresponds to a different generalized spectrum estimator or to the singular spectrum analysis result. The PER size was 30 pulse lengths × 30 uncorrelated acoustic scan lines. Figure 3.17(a) shows that the detection of the fundamental frequency with the single taper and multitaper estimates of the generalized spectrum, as well as with the singular spectrum analysis, practically falls to zero when the spacing is larger than about three wavelengths. The fundamental frequency corresponding to this spacing is 1MHz. Beyond this spacing, the detection of the periodic component is done though the harmonics, thus leading to close to perfect detection in Fig. 3.17(b) with the GS estimates. The multitaper estimator GS leads to perfect detection over a wider range of scatterer spacing values compared to the other GS estimates and the singular spectrum analysis.

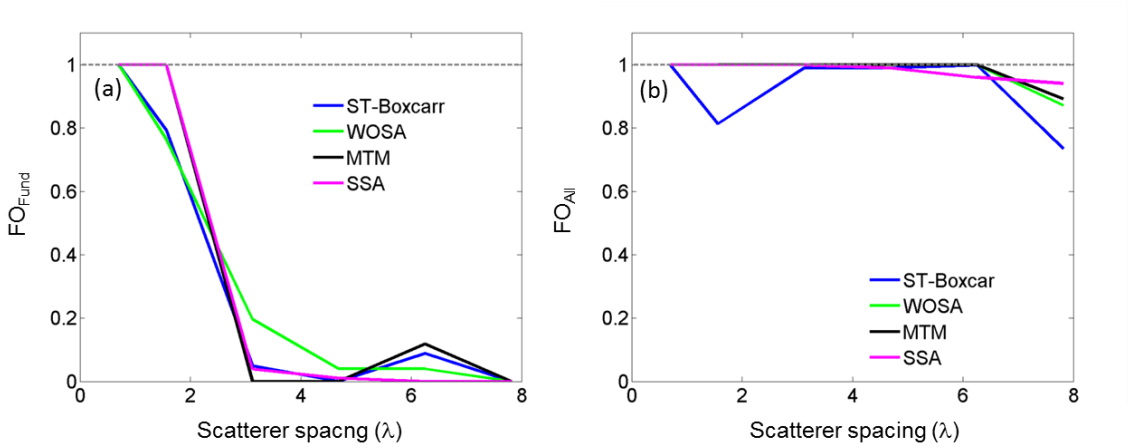

Figure 3.17 Scatterer spacing dependence of the fractional occurrence of (a) the fundamental frequency FO_{Fund} and (b) the fundamental plus its harmonics FO_{All} related to the spacing of the periodic scatterers and detected as the maximum value of the collapsed average. Results are shown for single taper with a boxcar taper (blue), Weighted Overlapped Segment Average estimator (WOSA, green) and multitaper (MTM, black) estimates of the generalized spectrum, as well as for the maximum value of the power spectral density of the reconstructed periodic component using singular spectrum analysis (SSA). Scatterer spacing is quantified in units of wavelengths (λ=0.26mm). The gray dashed line indicates perfect detection (fractional occurrence equal to unity). Simulated conditions included a perfect lattice of 1.6λ (0.4mm) spaced periodic scatterers with scattering amplitude 12 times that of each of the surrounding random scatterers (48 scatterers/resolution cell).

Figure 3.18 analyzes the effect of reducing the scattering cross section of the periodic scatterers with respect to that of the random scatterers for a periodic scatterer lattice with 0.4mm spacing. The PER size is 30 pulse lengths × 30 uncorrelated scan lines. The horizontal axis in both panes of this figure is in units of the ratio of the coherent to incoherent scattering power ratio R defined in Eq. (3.71) and expressed in decibels. Note that for all GS methods and the singular spectrum analysis the cumulative fractional occurrence stabilizes at its lowest value for values of R smaller than -7dB. This agrees with the value at which the CNR of the periodicity peak shown in Fig. 3.12(a) approaches zero. Over the entire range of R, the multitaper estimator offered higher cumulative fractional occurrence FO_{All} than any of the other methods.

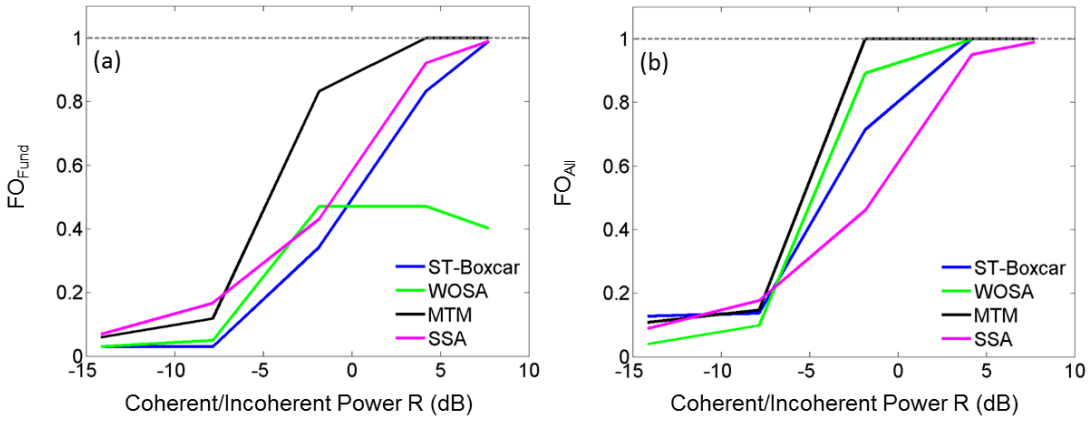

Figure 3.18 Fractional occurrence of (a) the fundamental frequency FO_{Fund} and (b) the fundamental plus its harmonics FO_{All} related to the spacing of the periodic scatterers as a function of the coherent to incoherent power R per periodic scatterer in dB. Results are shown for the single taper with a boxcar taper (blue), Weighted Overlapped Segment Average estimator (WOSA, green) and multitaper (MTM, black) estimators of the generalized spectrum, as well as for the maximum value of the power spectral density of the reconstructed periodic component using singular spectrum analysis (SSA). The gray dashed line indicates perfect detection (fractional occurrence equal to unity). Simulated conditions were a perfect lattice of periodic scatterers with scatterer spacing of 1.6λ (0.4mm) and surrounding random scatterers (48 scatterers/resolution cell). The PER size is 30 pulse lengths × 30 uncorrelated scan lines.

Figure 3.19 presents the variation of the fractional occurrence of the fundamental frequency in (a) and the fundamental plus its harmonics in (b) when the standard deviation of the periodic scatterer spacing is increased. The simulated conditions and PER size are the same as those in Figs. 3.17 and 3.18. One can see that both FO_{Fund} and FO_{All} reach a low detection plateau when the spacing SNR is lower than 2, which agrees with the observed CNR trends of Fig. 3.12(b). The WOSA and the multitaper estimates of the generalized spectrum are less sensitive to the randomization of the scatterer spacing. This also agrees with the higher CNR values of the WOSA estimator of the fundamental frequency observed in Fig. 3.12(b). Perfect detection of the fundamental frequency and its harmonics is obtained when the standard deviation of the spacing is less than 10% of the mean spacing when using the generalized spectrum methods.

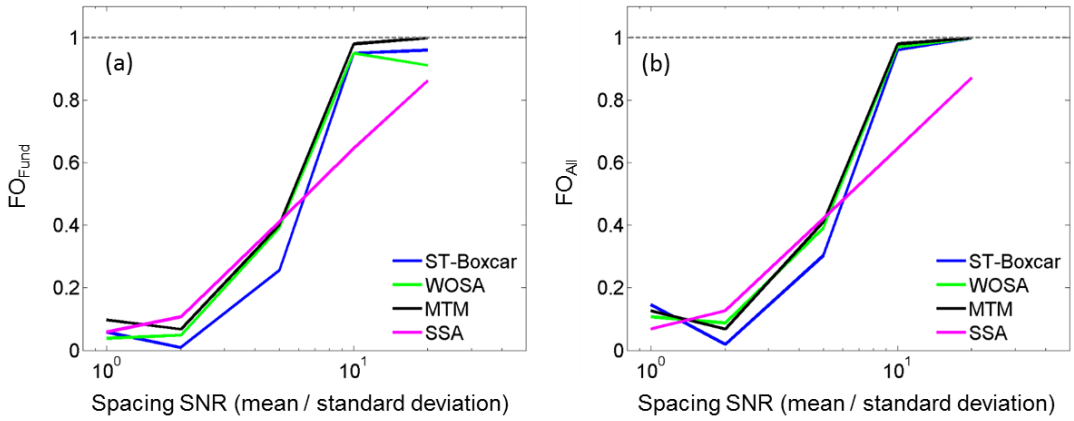

Figure 3.19 Fractional occurrence of (a) the fundamental frequency FO_{Fund} and (b) the fundamental plus its harmonics FO_{All} related to the spacing of the periodic scatterers as a function of the scatterer spacing SNR. FO_{Fund} and FO_{All} are detected as the maximum value of the collapsed average of single taper with a boxcar taper (blue), Weighted Overlapped Segment Average estimator (WOSA, green) and multitaper (MTM, black) estimates of the generalized spectrum, or using the maximum value of the power spectral density of the reconstructed periodic component using singular spectrum analysis (SSA). The gray dashed line indicates perfect detection (fractional occurrence equal to unity). Simulated conditions were a perfect lattice of periodic scatterers with scatterer spacing of 1.6λ (0.4mm) and surrounding random scatterers (48 scatterers/resolution cell). The PER size is 30 pulse lengths × 30 uncorrelated scan lines.

3.5.3 Results – Tissue mimicking phantom

Figure 3.20 presents the statistical analysis of the detection of the expected scatterer spacing frequency components by means of the maximum value of the collapsed average of the generalized spectrum or the singular spectrum analysis applied to backscattered echo data from Phantom D. Fig. 3.20(a) shows the fractional occurrence of the fundamental peak as the PER size is varied. Different curves correspond to different estimates of the generalized spectrum or to the singular spectrum analysis. Figure 3.20(b) shows the fractional occurrence of the fundamental peak plus its first harmonic. In general the fractional detection decreases as the PER size decreases. The multitaper estimate of the generalized spectrum led to the highest fractional occurrence of both the fundamental peak alone and the fundamental with its

harmonics. In addition, the fractional occurrence from the singular spectrum analysis remained mostly unaltered by considering only the fundamental peak or the fundamental plus its harmonic, as also observed in the simulations.

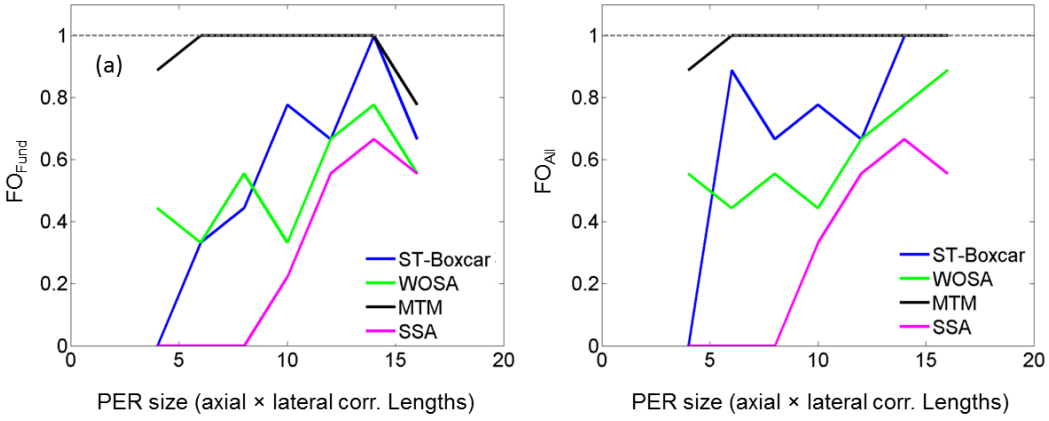

Figure 3.20 PER size dependence of the fractional occurrence of (a) the fundamental frequency FO_{Fund} and (b) the fundamental plus its harmonics FO_{All} related to the spacing of the periodic scatterers. FO_{Fund} and FO_{All} are detected as the maximum value of the collapsed average of the single taper with a boxcar taper (blue), Weighted Overlapped Segment Average estimator (WOSA, green) and multitaper (MTM, black) estimates of the generalized spectrum, or as the maximum value of the power spectral density of the reconstructed periodic component using singular spectrum analysis (SSA). The gray dashed line indicates perfect detection (fractional occurrence equal to unity). Estimates were performed in a tissue mimicking phantom with 0.4mm spaced nylon fibers in a medium with diffuse scattering. A PER size of 10, for example, corresponds to a region 10 axial correlation lengths long and 10 correlation widths wide.

3.6 Discussion

This chapter has investigated the use of various estimators of the generalized spectrum as well as singular spectrum analysis for detecting the presence of periodic scatterers in a scattering medium. Previous work such as that of Donohue *et al.*,[51,110,114-116,119,128,130] Varghese *et al.*,[50,93] Rubert and Varghese, [131] Machado *et al.*[134, 138, 139] and Pereira and Maciel,[53,137] independently investigated the use of these two techniques for the detection or characterization of tissue based on coherent scattering. Many of these studies[110,115,119,128-

[130,131,134,139] were focused on a particular mean scatterer spacing (MSS) value , such as expected in liver tissue or in breast tissues. The study presented in this chapter provides a more comprehensive investigation that considers a wide range of periodic scatterer spacing values, going from values smaller than the resolution cell (that push into the detection limit of the techniques), to values significantly larger than the resolution cell. This was done with the idea that the results derived from this analysis could have a widespread applicability.

We have also advanced previous investigations on the effect of reducing the strength of the coherent scattering component on the detection and characterization of this feature of scattering. These reductions are achieved by introducing random variations in the scatterer spacing and by reducing the scattering cross section of the periodic scatterers. We have expanded the ranges of these reductions compared to previous studies[50,93,131,139] to understand the detection limits of each technique. Rubert and Varghese,[131] Varghese and Donohue,[93] and Machado *et al.*[139] studied the bias and variance of MSS estimates when introducing random variations in the MSS with standard deviations up to a value of about 15%. Varghese and Donohue[93] also evaluated the bias and variance of MSS estimates as the scattering cross section of periodic scatterers was varied. Instead of concentrating on the estimation of MSS, the analysis presented here focused first on the conspicuity (contrast and CNR) of the periodicity feature in the generalized spectrum for the task of detection of the coherent scattering component and then in the accuracy of the frequency corresponding to this feature. By extending the range of spacing standard deviations to over 100%, we were able to probe the detection limits of various estimators of the generalized spectrum and the singular spectrum analysis. Furthermore, our results extend previous observations from Varghese and Donohue[93] that the accuracy of the periodicity features decreases as the coherent to incoherent scattering power ratio is decreased by including the multitaper estimator of the generalized spectrum and the singular spectrum analysis. More importantly, given our focus on the task of creating parametric images, we have explored the detection and accuracy performance of each of the investigated techniques as the size of the parameter estimation region is severely reduced.

In this work we have focused first on the task of detection, and thus centered the analysis to analyze the conspicuity of the periodicity features of the Generalized Spectrum by performing first a theoretical analysis of different windowing functions and then a quantification of the contrast and contrast-to-noise ratio of the periodicity features. In this chapter, we studied the accuracy of the periodicity feature (the frequency of the maximum value of the CAGS), which is directly related to the accuracy of the estimates of the mean scatterer spacing. Our results, which also include the multitaper estimator of the generalized spectrum and the singular spectrum analysis, agree with those of Varghese and Donohue, which show that the accuracy of the periodicity features decreases as the coherent to incoherent scattering power ratio is decreased and as random variations in the scatterer spacing increase.

In general, it was found that the multitaper estimator of the generalized spectrum had a better detection performance than other estimators of the generalized spectrum. This agrees with results from Rubert and Varghese,[131] who compared the accuracy and precision of MSS estimates obtained through single-taper, WOSA and multitaper estimates of the generalized spectrum computed from simulated RF echo signals where it was assumed there were periodic scatterers with a 1mm spacing. Our results demonstrate that this advantage prevails as the scatterer spacing is varied from subresolution values to large resolved values, as long as it is above the detection threshold (see discussion below). As demonstrated by the theoretical analysis of the effects of the different estimators, the multitaper estimator concentrates the energy within the periodicity cells along their diagonals, which contributes to an increase of the signal of any periodic scatterer peaks observed in the collapsed average of the generalized spectrum. This enhances the coherent addition of phases along the diagonals of the bifrequency plane of the generalized spectrum observed by Varghese and Donohue.[93] In addition, we expanded the work of Rubert and Varghese[131] by investigating the effect of the time-half bandwidth product *NW* of the multitaper estimator on the conspicuity of the periodicity peak in the collapsed average of the generalized spectrum. Our theoretical derivations (Fig 3.7) and CNR analysis in Fig. 3.10(b) suggested that variations in the *NW* value become inconsequential as long as the periodicity cells centered at multiples of ($c/2\Delta$, $c/2\Delta$) in the bifrequency plane overlap.

Previous studies on the use of the singular spectrum analysis to characterize coherent scattering from periodic scatterers was performed by Machado *et al.*[134,138,139] in the context of using the estimated MSS values to diagnose fibrotic and cirrhotic liver. The authors found that MSS estimates derived from the generalized spectrum provided a more accurate diagnosis of liver fibrosis, while MSS estimates derived from SSA provided higher specificity.[134] In a later study, the performance of the single-taper generalized spectrum and the SSA was compared in terms of the accuracy and precision of MSS estimates that were smaller than the resolution cell size (MSS=0.8mm and 1.2mm for pulse lengths= 4.28 and 1.26mm).[139] The accuracy of MSS estimates from the single-taper generalized spectrum and the singular spectrum analysis were comparable. This agrees with our results when using large parameter estimation regions. At large PERs, both the generalized spectrum and the SSA succeed at identifying the expected spacing value. However, as the PER is reduced below 15 pulse lengths × 15 uncorrelated scan lines, the SSA method significantly degraded while the generalized spectrum, and the multitaper estimator in particular, maintained good detection and accuracy. One possible cause of the limited success of Singular Spectrum Analysis is that it only uses the shape of the envelope of the RF data to perform the detection of coherent scattering, while the generalized spectrum methods make use of both the phase and the magnitude of the RF echo signals. In general, the same trends were observed in the phantom results.

Figure 3.9(b) showed how the CNR of the periodicity peak decreased as the size of the estimation region was reduced. In general, when the PER size was reduced below 20 pulse lengths × 20 uncorrelated scan lines, the CNR started to decrease at a faster rate. We suggest 15 pulse lengths × 15 uncorrelated scan lines as a PER size that offers a reasonable tradeoff between resolution and CNR of the periodic features. This PER length is within the range of 3-6mm that has been used in other investigations of the generalized spectrum for estimation of mean scatterer spacing.[110,119,131] In the lateral direction, Rubert and Varghese[131] obtained stable estimates of the mean scatterer spacing when including more than 10 scan lines segments within the PER, which is similar to the value observed here.

Figure 3.10(a) demonstrated that the minimum detected spacing was 0.7λ. This can be explained in terms of the resolution limit of the generalized spectrum for the detection of periodicity features. A periodicity

cell will appear in the Generalized Spectrum when the spectral peak corresponding to the periodic scatterer spacing ($f=c/2\Delta$) and its first harmonic appear within the useful spectral bandwidth of the acoustic pulse. Thus, the frequency corresponding to the smallest spacing that can be detected would be

$$f_{Max} = f_H / 2, \tag{3.74}$$

where f_H is the highest frequency of the available bandwidth. This assumes that $f_H/2$ is larger than f_L, the lower limit of the available bandwidth, which was, in general, true for the transducer and experimental set up used in our protocols. Note that the subindex 'Max' indicates that the periodicity frequency line is maximum when the smallest spacing is detected. In this work, we set this bandwidth to be +10dB above the spectral noise floor as conventionally done in our laboratory.[24] For these conditions, f_H=10MHz, and therefore, f_{Max}=5MHz. This corresponds to a minimum spacing of $\Delta_{Min}=0.6\lambda$ or 0.155mm at 5MHz. This agrees with the observation that the periodicity peak in the collapsed average of the generalized spectrum from a 0.5λ spacing was not detected. A similar statement was presented in Ref. 93 and Ref. 114 about the dependence of the resolution limit of the generalized spectrum on the high frequency of the available bandwidth. However, in general it has been assumed that the periodicity will be detected if the scatterer spacing is larger than the resolution cell.[50,93,114] Others have suggested that the limit would be twice the pulse length.[119] For the simulated conditions (pulse length = 0.29mm), this would correspond to a frequency of (1.54mm/μs)/(2×2×0.29mm)=1.33MHz. In contrast, our results demonstrate that even subresolution spacing could be detected as long as the fundamental frequency and its first harmonic of the spacing are contained within the useful echo signal bandwidth. Detection of subresolution spacing values with the single-taper generalized spectrum and the SSA method was also reported by Machado *et al*.[139] The authors reported problems in the detection of 0.8mm spacing using an acoustic pulse with f_H=1.51MHz (measured at a -6dB level). According to our criterion, the minimum detectable spacing with this pulse would be approximately 1mm in water considering that value of f_H. Although this limit refers to a -6dB bandwidth measure (which could be conservative in terms establishing detection limits based on the "available" bandwidth), the significant reduction of the detection rate agrees with our criterion. The

largest frequency that can be detected is imposed by the signal length within the estimation region because at least two periodic scatterers should be present within it.[50,93]

Compare now Fig. 3.10(a) with Fig. 2.13 (Chapter 2). The two figures present the CNR_q of a parameter aimed at detecting the presence of quasi-periodic scatterers as a function of the periodic scatterer spacing. It is interesting to notice that in the short spacing region, where the generalized spectrum method fails to detect these periodicities ($<0.6\lambda$), the speckle statistics method (based on the SNR of the envelope) has its highest detection rates. Therefore, the speckle statistics analysis allows us to extend the detection region to smaller scatterer spacings. This conclusion could only be achieved by investigating a wide range of spacing values that were below and above the resolution cell size. This is a significant contribution over previous studies that focused on detecting specific scatterer spacing values. [110,115,119,128-131,134,139] The combination of the two methods for the detection of the presence of quasi-periodic scatterers will require the use of different methods for the estimation of the mean scatterer spacing. This topic will be presented in Chapter 4. Note that in the region $0.6\lambda<\Delta<1.3\lambda$ corresponding to sub-resolution periodicity where both methods are able to detect the presence of coherent scattering the generalized spectrum offers higher CNR values than the speckle statistics method.

Flawed detection of the correct maximum in the collapsed average of the generalized spectrum (CAGS) can be attributed to two factors: (1) small fluctuations in the location of the fundamental spacing (jitter) due to variance in the spacing of the scatterers and a noisy estimate of the CAGS, and (2) the presence of a maximum value with a frequency not related to the spacing among periodic scatterers due to the low amplitude of the coherent component with respect to the diffuse component and also to a noisy estimate of the GS.[121] The statistical analysis of the detection method based on finding the frequency of the maximum value of the CAGS focused mainly on the second type of error because the search for the correct peak was done within a 0.2MHz bandwidth, allowing some jitter in the location of the CAGS peaks. In Chapter 4 we will look at the statistics of the estimates of the mean scatterer spacing, which will be sensitive to jitter because the frequency of the actual CAGS maximum is used. Regardless of the

nature of the error, the results from this chapter support the notion that the multitaper estimator of the generalized spectrum improves the detection over a wider range of scatterer spacings and under limitations of the PER size and of the amplitude of the coherent component.

Our theoretical analysis also demonstrated that, for limited PER sizes, the functional form of the generalized spectrum depends on the tapering function. On this regard, it has been customary to affirm that $S(f_1,f_2)=0$ whenever $f_1 \neq f_2$.[51,93,129] Strictly speaking, this is only true when using infinite length signal segments. Furthermore, any nonzero value of the integral of the generalized spectrum elements off the main diagonal in the bifrequency plane is assumed an indicator of the presence of non-stationary signals.[129] In our case of limited signal segments, the off-diagonal values depend on the frequency response of the gating/tapering operation. Thus, these nonzero values when only diffuse scattering is expected need to be taken into account when deciding on the significance of nonzero values as an indication of the presence of a source of coherence.

When not considering the response of the transducer, Simon *et al.*[121] demonstrated that when the scatterer spacing is a random variable itself, the spectrum peaks appearing from the presence of a periodic array of scatterers are exponentially attenuated, becoming smaller and wider with increasing frequency. Thus, ideally, the detection methods should perform better at the fundamental peak. However, the pulse spectrum and the normalization steps also affect the magnitude of the peaks and it might happen that a harmonic has higher amplitude that the fundamental.[51,119,121] Thus, it is of interest to study the statistics of the frequency of the detected maximum value of the collapsed average. In many of the analyzed cases, a harmonic of the fundamental frequency component related to spacing of the periodic scatterers was detected as a maximum instead of the fundamental itself. This is very important because only using the maximum value of the generalized spectrum to estimate the mean scatterer spacing, such as done in Refs. 134 and 139, would result in biased estimates when a harmonic is detected instead of the fundamental. Thus an algorithm to estimate the mean scatterer spacing from the detected maximum in the CAGS must decide whether these maxima correspond to the fundamental component or one of its harmonics. It must

also produce accurate results over a wide range of mean scatterer spacing values. This topic will also be investigated in Chapter 4.

The work presented here has some differences from previous assessments on the performance of the generalized spectrum to detect periodic scatterers. With respect to the shape of the acoustic pulse, our simulations used a Gaussian modulated pulse which, due to its symmetric properties, leads to linear phase patterns.[119] Other authors have used an asymmetric Rayleigh pulse as a better model to the pulses produced experimentally.[119,126] We do not expect the conclusions from this work to change dramatically when using an asymmetric pulse because the same effects would be present in all the estimators of the generalized spectrum, and because the singular spectrum analysis is performed on the envelope signal, from which the phase information has been removed. With respect to the averaging procedures to reduce the variance of the estimate of the generalized spectrum, an alternative method based on sweeping an averaging window along the diagonal of the generalized spectrum was also proposed by Varghese and Donohue.[50] This averaging method was not directly implemented here because diagonal averaging is already been performed when computing the collapsed average of the generalized spectrum. Finally, other methods to normalize the generalized spectrum have been proposed. One of these methods is the magnitude normalization, in which each complex-valued element of the generalized spectrum is divided by its magnitude.[110,119] This removes all magnitude modulations caused by the pulse spectrum even in the off-diagonal elements. However, its main drawback is that the estimates are more susceptible to noise. This is shown in Fig. 3.21 in which the CNR_q of the periodicity peak in the collapsed average of the generalized spectrum obtained with the multitaper estimator is compared for two different normalizations, the power spectral density normalization from Eq. (3.31), and the magnitude normalization. As can be seen, the power spectral density normalization offered a higher CNR_q over a wider range of periodic spacing values compared to the magnitude normalization. This is because the power spectrum normalization retains the magnitude modulations caused by the presence of coherent scattering in addition to retaining the phase. The magnitude normalization only takes advantage of the phase information.[119] In

addition this normalization method has been suggested to be more robust when dealing with more complicated structures such as tissue.[51]

In summary, the most important findings of this chapter are the following:

1. The multitaper estimator of the generalized spectrum offers better detection performance of coherent scattering introduced by the presence of periodic scatterers than other estimators of the generalized spectrum and the singular spectrum analysis. This advantage was particularly important when dealing with a reduced amount of data, such as when creating parametric images that have good spatial resolution.
2. The advantage of the multitaper estimator was mainly due to its morphological features, i.e., the concentration of the energy along the diagonals of the periodicity cells that are repeated at points ($kc/2\Delta, k'c/2\Delta$) in the bifrequency plane, where k and k' are integers, rather than to its variance reduction efficiency.

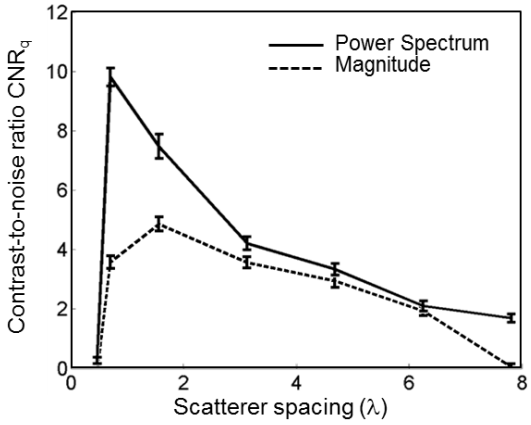

Figure 3.21 CNR$_q$ of the periodicity peak in the Collapsed Average of the Generalized Spectrum as a function of the scatterer spacing in units of wavelengths (λ=0.256mm). The generalized spectrum was computed with the multitaper estimator with *NW*=6 and *K*=11 tapers. The two curves correspond to different normalization methods: power spectrum normalization (solid), or magnitude normalization (dashed). The simulated sample phantom consisted of a random scatterer concentration of 48 scatterers per resolution cell and a periodic array of scatterers with 12 times the scattering cross section of the random scatterers. The simulated reference had a random scatterer concentration of 48 scatterers per resolution cell. The PER size was 15 pulse lengths × 15 uncorrelated scan lines.

3. Our results suggest that the minimum spacing that can be detected with the generalized spectrum (0.6λ for our spectral conditions) corresponds to a frequency f_{Max} that is half the high-frequency end of the available echo signal bandwidth, assuming f_{Max} is larger than the low-frequency end of the available echo bandwidth. This limit can correspond to a spacing that is below the size of the resolution cell.
4. Beyond f_{Max} (or for $\Delta z<0.6\lambda$ in our study), the methods from speckle statistics studied in Chapter 2 can be used for the detection of coherent scattering since their detection performance peaks at $\Delta z<0.6\lambda$. The combination of the two methods will require the implementation of different approaches to estimate the mean scatterer spacing.

In the next chapter, a statistical method is presented to decide if the maximum value of the collapsed average of the generalized spectrum is significantly different from a situation when only diffuse scattering occurs to rule on the presence of non-stationary signals. If a significant non-stationarity occurs, the shape of the generalized spectrum is analyzed to decide on the nature of the source that might be causing it. Then we combine this analysis with the tools of speckle statistics from Chapter 2 to decide whether some source of subresolution periodicity is present when the signals are stationary. Finally, in those cases where periodicity is detected, methods for the estimation of the mean scatterer spacing are evaluated.

Appendix B. Analysis of false coherence from randomly distributed scatterers

B.1 Background

As widely discussed in the background section of Chapter 3, the generalized spectrum is a useful tool for the detection of coherent scattering. In the theoretical analysis, it was demonstrated that when only random scatterers are present within the analyzed medium, the expected values of the off-diagonal elements of the generalized spectrum are zero. The expected values are approximated by the various averaging steps performed in the estimation of the generalized spectrum. However, when the averaging steps are not sufficient, a remaining phase component will be present in the analyzed backscattered echoes, leading to the detection of coherence in the generalized spectrum. This insufficient averaging can occur under two circumstances.

1. The concentration of random scatterers is very low.
2. The number of samples of the resolution cell is severely constrained. This scenario occurs when severely limiting the size of the parameter estimation region.[142]

This is illustrated in Fig. B.1 which shows a scatter plot of the maximum values of 100 independent estimates of the collapsed average of the generalized spectrum and the corresponding frequency obtained with the multitaper estimator. Three simulated scattering scenarios are included: an array of periodic scatterers with 0.4mm spacing within an cloud of 48 random scatterers per resolution cell (red circles), an array of only random scatterers with a concentration of 2 scatterers per resolution cell (blue circles), and an array of only random scatterers with 48 scatterers per resolution cell (black circles). The latter scenario mimics diffuse scattering. The PER size was the largest we explored (30 pulse lengths × 30 uncorrelated scan lines). In the case of periodic scatterers, the circles concentrate at the fundamental frequency corresponding to the periodic scatterer spacing (1.93MHz). The collapsed average values are about three

times larger than the values from the diffuse scattering scenario (black circles). When only random scatterers are present, the data points are spread across the useful bandwidth of the collapsed average. This is expected from the random nature of the scatterers. However, the collapsed average values in the case of a concentration of 2 scatterers per resolution cell are about twice the values for the case of diffuse scattering. Since this increase in the coherence level occurs as a consequence of insufficient averaging of the phase from backscattered echoes from randomly distributed scatterers and not from an organized array of scatterers, we will refer to it as "false coherence".

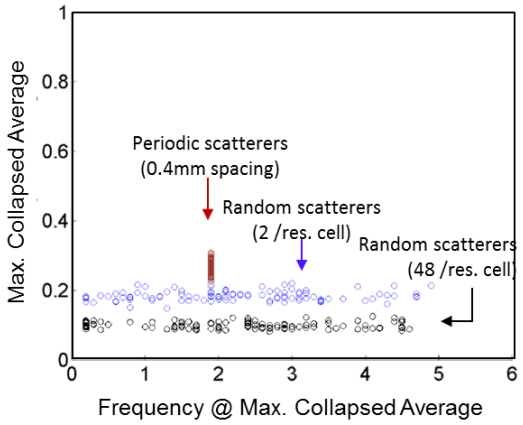

Figure B.1 Scatter plot of the maximum value of the collapsed average of the generalized spectrum and its corresponding frequency from 100 estimates obtained with the multitaper method. Colors indicate: red, 0.4mm spaced periodic scatterers within a cloud of 48 random scatterers/resolution cell; blue, cloud of 2 random scatterers per resolution cell; black, cloud of 48 random scatterers per resolution cell. The PER size was 30 pulse lengths × 30 uncorrelated scan lines.

The increase in false coherent scattering levels as detected by the collapsed average of the generalized spectrum has been studied by Donohue *et al.*[116] using the average CAGS as an overall measure of coherence. In this Appendix, we extend this analysis by considering, not only reductions in the concentration of randomly positioned scatters, but also we investigate how false coherence originates from reductions in the size of the parameter estimation region. Furthermore, instead of looking at changes in average CAGS level we look at the statistics of the maximum value of the CAGS estimated with the

multitaper technique and its corresponding frequency since these are the relevant parameters used in this work for detecting coherent scattering. Using both simulated and phantom-based data, we will identify the conditions in which false coherence becomes significant.

B.2 Methods

This procedure was applied to simulated echo signals and signals obtained from tissue mimicking phantoms using a commercial ultrasound system. The simulated echo signals were obtained using the simulation tool described in Chapter 2. Scatterers were assumed to be randomly distributed within the resolution cell according to a uniform distribution. The number of scatterers within the resolution cell was a Poisson-distributed random variable, with mean density varying from 2 to 48 scatterers per resolution cell. As explained in Chapter 2, 48 scatterers per resolution cell will be used as the concentration under which the Rayleigh statistics limit has been practically achieved. Backscattered echo signals were sampled at 40MHz for both the experimental and the simulated data. The center frequency (6 MHz) and -6dB fractional bandwidth (72%) in simulations were set to mimic the properties of the ultrasound transducer used in the clinic. This led to an effective pulse duration of 0.38μs, or a spatial pulse length of 0.29mm. The propagation speed of the acoustic pulse was assumed to be 1540m/s. Thus, the ultrasound wavelength was 0.26mm.

The tissue mimicking phantoms used in the experimental part of this appendix were phantoms A, B, and C used in Chapter 2, which have different scatterer concentrations. The diameter of the glass beads in Phantom A ranged between 5 and 40 μm (3000E, Potter Industries, Malvern, PA) with a mean concentration of 236 scatterers/mm^3. The glass bead diameter range and concentration in Phantom B were 75-90μm and 9 scatterers/mm^3. The glass bead diameter range and concentrations in phantom C were 126-151μm and 3 scatterers/mm^3. The phantoms were scanned with a Siemens Acuson S2000 (Siemens Medical Solutions USA, Inc, Malvern, PA) using an 18L6 linear array transducers operated at a 10MHz

excitation frequency. Radiofrequency (RF) data frames were acquired from the system's Axius Direct Research Interface.[86] RF data frames were acquired from 10 independent planes in each phantom.

The PER sizes ranged axially from 5 to 30 pulse lengths and from 5 to 30 uncorrelated scan lines in the case of the simulations. A total of 100 uncorrelated PERs from each simulated scenario were obtained. In the case of the phantom experiments with the 18L6 transducer, the PER ranged from 5 to 30 axial correlation lengths and 3 to 30 lateral correlation lengths. This allowed a total of 36 uncorrelated PERs within the frame of sample echo signals. Within each PER, the generalized spectrum was estimated using the multitaper estimator with NW=6. The maximum value of the collapsed average of the generalized spectrum was determined and its value and its corresponding frequency were stored. These led to a total of 36 values of the maximum of the Collapsed average and 36 values of their corresponding frequency for each random scatterer concentration and PER size. The statistical significance between the means of the distributions of these two parameters drawn from different random scatterer concentrations and PER sizes was determined using a t-test analysis.

B.3 Results

Figure B.2 shows box plots of (a) the maximum values of the collapsed average of the generalized spectrum (CAGS) and (b) the corresponding frequencies as a function of the PER size for simulated echo signals. Each block includes the following information: the central red line is the median, the upper and lower edges are the 75^{th} and the 25^{th} percentiles, and the error bars encompass the range of values not considered to be outliers. Red crosses are outliers (+/-2.7 standard deviations from mean value). These results correspond to a simulated phantom with 48 scatterers/ resolution cell. Figure B.2(a) shows that as the PER size decreases the maximum value of the CAGS increases. Every incremental step in the maximum value of the collapsed average caused by each incremental reduction of the PER size in Fig. B.2(a) was significantly larger than the previous value. This is a consequence of the reduction of the number of averages of the scattering statistics. In Fig. B.2(b), only the mean frequency of the maximum

CAGS value obtained with the smallest PER was significantly larger than the values at larger PERs ($p<0.0003$). The values from PERs larger than 5 pulse-echo correlation lengths (PECLs) were not significantly different from each other.

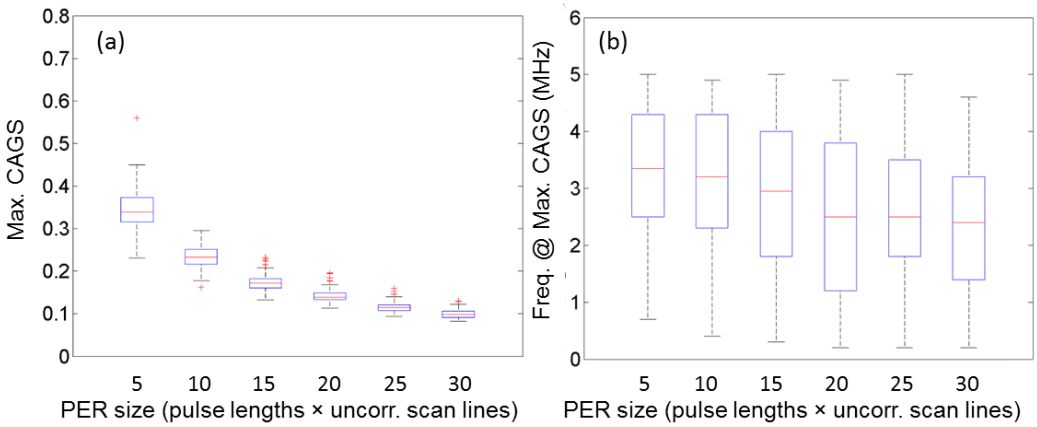

Figure B.2 Box plots of the (a) maximum value of the collapsed average of the generalized spectrum (CAGS) and (b) its corresponding frequency from 100 estimates of the generalized spectrum using the multitaper estimator, as a function of the PER size. The size is the number of pulse lengths times uncorrelated scan lines. The simulated phantom included 48 random scatterers per resolution cell. In each block, the red line indicates the median, the lower and upper boundaries of the box indicate the 25th and 75th percentile, and the error bars indicate the range without considering outliers. Red crosses indicate outliers.

Figure B.3 replicates Fig. B.2 but for a simulated phantom including only 2 scatterers per resolution cell. In this case the maximum values of the collapsed average are larger than the case with the larger scatterer concentration shown in Fig. B.2. Furthermore, significant reductions ($p<0.01$) in the frequency of the maximum were observed when reducing the PER size from 25 to 20 pulse lengths × uncorrelated scan lines and from 10 to 5 pulse lengths × uncorrelated scan lines. Furthermore, the frequency of the collapsed average from the 2 scatterers/resolution cell condition was significantly smaller ($p<0.03$) than the value from 48 scatterers per resolution cell for a PER size of 15 pulse lengths × 15 uncorrelated scan lines, although the difference was only 0.4MHz.

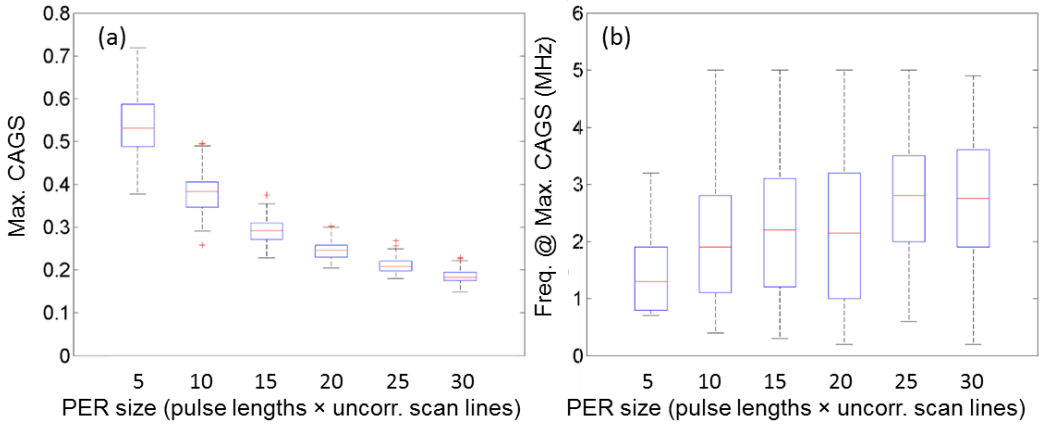

Figure B.3 Box plots of the (a) maximum value of the collapsed average of the generalized spectrum (CAGS) and (b) its corresponding frequency from 100 estimates of the generalized spectrum using the multitaper estimator as a function of the PER size. The size is the number of pulse lengths times uncorrelated scan lines. The simulated phantom included 2 random scatterers per resolution cell. In each block, the red line indicates the median, the lower and upper boundaries of the box indicate the 25th and 75th percentile, and the error bars indicate the range without considering outliers. Red crosses indicate outliers.

Figure B.4 presents box plots of (a) the maximum value of the collapsed average and (b) the corresponding frequencies as a function of the random scatterer concentration from 100 estimates of the generalized spectrum using the multitaper approach and a PER size of 15 pulse lengths × 15 uncorrelated scan lines. The maximum values of the collapsed average significantly increased ($p<0.034$) as the random scatterer concentration was reduced. The frequency of the maximum value of the collapsed average from the smallest concentration of 2 scatterers per resolution cell was only significantly smaller ($p<0.0055$) than the values from concentrations larger than 24 scatterers per resolution cell. This suggests that although the maximum value of the collapsed average increases, there is no preferential frequency (or spacing) associated to the occurrence of that maximum value.

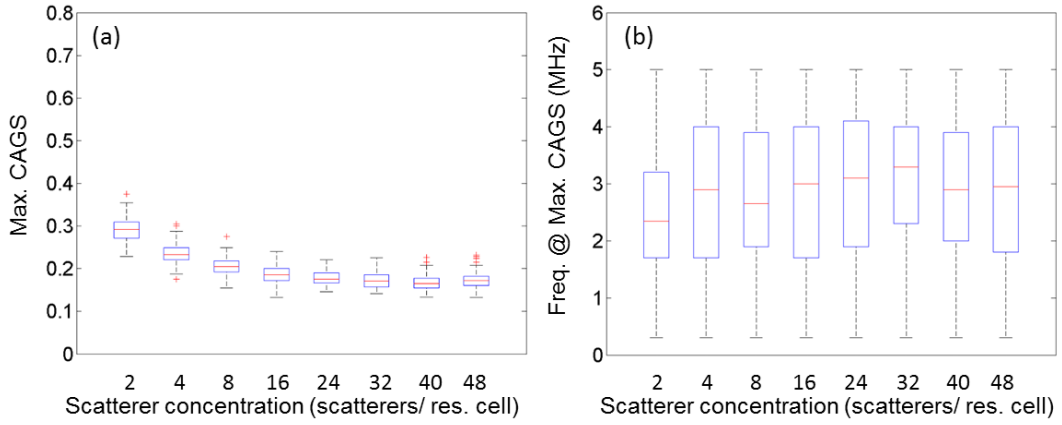

Figure B.4 Box plots of the (a) maximum value of the collapsed average of the generalized spectrum (CAGS) and (b) its corresponding frequency from 100 estimates of the generalized spectrum using the multitaper estimator, plotted as a function of the random scatterer concentration. The PER size is 15 pulse lengths × 15 uncorrelated scan lines. In each block, the red line indicates the median, the lower and upper boundaries of the box indicate the 25th and 75th percentile, and the error bars indicate the range without considering outliers. Red crosses indicate outliers.

Figure B.5 presents the PER dependence of (a) the maximum value of the collapsed average and (b) the corresponding frequencies for 36 independent estimates of the generalized spectrum using the multitaper approach obtained from Phantom C (high concentration of random scatterers). The same trends observed in the simulations can also be observed in the phantom results: a significant increase of the maximum value of the collapsed average, and slightly larger frequency ($p<0.04$) of the maximum value of the collapsed average at the smallest PER size (4 axial × 4 lateral correlation lengths).

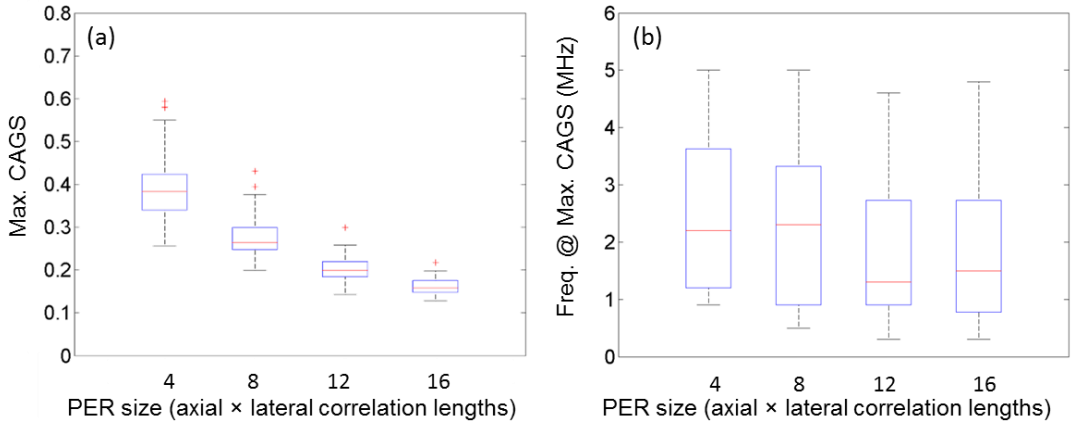

Figure B.5 Box plots of the (a) maximum value of the collapsed average of the generalized spectrum (CAGS) and (b) its corresponding frequency from 36 estimates of the generalized spectrum using the multitaper estimator, as a function of the PER size (axial times lateral correlation lengths). Phantom C has a random distribution of scatterers with 236 scatterers/mm^3. In each block, the red line indicates the median, the lower and upper boundaries of the box indicate the 25th and 75th percentile, and the error bars indicate the range without considering outliers. Red crosses indicate outliers.

Finally Fig. B.6 presents the scatterer concentration dependence of (a) the maximum value of the collapsed average and (b) the corresponding frequencies of 36 multitaper estimates of the generalized spectrum from phantoms A (low concentration, 3 scatterers/mm^3), B (medium concentration, 9 scatterers/mm^3) and C (high concentration, 236 scatterers/mm^3) with a PER size of 16 axial × 16 lateral correlation lengths. As expected, the reduction of the scatterer concentration led to a significant increase of the maximum value of the collapsed average of the generalized spectrum. The reduction of the frequency of the maximum value of the collapsed average was significant for the medium and low concentrations ($p<0.00025$).

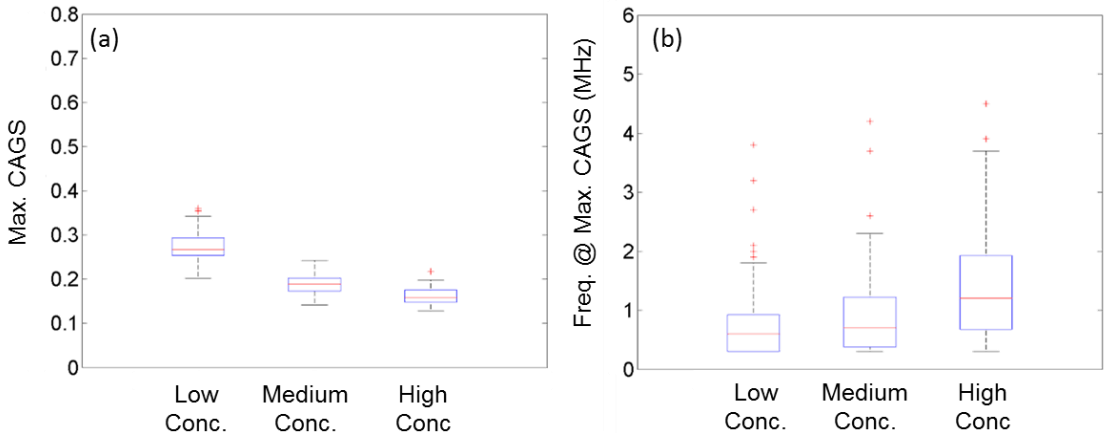

Figure B.6 Box plots of the (a) maximum value of the collapsed average and (b) its corresponding frequency from 36 estimates of the generalized spectrum using the multitaper estimator for each of the three phantoms with different (high, medium, low) concentrations of random scatterers. The PER size is 16 axial × 16 lateral correlation lengths. In each block, the red line indicates the median, the lower and upper boundaries of the box indicate the 25th and 75th percentile, and the error bars indicate the range without considering outliers. Red crosses indicate outliers.

A possible explanation for the significant reduction of the frequency of the maximum value of the collapsed average in the phantom experiment is the finite size of the scatterers in the low concentration phantom, which were about half the size of the resolution cell. As a result, many of them acted as a dominant scatterer within the resolution cell, thus increasing the values of the collapsed average of the general spectrum at low frequencies over the values at high frequencies. This is shown in Fig. B.7, which shows the average (black) and average ± one standard deviation (red) of the collapsed average from (a) the simulations (point-like scatterers) with 2 scatterers per resolution cell and (b) the phantom with a low concentration of scatterers. Observe that the slope at which the collapsed average decreases vs frequency is slightly steeper in the case of the phantom results.

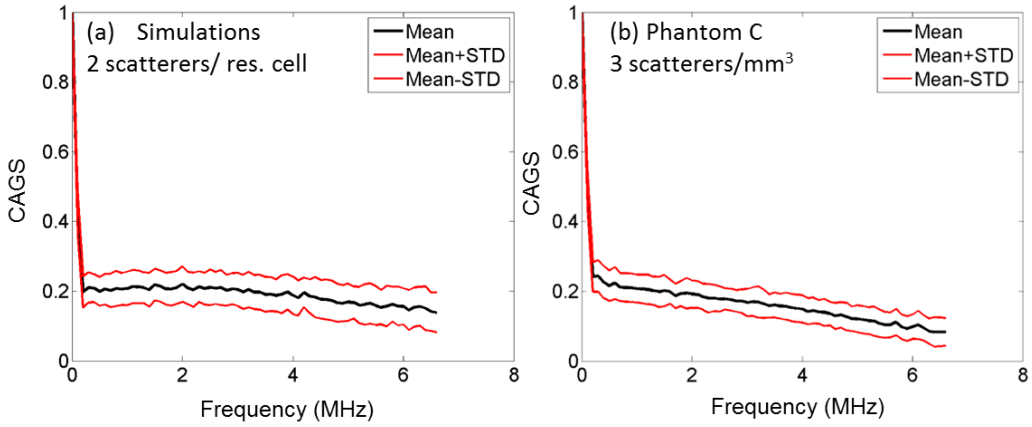

Figure B.7 Average (black curve) and Average ± one standard deviation (red curves) of the collapsed average of 100 multitaper estimates of the generalized spectrum from a simulated phantom with 2 scatterers/ resolution cell and (b) 36 multitaper estimates of the generalized spectrum from a phantom with 3 random scatterers/mm^3.

B.4 Discussion

The overall values of the elements off the main diagonal of the generalized spectrum decrease as the number of diffuse scatterers within the resolution cell increases. These overall values become diffuse for large concentrations (>10 scatterers/ resolution cell).[93,114] However, in this work we found that each step in the reduction of the scatterer concentration led to a maximum value of the collapsed average that was significantly different from the values of the previous, higher concentration. The difference between results might be due to the parameter used here compared to the one used in other works.[51] In this work we analyzed the statistics of the maximum value since this is the parameter that will be used for the detection and characterization of the coherent scattering component. In previous publications, researchers explored the mean value of the collapsed average for $\Delta f \neq 0$.[93,114] Thus the maximum value might be more sensitive to variations in scatterer concentrations. Regarding the frequency distribution of the maximum values of the collapsed average of the generalized spectrum as the scatterer concentration is reduced, no preferential frequency was observed. This is expected since no preferential phase is expected from the random interference of waves scattered from random scatterers.

There is an ambiguity in the detection of the maximum values of the collapsed average of the generalized spectrum (MaxCAGS): if the MaxCAGS is significantly different from the value of the collapsed average at that particular frequency when diffuse scattering is present (let us name this value CA_{REF}), then it can indicate a) subresolution periodicity, b) resolved periodicity, or c) false coherence. In Chapter 2 a similar ambiguity was observed: the values of SNR_V were smaller than the value from diffuse scattering when the random scatterer concentration was low and also when the spacing among periodic scatterers was larger than the resolution cell. In order to partially solve this ambiguity, we can combine the generalized spectrum analysis with the amplitude statistics analysis and with the analysis of the frequency of the maximum value of the Collapsed Average f_{MaxCA} as follows:

1. If $MaxCA>CA_{REF}$, $SNR_V>SNR_{V,REF}$, and $f_{MaxCA}>f_{PL}$, where f_{PL} is the frequency corresponding to the pulse length ($f_{PL}=c/2PL$), then the source of coherence is most likely a periodic array of scatterers with sub-resolution spacing.
2. If $MaxCA>CA_{REF}$, $SNR_V<SNR_{V,REF}$, and $f_{MaxCA}>f_{PL}$, then the source of coherence is more likely insufficient averaging leading to false coherence.
3. If $MaxCA>CA_{REF}$, $SNR_V<SNR_{V,REF}$, and $f_{MaxCA}<f_{PL}$ then the source of coherence can be either an array of periodic scatterers with spacing larger than the resolution cell, or false coherence.

In this way, the ambiguity has been reduced to only two scattering conditions and over a limited bandwidth. Notice also that situations where $MaxCA\sim CA_{REF}$ and $SNR_V>SNR_{V,RE}$ can be produced by the presence of periodic scatterers with spacing smaller than 0.6λ.

An interesting observation when comparing Figs. B.2 and B.4 is that the reduction of the PER size has a more severe effect in terms of creating false coherence than the reduction of the scatterer concentration over the range of analyzed concentrations. Regarding the frequency distribution, in general no significant differences were observed among the means of the distributions as the PERs were reduced down to 10 correlation lengths axially and laterally.

In conclusion, false coherence occurring from a limited PER size is expected to create false positive detection when looking for coherent scattering from organized structures. This limitation needs to be considered when designing the algorithm to ponder on the statistical significance of levels of coherent scattering.

4. Decision and classification of estimation regions with coherent scattering

In previous chapters various parameters were investigated for the tasks of detecting features in the echo signals that are related to the presence of coherent scattering. In Chapter 2, it was shown that, among the parameters that were analyzed, the signal to noise ratio of the echo amplitude SNR_V produced the highest contrast to noise ratio when studying the statistics of the echo amplitude in regions containing periodic scatterers with spacing smaller than the resolution cell. This parameter was also useful for detecting zones of low scatterer density, although CNR values were ambiguous when compared to regions with periodic scatterers with spacing larger than the resolution cell. In Chapter 3, it was demonstrated that parameters obtained from a multitaper estimator of the generalized spectrum of echo signals offered the highest detection power of features related to coherent scattering from periodic scatterers with spacing larger than the resolution cell compared to other estimators and to the singular spectrum analysis method. Thus, the combination of the analysis of stationary echo signals based on SNR_V and the analysis of non-stationary echo signals based on the generalized spectrum allow probing the scattering field for organized structures with organization scale below and above the resolution cell size.

Once the parameters for detecting coherent scattering have been defined, the next question to answer is whether the values of these parameters are large enough to rule in the presence of a significant source of coherent scattering. Given our interest in the formation of parametric images, we need to define a method that allows us to answer this question at every parameter estimation region, or PER, defined to form the parametric image. If a source of coherent scattering is present, parameters describing its nature are to be quantified. Particular interest is devoted to defining a method for the estimation of the mean scatterer spacing (MSS) when the algorithm concludes that periodic scatterers are the source of coherent scattering within the PER. This algorithm must have good accuracy and precision over a wide range of scatterer

spacing values. Also these properties must be robust to constraints of the PER size for a parametric image that involves these properties needs to have good spatial resolution.

4.1 Aim

The aim in this chapter is to design a fully automated algorithm that provides a model-free, automated classification of the PERs when forming a parametric image. Also, this algorithm automatically decides on the best MSS estimator when the algorithm decides that periodic scatterers are present within a particular PER. To achieve this goal, this chapter is organized as follows: Section 4.2 describes a test for deciding on the statistical significance of the values of the detection parameters related to coherent scattering leading to non-stationary features (MaxCAGS, the maximum value of the collapsed average of the generalized spectrum) or to stationary features (SNR_V). This test exploits the availability of echo data from a reference material designed to mimic diffuse scattering conditions. Section 4.3 focuses on the combination of the analyses of the statistical significance for non-stationary features and pre- or post-Rayleigh statistics to classify the PERs into four final classes: diffuse scattering, low scatterer density, scatterer periodicity, or presence of specular reflectors. This classification scheme is applied to a simulated contrast phantom formed of regions with different scattering conditions. It combines conditions of low scatterer density, sub-resolution and resolved periodic scatterer spacing, and diffuse scattering. Section 4.4 describes, compares, and analyzes the performance of various methods for MSS estimation that can be applied in the context of the algorithm. Section 4.5 puts together the results from sections 4.2, 4.3, and 4.4 and presents the final algorithm. The algorithm is applied again to the simulated contrast phantom to generate final images of the mean scatterer spacing. These images are generated automatically and do not require user-dependent segmentation. In Section 4.6, the performance of the algorithm is investigated in tissue mimicking phantoms, specifically Phantoms C and D described in Chapter 2. Finally, Section 4.7 presents the summary and the discussion of this chapter. Appendix B presents a method to improve the registration of the estimated parameters as well as the classification results. This

method will be tested for parameters based on incoherent scattering as well as parameters based on coherent scattering.

4.2 Decision

The first step the algorithm needs to perform is to estimate the parameters on which the decision about the presence of a significant source of coherent scattering is made. Based on the results from Chapters 2 and 3, these two parameters are the maximum value of the collapsed average of the generalized spectrum (MaxCAGS) and the signal-to-noise ratio of the echo amplitude (SNR_V). These two parameters are to be combined to perform a decision test that exploits the entire bandwidth of the pulse spectrum for the detection of stationary and non-stationary features in the echo signals.

As described in Chapter 1, in the context of creating a parametric image, a region of interest (ROI) is first chosen within the frame of echo data. We are interested in learning something about the spatial variation of a tissue property within the ROI. Then, a set of locations within the ROI are defined at which the value of this tissue property is to be estimated. At each of these locations, a parameter estimation region (PER) is defined. Within that PER we would like to know first if there is a significant amount of coherent scattering in the echo signal. To do this we estimate the MaxCAGS and SNR_V using the estimation methods described in the corresponding chapters:

- **MaxCAGS:** The generalized spectrum from each scan line segment within the PER is estimated using the multitaper estimator, using a time-half bandwidth product NW=6 and K=11 tapers. Note that this requires the use of the adaptive tapers $d_k(f)$ as described in Chapter 3. Then, the estimates from individual scan line signal segments within the PER are averaged and normalized with respect to the power spectral density. The CAGS is obtained by averaging the complex values of the normalized average generalized spectrum along its diagonals. Finally, the maximum value, MaxCAGS is obtained by finding the frequency bin with the highest CAGS within a search region running from

$f_{Min}=c/(2\times0.9\times L)$,[118] where L is the PER length, to $f_{Max}=f_H/2$, where f_H is the highest frequency of the available bandwidth.

- **SNR_V:** It is estimated by computing the amplitude signal of each of the radiofrequency scan line segments using the Hilbert transform as described in Chapter 2. The SNR_V is quantified by computing the ratio of the mean and standard deviation of the uncorrelated amplitude values.

Once the parameters have been estimated, the next step is to decide whether they are statistically significantly different from their values under conditions of diffuse scattering. In other words, we need to determine if the probability of finding the values of MaxCAGS and SNR_V measured for a sample for which there is coherent scattering, yet falling within the range of values measured under conditions of diffuse scattering, is very small. In this context, the first-order statistical property that interests us is the cumulative distribution function $F(q_0)$ of the parameter q (either MaxCAGS or SNR_V) under conditions of diffuse scattering. $F(q_0)$, which expresses the probability p that a parameter q is smaller than or equal to a particular value q_0, is given by:[143]

$$F(q_0) = p(q \le q_0) \,. \tag{4.1}$$

The goal is to define a threshold q_0 and declare that if $q_{sample}>q_0$ (where q_{sample} is the value of the parameter q measured from sample data), a source of coherent scattering is present in the medium. By knowing the cumulative distribution of the values of the parameter q under conditions of diffuse scattering, we can compute the probability of false detection PFD of coherence, i.e., the probability of deciding there is a source of coherent scattering under conditions of diffuse scattering. This is given by:[144]

$$PFD = 1 - F(q_0) = 1 - p(q \le q_0) = p(q > q_0) = \beta \,. \tag{4.2}$$

In other words, if 100 values of the parameter q are measured under conditions of diffuse scattering, then we would expect that about $\beta\times100$ of them will be larger than the threshold used to declare the presence of coherent scattering. In the ensuing analysis, an arbitrary probability of false detection of 5% will be used. This process is portrayed in Fig. 4.1. Figure 4.1(a) shows the probability density function $P(q)$ of a

random number q, and Fig. 4.1(b) shows its cumulative distribution $F(q)$. Note that $F(q)$ is just the integral or area under the curve of $P(q)$. The red lines in Fig. 4.1(b) indicate the value of q, $q_{0,}$ at which $F(q_0)$=0.95. This is represented by the area under $P(q)$ in Fig. 4.1(a) that is shaded in red. Thus, the probability of false detection *PFD* is indicated by the area shaded in blue in Fig. 4.1(a). Values of q larger than q_0, such as the green square in Fig. 4.1(b) have $\underline{F}(q)$>0.95. Values of q smaller than q_0, such as the blue square, have $F(q)$<0.95.

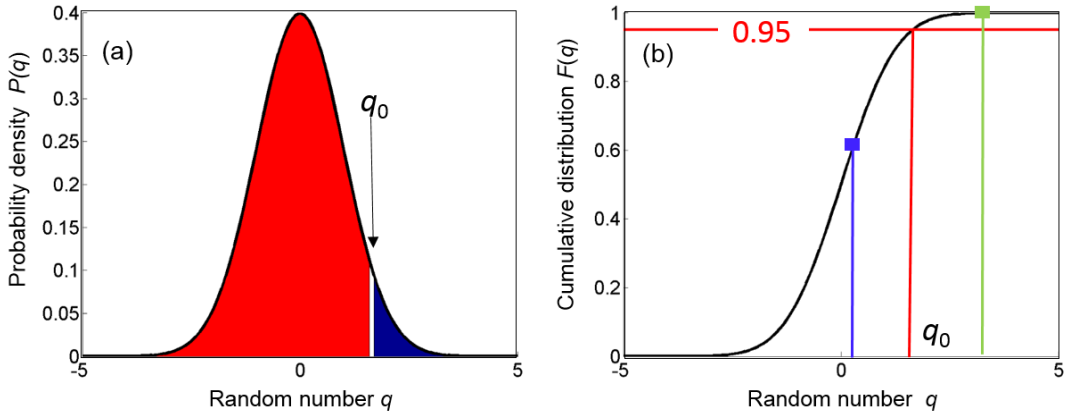

Figure 4.1 (a) Probability density function. Shaded in red is the probability that q is smaller than q_0, while in blue is the probability that q is larger than q_0. (b) Cumulative distribution of the random number q. The red vertical line indicates a value of q_0 for which the cumulative distribution is 0.95, and is equal to the red shaded area in (a). The red and blue squares indicate values of q with cumulative distributions smaller and larger than q_0, respectively.

Ideally, a theoretical expression of $P(q)$ and $F(q)$ under conditions of diffuse scattering would be derived. The task is complicated by the fact that a parametric image is being created, and the statistical properties of the parameters vary across the acoustic field. This is a result of the long-range variations in the acoustic beam (diffraction, attenuation) and the estimation method used to get the values of the parameters. Therefore, a specific threshold q_0 has to be defined for each location of the estimation region and for each of the parameters. As a result, a theoretical derivation becomes unmanageable.

An alternative is to approximate $F(q)$ with an empirical cumulative distribution, $F_E(q)$, [145] obtained from a reference material fabricated to offer conditions of diffuse scattering. Backscattered echo data from the

reference is to be obtained using the same system setup used to obtain the data from the sample. In addition, the reference material must have a sound speed and attenuation close to those of the sample being classified.[84] The empirical cumulative distribution $F_E(q)$ of the parameter q under conditions of diffuse scattering is obtained by first ordering the reference values of the parameter q_m, m=1,…,M, so that $q_1<...q_m<\ldots q_M$. Then, $F_E(q)$ is constructed according to:[145]

$$F_E(q)=\begin{cases} 0 & \text{for } q<q_1 \\ m/M & \text{for } q_m \le q < q_{m+1} \\ 1 & \text{for } q \ge q_M \end{cases} . \tag{4.3}$$

Figure 4.2 illustrates this concept. In Fig. 4.2(a), the blue bars show the histogram of 100 normally distributed random numbers of zero mean and unit standard deviation. The black curve shows the theoretical Gaussian distribution with the parameters used to generate the random numbers q. Figure 4.2(b) shows three curves: the empirical cumulative distribution computed according to Eq. (4.3) in red, the integrated histogram computed using the trapezoid rule to the histogram values from Fig. 4.2(a) in blue, and the theoretical cumulative distribution in dashed black. For this realization, the empirical cumulative distribution follows the theoretical curve more closely than the integrated histogram. We choose to work with the empirical cumulative distribution instead of the integrated histogram because it does not require the definition of bins. The empirical cumulative distribution was previously used by Georgiou *et al*.[145] to segment echo signals with pre-Rayleigh statistics by comparing it with the theoretical K distribution. Now we proceed to define empirical thresholds based on the empirical cumulative distribution for the two parameters of interest: MaxCAGS and SNR_V.

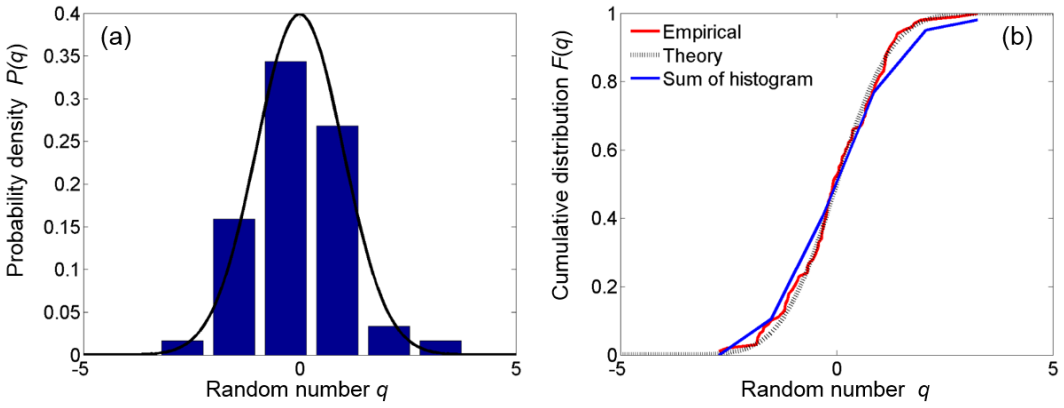

Figure 4.2 (a) Histogram and theoretical probability density function (black curve) for 100 Gaussian-distributed random variables with zero mean and unit variance. (b) Empirical cumulative distribution (red), sum of histogram values (blue), and theoretical cumulative distribution (dashed black curve) for a Gaussian distributed random variable.

4.2.1 Threshold for non-stationary features

Here a method is presented to define an empirical threshold to determine if the maximum value of the collapsed average of the generalized spectrum (CAGS) measured within a PER in the sample data frame is significantly larger than the value of the collapsed average under conditions of diffuse scattering. To determine this, the following algorithm is followed:

1. A set of M non-overlapped parameter estimation regions are defined in each of the available reference data frames. These estimation regions must be located at the same depth as the estimation region in the sample data frame that is to be classified.
2. The CAGS(f) is estimated at each of the reference PERs following the same estimation methods used in the sample data frame.
3. The maximum value of the CAGS(f) from the sample (MaxCAGS) and its frequency (f_{MaxCAGS}) are obtained within the search region defined above.
4. The empirical cumulative distribution function of MaxCAGS under conditions of diffuse scattering at f_{MaxCAGS} is computed from the values of the parameter in the reference. To do this, we find the maximum value of each one of the M reference CAGS estimates.

5. A threshold q_a for MaxCAGS is chosen for a probability of false detection of 5%.
6. If MaxCAGS>q_a, then the presence of some source of coherent scattering causing the echo signals to be non-stationary is declared.
7. If MaxCAGS≤q_a, then it is concluded that a source of coherent scattering causing the signal to be non-stationary is not present.

This process is illustrated in Fig. 4.3 which shows each of these steps in detail. The top part of the figure shows B-mode images from the sample and reference RF data frames, from which the parameter estimation regions are defined. Note that they are located at the same depth. Going down in the diagram, a collapsed average plot is shown: the mean CAGS from all the PERs in the reference at the same depth of the sample PER (blue curve) is depicted as well as the CAGS from the sample (black curve) within the search region delimited by f_{Min} and f_{Max}. The bottom panel shows the threshold from the plot above. The MaxCAGS value for the sample is shown by a green square. The bottom plots show the cumulative distribution of the maximum values of MaxCAGS from the reference. The threshold q_a is defined at $F(q_a)$=0.95 and is indicated by the horizontal and vertical red dashed lines. On the left, the value of MaxCAGS, indicated by a green vertical line, is larger than the threshold q_a and the test for non-stationary features is positive. On the right, MaxCAGS, indicated by a blue vertical line, is smaller than q_a, indicating a negative test on non-stationarity.

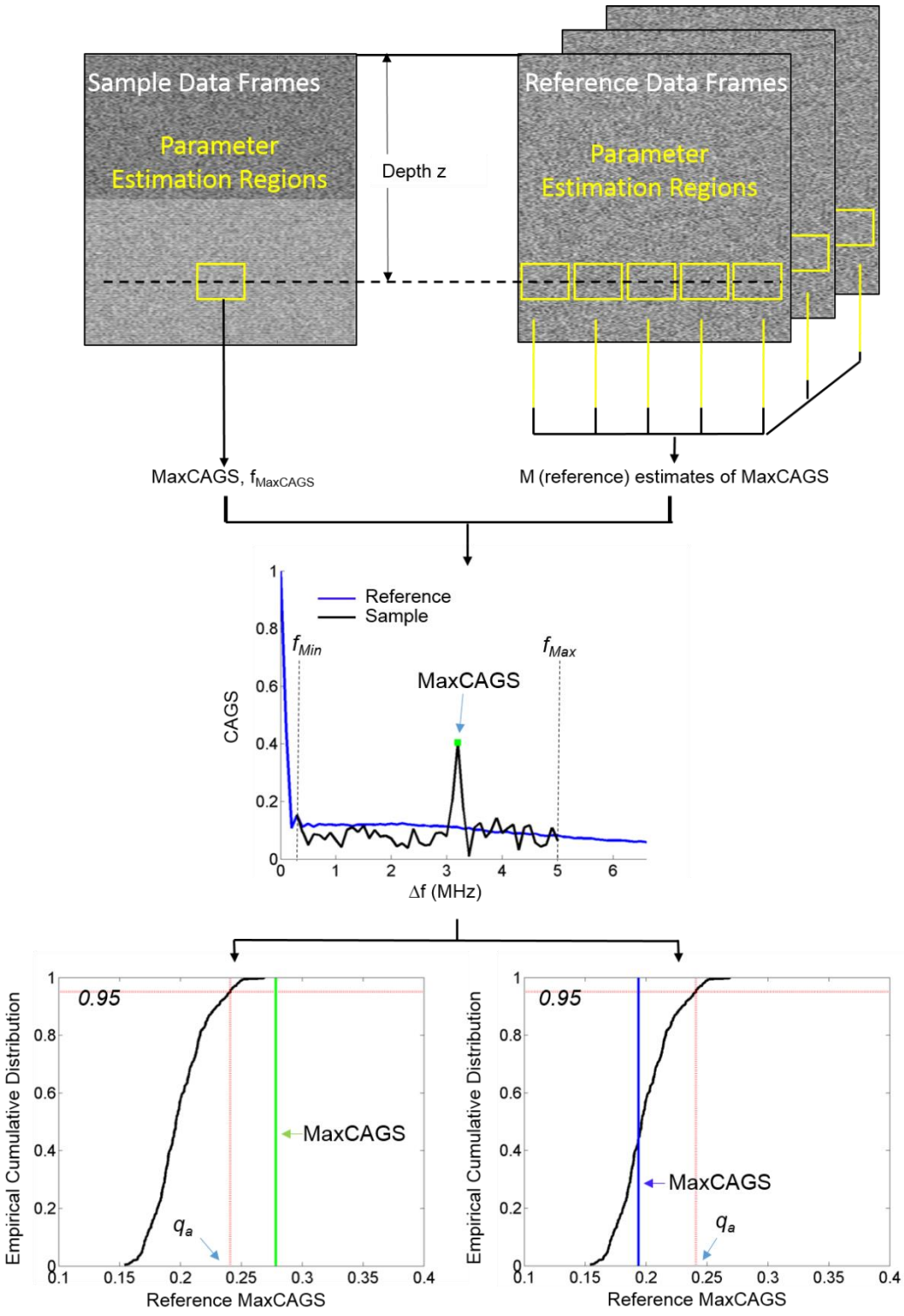

Figure 4.3 Graphical representation of the algorithm to determine the statistical significance of the maximum value (MaxCAGS) of the collapsed average of the generalized spectrum (CAGS) to declare the presence of non-stationary features.

A particular case positive to the detection of non-stationary features is the presence of specular reflectors. As discussed by Donohue *et al*.[51] and by Luchies *et al*,[126] the presence of such structures within the PER results in an increase of the correlation level among all frequencies. Based on this idea, these authors used the integrated CAGS to detect specular reflectors. Initial tests of this parameter (not reported here) showed that, in cases where the specular reflector had moderate reflectivity or was not highly localized, the values of the integrated CAGS were similar to the values from cases where the CAGS contained a number of maxima resulting from periodic scatterers with large spacing. To circumvent this ambiguity and based on the idea that specular reflectors introduce correlation among all frequency components of the echo signal, we instead measure the "correlation length" of the spectral correlation as an assessment of "specularity". This correlation length is expected to increase significantly when a specular reflector is present within the PER.[51] This correlation length is quantified as the width of the 0MHz peak of the CAGS, referred here to as the "main lobe width", and is a measurement of the spectral correlation bandwidth. In these situations, the maximum value of the CAGS within the search region is expected to occur right at its lower end, i.e., at f_{Min}. An example is shown in Fig. 4.4, which was obtained from a PER containing an axially localized reflector. We use this fact to separate PERs containing this type of structure from other sources of non-stationarity.

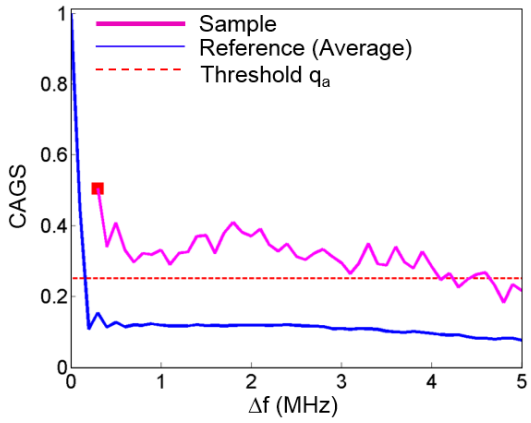

Figure 4.4 Collapsed average of the generalized spectrum (CAGS) of a region containing a specular reflector. Magenta: sample CAGS, blue: average of reference CAGS, dashed red: threshold q_a.

4.2.2 Thresholds for stationary features

Here we define an empirical threshold to determine if the value of SNR_V estimated within a PER in the sample data frame is significantly different from its value under conditions of diffuse scattering. To achieve this, the following algorithm is followed:

1. A set of M non-overlapped parameter estimation regions in each of the available reference data frames is selected. These estimation regions must be located at the same depth as the estimation region in the sample data frame that is to be classified.
2. The SNR_V is estimated at each of the reference PERs following the same estimation methods used in the sample data frame.
3. The empirical cumulative distribution function of SNR_V under conditions of diffuse scattering is computed from the M reference SNR_V values.
4. A two-tail test is used to decide whether the measured value in the sample is significantly smaller (pre-Rayleigh) or larger (post-Rayleigh) than the value from diffuse scattering. Thus, for a total probability of false detection of 5%, we determine two thresholds:
    a. q_b, for which the empirical cumulative distribution is 97.5%
    b. $q_{b'}$, for which the empirical cumulative distribution is 2.5%.
5. The measured SNR_V is compared to the thresholds q_b and $q_{b'}$. If $SNR_V > q_b$, the presence of post-Rayleigh statistics is declared. If $SNR_V \leq q_{b'}$, the presence of pre-Rayleigh statistics is declared. Otherwise, Rayleigh statistics are present.

Figure 4.4 shows the analysis of SNR_V values. As in Fig. 4.3, the top part of the figure shows B-mode images from the sample and reference RF data frames, from which the parameter estimation regions are defined. The three plots at the bottom show the cumulative distribution of the SNR_V values in the reference in black. The horizontal dashed red lines show the 0.975 and 0.025 levels of the cumulative distribution. The vertical dashed red lines show the corresponding thresholds q_b and $q_{b'}$, respectively. In the case on the right, $SNR_V > q_b$ and the statistics are post-Rayleigh. In the case of the left, $SNR_V < q_{b'}$, and

the statistics are Pre-Rayleigh. Finally, in the plot at the center, $q_{b'}<\mathrm{SNR_V}\leq q_b$, and the statistics are Rayleigh.

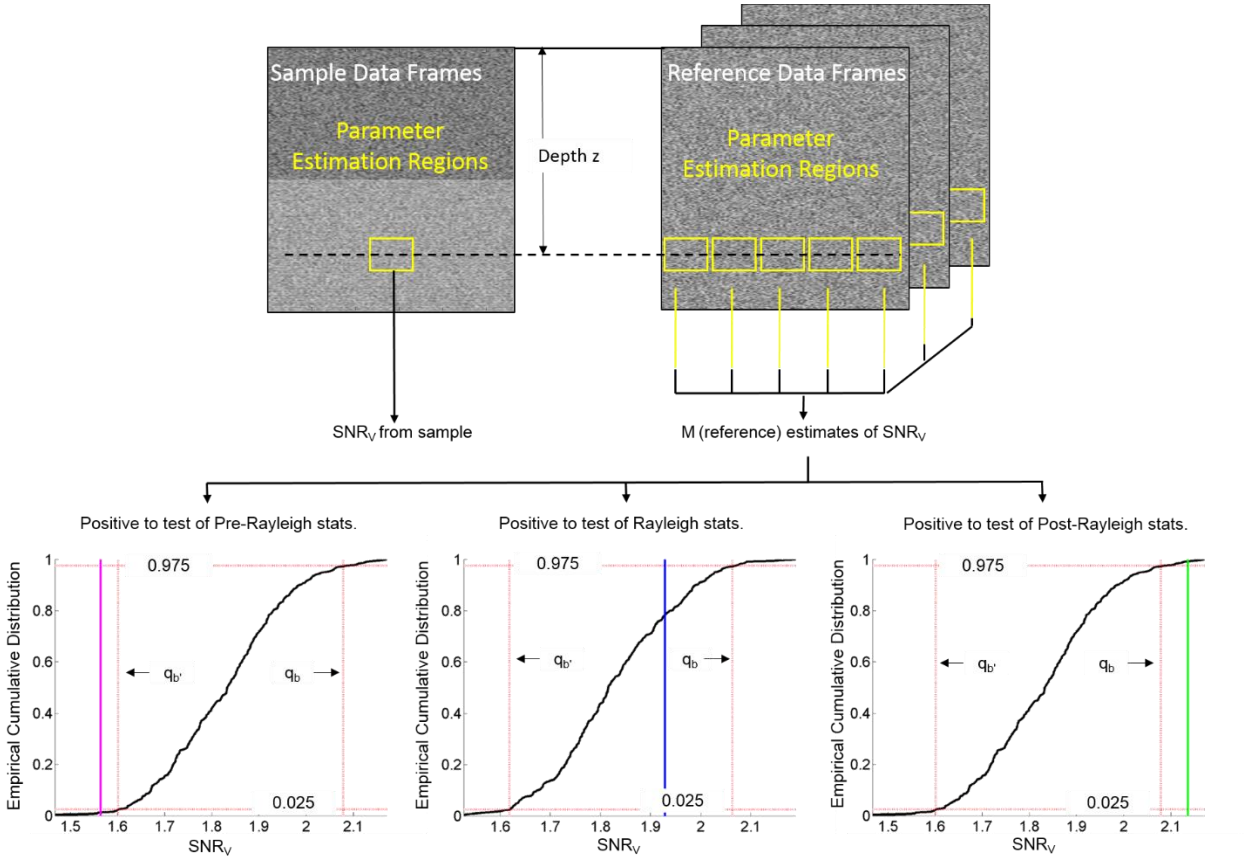

Figure 4.5 Graphical representation of the algorithm to determine the statistical significance of the measured $\mathrm{SNR_V}$ values to declare the presence of pre-Rayleigh, Rayleigh, or post-Rayleigh echo amplitude statistics.

4.2.3 Ambiguity between low scatterer density and resolved periodic scatterers

As discussed in Appendix B, regions with low random scatterer density also show increased CAGS values. Thus, the differentiation between regions of low scatterer density and organized scatterers by means of the CAGS is ambiguous. As also discussed in Appendix B, a possible way to solve this ambiguity could be to look at the frequency of the maximum value of the CAGS, i.e., f_{MaxCAGS}. The values of f_{MaxCAGS} in the case of low scatterer density are expected to spread evenly between f_{Min} and f_{Max}, while for resolved periodicity, f_{MaxCAGS} should be below f_{PL}, i.e., the frequency spacing corresponding to the

pulse length. However, the analysis of $f_{MaxCAGS}$ has three difficulties: (1) Only a single value of $f_{MaxCAGS}$ is obtained from a PER, so its statistics in the sample data frame are not available. (2) The band from f_{Min} to f_{PL} is still ambiguous. (3) The value of $f_{MaxCAGS}$ could actually be a harmonic of the frequency corresponding to the actual scatterer spacing.

An alternative is to look at the distribution of the phase of the backscatter echo within the PER, as suggested by Shankar *et al.*[71,72] and Molthen *et al.*[54] This analysis is motivated by the fact that even when a few scatterers are randomly distributed within the resolution cell, the resulting phases of the backscattered echoes are expected to be uniformly distributed between 0 and 2π. In the case where periodic scatterers are present, the distribution of the phase values is expected to depart from uniform. This is illustrated by the phase histograms shown in Fig. 4.6. Fig. 4.6(a) shows a phase histogram corresponding to a scattering scenario with only randomly distributed scatterers. Fig. 4.6(b) shows a phase histogram for a condition of periodically spaced scatterers, which is clearly not uniformly distributed.

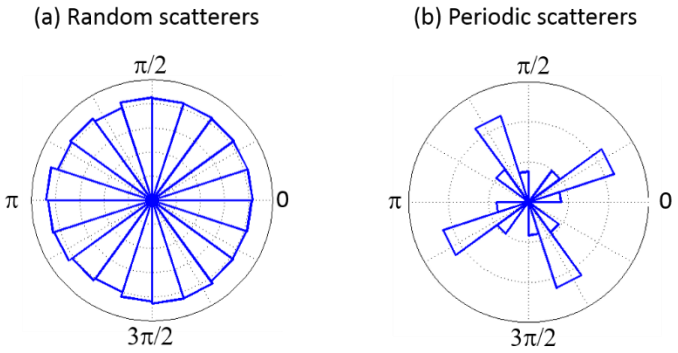

Figure 4.6 Polar histograms of the phase of echo signals generated from a medium with (a) randomly distributed scatterers (48 scatterers/resolution cell) and (b) periodic scatterers in a cloud of random scatterers with a coherent to incoherent scattering power ratio of 1.5dB.

In Chapter 2 it was stated that maximum constructive interference among the echoes from individual scatterers occurs when the spacing is equal to $c/2f_0$, where f_0 is the center frequency of the echo signal spectrum. When the spacing is different from this value, the interference of the harmonic components of

frequency f_0 will be "less constructive", and maximum constructive interference will then occur at a frequency $f=c/2\Delta z$. To exploit this phenomenon, Molthen *et al.*[54] proposed to probe the entire bandwidth of the acoustic pulse in search of the maximum constructive interference. This is done by analyzing the statistics of the phase (or the amount of constructive interference) at different demodulation frequencies. Thus, a search is performed for the demodulation frequency at which the histogram of the phase becomes less uniform. To quantify the departure from uniformity, a chi squared χ^2 measure of the histogram of the values of the phase within the PER with respect to values for a uniform phase distribution can be used. To compute χ^2, a histogram of the phase values is constructed by dividing the range $-\pi$ to π into N_{PB} phase bins (i.e., 20 as in Ref. 54) Then, the χ^2 measure is computed as[54]

$$\chi(f_d)^2 = \sum_{i=1}^{N_{PB}} \frac{(n_i - \langle n \rangle)^2}{\langle n \rangle} \quad . \tag{4.4}$$

where n_i is the number of phase estimates within the i^{th} phase bin, and the brackets indicate the average of the number of phase estimates in all the bins. As the distribution of the phase approaches a uniform distribution, the χ^2 measure approaches a value of zero. Notice that the χ^2 measure has been defined as dependent on the demodulation frequency f_d, and is thus referred to as the chi squared spectrum. The procedure to compute $\chi^2(f_d)$ is the following:

1. A parameter estimation region is defined.
2. A set of demodulation frequencies, $f_{d,Min}<f_d<f_{d,Max}$ is defined. This interval is the same useful echo signal bandwidth defined for the analysis of the generalized spectrum (+10dB above the noise floor).
3. Each radiofrequency echo signal segment is demodulated within the estimation region with each of the demodulation frequencies.
4. A histogram of the phases for each demodulation frequency is constructed and the χ^2 measure for each frequency is computed.

This procedure will lead to a χ^2 spectrum such as the ones shown in Fig. 4.7. Figure 4.7(a) shows the case of a χ^2 spectrum for a simulated diffuse scattering scenario (random scatterers with 48 scatterers/resolution cell), while Fig. 4.7(b) corresponds to a case of periodic scatterers with 0.2mm spacing embedded in a cloud of 48 random scatterers/resolution cell. The next step is to define if the departure from uniformity is statistically significant, i.e., if the maximum value of χ^2 (f_d) is significantly larger than the value under conditions of diffuse scattering. To do this, an analysis similar to the one used to decide on the statistical significance of non-stationary features is performed:

1. A set of M non-overlapped parameter estimation regions is defined in each of the available reference data frames. These estimation regions must be located at the same depth as the estimation region in the sample data frame that is to be classified.
2. The $\chi^2(f_d)$ is estimated at each of the reference PERs following the same estimation methods used in the sample data frame.
3. The maximum value of the $\chi^2(f_d)$ from the sample and its frequency are obtained from within the range of demodulation frequencies.
4. The empirical cumulative distribution function of the maximum value of $\chi^2(f_d)$ is computed under conditions of diffuse scattering. To do this, the maxima of each of the reference $\chi^2(f_d)$ estimates are obtained.
5. An empirical threshold q_c is determined for the maximum of $\chi^2(f_d)$ for a probability of false detection of 5%.
6. If the maximum of $\chi^2(f_d) > q_c$, then the phase within the PER is not uniform.
7. If the maximum of $\chi^2(f_d) \leq q_c$, then the phase within the PER is uniform.

In Figs. 4.7(a) and (b) the blue curve corresponds to the average $\chi^2(f_d)$ spectrum from all the reference PERs. The red line is the threshold determined from the cumulative distribution of the maximum χ^2 values in the reference. Note that the figures have different scales. In the case of diffuse scattering in Fig. 4.7(a), the maximum χ^2 value in the sample (blue square) does not surpass the threshold and, as

consequence, the phase is assumed to be uniformly distributed. In Fig. 4.7(b), periodic scatterers are present and the maximum $\chi^2(f_d)$ surpasses the threshold q_c.

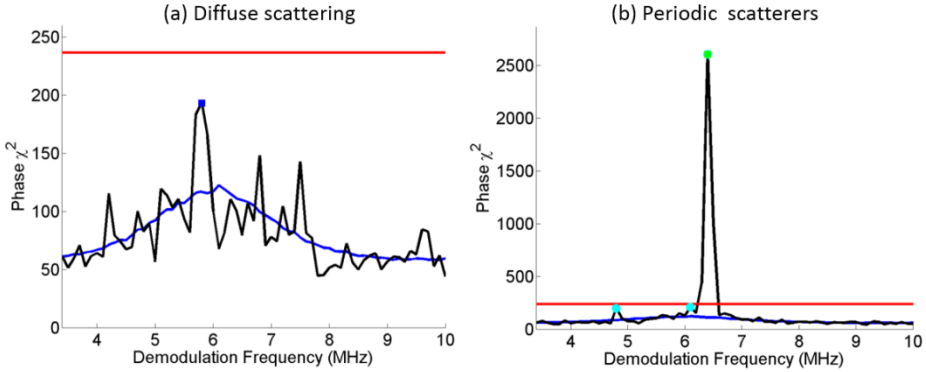

Figure 4.7 χ^2 spectra of the echo phase measured in (a) a sample with 48 scatterers per resolution cell and (b) a sample with periodic scatterers in a cloud of random scatterers with a coherent to incoherent scattering power ratio R=1.5dB. Black curve: spectrum from a single PER in the sample. Blue curve: average of 100 spectra from a reference with 48 scatterers per resolution cell. Red curve: Threshold for statistical significance q_c.

4.2.4 Decision test: Simulations

The first test that was performed was to verify if the statistical methods just presented produced a probability of false detection of 5%. To do this, 15 independent frames of backscattered echo data were simulated for different concentrations of random scatterers (2, 4, 8, 16, 24, 32, 40 and 48 scatterers/resolution cell). The pulse characteristics were 6MHz center frequency and a 72% -6dB bandwidth, leading to a pulse length of 0.296mm. Each frame consisted of a set of 200 independent scan lines spanning 60mm in depth. The reference data frames consisted of 3000 independent simulated scan lines with a concentration of 48 scatterers/resolution cell and the same pulse characteristics. A parameter estimation region of 4mm axially and 4mm laterally was moved across each one of the sample frames. The PERs were not overlapped to assure independent estimates of the parameters for their statistical analysis. This originated a total of 13 (axially) × 26 (laterally) PERs in each of the sample frames. At each of the 13 axial locations of the PERs in the sample data frames, 333 independent PERs were defined in the reference data frames. This led to 333 reference estimates of the CAGS(f), SNR_v and $\chi^2(f)$ that

were used to construct the empirical cumulative distribution of the values of these parameters under conditions of diffuse scattering.

Three metrics were quantified for this analysis:

- Detection ratio of PERs classified as non-stationary: number of PERs in each sample data frame in which non-stationary features were detected, normalized to the total of 13×26 PERs per frame.
- Detection ratio of PERs classified as pre-Rayleigh: number of PERs in each sample data frame in which pre-Rayleigh statistics were detected, normalized to the total of 13×26 PERs per frame.
- Detection ratio of PERs classified as having non-uniform phase: number of PERs in each sample data frame in which non-uniform echo phase was detected, normalized to the total of 13×26 PERs per frame.

The scatterer concentration was varied to observe the change in the detection ratios. This is shown in Fig. 4.8, which shows the detection ratio for non-stationary features (blue), pre-Rayleigh statistics (black), and of non-uniform phase (red) as a function of the scatterer density. The reference gray dashed line indicates the probability of false detection of 5%. The error bars show the standard deviation across the 15 independent frames. As can be observed, the detection ratio of the non-stationary features and the non-uniform phase tend to the 5% value when the scatterer concentration tends towards that of the reference (48 scatterers/resolution cell). The detection ratio for the pre-Rayleigh features tends to 2.5% as expected from the two tailed test to account for both post-Rayleigh and pre-Rayleigh statistics. The detection ratio of the non-stationary features and the non-uniform phase becomes significantly larger than the expected probabilities of false detection for concentrations smaller than 24 scatterers/resolution cell. This indicates that, for the test proposed here, random scatterer concentrations larger than 24 scatterers/resolution cell can be considered to produce stationary signals and Rayleigh statistics. The detection ratio of the non-uniform phase becomes significantly larger than the 5% probability of false detection for concentrations smaller than 8 scatterers/resolution cell.

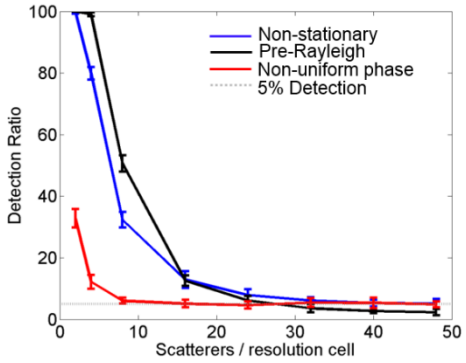

Figure 4.8 Detection ratio as a function of the random scatterer concentration. Blue: detection ratio of non-stationary features, Black: detection ratio of pre-Rayleigh statistics, red curve: detection ratio of non-uniform phase.

4.3 Classification

The next test was to analyze the performance of the decision test to classify the PERs in a simulated contrast phantom containing regions with different scattering properties. The phantom is described in Fig. 4.9. Figure 4.9(a) shows the schematic of the simulated conditions. The phantom is divided into eleven regions. The three leftmost regions (yellow) had only random scatterers with concentrations of 2, 16, and 32, scatterers per resolution cell. The top right region in blue has only random scatterers with a concentration equal to that of the reference (48 scatterers/resolution cell). The bottom right regions (green) had, in addition to random scatterers with 48 scatterers/resolution cell, an array of periodic scatterers with spacings 0.06mm, 0.12mm, 0.24mm, 0.3mm (one pulse length), 0.4mm (mimicking phantom D), 0.8mm, and 1.20mm. Sixty independent realizations of the scattering arrangements were created, leading to 60 independent frames of RF data from the phantom. The scattering amplitude was adjusted to keep a constant coherent to incoherent power ratio of 1.5dB. The simulated pulse conditions were consistent to those used in Chapters 2 and 3 (6MHz center frequency, 72% -6dB bandwidth). The resulting B-mode images are shown in Fig. 4.9(b).

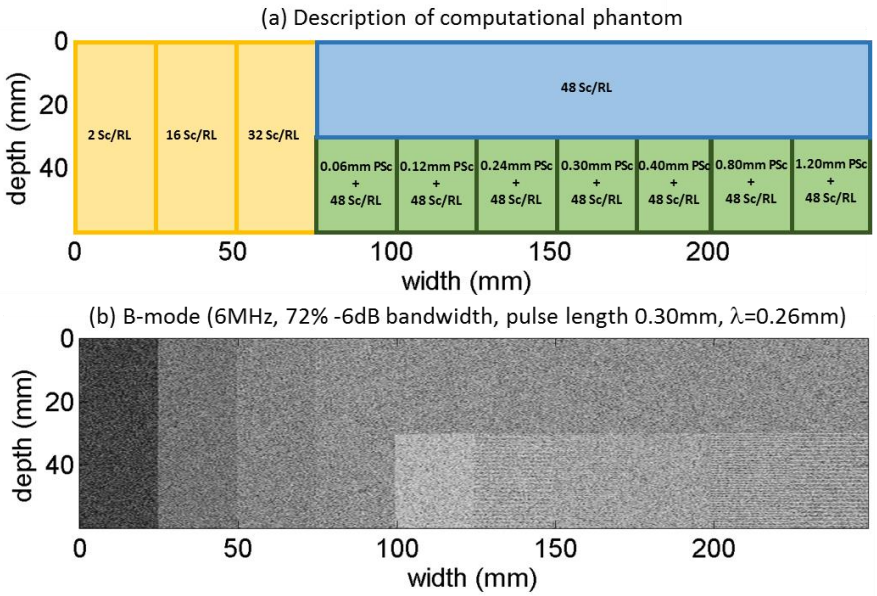

Figure 4.9 (a) Diagram and (b) B-mode image of the simulated phantom. Abbreviations are Sc/RL: scatterers per resolution length, PSc: periodic scatterers.

A PER of 4mm axially and 4mm laterally was swept across the simulated phantom with no overlap to perform the characterization at uncorrelated positions in the phantom. This generated a total of 715 (13 axial × 55 lateral) uncorrelated PERs. Within each PER, the CAGS(f), SNR_V, and $\chi^2(f)$ were estimated as described above. The three decision tests based on these parameters (non-stationary features, departure from Rayleigh statistics, and non-uniformity of the phase) were performed separately, each with a probability of false detection of 5%. To quantify the adequacy of the decision process in every PER location, the detection ratio of each PER was computed as the number of frames in which a particular test was positive, normalized to the total number of frames. Thus, a detection ratio of 0% at a particular PER indicates that the test was negative in all of the 60 independent frames, while a value of 100% indicates that the test was positive in all of the sixty independent frames.

Figure 4.10 shows images of the detection ratio for each PER in which the detection ratio was color coded, ranging from blue for a detection ratio of 0% to red for a maximum detection ratio of 100%. Figure 4.10(a) shows the detection ratio of the analysis of non-stationary features (statistically significant

MaxCAGS values), while Fig. 4.10(b) shows the detection ratio for stationary features (not statistically significant MaxCAGS values). In the three regions with scatterer density smaller than the reference, the detection ratio (averaged over the entire region) was 96±9% for Region 1 (2 scatterers/resolution cell), 13±6% for Region 2 (16 scatterers per resolution cell), and 6±4% for Region 3 (32 scatterers/resolution cell). This agrees with the results from Fig. 4.8. In Regions 5-11 where periodic scatterers were present, only Regions 7 to 12 were positive to the detection of non-stationary features. This is because the corresponding spacing values were larger than the detection limit c/f_H of the generalized spectrum discussed in Chapter 3. The minimum detection ratio was 90±6%. In Region 4, the one with the same composition as the reference, the detection ratio of non-stationary features was 5±3%, as expected from the chosen probability of false detection. Thus, although useful for the detection of non-stationary features, this test result is insufficient for the task of classification because it misses regions with periodic scatterers with spacing smaller than c/f_H and is ambiguous to separate zones of very low scatterer density from zones with periodic scatterers with spacing larger than c/f_H.

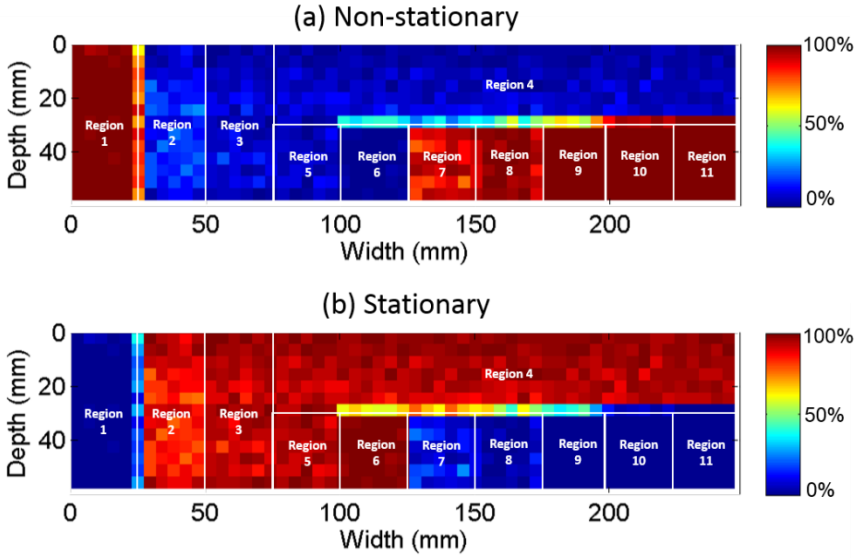

Figure 4.10 Images of the detection ratio for (a) non-stationary features and (b) stationary features in the simulated phantom.

Figure 4.11 shows images of the detection ratio for the test of post- and pre-Rayleigh statistics. Figure 4.11(a) is the detection ratio for PERs classified as pre-Rayleigh, Fig. 4.11(b) for PERs classified as Rayleigh, and Fig. 4.11(c) for PERs classified as post-Rayleigh. The detection ratios of pre-Rayleigh conditions for regions with scatterer densities lower than the reference were 100% for Region 1, 22±7% for Region 2, and 5±4% for Region 3. This agrees with the results from Fig. 4.8. As discussed in Chapter 2, periodic scatterers with spacing larger than the resolution cell are expected to present pre-Rayleigh statistics. For our computational phantom, statistically significant departure from Rayleigh statistics to pre-Rayleigh statistics occurred for spacing values larger than 0.4mm, for which the minimum pre-Rayleigh detection ratio was 25±33%. For Regions 10 (0.8mm) and 11 (1.2mm) the pre-Rayleigh detection rate was 100%.

The Rayleigh detection ratio (Fig. 4.11(b)) was 95±3% in both Regions 4 and 5. The coherent component from region 5 was not sensed by the pulse because the frequency corresponding to the spacing (12.8MHz) is beyond the high end of the available bandwidth f_H (10MHz). Regions 8 (0.3mm) and 9 (0.4mm) had relatively large Rayleigh detection ratios of 95±5% and 75±33%, respectively. This is because the corresponding scatterer spacing values are close to the size of the resolution cell (0.3mm) and, as discussed in Chapter 2, CNR_q approaches zero under this condition. Finally, the post-Rayleigh detection ratio (Fig. 4.11(c)) was 100% for Region 6 and 70% for Region 7. The corresponding spacing values (0.12mm for Region 6 and 0.24mm for Region 7) are close to the values 0.5λ (0.13mm) and 1.0λ (0.26mm) where the CNR_q of SNR_V is maximized (Fig. 2.13). The fact that the CNR_q of SNR_V was smaller for 1.0λ than for 0.5λ results in a lower post-Rayleigh detection ratio in Region 7.

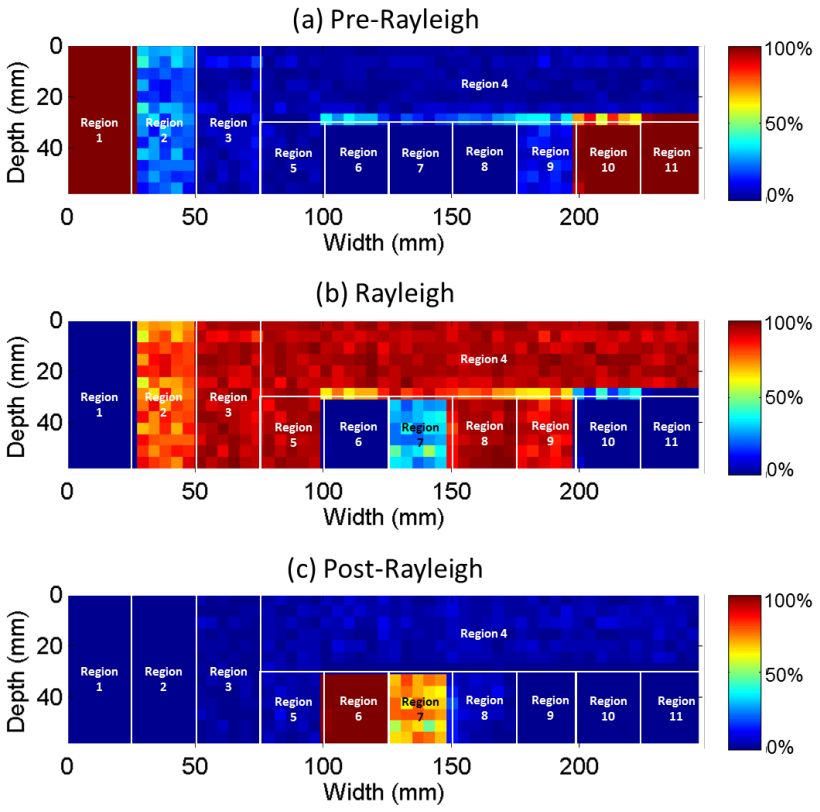

Figure 4.11 Images of the detection ratio for (a) pre-Rayleigh statistics (b) Rayleigh statistics and (c) post-Rayleigh statistics in the simulated phantom.

Figure 4.12 shows the detection ratio for the test of non-uniformity of the phase based on the $\chi^2(f)$ metric. Figure 4.12(a) shows the detection ratio for non-uniform phase, while Fig. 4.12 (b) shows the detection ratio for a uniform phase. It is interesting to note the high sensitivity of this metric to the presence of periodic scatterers. The detection ratio was 100% in Regions 6 to 11. As mentioned before, the fact that the frequency corresponding to the spacing of the scatterers in Region 5 is beyond the high end of the useful bandwidth turns this method insensitive to this spacing and this region is classified as of uniform phase with a detection ratio of 95±3%. Note also that the $\chi^2(f)$ analysis is not as sensitive as the other two tests to the presence of a very low concentration of random scatterers, such as in Region 1. The detection ratio in Regions 1, 2, and 3 were 33±12%, 6±3%, and 5±3%, respectively. Thus, this method, although

useful to detect coherent scattering from periodic scatterers, offers low sensitivity to low scatterer densities.

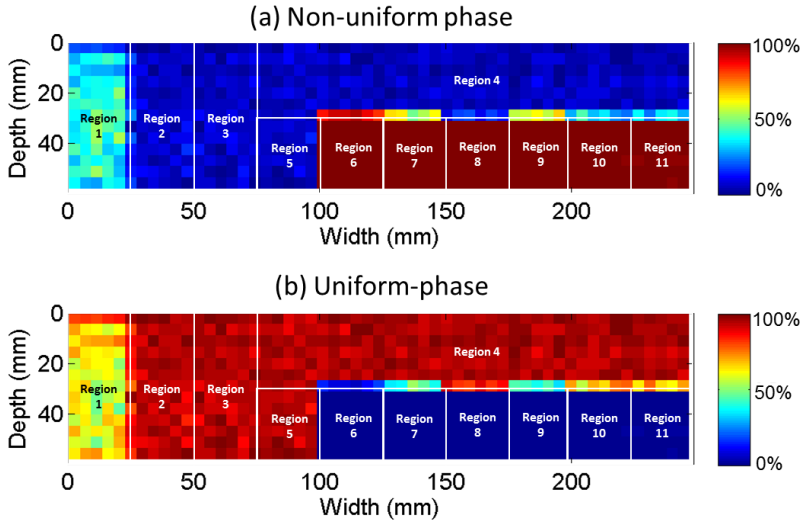

Figure 4.12 Images of the detection ratio for (a) non-uniform phase and (b) uniform phase in the simulated phantom.

As shown in Figs. 4.10, 4.11, and, 4.12, each of the three decision tests has its specific limitations to offer a complete classification of the different regions in the simulated phantom. We can, however, combine the strengths of the three analyses to improve the classification performance. To improve the classification of the regions with different statistics, we form twelve possible categories that are mutually exclusive. These are described in Fig. 4.13 as the intersections of the three decision tests and are:

(a) PERS classified as non-stationary, pre-Rayleigh, and of uniform phase.

(b) PERs classified as non-stationary, pre-Rayleigh, and of non-uniform phase.

(c) PERs classified as non-stationary, Rayleigh, and of uniform phase.

(d) PERs classified as non-stationary, Rayleigh, and of non-uniform phase.

(e) PERs classified as non-stationary, post-Rayleigh, and of uniform phase.

(f) PERs classified as non-stationary, post-Rayleigh, and of non-uniform phase.

(g) PERs classified as stationary, pre-Rayleigh, and of uniform phase.

(h) PERs classified as stationary, pre-Rayleigh, and of non-uniform phase.

(i) PERs classified as stationary, Rayleigh, and of uniform phase.

(j) PERs classified as stationary, Rayleigh, and of uniform phase.

(k) PERs classified as stationary, post-Rayleigh, and of uniform phase.

(l) PERs classified as stationary, post-Rayleigh, and of non-uniform phase.

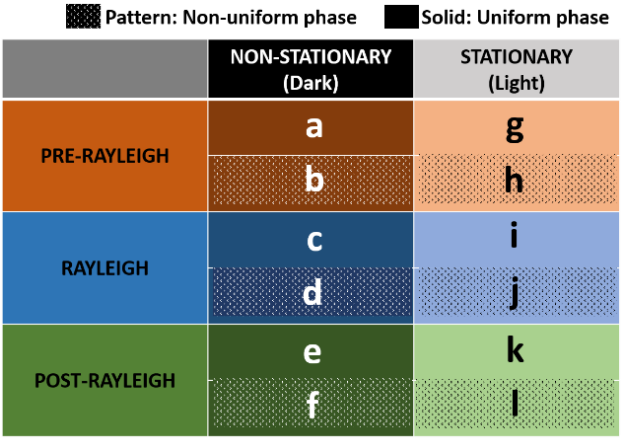

Figure 4.13 Diagram showing the generation of twelve categories from the three decision test of non-stationary features, pre- and post-Rayleigh statistics, and non-uniform phase.

Images of the detection ratio for each of these categories when applied to the simulated phantom are shown in Fig. 4.14. These categories are to be regrouped into three final classes:

1. Low density (ideally uniform phase, non-stationary, and pre-Rayleigh, or category (a)).
2. Diffuse scattering (ideally uniform phase, stationary, and Rayleigh, or category (i)).
3. Periodic scatterers (ideally non-uniform phase).

We can optimize the combination of the twelve categories to obtain the best classification possible. To do this, in categories where ambiguity exists, the category was assigned to the scattering condition in which the maximum detection ratio was achieved. As a result, the categories were grouped as follows:

1. Low density: categories (a), (g), and (h).
2. Diffuse scattering: categories (c), (i), (j), (k)
3. Periodic scattering: categories (b), (d), (e), (f), and (l).

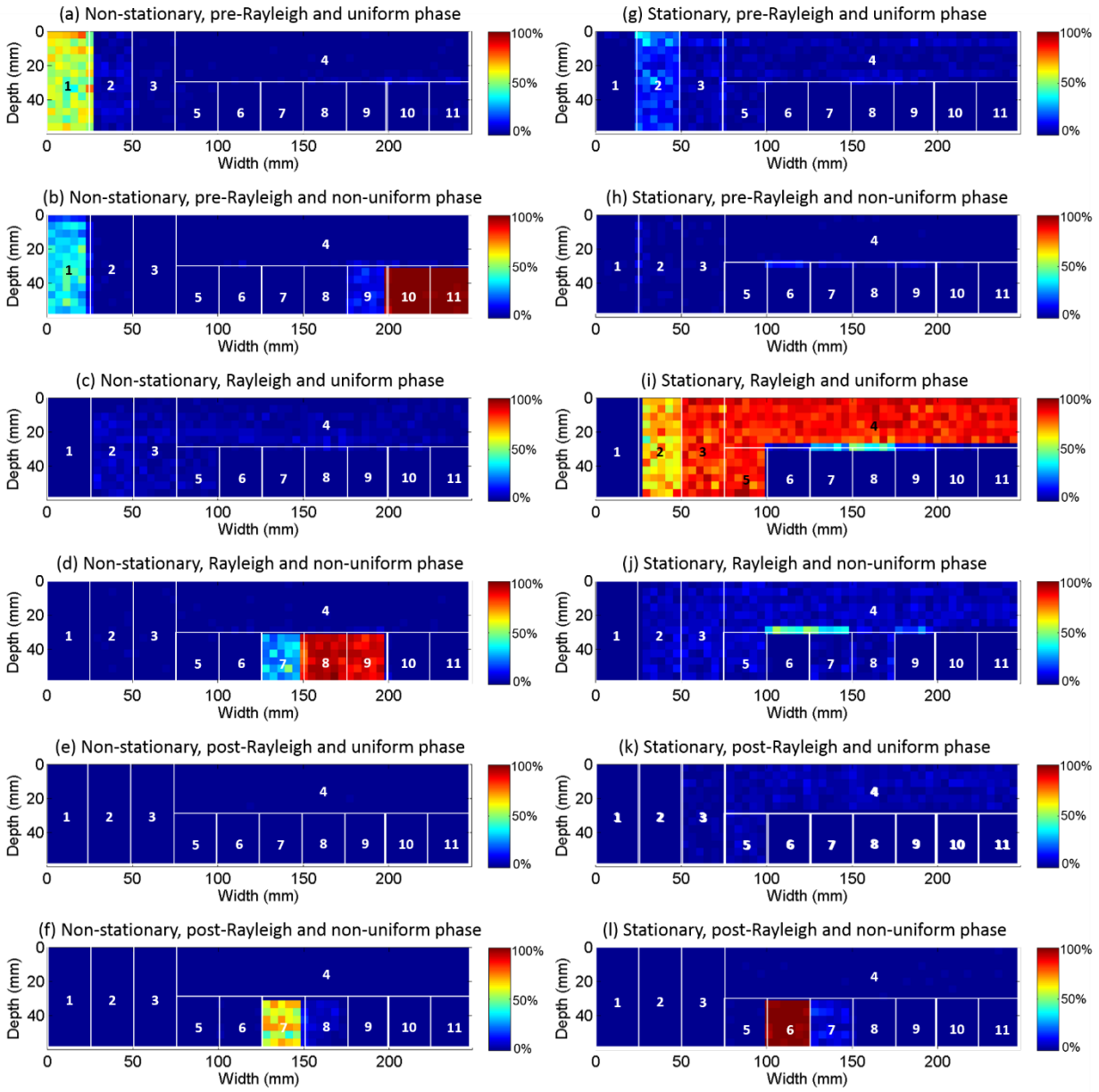

Figure 4.14 Detection ratio images for each of the twelve categories described in Fig. 4.13.

Images of the final classes are shown in Fig. 4.15. To the three classes, a fourth one corresponding to the detection of specular reflectors has been added. Region 1 was classified 60±11% times as a region of low-scatterer density, and 29±11% times as a region with periodic scatterers (possibly due to the presence of two scatterers within the resolution cell), and 11±3% as a region with a specular reflector (possibly due to the presence of a single scatterer per resolution cell). Most importantly, the detection ratio of diffuse

scatterers within this region was 0%, thus completely excluding it from further analysis that assume diffuse scattering conditions. Region 2 was classified 20±11% as a region with low scatterer density, which is roughly the expected detection ratio from the PERs with non-stationary features and pre-Rayleigh statistics in Fig. 4.8. It was classified as a zone with diffuse scattering in 74±7% of the cases. Regions 3, 4, and 5 were classified as zones of diffuse scattering in 92±4%, 95±3%, 95±3%. Finally, regions with periodic scatterers (excluding Region 5 which was beyond the sensitivity limits of the acoustic pulse), were classified as such with detection ratios larger than 97±4%. Finally, Fig 4.15(d) shows the detection ratio of the PERs classified as including a specular reflector. Most of the detection ratio is located at the boundaries between regions. The highest detection rate occurs in the boundary between Region 4 and Regions 10 and 11.

Now that a classification method has been devised to detect all PERs with periodic scatterers, we proceed to find a method to estimate the mean scatterer spacing in those cases. The challenge is to have a method that offers accurate and precise MSS estimates over a wide range of scatterer spacing values.

4.4 Mean scatterer spacing estimation

The results just shown demonstrate that the combination of the three decision tests (non-stationary features, departure from Rayleigh statistics, and the presence of non-uniform phase) is needed to improve the classification of the parameter estimation regions when creating a parametric image. In those cases where a periodic array of scatterers is present, an appropriate method for estimating the mean scatterer spacing is required. When the test for non-stationarity is positive, the maxima of the collapsed average of the generalized spectra can be analyzed to estimate the mean spacing among the periodic scatterers.[119,134,139] When the test for non-stationary features is negative, but the test for post-Rayleigh statistics is positive, then the $\chi^2(f)$ spectrum can be analyzed to estimate the mean scatterer spacing, as proposed by Molthen *et al*.[54]

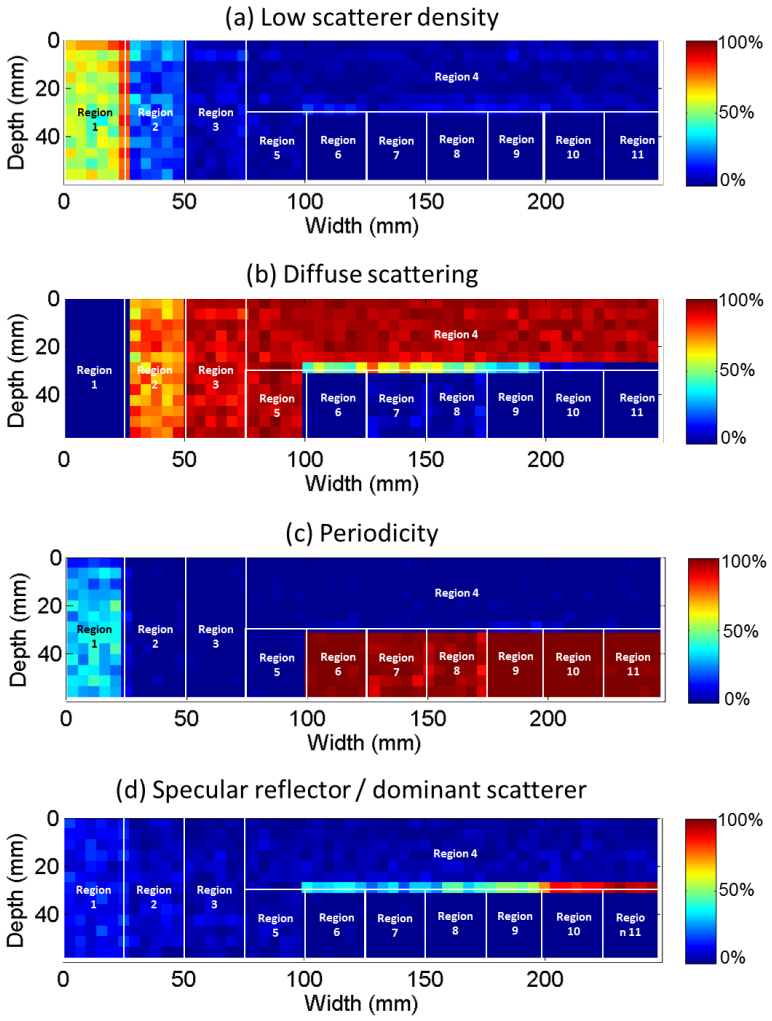

Figure 4.15 Detection ratio images for the final classification: (a) Low scatterer density, (b) Diffuse scattering, (c) scatterer periodicity, and (d) specular reflectors or dominant scatterers.

4.4.1 Periodicity with non-stationary features

As mentioned in Chapter 3, ideally the maximum value of the collapsed average of the generalized spectrum will occur at the frequency related to the mean spacing Δ, given by the equation $f=c/2\Delta$. However, as observed in other independent studies,[51,119,134,139] our results showed that under many circumstances a harmonic of this frequency can be detected instead. Therefore, the spacing estimation method needs to be able to identify harmonics and the corresponding fundamentals.

In order to identify possible harmonics, it was assumed that their corresponding CAGS values have to be statistically significantly larger than those from the reference CAGS. Thus, in order to find possible harmonics, the analysis of statistical significance was performed at each frequency bin within the search region to find all the points that are significantly larger than the CAGS from the reference. This resulted in a frequency dependent threshold $q_d(f)$ based on the statistics of the reference CAGS at each frequency bin, which was created based on a probability of false detection of 5%. This procedure is described in Fig. 4.16, which shows the CAGS of a material with periodic scatterers separated by 0.8mm, creating maxima at multiples of f=c/2Δ=0.96MHz. The blue curve indicates the average reference CAGS among all the uncorrelated PERs described in Fig. 4.4. The red curve shows the threshold for each frequency bin within the search region. Note that this threshold is different from the threshold q_a defined in Fig. 4.4 because the one defined here is created from the statistics of the CAGS for each frequency, while q_a is created from the statistics of the maximum value of the CAGS, regardless of its frequency. The MaxCAGS value is indicated by the red square and red arrow. The maxima indicated by cyan circles and gray arrows (including MaxCAGS) are those points that were significantly larger than the frequency dependent threshold. Note that the corresponding peaks may have included more than one CAGS value. By choosing the maximum from adjacent points the algorithm is able to keep only the maximum value for each peak.

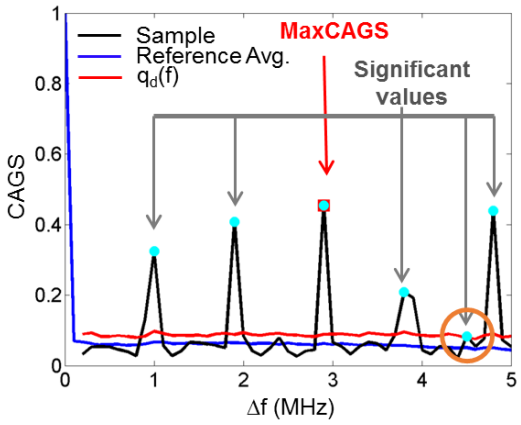

Figure 4.16 Schematics of the detection of significant CAGS values at each frequency bin.

Once the significant CAGS values were defined, they were used for the estimation of the mean scatterer spacing. If only one significant point was detected (i.e., the MaxCAGS value), that value was used for the estimation of the scatterer spacing as $\Delta=c/2f_{MaxCAGS}$. If two or more significant values were identified, the mean scatterer spacing was obtained by analyzing the relationship among their frequencies. Two different methods were explored:

1. **Median**: The difference among the frequencies of consecutive statistically significant CAGS values was computed and then the median was obtained. The median was chosen due to its robustness to outliers (for example, the frequency difference between the last significant point and the cyan dot enclosed in the orange circle in Fig. 4.16). The value of the median was used as the frequency corresponding to the spacing.
2. **Harmonic search**: The frequency of the MaxCAGS value was divided into consecutive integers to obtain a set of possible fundamentals: $f_2=f_{MaxCAGS}/2$, $f_3=f_{MaxCAGS}/3,\ldots,f_n=f_{MaxCAGS}/n$. The maximum value of n is the maximum integer by which $f_{MaxCAGS}$ can be divided and still be larger than the leakage limit f_{Min} of the search region. Then, these fundamental f_2, $f_3,\ldots,f_n$ were searched among the frequencies of the significant values of the CAGS (cyan dots in Fig. 4.16), allowing a variation of 0.1MHz. Finally, among those fundamentals that were within the set of significant values of the CAGS, the sum of the CAGS values of the corresponding harmonics of each fundamental was computed. The median of the difference between the harmonics with the largest sum of CAGS values is chosen as the spacing frequency.

These two methods were implemented and applied to the sets of simulated backscattered echo signals from a periodic array of scatterers embedded in a cloud of random scatterers, with 48 scatterers/resolution cell. The spacing among scatterers was varied from 0.7λ to 7.8λ with a coherent to incoherent scattering power ratio per periodic scatterer of R=1.5dB. To assess the performance of the two estimation algorithms, the normalized bias of the mean scatterer spacing (MSS) Δ was defined as:

$$\text{MSS Normalized Bias} = \frac{\langle \Delta - E[\Delta] \rangle}{E[\Delta]}. \tag{4.5}$$

where brackets indicate the average of 100 independent realizations of the scattering scenarios. The operator $E[\ ]$ indicates the expectation value of the spacing, which is the value used in the creation of the simulated data. Figure 4.17(a) shows the MSS normalized bias for a 0.7λ spacing as a function of the PER size for the two methods: median-based (blue curve) and harmonic search (black curve). The advantage of the harmonic search is evident and is due to its ability to constrain the search to specific frequency values. Note that for the 0.7λ spacing, a single peak in the CAGS is expected. The large bias of the median-based method is caused by "spurious peaks", i.e., values of the CAGS that were identified as significant but are not really harmonically related to the scatterer spacing (cyan dot enclosed in orange circle in Fig. 4.16). Figure 4.17(b) shows the MSS normalized bias for a PER of 15 pulse lengths and 15 uncorrelated scan lines for a range of spacing values. Note that as the number of harmonics present in the CAGS increases, the bias of the two methods stabilizes and tends to zero.

As an attempt to reduce the effects of the spurious peaks caused by inter-frequency variance, an inter-frequency variance threshold was implemented. It is inspired by the periodicity-detection algorithm from Donohue *et al*.[51] It includes the following steps, which are illustrated in Fig. 4.18:

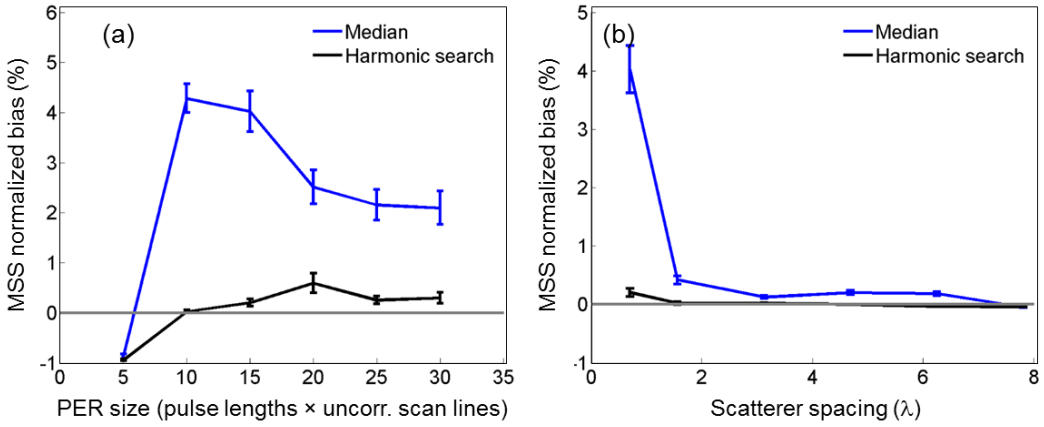

Figure 4.17 (a) Normalized bias of the mean scatterer spacing (MSS) estimates with the median-based (blue) and the harmonic-search (black) estimators as a function of (a) PER size for periodic scatterers with 0.7λ spacing, and (b) scatterer spacing in wavelengths for a PER of 15 pulse lengths × 15 uncorrelated scan lines.

1. The inter-frequency reference CAGS variance σ_f^2 was estimated by computing the variance across frequency bins of each of the CAGS estimates from the reference phantom and averaging across the different reference PERs.
2. The base coherence level of the sample CAGS was computed. To do this, the peaks corresponding to significant values of the CAGS (cyan dots in Fig. 4.16) were removed and a least-squares linear fit was applied to the remaining values within the search region, such as done to the log-transformed CAGS in Ref. 51. This is the dashed blue line shown in Fig. 4.18.
3. An inter-frequency variance-based threshold $q_\sigma(f)$ was computed as the value of the fit at each frequency bin plus $3\sigma_f$. If no CAGS values were found above this threshold, the variance dependent term was reduced by $0.5\sigma_f$. This was repeated until at least one value of the CAGS was above $q_\sigma(f)$. The values of $q_\sigma(f)$ are represented by the red dashed line in Fig. 4.18.

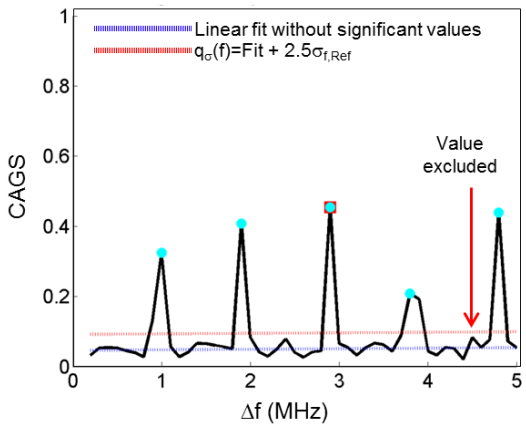

Figure 4.18 Schematics of the definition of a threshold based on the inter-frequency variance of the CAGS.

An adaptive computation of the factor of the inter-frequency variance in $q_\sigma(f)$ was chosen in lieu of a fixed value in order to adjust to conditions of different coherent to incoherent scattering power ratio R. In most of the cases simulated in this study, the final value of the factor was 2.5. Note that using this algorithm, the spurious significant value from Fig. 4.16 was discarded from further analysis, as shown in Fig. 4.18. Figure 4.19(a) is the same as Fig 4.17(a) but after the application of $q_\sigma(f)$ prior to the use of the two MSS estimation methods. Note the remarkable reduction in bias from the median-based method. For example, for a PER size of 15 pulse lengths and 15 uncorrelated scan lines, the bias was reduced by a factor of 10. The harmonic search method leads to practically unbiased estimates down to a PER size of 10 pulse lengths × 10 uncorrelated scan lines. In the context of typical breast imaging performed with the 18L6 high frequency transducer, these dimensions would correspond to about 2.6mm axially and 3.7mm laterally. Figure 4.19(b) is the same as Fig. 4.17(b), but after the use of $q_\sigma(f)$. Note the different scales in Fig. 4.17(b) and Fig. 4.19(b). For scatterer spacing values larger than approximately 1.2λ, both methods perform similarly. For spacing values smaller than 1.2λ (0.3mm), the harmonic search outperforms the median-based method. This is because for spacing values smaller than 1.2λ, there is only a single peak in the CAGS due to scatterer periodicity. Thus, although the effect was reduced by using the adaptive threshold $q_\sigma(f)$, the median-based method is still sensitive to spurious peaks. Note that no estimate can be

obtained with either of these methods if the spacing is smaller than $c/f_H = 0.6\lambda$ (the detection limit of the generalized spectrum technique).

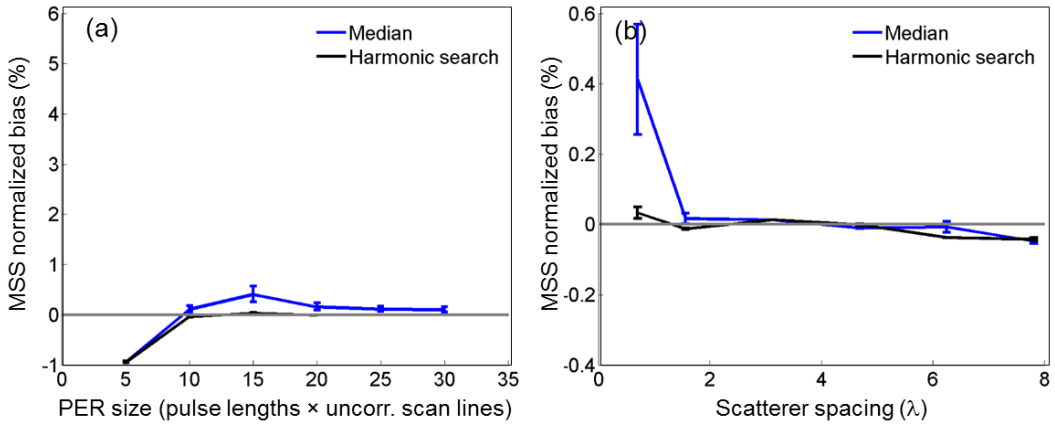

Figure 4.19 (a) Normalized bias of the mean scatterer spacing (MSS) estimates with the median-based estimator (blue) and the harmonic-search estimator (black) as a function of (a) PER size in pulse lengths × uncorrelated scan lines for periodic scatterers with 0.7λ spacing, and (b) scatterer spacing in wavelengths for a PER of 15 pulse lengths × 15 uncorrelated scan lines. Estimates were obtained after the application of the frequency-variance threshold.

4.4.2 Periodicity with stationary features

As mentioned in the discussion above, the generalized spectrum is able to sense periodicity in the scatterer organization when the spacing is larger than $\Delta = c/f_H$, where f_H is the highest frequency of the available bandwidth. When the scatterer spacing is smaller than this limit, tools from echo statistics can be used in the detection process. In these situations, Molthen *et al.*[54] proposed the analysis of the non-uniformity of the phase, i.e., the $\chi^2(f)$ spectrum, to estimate the scatterer spacing. As discussed previously, the $\chi^2(f)$ will be maximized at a demodulation frequency equal to $c/2\Delta$. This method was tested on simulated echo data following the same simulation procedure as for the test presented in the section above, but for periodic scatterer spacing values ranging from 0.23λ to 3.5λ.

Figure 4.20(a) shows the frequency at which the maximum value of the $\chi^2(f)$ spectrum occurs as a function of the periodic spacing value expressed in multiples of the wavelength. The error bars indicate

the standard deviation from 300 independent realizations. The blue line indicates the frequency values expected for each simulated spacing value. The frequency values of the maximum $\chi^2(f)$ analysis match the expected values when the spacing ranges from 0.3λ to 0.7λ. For spacing larger than 0.8λ and smaller than 1.2λ, the maximum value occurs at a frequency twice the value of $c/2\Delta$. For this spacing range, the corresponding spacing frequencies $c/2\Delta$ range from 3.9MHz down to 2.6MHz, while their first harmonics range from 7.8MHz down to 5.2MHz. Note that the harmonics occur closer to the maximum of the pulse spectrum. Therefore, the harmonics have higher energy than the corresponding fundamentals. When the spacing is smaller than 0.3λ ($c/2f_H$), the corresponding frequency is beyond the maximum frequency of the available spectrum and is not sensed by the acoustic pulse. Therefore, the maximum $\chi^2(f)$ value occurs at the frequency where the energy of the pulse spectrum is maximum, i.e., 6MHz. When the spacing is larger than 1.2λ (i.e., the pulse length), the frequency of maximum $\chi^2(f)$ goes back to the frequency of the maximum value of the pulse spectrum. This is because the periodic spacing is now larger than the resolution cell, and the samples of the phase occur mostly within the spacing of the periodic features.

Figure 4.20(b) shows the corresponding MSS normalized bias, as defined in Eq. (4.5), using the frequency of the maximum values of the $\chi^2(f)$ for the estimation. As expected from Fig. 4.20(a) the MSS estimates for spacing ranging from 0.3λ to 0.7λ are unbiased. For spacing ranging from 0.8 λ to 1.2 λ the normalized bias is -0.5, indicating that the spacing is underestimated by half of the expected value. This is a consequence of the maximum $\chi^2(f)$ values occurring at twice the expected frequency. When the spacing is below 0.3λ or above 1.2λ, the estimation method is not capable of producing reliable estimates. Thus, the $\chi^2(f)$ method for estimating scatterer spacing as proposed by Molthen *et al.*,[54] is constrained to the range 0.3λ to 0.7λ.

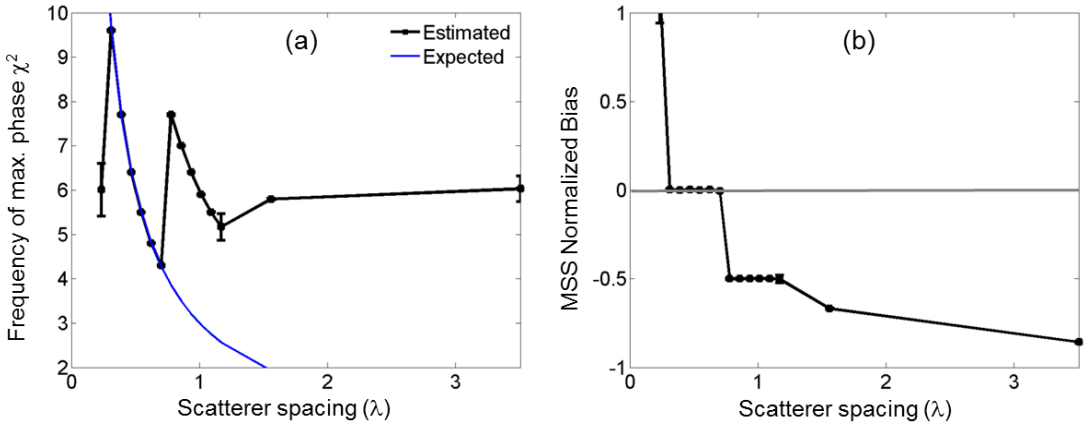

Figure 4.20 (a) Frequency of the maximum phase $\chi^2(f)$ value and (b) normalized bias of the MSS estimates obtained from the frequency values in (a). Blue curve in a shows the expected frequency for the simulated conditions.

In order to extend this range, we propose a combination of this method with the analysis of statistical significance based on the $\chi^2(f)$ spectrum (Eq. (4.4) and Fig. 4.7), but now performed at each frequency bin, just as done to find harmonics in the CAGS. This allows one to determine if the frequency of the maximum $\chi^2(f)$ is a fundamental or a first harmonic. The latter case will occur if one of the statistically significant $\chi^2(f)$ values occurs at a frequency half the frequency at which the maximum $\chi^2(f)$ occurs. In case the frequency of the maximum $\chi^2(f)$ is the first harmonic, the spacing is estimated from the difference between it and its fundamental. Note that within the bandwidth in which the $\chi^2(f)$ method is useful, only a first harmonic is expected. Thus, no harmonic search is required as in the case of the CAGS. Figure 4.21(a) shows the frequency used for the spacing calculation after the analysis of statistical significance is performed. The horizontal red lines bound the useful bandwidth. As observed, the addition of the analysis of statistical significance is able to extend the range of spacing in which the analysis of the $\chi^2(f)$ value is able to provide unbiased estimates. This range now includes spacing values for which the fundamental is within the useful bandwidth, which corresponds to 0.3λ ($\boldsymbol{c}/2\Delta$=10MHz) to 0.9λ($\boldsymbol{c}/2\Delta$=3.4MHz). This is shown in Fig. 4.21(b), which shows the MSS normalized bias, which is practically zero from 0.3λ to 0.9λ.

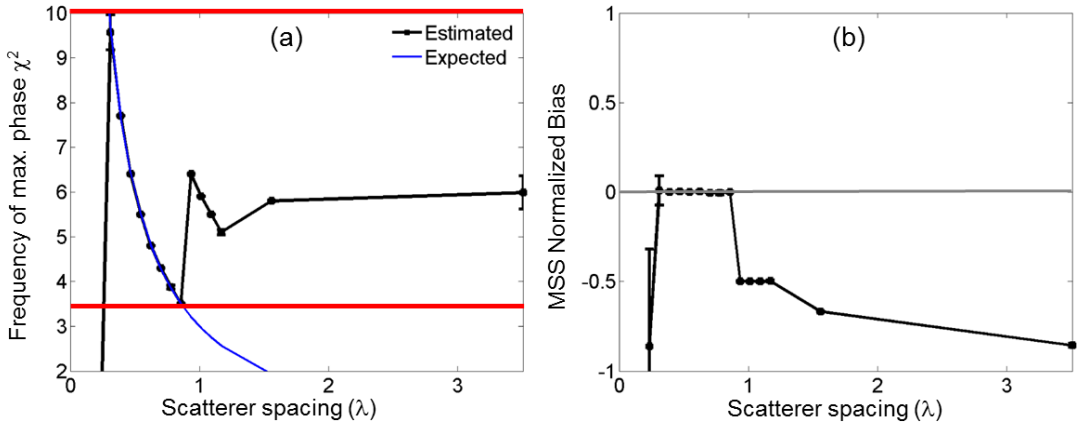

Figure 4.21 (a) Frequency used in the estimation of the scatterer spacing after the test for statistical significance of the phase $\chi^2(f)$ values. (b) Normalized bias of the MSS estimates obtained from the frequency values in (a). Blue curve in a shows the expected frequency for the simulated conditions.

Comparing Figs. 4.19(b) and 4.21(b), it is possible to see that where the MSS estimates obtained from the CAGS become biased (<1.2λ), the $\chi^2(f)$ algorithm offers MSS estimates with good bias properties. Thus, the combination of both analyses can be used to estimate quasi-periodicity spacing values as small as 0.3λ, as long as the CNR_q of the periodicity features is high enough to be detected by the test of statistical significance. The remaining question is how to decide when to use the CAGS-based method or the $\chi^2(f)$ method. As observed in Fig. 4.11(c), the analysis of post-Rayleigh statistics can be used as a decision method because in the range in which the $\chi^2(f)$ is useful, the statistics of the echo amplitude are expected to be post-Rayleigh. Thus, if a PER is classified as containing periodic scatterers (Fig. 4.15(c)), the $\chi^2(f)$ spacing estimator will be used if the test for post-Rayleigh features is positive (category (l) in Fig. 4.14). Otherwise, the CAGS-based estimator will be used. This decision is shown in the diagram of Fig. 4.22.

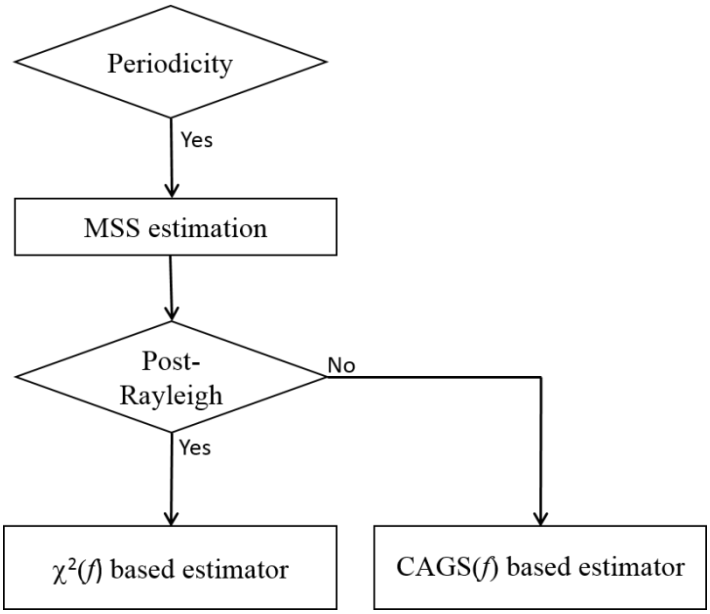

Figure 4.22 Flow chart of the decision algorithm for the use of either the $\chi^2(f)$-based MSS estimator or the CAGS(f)-based MSS estimator.

4.5 The complete algorithm

Figure 4.23 shows a flow chart with the complete algorithm including the decision tests, the classification methods, and the MSS estimation. The inputs for the analysis, indicated by the black ellipses, are the three parameters of interest: maximum value of the CAGS for the analysis of non-stationary features, SNR_V for the analysis of the departure from Rayleigh statistics, and finally, the maximum value of the $\chi^2(f)$ for the analysis of phase non-uniformity. From these, a PER can be classified as either containing a specular reflector or a dominant scatterer (black) or other non-stationary features (dark blue) or stationary (light blue); as either pre-Rayleigh (dark green) or Rayleigh (green) or post-Rayleigh (light green); and either as of uniform phase (red) or non-uniform phase (orange). Discarding the specular reflector/dominant scatterer classification, the combination of the classes generates twelve exclusive subcategories, (a) through (l), as described in Fig. 4.13. Then these categories are combined into three final classes: low scatterer density (dark gray), diffuse scattering (gray), and periodic scatterers (light gray). The final outputs are indicated in purple. When periodic scatterers are detected, then the mean

scatterer spacing is estimated using either the $\chi^2(f)$-based estimator under post-Rayleigh conditions or the CAGS(f)-based estimator otherwise. When diffuse scattering conditions are identified, then this algorithm can be coupled with algorithms for attenuation and backscatter estimation. Finally, if the region contains a specular reflector or dominant scatterer, the width of the CAGS main lobe can be used as an indirect measure of its influence over the PER.

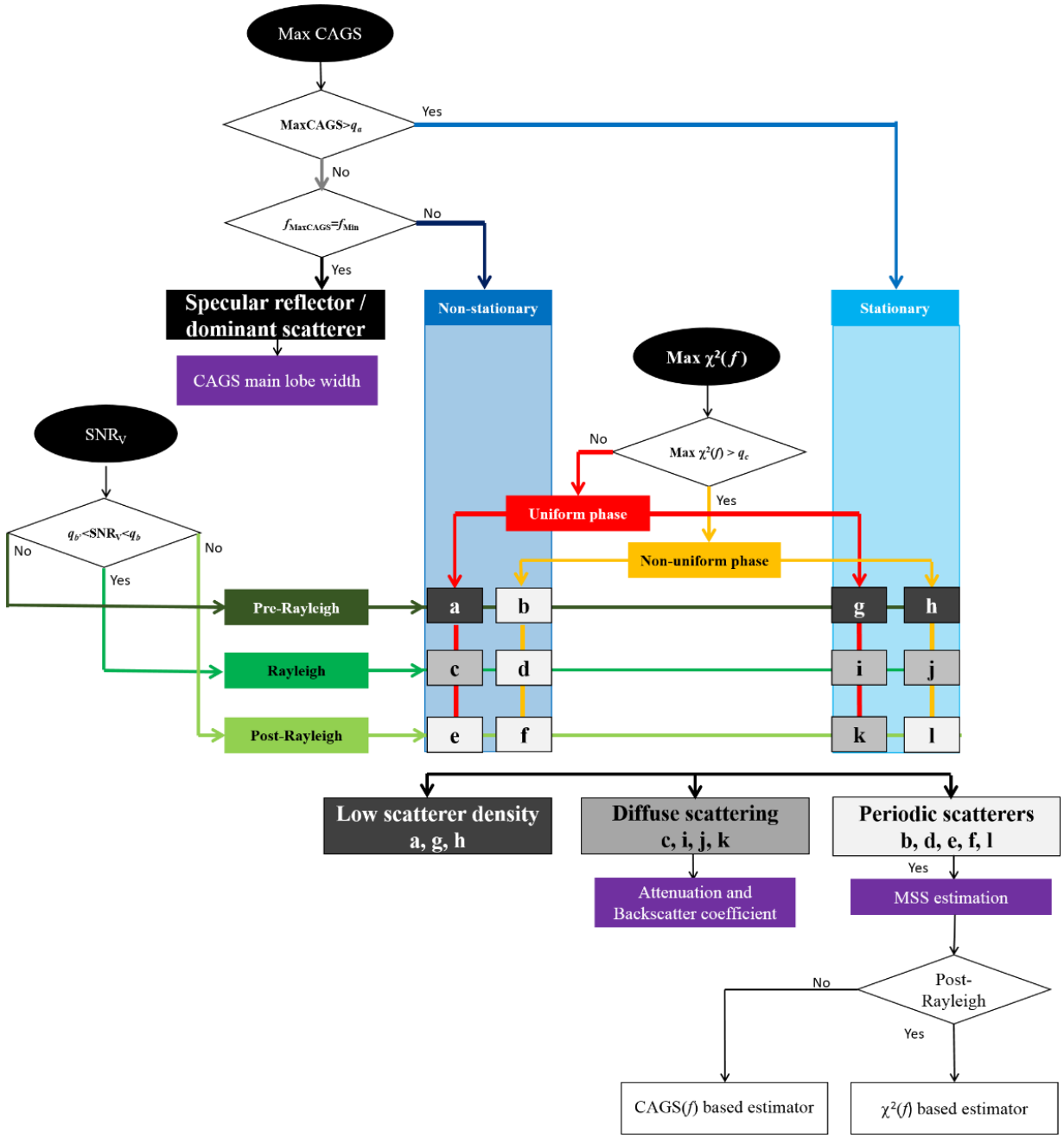

Figure 4.23 Schematics of the complete detection/classification algorithm

The complete algorithm was applied to the simulated contrast phantom to obtain a final image of the mean scatterer spacing. The results are shown in Fig. 4.24, which shows parametric images of the mean scatterer spacing. In those cases where non-stationary periodicity was detected, the MSS was assessed using (a) the median-based estimator or (b) the harmonic search estimator. The images are the average of 60 independent frames. Table 4.1 includes the average and the standard deviations of the MSS estimates for each of the regions demarcated by the white boxes over the 60 frames and over each one of the regions. In Region 1, which was classified as containing periodic scatterers with a detection rate of 26%, the average of the mean scatterer spacing was about 0.20mm with both estimators. Note that this average includes those cases in which each PER was classified as having a low scatterer density and, therefore, zero MSS. The large standard deviation agrees with the spread of the frequencies of the maximum values of the CAGS discussed in Appendix B. In Regions 2, 3, 4, and 5, the estimates of the scatterer spacing is zero as expected from their classification regions with diffuse statistics. The average of the scatterer spacing in Regions 6 to 11 agree with the expected values. The largest bias was observed in Region 9, which can be attributed to the PERs located at the boundary between the regions with 0.40mm and with 0.80mm spacing, which were more sensitive to the larger spacing. It is also possible to observe that the median-based estimator produces estimates with more variance, especially in Region 8. As shown in Fig. 4.19(b), when the spacing is smaller than 1.2λ, the median-based estimator produces estimates with larger bias and variance than the harmonic search estimator due to the larger sensitivity to spurious peaks in the collapsed average.

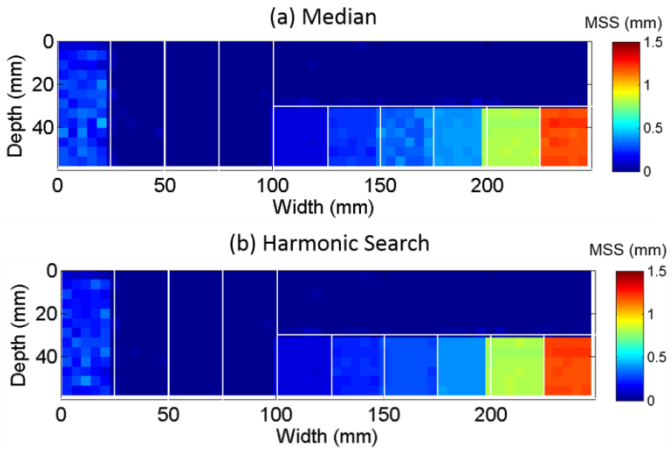

Figure 4.24 Images of the mean scatterer spacing (MSS) from the simulated contrast phantom. Images are the average of 60 independent frames. (a) Median-based MSS estimator, (b) harmonic search MSS estimator.

Table 4.1 Average and standard deviation (Std. Dev.) of the mean scatterer spacing (MSS) values within each of the 11 regions of the contrast phantom. Statistics were obtained from 60 independent frames and within each region.

		Median		Harmonic Search	
Region	**Expected MSS (mm)**	**Average (mm)**	**Std. Dev. (mm)**	**Average (mm)**	**Std. Dev. (mm)**
1	0	0.21	0.39	0.19	0.39
2	0	0.00	0.06	0.00	0.05
3	0	0.00	0.01	0.00	0.01
4	0	0.00	0.07	0.00	0.06
5	0	0.00	0.01	0.00	0.01
6	0.12	0.12	0.02	0.12	0.02
7	0.24	0.24	0.09	0.23	0.05
8	0.30	0.33	0.25	0.29	0.05
9	0.40	0.47	0.04	0.46	0.01
10	0.80	0.81	0.04	0.81	0.06
11	1.20	1.20	0.10	1.20	0.08

4.6 Phantom-based experiments

Finally, we apply the algorithm to tissue mimicking phantoms. Two analyses are presented. In the first analysis, the algorithm was applied to a sample containing only random scatterers (Phantom C from previous chapters). The reference data were independent data frames from the same phantom. The goal of this analysis was to verify experimentally the probability of false detection. To do this, ten independent sample frames were obtained by moving the transducer in the elevational direction by at least the thickness of the transducer. Twelve independent reference frames were obtained in the same fashion. Both data sets were obtained with the SIEMENS S2000 system with the 18L6 transducer used in the clinical protocol, under conditions described in Chapter 3. The PERs had an area of 4mm axially (15 pulse-echo correlation lengths) × 4mm laterally (11 pulse-echo correlation lengths) and contained uncorrelated echo data. This was achieved by leaving one axial correlation length and four adjacent scan lines between consecutive PERS.

The algorithm was applied to each of the sample data frames. For each PER axial location, a set of uncorrelated PERs was defined at the same axial location in all the reference data frames. The reference frames were selected within a lateral span that excluded locations less than 1cm from the edges of the reference data to account for any effects of differences in the diffraction field when the active aperture of the transducer reaches the edges of the array. This led to a total of nine uncorrelated PERs per frame, or a total of 108 uncorrelated reference PERs. This produced a total of 108 reference CAGS(f), SNR_V, and $\chi^2(f)$ estimates for each axial PER location. In the sample, a total of 8 axial × 11 lateral PER locations were defined. After applying the algorithm to each sample frame, the number of PERs negative to the detection of non-stationary features, pre- or post-Rayleigh statistics, and non-uniform phases was determined. This defined the detection ratio for each of the detection tests. The statistics of the detection ratios for the ten sample frames are summarized in Table 4.2. As observed, the detection ratios are within 4% of the expected probability of false detection.

Table 4.2 Statistics of the detection ratio for stationary features, Rayleigh statistics and uniform phase for PERs in Phantom C containing only random scatterers.

	Detection ratio				
PER	Expected	Average	Std. Dev.	Minimum	Maximum
Stationary	0.95	0.95	0.02	0.92	0.98
Rayleigh	0.95	0.93	0.02	0.91	9.96
Uniform phase	0.95	0.95	0.03	0.91	0.97

The second analysis involved the application of the algorithm to a frame of echo data from Phantom D. As described in Chapter 2, this phantom has a plane of periodically spaced nylon fibers 0.1mm in diameter and separated by 0.4mm. The fibers are embedded in a material with only random scatterers. The reference data frames were twenty two frames from phantom C. Note that the more reference frames are acquired, the better the estimate of the cumulative density function of the parameters.

Figure 4.25 shows (a) the B-mode image of the data frame from phantom D as well as images showing regions classified as (b) diffuse scattering, (c) low scatterer density, (d) specular reflectors, and (e) periodic scatterers. Positive classification is colored in red, while negative classification is shown in blue. In general, the classification achieved by the algorithm agrees with the structural composition of the phantom. In the top part ranging in depth from 0 to 25mm, the phantom consisted of only random scatterers. The algorithm classified 77% of this area as a region with diffuse scattering conditions, while 20% was classified as regions with low scatterer density. Although it is not possible to verify if these zones truly had low scatterer number densities, it is interesting to note that the PERs classified as such were clustered rather than randomly scattered over the data frame. This suggests that there might be spatial variations in the scatterer concentration in the phantom that the algorithm is sensitive to. In the region of the periodically spaced nylon fibers, 84% of the area was classified as a region with periodicity, while 16% was classified as a region containing specular reflectors. The area classified as containing specular reflectors is mainly the interface between the background and the fibers array.

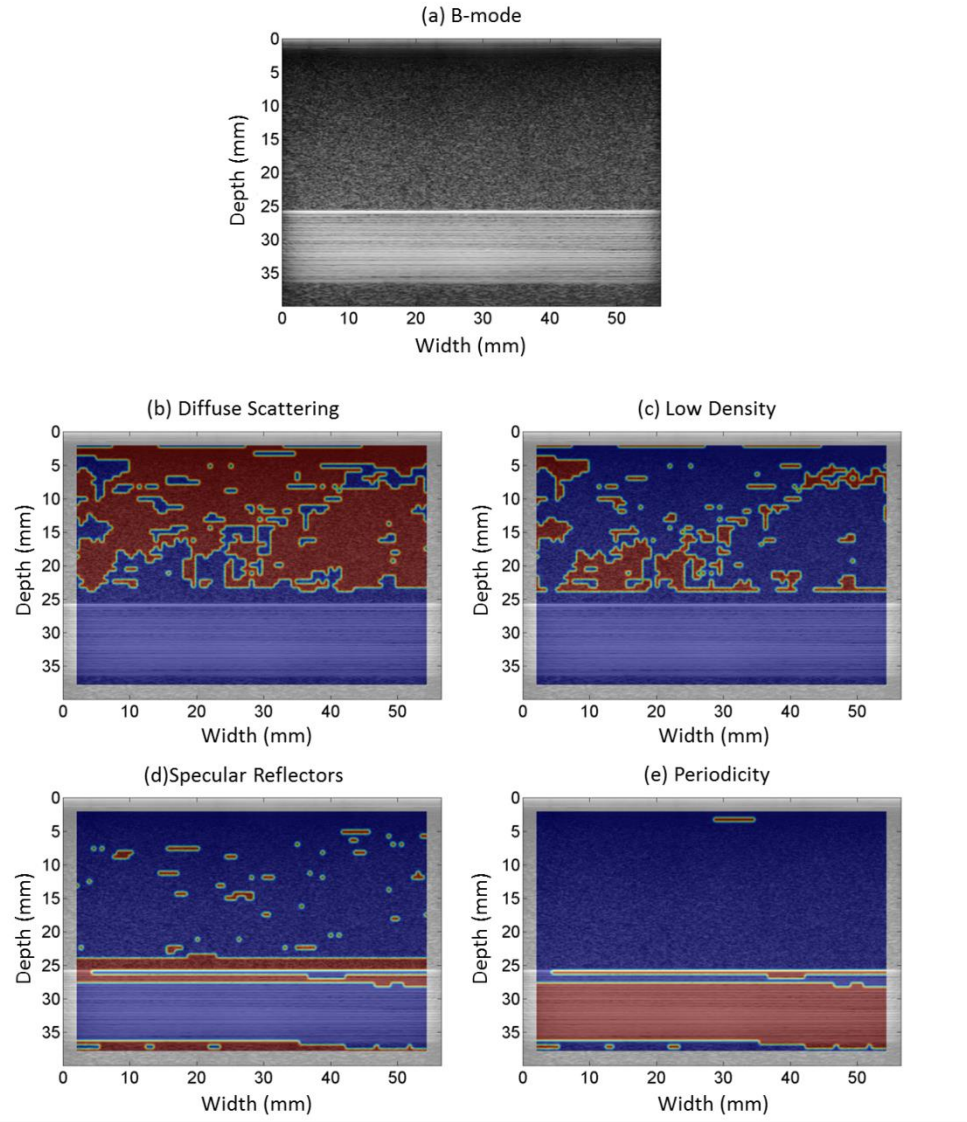

Figure 4.25 Zones in a single data frame of (a) Phantom D classified as (b) diffuse scattering, (c) low scatterer density, (d) specular reflectors and (e) periodic scatterers. Red pixels= positive test for a feature; blue pixels= negative test for a feature.

Figure 4.26 shows a combination of the four images shown above. Regions classified as diffuse scattering zones are colored in blue, regions classified as zones of low scatterer density are shown in green, and regions classified as zones with periodic scattering are shown in red. Zones that were not colored within the region of interest were classified as zones with specular reflectors. Note that the zone boundary between the homogeneous background and the fiber plane was classified as containing a specular

reflector. This can be attributed to the presence of the horizontal array of fibers in the plane perpendicular to the direction of propagation of the acoustic pulse aligned with the first fiber of the axial array. Due to the coarser spatial resolution in the elevational direction, the pulse might have included two or more fibers of the elevational array, thus effectively strengthening the reflectivity of the first fiber. Also note that the zone of detection of specular reflectors extends about half a PER length above and below the boundary. This is due to the blurring effect resulting from raster-scanning a finite-size PER in an overlapped fashion. Appendix C presents a method for reducing this blurring effect and the bias that can be associated with it.

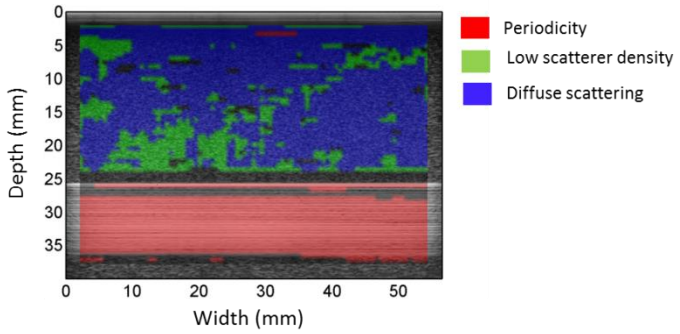

Figure 4.26 Zones in a single data frame of Phantom D classified as diffuse scattering (blue), low scatterer density (green) and scatterer periodicity (red).

Figure 4.27(a) shows a Mean Scatterer Spacing image of the phantom. To generate this image, the algorithm automatically detected the regions were periodic scatterers were present and estimated the spacing only in these regions. Comparing to the color bar on the right, it is possible to see that in most of the area classified as containing periodic scatterers, the MSS estimates were about the expected 0.4mm. To express this quantitatively, a histogram of the MSS values estimated in those PERs classified as containing periodic scatterers is shown in Fig. 4.27(b). The vertical axis of this plot shows the occurrence, i.e., the number of PERs in which a particular MSS value was obtained expressed as a fraction of the total number of PERs classified as containing periodic scatterers. The MSS value corresponding to the fiber spacing shows maximum occurrence (73%). The next highest occurrence values are at 1.5mm and 1.9mm

and show up close to the upper limit of the fiber region. These large spacing values, and the corresponding low frequencies can be caused by the overall increase in the frequency correlation occurring when the fibers act as specular reflectors.

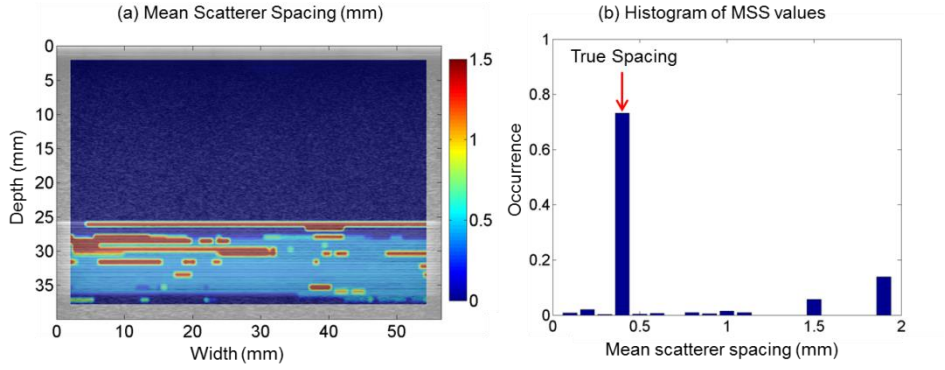

Figure 4.27 (a) Parametric image of the mean scatterer spacing of Phantom D generated by the detection/classification algorithm. (b) Histogram of MSS estimates.

Finally Fig. 4.28 shows an image of the main lobe width (MLW) of the CAGS. This parameter was computed only in regions that were classified as containing specular reflectors. The highest MLW values occur at the boundary between the background and the fiber region. Note that regions classified as containing specular reflectors in the background of the phantom had very small MLW values, which agrees with the fact that no true reflectors were present. This parameter can thus be used to further improve the classification of regions deemed as containing specular reflectors. This improvement will remain a subject of future research.

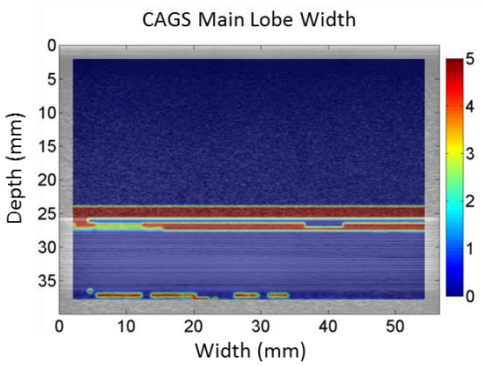

Figure 4.28 Parametric image of the main lobe width of the collapsed average of the generalized spectrum

4.7 Discussion

In this chapter a stand-alone algorithm for the classification of parameter estimation regions into classes describing the underlying scattering conditions has been developed. This algorithm is based on comparing the detection parameters that were described in previous chapters to their statistics under conditions of diffuse scattering. These statistics are assessed in a reference medium constructed to achieve such scattering conditions. It is important to mention that the acquisition of the reference data is a standard of practice in our protocol to compensate for spatial variations of the acoustic energy caused by diffraction, attenuation, and system dependent factors when estimating the attenuation and the backscatter coefficients. Thus, the proposed coherence analysis involving reference phantom data does not imply an additional workload to the person involved in the acquisition of data in our clinical protocols.

Our algorithm can be used as an automated segmentation stage prior to the use of the conventional algorithms to estimate the attenuation and the backscatter coefficients. Three similar algorithms have been developed by Luchies *et al.*,[126] Georgiou *et al.*,[145,146] and Donohue *et al.*[130] The focus of Luchies' algorithm was to detect the presence of specular reflectors in PERs to reduce bias and variance in estimates of incoherent-scattering QUS parameters, i.e., the effective scatterer size and the acoustic concentration.[126] The presence of specular reflectors was detected by means of quantifying either the envelope SNR or different metrics of the WOSA-estimated generalized spectrum. Thresholds for these metrics to decide on the presence of specular reflectors were chosen by minimizing errors in the estimation of QUS parameters when the true values were known (as in simulations), or by minimizing the divergence of estimates obtained from adjacent PERs when the true values of the QUS parameters were unknown (as for tissue samples). The authors found that the optimum metric, i.e., the one that resulted in the largest reduction in the QUS-parameter errors, depended on the parameter itself (either the effective scatterer size or the acoustic concentration). Also their results suggested that the optimum metrics and the corresponding thresholds depended on the nature of the tissue structure. In this work, we have provided a method to detect not only specular reflectors but also other scattering scenarios that can

affect the estimation of incoherent-scattering QUS parameters, such as periodic scatterers and low scatterer number densities. Furthermore the proposed method does not depend on the estimation of a particular incoherent-scattering QUS parameter and, as a consequence, does not rely on having multiple estimates to evaluate their convergence when dealing with tissue. In addition, we used the envelope SNR as a complement to the generalized spectrum when the latter failed at detecting coherent scattering, rather than as an alternative for the detection of specular reflectors. Our approach is based on the point-wise definition of the SNR by Wagner *et al.*,[29] in which the 1.91 value of SNR_V obtained under diffuse scattering conditions assumes sampling multiple realizations of the same scattering process. Thus, when performing a spatial sampling of the echo signal, the scattering process must have the same statistical properties throughout the sampling area (the PER). This is achieved only when the scattering process is stationary. This is why we restricted the use of SNR_V to the analysis of stationary signals and the use of the generalized spectrum to the analysis of non-stationary signals.

The Georgiou algorithm was based on the WOLD decomposition of the echo signals, which separated them into a predictable component (the coherent component) and a non-predictable component (the incoherent component).[147] The incoherent component was modeled as an autoregressive process. The detection of the coherent component, which was focused on resolved periodic scatterers, was done by using a maximum likelihood statistic to decide on the presence of line components in the power spectrum. Once separated, the echo amplitude of the incoherent component was used to test for the presence of pre-Rayleigh conditions by comparing the statistical properties of the incoherent component to the K-distribution. Some limitations of this algorithm can be attributed to the dependence of its performance on the model order chosen to model the incoherent component. In particular, Wear *et al.*[120] demonstrated that the order of autoregressive models of the incoherent component will affect the bias and variance of estimates of the effective scatterer size obtained from the frequency dependence of the backscatter coefficient. Furthermore, the classification performance of this algorithm will depend on how well the K-distribution models the echo statistics. In addition, the detection of the coherent component is performed with the echo spectrum which, as stated in Chapter 2, provides less detection power than spectral

correlation techniques such as the generalized spectrum. In contrast, the algorithm proposed here is not based on models of the echo signal and is, therefore, expected to provide a more robust classification. Further investigations will compare both algorithms to verify this hypothesis. Georgiou *et al*. developed further classification methods based on "wavelet analysis".[148,149] In these works the detection of the coherent component was focused on structures of the order or larger than the resolution cell. In this sense, the algorithm proposed here offers a more comprehensive analysis of the coherent component.

Donohue *et al.*[130] used the Kolmogorov-Smirnov test as a pre-classifier to test for the presence of Rayleigh statistics. The authors then applied the generalized spectrum to quantify coherent scattering in cases where the test was negative. As shown by our results, the generalized spectrum fails to detect coherent-scattering from periodic scattering with spacing smaller than c/f_H. These cases can result in Post-Rayleigh statistics that can also be negative to the Kolmogorov-Smirnov test. Thus, by first probing for non-stationary features and then for stationary, non-Rayleigh statistics, our approach is able to include these scenarios.

In summary, the algorithm proposed here has six important properties:

1. It is based on input parameters that have been optimized for the Decision stage.
2. It does not depend on segmentation stages performed by the user, making it a stand-alone method.
3. It does not assume an autoregressive model to the echo signal.
4. It does not assume a model to the probability density function of the echo amplitudes.
5. It automatically segments regions where the echo signals are consistent with a stationary random process and therefore suitable for the estimation of the attenuation coefficient and the backscatter coefficient.
6. It automatically decides on the best way to estimate the mean scatterer spacing depending on the properties of the echo signals.

In the next chapter, a preliminary application of this algorithm to echo data acquired *in vivo* from breast lesions of human subjects will be presented.

Appendix C. The adaptive trimming algorithm

The creation of parametric images as described in this work involves moving a finite size PER across the data frame. At each location of the PER, the parameter of interest is estimated and the value mapped to the center of the PER. When the PERs are overlapped, a structure in the data frame, such as a specular reflector, can be sensed by consecutive PERs and, therefore, affects the estimation of the parameter in each of them. This is illustrated in Fig. C.1, which shows a B-mode image of a homogeneous phantom containing random scatterers with a specular reflector spanning the full width of the data frame. Five PERs at different axial locations are shown. Note that due to their finite length, they would overlap axially if they had the same lateral location. The PERs at the extremes do not sense the specular reflector, while the three PERs at the center shown in yellow sense the specular reflector. As a result, the values of the parameters obtained from the three central PERs will be affected by the presence of the specular reflector. This will result in blurred values of the parameter. This is the reason why the parametric images based on the main lobe width of the collapsed average of the generalized spectrum from Phantom D in Chapter 4 (Fig. 4.24) showed large values in regions above and below the boundary between the homogeneous background and the array of nylon fibers.

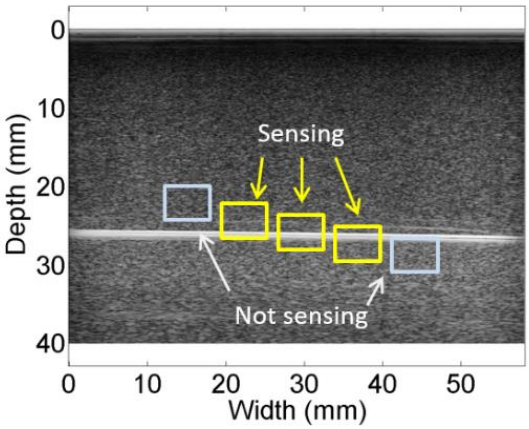

Figure C.1 Schematic showing the inclusion of the same specular reflector by a set of axially overlapped parameter estimation regions.

Here a method is developed to reduce this blurring artifact caused by the finite-sized PER. The rationale for the reduction of this effect is that it introduces bias to the estimate of the parameter that is expected for a particular point in space. This bias can result in reduced diagnostic value of the estimated parameter, particularly for small lesions that are comparable to the PER size. This method, referred here to as the adaptive trimming algorithm, will be implemented for the creation of parametric images based on parameters from incoherent scattering and coherent scattering. Its performance regarding the improvement of the registration and the reduction of bias caused by blurring will be compared to the conventional registration involving raster-scanned PERs.

C.1 The adaptive trimming algorithm

The main premise behind the design of this algorithm is that, when a large inhomogeneity exists in the scanned material, the only PER that should show the value of the parameter corresponding to that inhomogeneity is the one whose center is aligned with the inhomogeneity (the central PER in Fig. C.1). If a PER senses the inhomogeneity but is not centered with it (the lateral yellow PERs in Fig. C.1), then the estimated value of the parameter must come from the material properties spanning the largest area of the PER. This is illustrated in Fig. C.2, which shows a backscatter echo RF signal (blue) as well as its envelope (black). The echo signal comes from a PER that includes the boundary between the homogeneous background and the fiber plane from phantom D. The signal segment contained 350 axial samples. We would like to design a method that forces the estimation of the parameter to provide a value representative of the change in scattering properties only when the center of the PER (red vertical line) is aligned with the discontinuity (green vertical line). This is not the case in Fig. C.2 because the red and green lines do not coincide. Thus, in this case the value of the parameter must come from the section of the signal that has the same statistical properties over most of the signal length, i.e., the left part indicated by the purple double arrow. To achieve this, the algorithm will identify this part of the signal and use it for parameter estimation. The rest will be removed and discarded from the analysis within this particular

PER. Note that this algorithm exploits the fact that the parameters chosen in Chapters 2 and 3 were the most robust to reductions in the echo signal lengths.

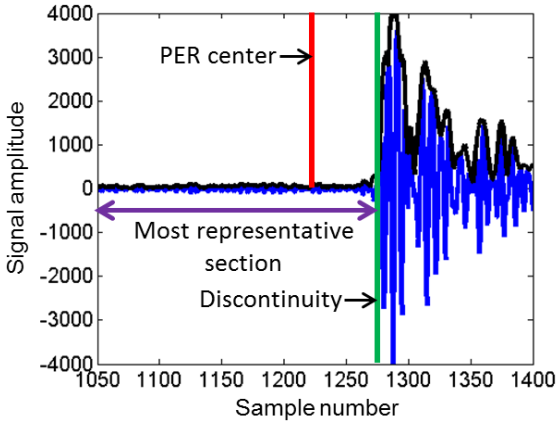

Figure C.2 Schematic showing the rationale behind the adaptive trimming algorithm.

The algorithm performs the following steps iteratively:

1. It obtains the envelope of each echo signal segment within the PER by means of the Hilbert transform.
2. It divides each envelope signal segment in two halves of equal length with respect to the center of the PER.
3. It computes the mean μ and standard deviation σ of the two halves: μ_1, σ_1, μ_2, σ_2.
4. It computes the mean symmetry M.S. and the variance symmetry V.S. as:

$$\text{M.S.} = \left|1 - \frac{\mu_1}{\mu_2}\right|, \ \text{V.S.} = \left|1 - \frac{\sigma_1^2}{\sigma_2^2}\right| \tag{C.1}$$

5. If both M.S. and V.S. are larger than a chosen symmetry index S.I., it proceeds to trim the signal segment as follows:
    a. If σ_2 is larger than σ_1, then removes the last element of the segment.
    b. If σ_1 is larger than σ_2, then removes the first element the segment.

6. Repeats steps 1 through 5 until both M.S. and V.S. are smaller than S.I. or until the segment length becomes equal to half its original length.

The flow chart in Fig. C.3 describes graphically this algorithm. Note that the smaller the symmetry index, the more restrictive the algorithm is regarding asymmetries in the mean and variance of both halves of the echo signal. In other words, the smaller the symmetry index, the more the signals are trimmed. It is important to note that after applying the algorithm to each signal segment within the PER, the resulting trim segments will have different lengths. When Fourier transforms are computed for the estimation of the various parameters required by the decision/classification algorithm developed in Chapter 4, the Chirp-Z transform can be used to obtain the spectrum values at the same frequency bins regardless of the segment length.[131]

When estimating parameters based on incoherent scattering using the reference phantom method, the power spectral density estimate from each signal segment needs to be normalized by the power spectral density from the reference obtained with the same segment length. Thus, the reference power spectral densities for all signal segment lengths ranging from the PER length down to half the PER length can be computed and stored beforehand. In the case of coherent-scattering based parameters, and in particular of the generalized spectrum, handling 2D matrices of complex numbers for each segment length for each echo signal within each PER severely slowed down the computation time and required significant amounts of memory. Since the reference generalized spectrum is not used to normalize the sample reference spectrum but rather for a statistical analysis, we used the full echo signal segment lengths for reference data processing.

Now we proceed to evaluate the performance of the adaptive trimming algorithm in the creation of parametric images using QUS parameters based on incoherent and coherent scattering and how it compares to the conventional PER raster scan. An analysis of the registration and bias of QUS parametric images from tissue mimicking phantoms for both types of parameters is presented.

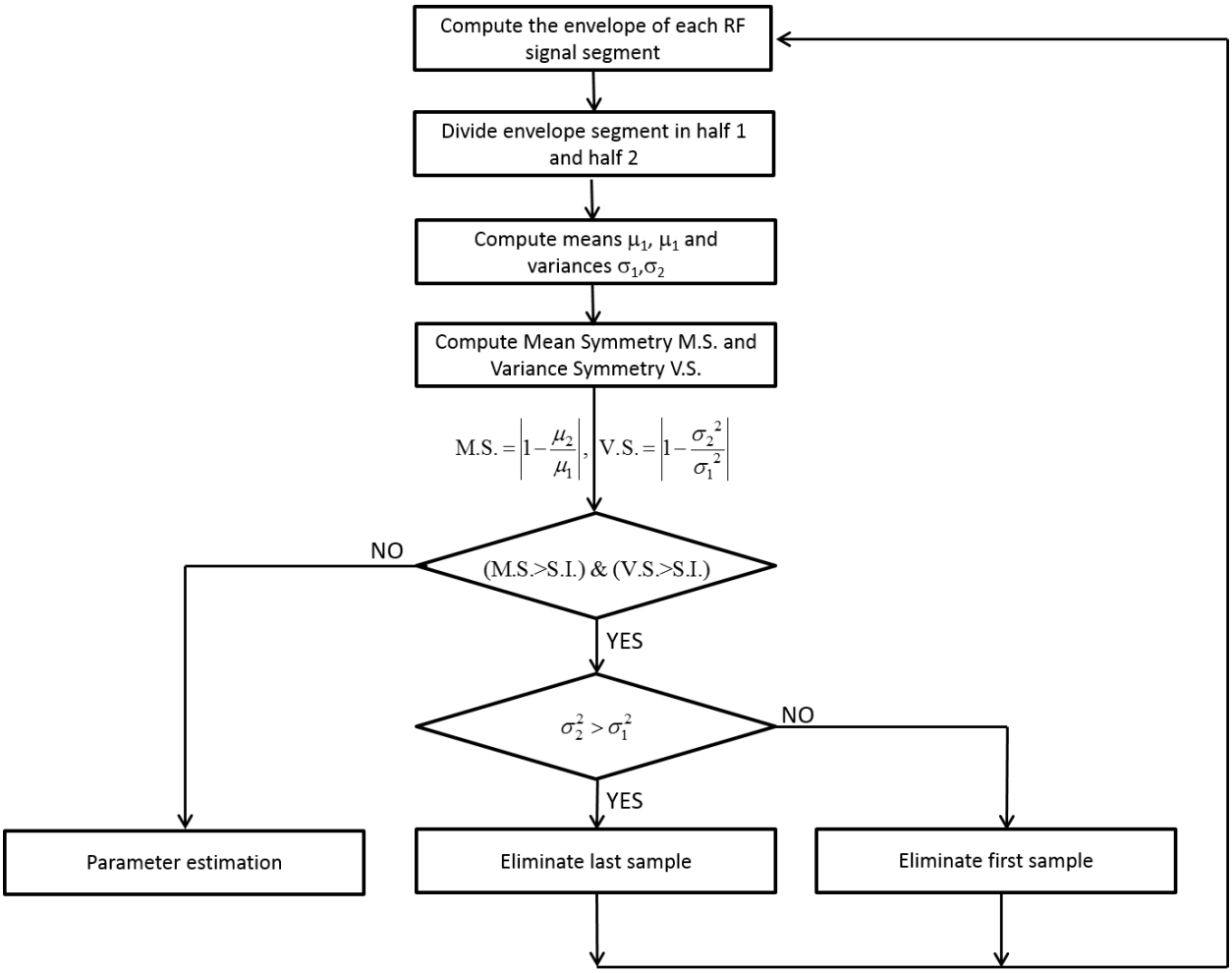

Figure C.3 Flow chart showing the different steps of the adaptive trimming algorithm.

C.2 Parameters based on incoherent scattering

In the first analysis we quantify the blurring effect caused by scanning a finite-size PER when creating parametric images, as well as how this effect is reduced wen using the adaptive trimming algorithm with different symmetry indices. The tissue mimicking phantom was phantom D described in Chapter 2. In this case, however, the scanned data frame did not include the array of fibers periodically arranged in the axial direction but only a section of the array of fibers periodically arranged in the elevational direction. As described in Chapter 2, at a depth of 26mm phantom D contains an array of nylon fiber of 0.1mm in diameter periodically spaced (0.4mm) in the plane perpendicular to the propagation of the acoustic pulse.

Because of the coarser resolution of the diffraction field in the elevational direction and the location of the elevational focus above the fiber plane, at least two of these fibers would have been included within the resolution cell, resulting in a highly reflective reflector compared to the axial array of fibers. The reference phantom was phantom C used in previous experiments. Its attenuation coefficient $\alpha_{ref}(f,z)$ is reported in Table 2.3, and its backscatter coefficient was measured using single-element transducer techniques.[150] Both phantoms where scanned with the Siemens S2000 system with a nominal excitation frequency of 10MHz. The transmit focus was located as close to the fiber as possible (30mm). One and ten frames were acquired from the sample and the reference respectively.

The parameter that was used to quantify the blurring effect was the average backscatter coefficient. The backscatter coefficient was computed using the reference phantom method.[40] For a PER at depth z and frequency f, the backscatter coefficient $\eta_{sample}(f,z)$ was estimated as:

$$\eta_{\text{sample}}(f,z)=\eta_{\text{ref}}(f,z)\frac{P_{\text{sample}}(f,z)}{P_{\text{ref}}(f,z)}\exp\left[4\int_0^z\left(\alpha_{\text{sample}}(f,z)-\alpha_{\text{ref}}(f,z)\right)dz\right] \tag{C.2}$$

where $\eta_{ref}(f,z)$ is the backscatter coefficient of the reference, $P_{sample}(f,z)$ and $P_{ref}(f,z)$ are the power spectral densities of the sample and the reference, and $\alpha_{sample}(f,z)$ and $\alpha_{ref}(f,z)$ are the attenuation coefficients from the sample and reference. The average backscatter coefficient ABSC was computed by integrating $\eta_{sample}(f,z)$ expressed in decibels with respect to 10^{-4} cm^{-1} sr^{-1} :

$$\text{ABSC}(z)=\frac{1}{f_L-f_H}\int_{fL}^{f_H}10\log10\left(\frac{\eta_{\text{sample}}(f,z)}{10^{-4}\text{cm}^{-1}\text{sr}^{-1}}\right)df \tag{C.3}$$

where f_L and f_H are the lowest and highest ends of the useful bandwidth of the transducer (+10dB above noise floor, 5-11MHz for this experiment. $P_{sample}(f,z)$ was estimated using the multitaper estimator with a time-half bandwidth product NW=4 (7 tapers) within a PER size of 4mm × 4mm. To create images of the average backscatter coefficient, the PERs were scanned over the sample data frame with an overlap of 85% laterally and 85% axially.

The exponential factor in Eq. (C.3) compensates for the two way trip attenuation of the pulse and its echo from and towards the transducer. For this purpose, it is necessary to estimate the attenuation coefficient of the background material of the sample. To achieve this, a frame of RF echo data from the background material without the nylon fibers was obtained. The attenuation coefficient was estimated using the spectral slope algorithm. This algorithm requires the application of a least-squares linear fit to the logarithm of the ratio of the power spectral densities of the sample and the reference as a function of depth at each frequency bin. The attenuation coefficient of the sample at each frequency bin is obtained from the slope of the linear fit. This is described in detail by Rosado-Mendez *et al*.[24] Figure C.4 shows the estimated attenuation coefficient of the sample as well as a least-squares polynomial fit used for attenuation compensation in Eq. (C.3).

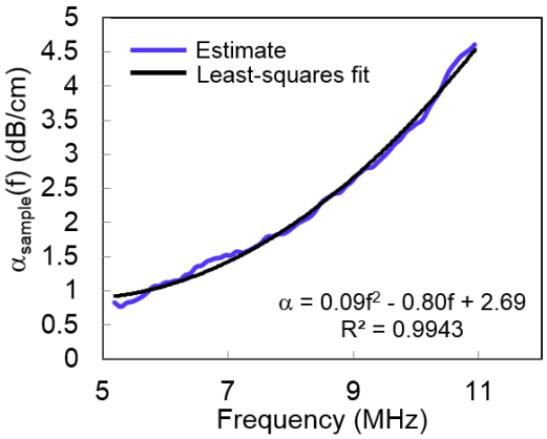

Figure C.4 Reference phantom estimate of the attenuation coefficient of the background material of the phantom.

Figure C.5 shows the B-mode image of the sample data frame in (a), as well as ABSC parametric images combined with the B-mode image using conventional registration in (b) and the adaptive trimming algorithm with symmetry index 1.0 in (c) and 0.2 in (d). Notice that in the background surrounding the nylon fibers, the ABSC values are relatively constant. This verifies the correct attenuation compensation. About the fibers, the ABSC increases. The area of increased ABSC spans about 4mm in depth with the

conventional registration. As shown in Figs. C.5(c) and (d), the use of the adaptive trimming algorithm reduces this blurring effect as the symmetry index is reduced.

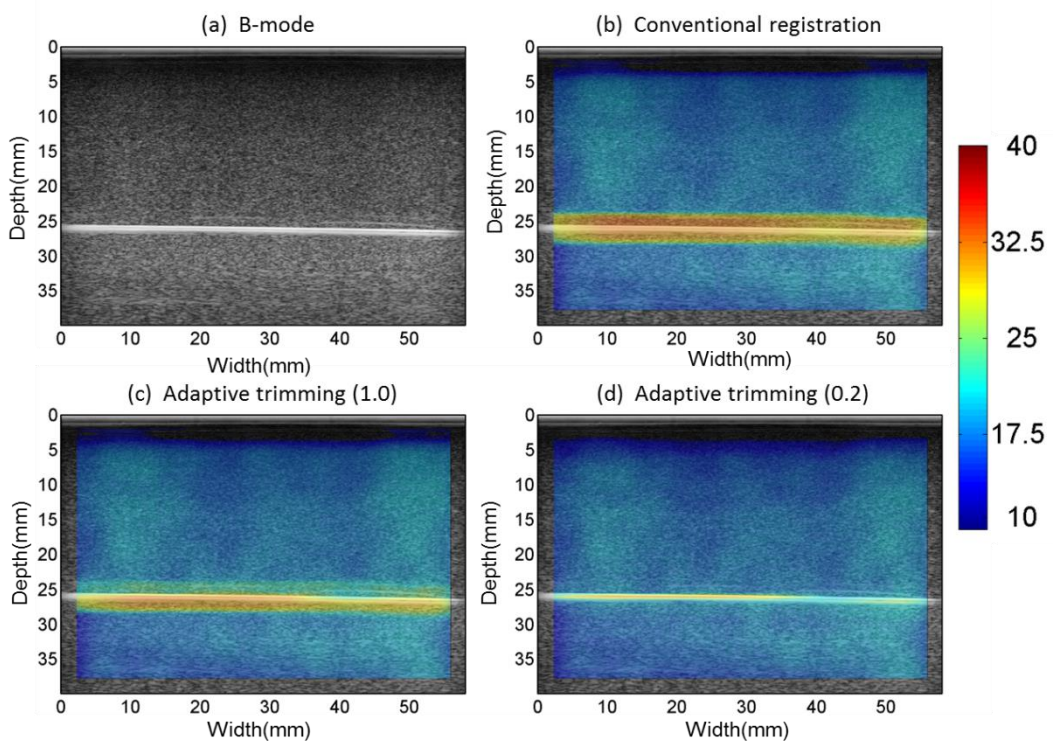

Figure C.5 (a) B-mode image and parametric images of the average backscatter coefficient expressed in dB with respect to 10^{-4} cm^{-1} sr^{-1}. (b) Conventional registration. (c) Adaptive trimming with symmetry index 1.0, (d) Adaptive trimming with symmetry index 0.2.

To quantify this effect, the ABSC parametric images were averaged laterally to obtain an axial profile of the average ABSC values. These are shown in Fig. C.6, which shows the lateral ABSC average from Figs. C.5(b) and C.5(d), i.e., the parametric images resulting from conventional registration (blue) and from the use of the adaptive trimming with a symmetry index of 0.2 (red). The vertical dashed line indicates the location of the nylon fiber as measured in the B mode image. As observed, the width of the peak corresponding to the fiber is wider when using conventional registration compared to the use of the adaptive trimming. Furthermore, the maximum ABSC value does not occur at the expected location. The adaptive trimming algorithm is able to reduce these effects by reducing the width of the peak as well as

correctly placing the maximum at the expected location. For the ABSC parameter, this comes at the expense of reducing its dynamic range, i.e., the difference between the maximum value at the nylon fiber location and the base value in the background.

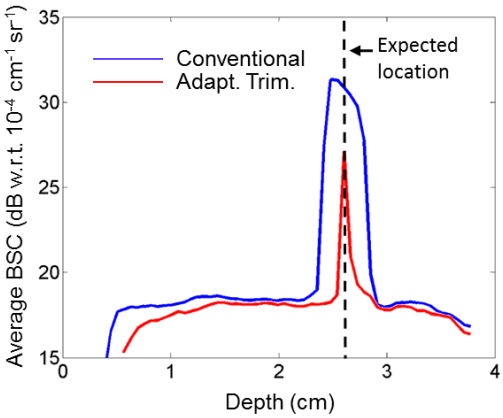

Figure C.6 Lateral profiles of the Average Backscatter Coefficient obtained by averaging laterally the parametric images in Figs. 6(b) and 6(d). Blue: conventional registration, red: adaptive trimming with symmetry index equal to 0.2. The vertical black dashed line shows the location of the nylon fiber.

Figure C.7(a) analyzes the reduction of the peak width as well as the location of the maximum value as a function of the symmetry index. The peak width is measured as the full-width at half maximum (FWHM) in units of millimeters. The blue curve shows the FWHM value obtained with the conventional registration. Note that it is close to 4mm, the PER length. The FWHM decreases as the symmetry index is reduced down to 0.2. Further reductions of the symmetry index (or more sever trimming) do not result in further reduction of the blurring effect. Also the location of the maximum ABSC is shown by the labels in the figure. When the symmetry index is equal or smaller than 0.5, the maximum occurs at the expected location of 26mm. Figure C.7(b) shows the loss of the dynamic range of the ABSC as a function of the symmetry index. As in C.7(a), the blue curve shows the dynamic range for the conventional registration (13dB). The dynamic range is reduced down to 9dB when the symmetry is reduced down to 0.2. Further reductions do not further reduce the dynamic range. Thus, for this parameter, the best possible results can be achieved with a symmetry index of 0.2.

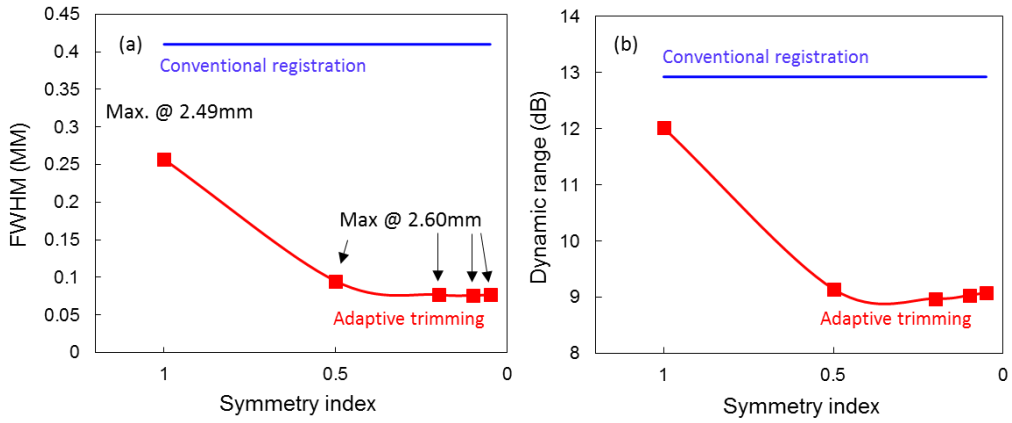

Figure C.7 (a) Full width at half maximum (FWHM) and (b) dynamic range (maximum minus base level) of the average backscatter coefficient peak occurring because of the presence of the nylon fiber as a function of the symmetry index. Blue: conventional registration, red: adaptive trimming.

Although the ABSC parameter of the specular reflector is useful to investigate the registration and the blurring effects caused by the conventional registration as well as their improvement by the adaptive trimming algorithm, it does not offer a direct analysis of the bias that the effective shortening of the scan lines segments might introduce when using the adaptive trimming. To look at this problem, the bias in the backscatter coefficient at the boundary between two regions with different scattering properties was investigated. For this purpose, a tissue mimicking phantom composed of two layers with different scattering properties was analyzed. The phantom was designed to have constant attenuation over its two layers, but higher backscatter (+6dB) in the bottom layer compared to the top one. The phantom was a rectangular cuboid made of gelatin with ultra-filtered milk added to control the attenuation as well as glass microspheres (Spheriglass ® 3000E, Potters Industries, Alley Forge, Pennsylvania) acting as scattering agents. The attenuation and backscatter coefficients were measured using single-element transducer techniques on test samples of the phantom materials, as described in detail elsewhere.[48] Fig C.8(a) shows the schematic of the phantom composition. The phantom was scanned with the Siemens S2000 system and the 18L6 transducer operated at a nominal center frequency of 10MHz. Reference data was obtained by scanning the top layer of the phantom from its lateral face, as indicated in Fig. C.8(b).

Ten sample frames and fourteen reference frames were obtained for the purpose of estimating the backscatter coefficient using the reference phantom method described above. A B-mode image of one of the sample data frames is shown in Fig. C.8(b).

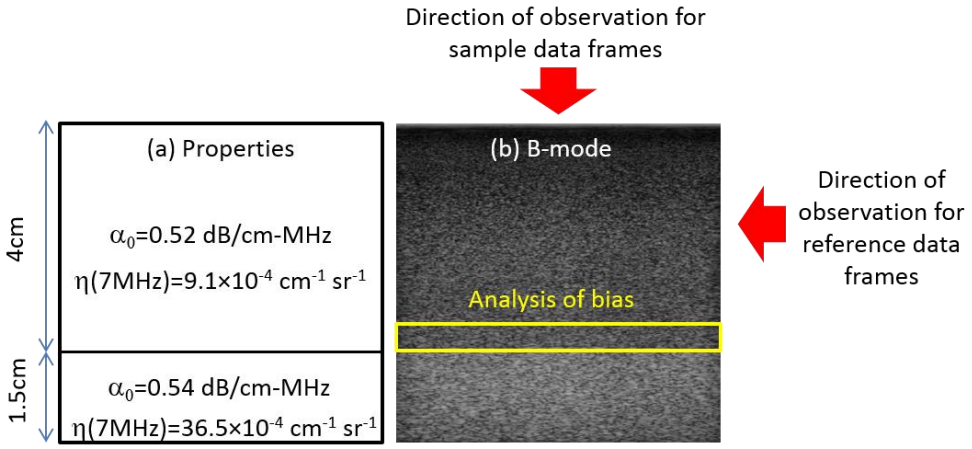

Figure C.8 (a) Schematic and (b) B-mode image of the layered phantom. The schematic shows values of the slope of the attenuation coefficient vs. frequency α_0 and the backscatter coefficient η at 7MHz measured through laboratory characterization.

Figure C.9 shows the statistics of the backscatter coefficient as a function of frequency over the region within the yellow box in Fig. C.8(b) and over the 10 sample frames: the average in blue, and the average plus and minus one standard deviation at each frequency bin in red. The black curve is the backscatter coefficient of the top layer measured with single-element transducer techniques, and is considered to be the gold standard. In the case of conventional registration in Fig. C.9(a), the backscattered coefficient is over-estimated as a result of the inclusion of part of the high scattering layer within the PERs. This bias is successfully reduced by using the adaptive trimming algorithm with a symmetry index of 0.2

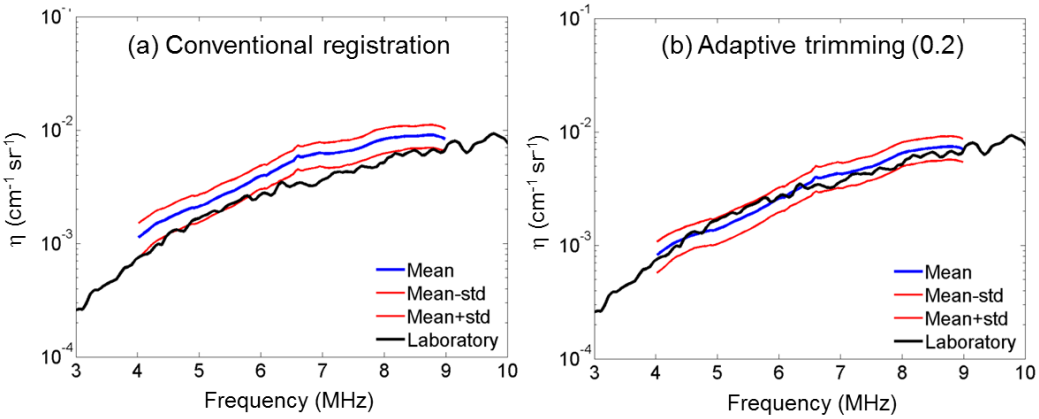

Figure C.9 Statistics of the estimates of the backscatter coefficient obtained using the reference phantom method within the yellow box in Fig. C.8. Estimates were registered in space using (a) the conventional registration or (b) the adaptive trimming algorithm. Blue: average, red: average ± one standard deviation, black: laboratory measure.

C.3 Parameters based on coherent scattering

Now we focus on the performance of the adaptive trimming algorithm when using the analysis of coherent scattering described in Chapter 4. The analysis is an extension of the phantom experiment presented in Section 4.5, which presented parametric images of the axial periodic array of nylon fibers in phantom D. Two types of parametric images are presented, one based on the mean scatterer spacing, and one based on the main lobe width of the collapsed average of the generalized spectrum, which is an indirect measure of the reflectivity of a specular reflector, as explain in Chapter 4.

First we analyze how the detection of specular reflectors at the boundary between the homogeneous background and the array of fibers is affected by the use of the adaptive trimming algorithm. Figure C.10 shows (a) a B-mode image of phantom D and overlaid parametric images of the CAGS main lobe width with (b) the conventional registration, and the adaptive trimming algorithm with symmetry index (c) 1.0 and (d) 0.2. Note that in Fig. C.10(b) the increase in the main lobe width starts at about 2mm above the location of the boundary between the zone of incoherent scattering and the zone with coherent scattering. As the symmetry index is reduced (and the trimming is more severe), the values above the boundary as

well as below the boundary are reduced. The maximum values occur right at the boundary in Fig. C.10(d).

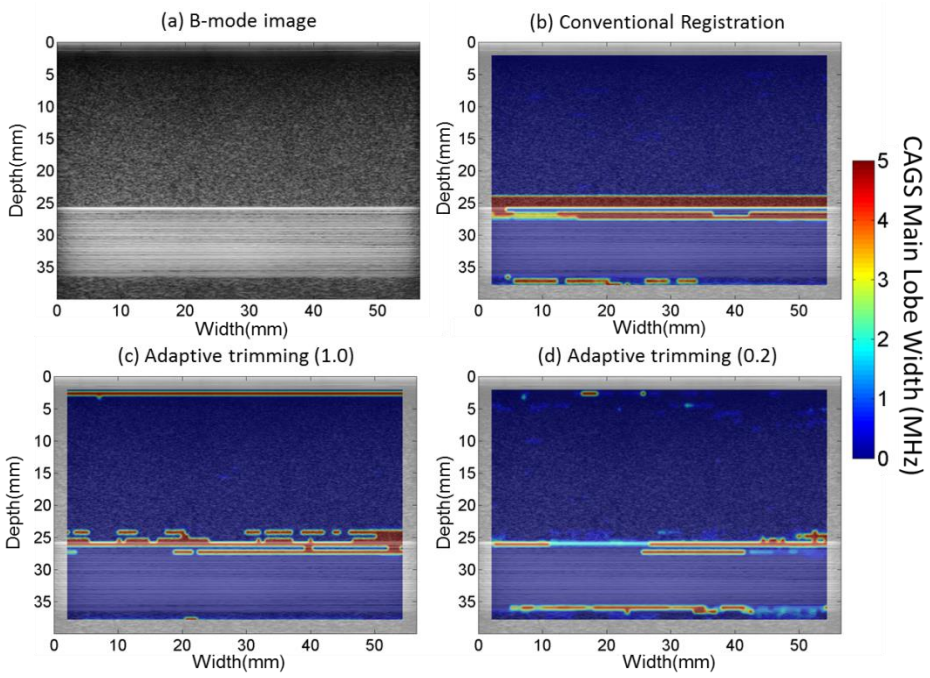

Figure C.10 (a) B-mode image and parametric images of the main lobe width of the collapsed average of the generalized spectrum from phantom D. (b) Conventional registration. (c) Adaptive trimming with symmetry index 1.0, (d) Adaptive trimming with symmetry index 0.2.

To express these effects quantitatively, Figs. C.11(a) and (b) show the average of the CAGS main lobe width within the regions above and below the boundary demarcated by the yellow and red boxes in the B-mode image of the phantom as a function of the symmetry index of the adaptive trimming algorithm. Figure C.11(a) shows the average value for the region above the boundary that is enclosed in a yellow box. Fig. C.11(b) shows the average value for the region below the boundary that is enclosed in a red box. In each curve, the red curve corresponds to the use of the adaptive trimming algorithm, while the blue line is the value obtained from the conventional registration. As observed, the use of the adaptive trimming algorithm reduces the influence of specular reflectors above and below the boundary. The effect is more accentuated as the symmetry index decreases, with no significant gain below 0.1.

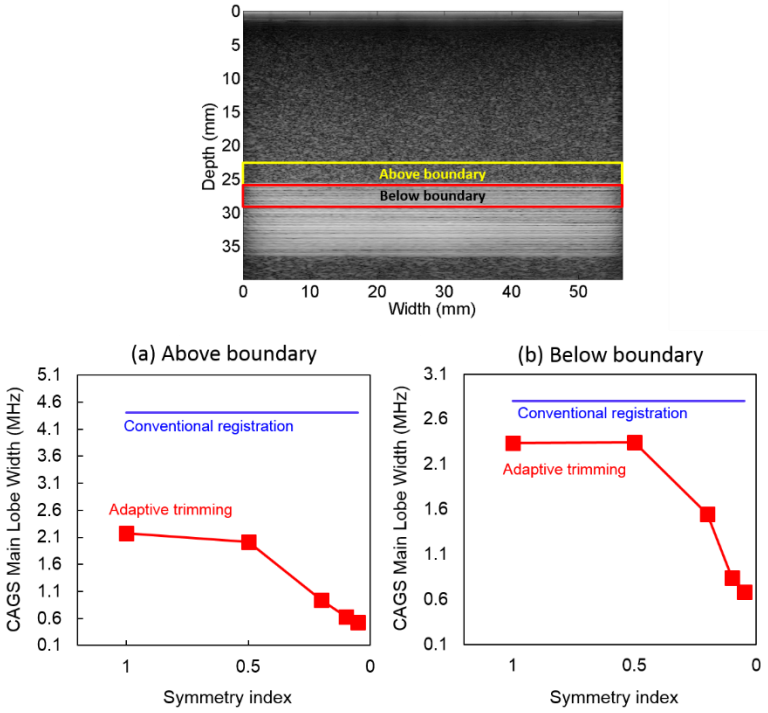

Figure C.11 Average values of the CAGS main lobe width in the regions (a) above and (b) below the boundary between the homogeneous background with random scatterers and the array of fibers in phantom D as a function of the symmetry index of the adaptive trimming algorithm. Blue: value obtained using conventional registration, Red: Values obtained using the adaptive trimming algorithm.

In order to analyze how well the values of the CAGS main lobe width are registered, Figure C.12 shows the lateral average of the values from the parametric images in Figs. C.10(b) and C.10(d) as a function of the axial location or depth. The blue curve corresponds to the use of the conventional registration, while the red curve corresponds to the use of the adaptive trimming algorithm with a symmetry index of 0.1. The vertical dashed lines indicate the upper and lower boundaries of the array of fibers. Note that the adaptive trimming algorithm correctly registers the CAGS main lobe width values compared to the conventional registration.

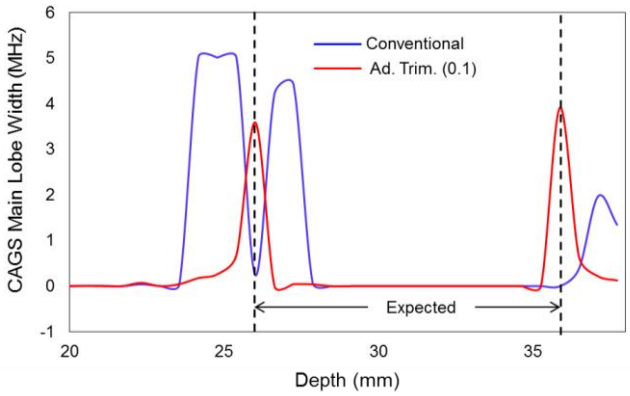

Figure C.12 Lateral profiles of the CAGS main lobe width from parametric images shown in Figs. C.10(b) and C.10(d) obtained by averaging laterally the estimated values. Blue: conventional registration, red: adaptive trimming with symmetry index 0.1. The two vertical dashed lines indicate the upper and lower boundaries of the fiber array.

We now look at the effects of using the adaptive trimming algorithm on parametric images of the mean scatterer size. Figure C.13 shows (a) the B-mode image of phantom D as well as combined images of the mean scatterer spacing obtained with (b) conventional registration and with the adaptive trimming algorithm with symmetry index (c) 1.0 and (d) 0.2. Note that Fig. C.13(b) is the same as Fig. 4.26. The main effect of the use of the adaptive trimming algorithm is the reduction of the large MSS values obtained at the boundary. Regions of the parametric images in which the expected spacing was estimated are not altered by the use of the adaptive trimming algorithm.

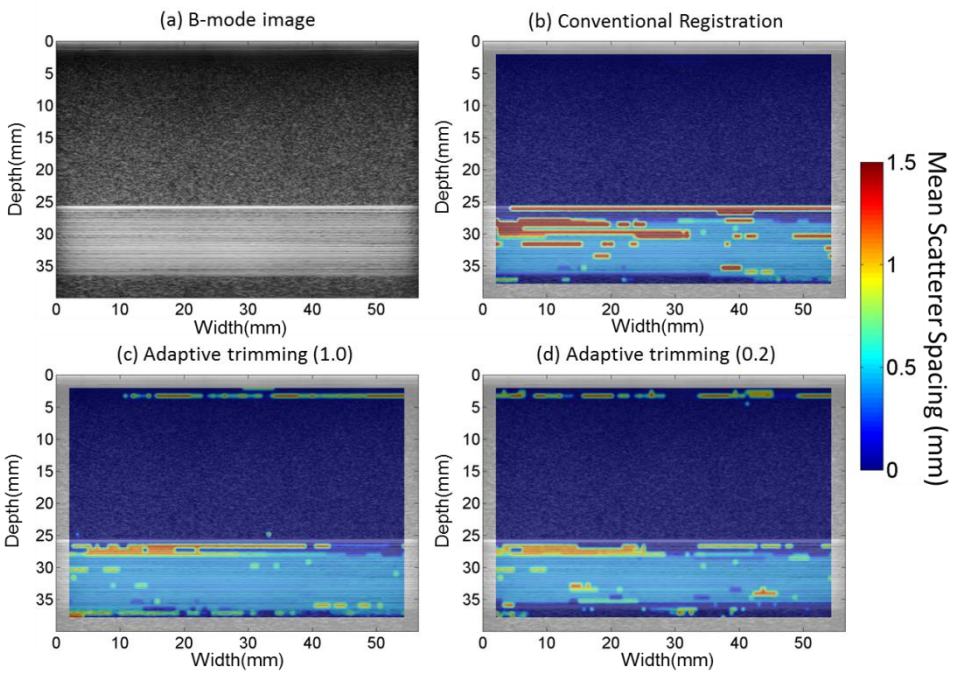

Figure C.13 (a) B-mode image and parametric images of the mean scatterer spacing from phantom D. (b) Conventional registration. (c) Adaptive trimming with symmetry index 1.0, (d) Adaptive trimming with symmetry index 0.2.

Figure C.14 illustrates the registration and accuracy improvements achieved with the adaptive trimming algorithm in terms of the mean scatterer spacing. It shows the lateral average of the parametric images shown in Fig. C.13(b) and 13(d) as a function of the axial location or depth. The blue curve corresponds to the use of the conventional registration, while the red curve corresponds to the use of the adaptive trimming with a symmetry index of 0.1. The black dashed curve shows the expected values of the mean scatterer spacing, which is 0 in the homogenous background and 0.4mm in the region of the fibers. Note that the red curve follows the expected values closer than the blue curve. Thus, the adaptive trimming algorithm reduces the bias and improves the registration of parametric images of the mean scatterer spacing.

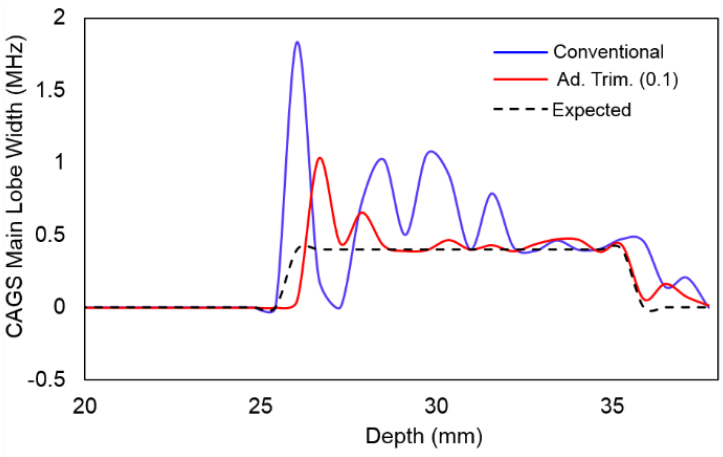

Figure C.14 Lateral profiles of the mean scatterer spacing from parametric images shown in Figs. 12(b) and 12(d) obtained by averaging laterally the estimated values. Blue: conventional registration, red: adaptive trimming with symmetry index 0.1. The black dashed curve indicates the expected spacing value.

Finally, Fig. C.15 shows the combined classification images where zones in blue are zones of diffuse scattering, zones in red were classified as containing periodic scatterers, and zones in green were classified as zones of low scatterer density. In Fig. C.15(a) the conventional registration was used, while in Fig. C.15(b) the adaptive trimming algorithm was used with symmetry index of 0.1. Fig. C.15(a) was presented in Fig. 4.26. Note that the use of the adaptive trimming algorithm results in a larger area of the homogeneous background being classified as diffuse scattering. Some of the zones classified as having low scatterer number density with the conventional registration might have originated from the zones classified as having a specular reflector using the adaptive trimming algorithm. Similarly, zones that were initially classified as having specular reflectors at the boundary between the homogeneous background and the fiber array are now classified as having low scatterer density. This suggests that the algorithm has low specificity between these two classes.

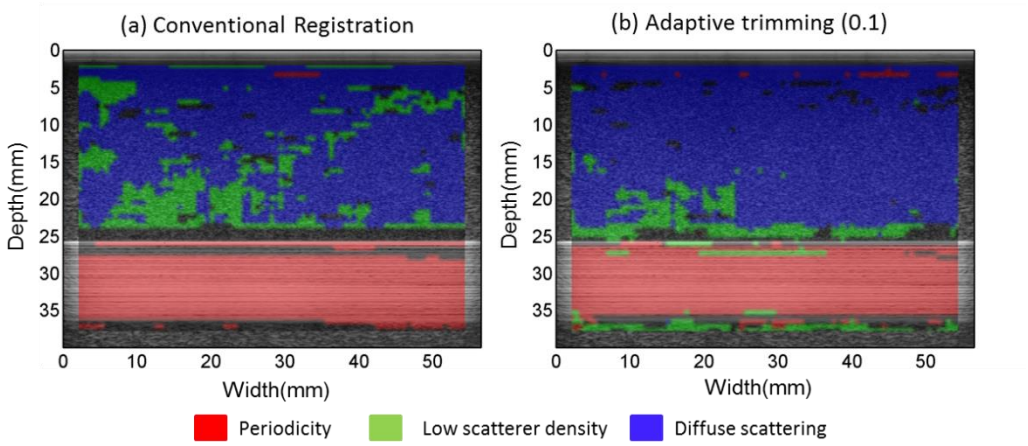

Figure C.15 Zones in a single data frame of Phantom D classified as diffuse scattering (blue), low scatterer density (green) and scatterer periodicity (red). (a) Conventional registration. (b) Adaptive trimming algorithm with symmetry index 0.1.

In summary, this chapter has presented a method to reduce the blurring effect caused by the raster scanned of a finite-size PER to create parametric images. This algorithm is based on iteratively trim each of the scan line segments within the PER to leave out of the analysis boundaries between regions with different statistical properties. This algorithm was shown to provide improvements in the registration and accuracy of parametric images based on parameters from incoherent scattering and coherent scattering. An important result regarding the analysis of parametric images based on coherent scattering parameters is that the effective reduction of the signal segment did not introduce bias in the parametric images. This method will be particularly useful when analyzing data planes containing lesions which are only slightly larger than the PER size. In those cases, the severe blurring introduced by the use of the conventional registration would severely bias the values of the estimated parameters.

5. Preliminary *in vivo* application of the coherent-scattering classification algorithm to breast masses

5.1 Aim

The final part of this dissertation is a preliminary application of the parameters studied in Chapters 2 and 3 and the algorithm developed in Chapter 4 for the analysis of breast masses. The aim of this seminal application is to investigate if the categories resulting from the classification algorithm can be used as a tool to distinguish between breast lesion types. This aim can be divided into two objectives:

- To investigate if the portion of a lesion presenting diffuse scattering statistics can be used as a diagnostic parameter to distinguish between the most typical solid benign lesions (fibroadenomas) and typical malignant lesions (invasive ductal carcinoma).
- To explore if this parameter can provide information about the anisotropy of the scattering process when performing steered-beam scanning of breast lesions.

5.2 Methods

5.2.1 Subject selection and data acquisition

Our laboratory is currently performing a data collection of backscattered echo signals following a protocol that has been UW HSC-IRB approved and is HIPPA compliant. Patients that have been scheduled for breast core biopsy (ACR BIRADS 3-5) are invited to enroll. The patients that agree to participate visit our scan laboratory the day of their biopsy. Patients are scanned in the supine position with a Siemens Acuson S2000 System (Siemens Medical Solutions USA, Inc., Malvern, PA) using an 18L6, high frequency linear array transducer operated at 15MHz. The Axius Direct Ultrasound Research Interface[86] available on the system allows the acquisition of unprocessed, post-beamformed radiofrequency echo data. The analysis presented in this chapter is restricted to two different lesion types:

fibroadenomas and invasive ductal carcinomas. Fibroadenomas are the most common benign solid breast tumor. Their incidence in asymptomatic women is about 25% and peaks between the ages of 15 and 35.[151] Invasive ductal carcinoma is the most common malignant breast lesion (80%).[152,153] The analysis described in this section includes the largest five fibroadenomas and five invasive ductal carcinomas included in the protocol.

Each mass is scanned in two planes: a radial plane (with the transducer scanning aperture parallel to a projected line from the center of the mass to the nipple) and an anti-radial plane (perpendicular to the radial). This is illustrated in the schematic in Fig. 5.1(a). At each plane, nine RF echo signal frames are obtained. In order to analyze any anisotropy of the quantified parameters, each one of these frames is acquired by steering the acoustic beam with an angle ranging from -20^{o} to $+20^{o}$ in increments of 5^{o}. Figure 5.1(b) shows a conceptual vision of the structure of the breast as viewed in the ultrasound image. Five layers can usually be distinguished as moving away from the transducer surface: subcutaneous fat, anterior fascia, fibroglandular tissue, posterior fascia, and pectoral muscle. This figure is just a simplified illustration, and the thickness of each layer does not represent population averages. In this example, a mass centered at the fibroglandular tissue layer protrudes through the fascia into the fat and muscle layers. Note that benign solid breast tumors only distort these layers while cancers tend to invade and grow through these layer boundaries. The black dashed line indicates the axis perpendicular to the transducer aperture. The blue lines demarcate the steered scanning geometry where the acoustic beam angle is indicated by the opening between the axis and the blue dashed line.

After scanning the mass, a reference phantom is scanned. The reference phantom was a homogeneous emulsion of gel with 70% safflower oil. The scattering agents were randomly distributed glass beads (3-45μm) with a concentration of 236 beads/mm^3. The scanning window consisted of a 25μm-thick Saran™ wrap (Dow Chemical, Midland, MI, USA). The sound speed (1502m/s at 2.5MHz)[18] and attenuation coefficients were measured with a substitution technique. A power law fit was applied to $\alpha(f)$,[101] the

measured attenuation at 2.5MHz, 5MHz, 7.5MHz and 10MHz and was $\alpha(f)=0.256f^{1.366}$, where f is the frequency in MHz.

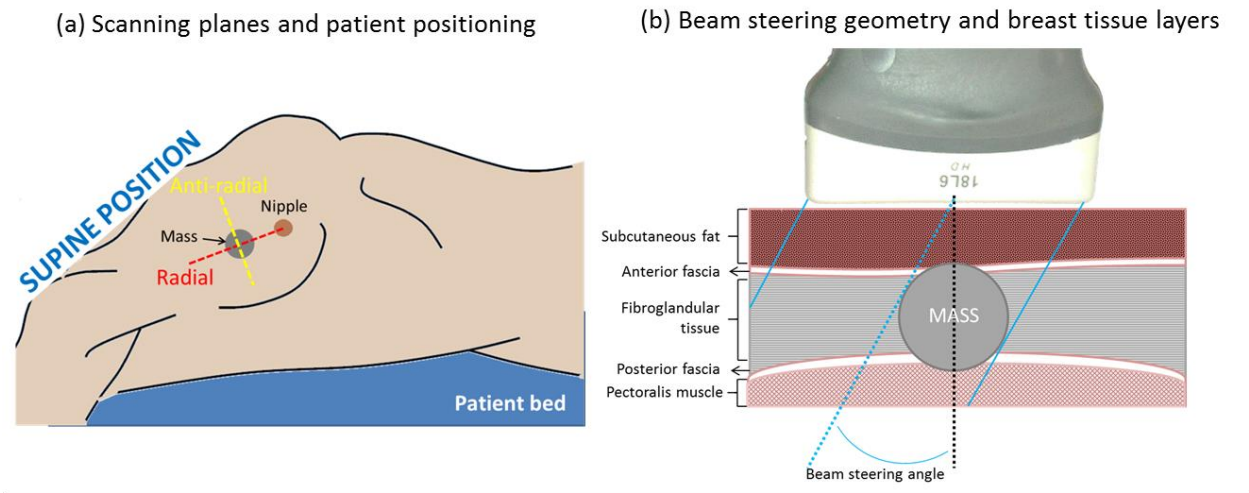

Figure 5.1 (a) Patient scanning geometry, indicating the anti-radial and the radial scanning planes. (b) Breast tissue layer distribution and beam steering geometry. Figure (a) was modified from Ref. 154.

The reference phantom data was acquired with exactly the same system settings as the corresponding mass. Five to seven independent data frames at each beam steered angle were acquired by moving the transducer in the elevational direction by at least the thickness of the transducer between frames. As shown in Chapters 2 and 3, at a concentration of 236 beads/mm^3, the reference provides conditions of diffuse scattering.

5.2.2 Data analysis

The data bank for each subject consisted of a total of 18 sample data frames: two planes, each one with nine beam-steering views. In addition, each sample data frame was accompanied with its corresponding reference data set. A diagram showing the flow logic for each subject is shown in Fig. 5.2. Each data frame was analyzed individually, and parametric and classification images (described below) were generated for each frame. Lesion-fitted regions of interest were selected from the B-mode image of each frame following the delineation made by the sonographer during data acquisition. An analysis of the first

order statistics of the values of the parameters within the lesion fitted ROI was then performed. The values were compared among different steered angles to identify possible anisotropy.

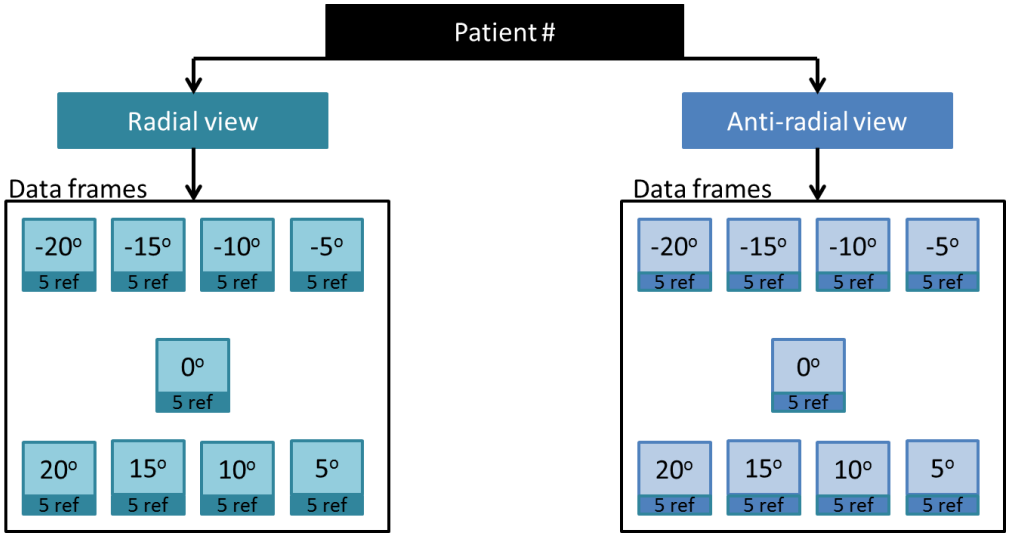

Figure 5.2 Diagram describing the organization of the data bank available for each subject.

Each of the sample frames was processed as follows: a 4mm×4mm parameter estimation region (PER) was scanned trough the data frame with 90% axial and lateral overlap between consecutive PERs. At each PER location, the following metrics where computed:

1. Collapsed average of the generalized spectrum (CAGS), computed with the adaptive multitaper estimator using a time-half bandwidth product *NW*=6, and a total of 11 tapers.
2. Echo amplitude signal-to-noise ratio (SNR_V), where the envelope was computed using the absolute value of the analytic radiofrequency echo signals.
3. Echo phase χ^2 spectrum, where the χ^2 measure of the phase uniformity (described in Chapter 4) was estimated for a range of demodulation frequencies.

The same metrics were estimated in each of the reference frames corresponding to each sample frame. However, the PERs in the reference frames were not overlapped in the lateral direction to have independent estimates of the metrics for the statistical analysis based on the cumulative distribution of the parameters derived from these metrics. The analysis of the CAGS and the χ^2 spectrum was restricted to

the same frequency range. This range was determined by selecting the bandwidth above the noise floor of the power spectral density at the bottom of each lesion included in the analysis. The mean of the low and high frequency limits of this bandwidth among the considered cases were 3.0MHz and 9.2MHz, respectively. These three metrics were used to perform the test of statistical significance for non-stationary features, departure from Rayleigh statistics, and phase non-uniformity described in Chapter 4.

After performing the test of the statistical significance of the parameters, two types of images were created: parametric images and classification images. The parametric images were based on "excess-parameters". The excess parameters are the difference between the values of the parameters used in the test of statistical significance of coherence scattering and the mean value of the parameter measured in the reference phantom. Four excess-parameter images were created:

1. Excess MaxCAGS: Parametric image showing the difference between the maximum value of the sample CAGS and the average value of the reference CAGS. This image depicts the strength of coherent scattering causing non-stationary features in the echo signals.
2. Excess CAGS main lobe width: Parametric image showing the difference between the CAGS main lobe width and the main lobe width of the reference CAGS. This image displays the relative strength of the signal contribution due to specular reflectors.
3. Excess SNR_V: Parametric image showing the difference between the sample SNR and the mean reference SNR. This image displays strength of coherent scattering causing stationary features in the echo signal.
4. Excess Max-χ^2: Parametric image showing the difference between the maximum value of the χ^2 spectrum and the average value of the reference χ^2 spectrum. This image depicts the regions where the phase was severely non-uniform.

Four types of classification images were created:

1. Generalized-spectrum based classification: This image shows regions classified as containing specular reflectors, non-stationary features associated to periodicity, or stationary features.

2. Echo-amplitude statistics based classification: This image shows regions classified as stationary and either containing pre-Rayleigh, post-Rayleigh or Rayleigh statistics.
3. Phase uniformity classification: This image shows regions classified as having either uniform or non-uniform phase based on the χ^2 spectrum.
4. Diffuse scattering images: This image shows regions classified as containing diffuse scattering conditions.

5.2.3 Lesion fitted - ROI Analysis

After creating the parametric images, a region of interest fitted to the shape of the lesion observed in the B-mode image was selected in each of the RF data frames acquired using different acoustic beam angles and in both anti-radial and radial planes. The selection of these ROIs was done based on fiducial marks placed by the sonographer at the lesion boundary in the B-mode image at the moment of scanning. An example of the selection of these ROIs is shown in Fig. 5.3, which presents a set of B-mode and parametric images of an invasive ductal carcinoma (FA-5 in Table 5.1). This figure is described in greater detail below. The lesion-fitted ROI was used to estimate the size of each lesion in each view and each acquisition angle. The lesion size is expressed as an area as well as an "equivalent diameter" corresponding to the diameter of a circle having the same area as the lesion. This metric is provided as a more direct guide to compare the dimensions of the lesion with the width and length of the parameter estimation regions. The equivalent diameter for the five fibroadenomas (FA) and the five invasive ductal carcinomas (IDC) is shown in Table 5.1 for each scanning plane and each beam-steering angle.

After the selection of the lesion-fitted ROI, parameter estimation regions, or PERs were selected within it. Two analyses were performed depending on the nature of the parametric image:

- **"Excess-parameter" parametric images:** The values of the excess parameters from the PERs within the lesion-fitted ROI were used to create box plots of the values of the excess parameters

as a function of the beam steering angle. The information shown in each of the boxes is the following:

Table 5.1 Equivalent diameter of the five fibroadenomas (FA) and the five invasive ductal carcinomas (IDC) for each beam steering angle and both the anti-radial and radial planes.

View	Beam steering angle (degrees)	Equivalent Diameter (mm)									
		FA 1	FA 2	FA 3	FA 4	FA 5	IDC 1	IDC 2	IDC 3	IDC 4	IDC 5
Anti-Radial	-20	9.0	16.5	19.5	17.0	16.6	13.6	17.6	19.0	7.1	10.5
	-15	9.3	15.4	19.5	16.8	17.2	14.8	17.5	19.7	7.2	10.9
	-10	9.0	15.2	19.7	17.2	17.8	15.0	17.5	18.9	6.9	11.4
	-5	9.2	15.8	19.7	16.6	18.1	14.6	17.4	20.2	6.7	11.7
	0	9.2	15.3	19.4	16.8	16.8	15.3	17.7	19.4	7.0	11.5
	5	9.4	16.0	19.2	16.9	16.9	15.4	17.5	19.8	7.3	11.6
	10	9.4	14.7	18.7	16.7	16.7	15.0	17.5	19.0	7.2	11.4
	15	9.4	13.8	18.7	16.8	17.0	17.7	17.5	19.1	7.2	11.0
	20	9.1	13.5	19.5	17.0	16.5	16.0	17.7	19.1	7.3	11.6
Radial	-20	8.5	16.4	22.4	17.9	16.9	17.3	16.3	16.7	7.6	6.9
	-15	8.5	16.6	23.5	18.0	18.5	18.3	15.4	18.0	7.9	7.0
	-10	8.9	16.9	22.4	18.3	17.6	19.0	15.6	16.8	8.0	6.9
	-5	8.8	17.9	21.8	18.2	18.0	18.2	15.8	17.7	7.9	7.2
	0	8.2	16.6	22.6	18.1	18.3	18.6	15.3	18.0	7.9	7.3
	5	8.5	16.7	22.5	18.1	18.8	18.3	13.8	17.8	8.0	6.9
	10	8.5	16.6	22.7	17.8	19.1	18.5	14.0	15.7	7.9	7.0
	15	8.8	16.8	20.8	18.2	18.6	18.3	13.3	14.8	7.9	6.9
	20	8.8	17.5	20.8	17.6	18.8	18.2	12.6	15.0	7.6	6.7

- A red line within the box indicates the median of the values of the excess parameters within the lesion-fitted ROI
- The upper and lower limits of the box indicate the 25 and 75 percentiles of the values of the parameters within the lesion-fitted ROI.
- The whiskers indicate the largest and smallest data points not considered as outliers.
- Red crosses beyond the whiskers are outliers. Upper outliers were those whose values were larger than the 75 percentile limit by more than 1.5 times the difference between the 75 and the 25 percentiles. Lower outliers were those whose values were smaller than the 25 percentile limit by more than 1.5 times the difference between the 75 and the 25 percentiles.

In addition to the boxes from the values of the parameters determined in the *in vivo* data, each box plot figure contains a gray band indicating the interval between the 25 and the 75 percentiles of the values of the excess parameters measured in a tissue-mimicking phantom containing only randomly-distributed scatterers leading to diffuse scattering conditions. This tissue-mimicking phantom was different from the one used as a reference and consisted of a homogeneous rectangular parallelepiped of a water-propylene glycol solution with agar and filtered milk with a scanning area of $10\times10cm^2$ and 16cm deep. The scanning area was covered by a 25μm thick Saran-Wrap® (Dow Chemical, Midland MI, USA). Glass beads ranging between 5 and 40μm in diameters (3000E, Potters Industries, Inc., Valley Forge, PA) were added to the phantom to a concentration of 236 scatterers/mm^3. Ten independent planes of this phantom were scanned and RF data frames (40mm depth, 30mm transmit focus) with the beam angled from -20^o to 20^o were obtained. Each of these frames was analyzed in the same fashion and with the same parameters as each of the *in vivo* data frames. The 25 to 75 percentile band for each excess parameter was obtained from considering the values of the parameters within a 1cm×1cm ROI centered at the field of view of each data frame. These plots were created to illustrate the variation of the values

of the parameters *in vivo* and in a tissue mimicking phantom as well as the detection process. These bands can show if any trends in the values of the parameters as a function of the beam steering angle also result from the analysis of the diffuse-scattering phantom. The box plots were not used in further quantitative analysis.

- **Classification images:** The fraction of the area encompassed by the lesion-fitted ROI that was classified as each of the categories described in Chapter 4 was determined by computing the number of PERs positive to the tests of stationary signals, Rayleigh scattering and uniform phase and dividing it by the number of PERs within the lesion-fitted ROI. The lesion area fraction was quantified for each beam-steering angle and each plane (anti-radial or radial). Plots of the lesion area fraction for each classification test were constructed. In addition to the *in vivo* data, every plot shows the average of the area fraction of the classification applied to the 10 data planes from the diffuse-scattering phantom.

5.3 Results

Figure 5.3 shows three types of images corresponding to the anti-radial plane of an invasive ductal carcinoma (IDC 5): conventional B-mode images (top row), excess-parameter parametric images (center row) and classification images (bottom tow). Both the excess parameter and the classification images are overlaid on top of the B-mode images to appreciate better the registration of structures. In this figure, the parameter being displayed is the maximum value of the collapsed average of the generalized spectrum (MaxCAGS) and is shown in the center row. The classification image assigns three colors to the PERs: red if a specular reflector was detected, green if a peak in the CAGS indicating periodic structures was detected, and blue, if the echo signals within the PER were deemed stationary. Columns show different beam steer angles: (a) 20^{o}, (b) 0^{o}, and (c) 20^{o}. As can be observed in the center row, the structural information provided in the MaxCAGS images agrees with structures present in the B-mode image, particularly the presence of specular reflectors at tissue boundaries. This agreement adapts to each of the

beam steer angles. Thus, each beam steer angle provides complementary information. In each of the figures the lesion-fitted ROI is shown as a white contour surrounding the lesion. Note that for this particular lesion, the values of MaxCAGS within the lesion are relatively low compared to the surroundings. As a consequence, a large part of the lesion is classified as having stationary scattering features. Figures 5.4 and 5.5 show the same three types of images (B-mode on the left, excess MaxCAGS on the center, and classification based on non-stationary features on the right) at 0^{o} beam-steering angle for the anti-radial plane of the five fibroadenomas and the five invasive ductal carcinomas, respectively. The white borders indicate the lesion-fitted ROIs that were used for the quantitative analysis presented below.

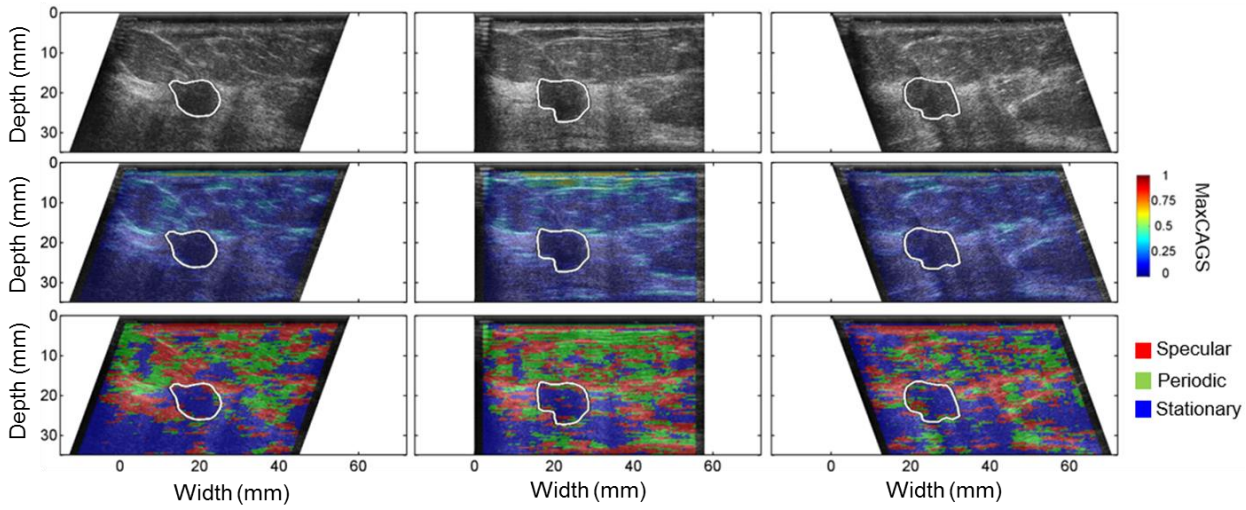

Figure 5.3 B-mode (Top row), excess parametric images based on the maximum value of the collapsed average of the generalized spectrum (MaxCAGS, center row), and classification image based on stationary features (bottom row) for the anti-radial view of Invasive Ductal Carcinoma 5, scanned at (a) -20^{o}, (b) 0^{o}, and (c) 20^{o}.

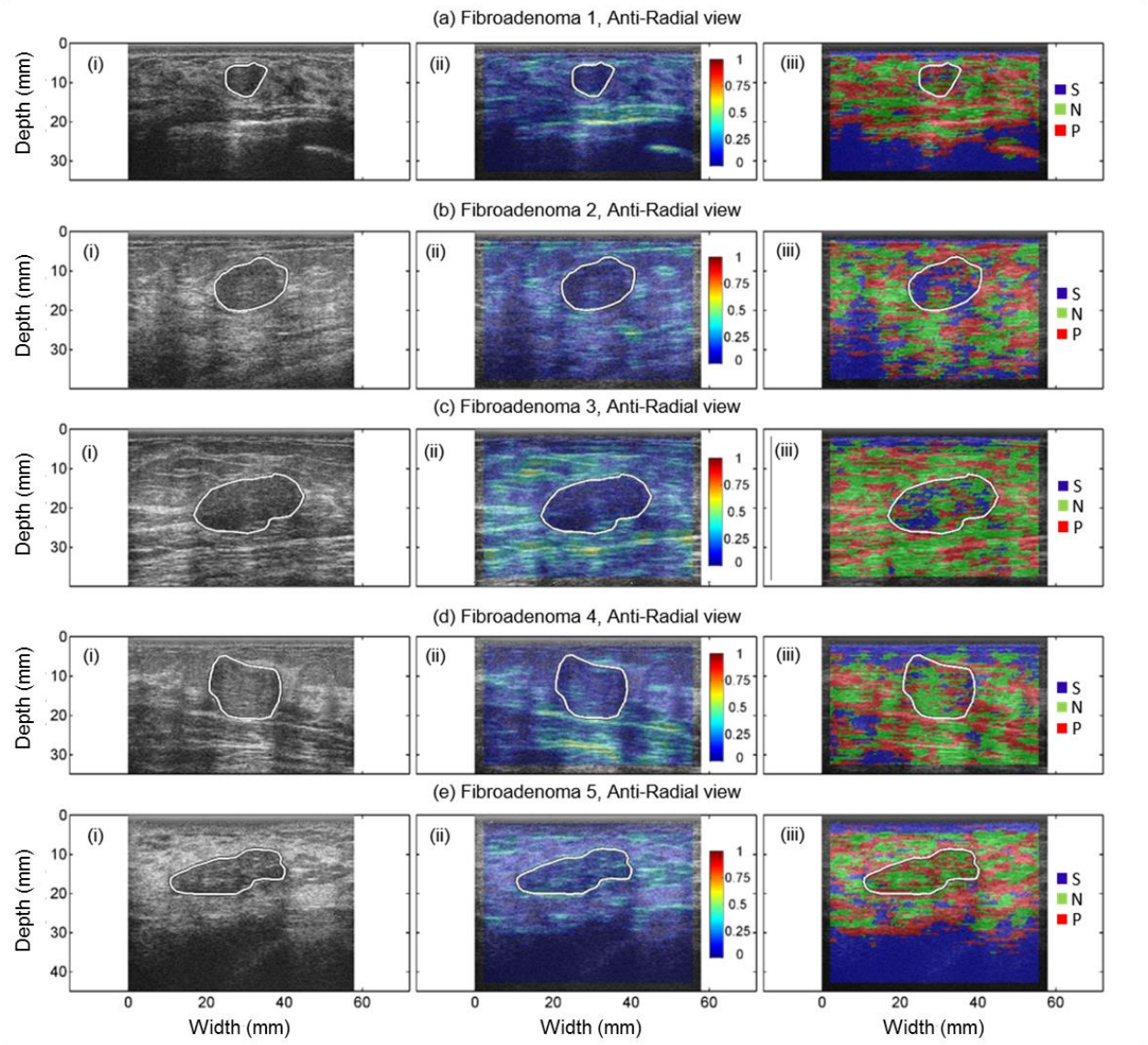

Figure 5.4 (i) B-mode, (ii) excess parametric images based on the maximum value of the collapsed average of the generalized spectrum (MaxCAGS), and (iii) classification images based on stationary features (bottom row) for the anti-radial view of the five fibroadenoma cases imaged at 0° beam-steering angle: (a) FA1, (b) FA2, (c)FA3, (d)FA4, (e)FA5. On the classification images, letters stand for S: Stationary, N: Non-stationary, P: Specular.

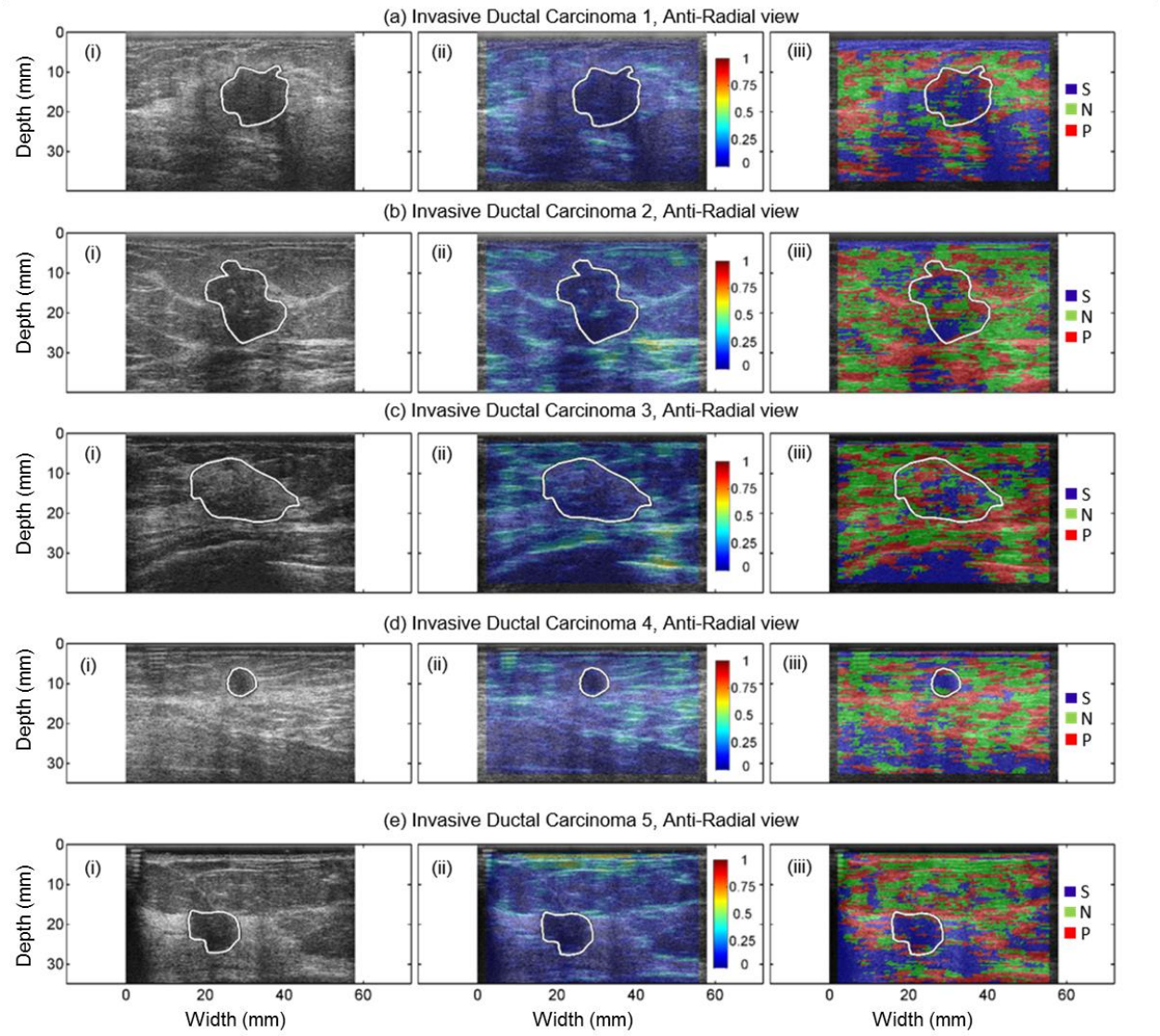

Figure 5.5 (i) B-mode, (ii) excess parametric images based on the maximum value of the collapsed average of the generalized spectrum (MaxCAGS), and (iii) classification images based on stationary features (bottom row) for the anti-radial view of the five invasive ductal carcinoma cases imaged at 0° beam-steering angle: (a) IDC1, (b) IDC2, (c)IDC3, (d)IDC4, (e)IDC5. On the classification images, letters stand for S: Stationary, N: Non-stationary, P: Specular.

Figure 5.6 shows plots of the excess parameters as a function of the beam steering angle, derived from subject 1 (fibroadenoma, FA 1). The left column corresponds to the anti-radial plane and the right column corresponds to the radial plane. The top row (Figs. 5.6(a) and 5.6(d)) shows the Excess MaxCAGS; the middle row (Figs. 5.6(b) and 5.6(e)) shows the Excess SNR_V, and the bottom row shows the excess phase χ^2. Figures 5.7-5.15 follow the same arrangement as Fig. 5.6 but show the results from subjects 2 to 10. The gray band in all the figures shows the 25-75 percentile range of the values of each parameter determined in the diffuse-scattering phantom. Some general comments can be drawn from these plots. In the case of the MaxCAGS and the SNR_V excess parameters, the values in the diffuse-scattering phantom are close to zero, and no observable dependence with the beam-steering angle was found. The MaxCAGS values in the *in vivo* data are in general larger than the diffuse-scattering values.

Comparing Figs. 5.6(a)-5.15(a) and Figs. 5.6(d)-5.15(d), the MaxCAGS values in the IDC cases tend to overlap with the diffuse-scattering band, suggesting that the underlying scattering process in IDC is closer to the diffuse scattering condition than the overall scattering process occurring within fibroadenomas. This is observable both in the radial and the anti-radial views.

The SNR_V values from different subjects and views are shown in Figs. 5.6(b)-5.15(b) and Figs. 5.6(e)-5.15(e). In general, *in vivo* SNR_V excess values were smaller than the values from the diffuse scattering phantom, which indicate pre-Rayleigh statistics. As discussed in previous chapters, this is in general attributed to the presence of a low random scatterer number density when the underlying scattering process is the same throughout the PER. However, this situation can also arise when there are spatial variations in the scattering conditions within the PER that are not large enough to produce a positive detection of non-stationary features. These spatial variations increase the variance of the echo signal within the PER over the mean value and thus result in lower SNR_V values. Because of the spatial heterogeneity of breast tissue, this might well explain the overall low SNR_V values. In some cases, such as in Figs. 5.6(b), 5.9(b), 5.10(e), and 5.14(b) the SNR_V values decrease as the steering angle approaches 0^o. This can be attributed to a reduction of the resolution cell volume, which results in a lower number of scatterers per resolution cell and a larger departure from Rayleigh statistics. The increase in the resolution

cell size is a consequence of a larger path traveled by the acoustic pulse to a particular tissue location as the beam is steered to larger angles. This can also result in larger sensitivity to spatial variations of the scattering process because the spatial scattering field is convolved with a smaller point spread function.

The excess χ^2 values from different subjects and views are shown in Figs. 5.6(c)-5.15(c) and Figs. 5.6(f)-5.15(f). In general, the phase χ^2 excess values in both the diffuse scattering phantom and the *in vivo* data have larger values and larger statistical variation (as indicated by the width of the gray band) as the beam steering angle approaches 0^o. A possible explanation to this trend can be a large sensitivity of the χ^2 parameter to variations of the size of the resolution cell with angle. As the beam steering angle approaches 0^o, the volume of the resolution cell decreases. Thus, the number of scatterers within the resolution cell also decreases, resulting in undersampling of the phase and a non-uniform distribution. This effect, in addition to the higher sensitivity to spatial variations of the scattering process when the resolution cell size decreases, can result in larger χ^2 values of the phase as the beam steering angle decreases.

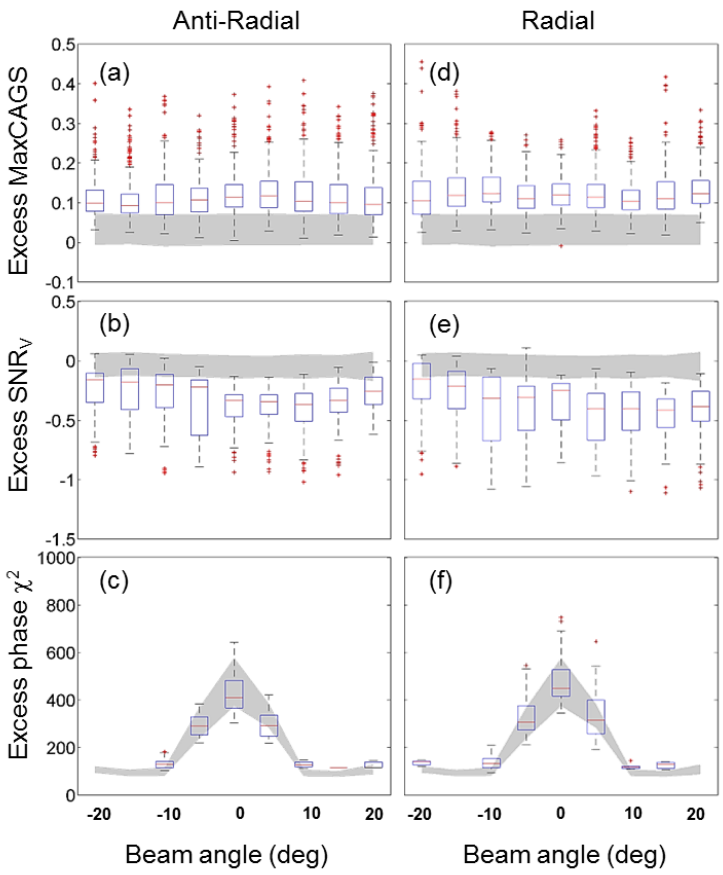

Figure 5.6 Box plots showing the parameters' excess values from the lesion-fitted ROI in Fibroadenoma 1 as a function of the beam steering angle. Left column: Anti-Radial view, right column: Radial view. Top row: Excess of the maximum value of the collapsed-average of the generalized spectrum (MaxCAGS); center row: excess of the echo amplitude SNR (SNR_V); bottom row: excess of the phase χ^2 measure. The gray band indicates the 25-75 percentile range measured in a diffuse-scattering phantom.

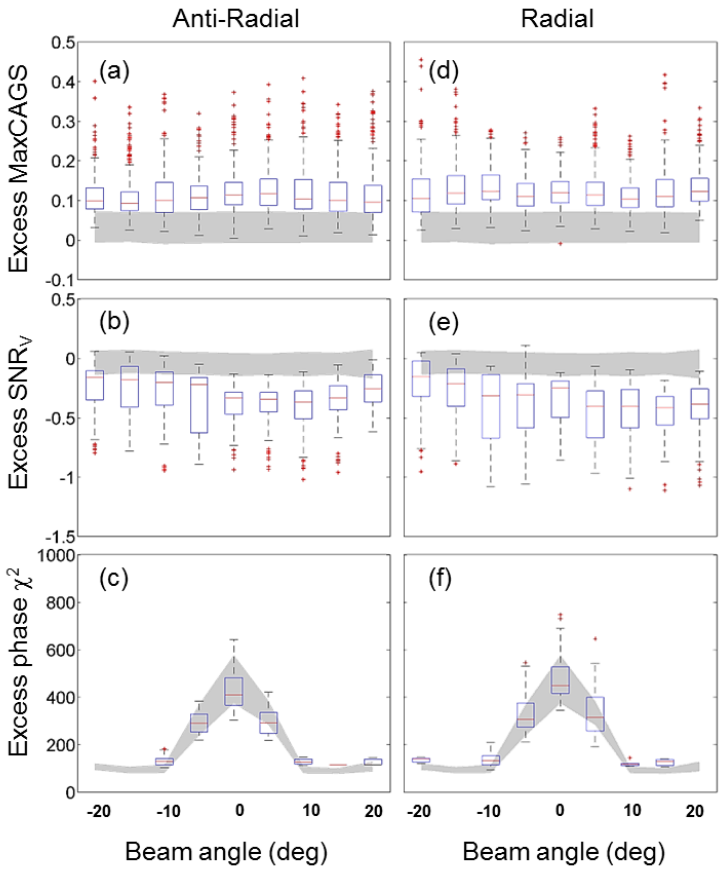

Figure 5.7 Box plots showing the parameters' excess values from the lesion-fitted ROI in Fibroadenoma 2 as a function of the beam steering angle. Left column: Anti-Radial view, right column: Radial view. Top row: Excess of the maximum value of the collapsed-average of the generalized spectrum (MaxCAGS); center row: excess of the echo amplitude SNR (SNR$_V$); bottom row: excess of the phase χ^2 measure. The gray band indicates the 25-75 percentile range measured in a diffuse-scattering phantom.

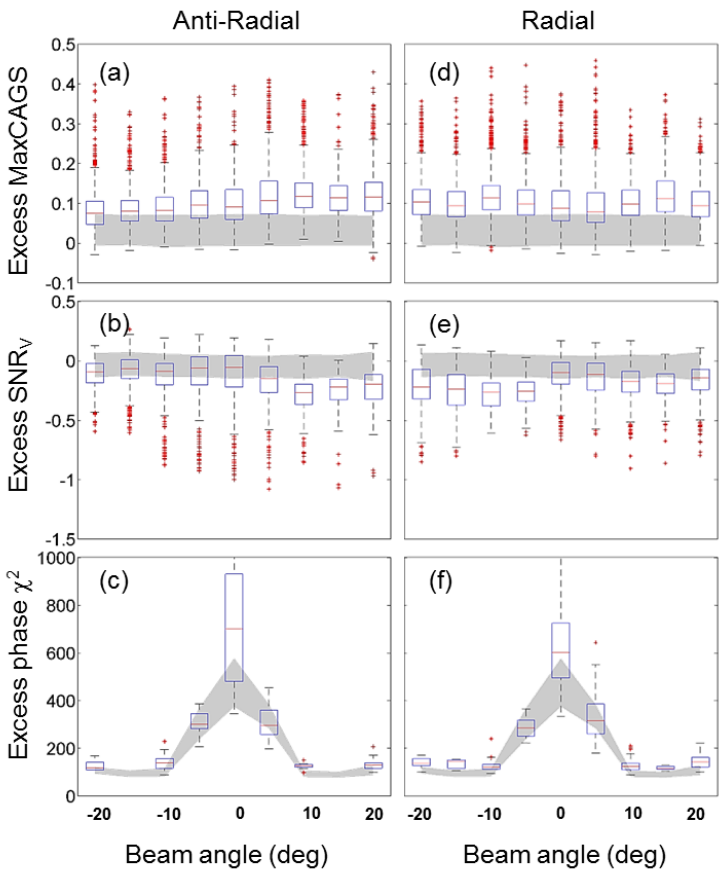

Figure 5.8 Box plots showing the parameters' excess values from the lesion-fitted ROI in Fibroadenoma 3 as a function of the beam steering angle. Left column: Anti-Radial view, right column: Radial view. Top row: Excess of the maximum value of the collapsed-average of the generalized spectrum (MaxCAGS); center row: excess of the echo amplitude SNR (SNR_V); bottom row: excess of the phase χ^2 measure. The gray band indicates the 25-75 percentile range measured in a diffuse-scattering phantom.

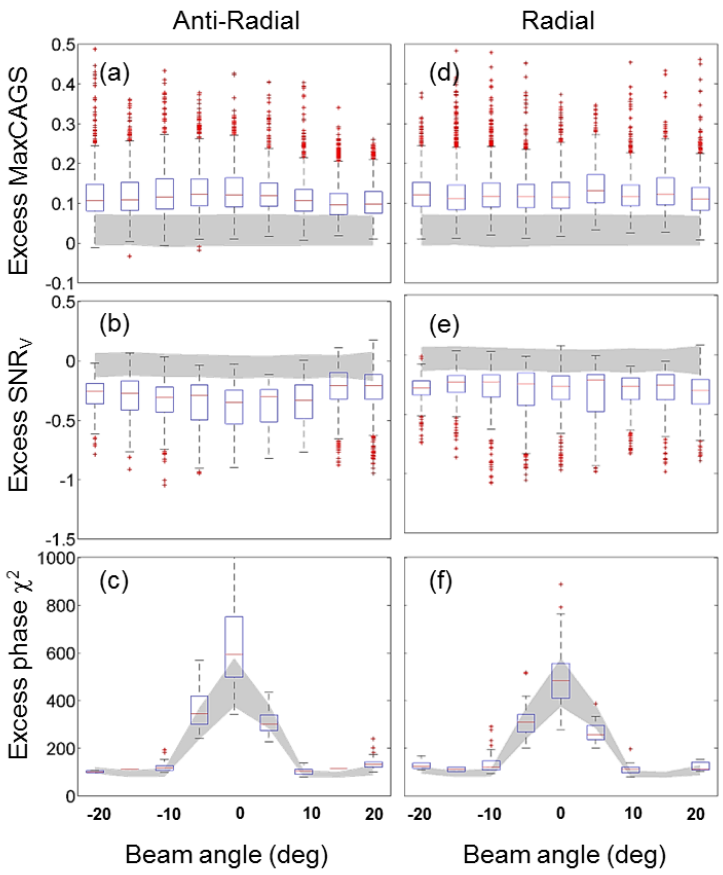

Figure 5.9 Box plots showing the parameters' excess values from the lesion-fitted ROI in Fibroadenoma 4 as a function of the beam steering angle. Left column: Anti-Radial view, right column: Radial view. Top row: Excess of the maximum value of the collapsed-average of the generalized spectrum (MaxCAGS); center row: excess of the echo amplitude SNR (SNR_V); bottom row: excess of the phase χ^2 measure. The gray band indicates the 25-75 percentile range measured in a diffuse-scattering phantom.

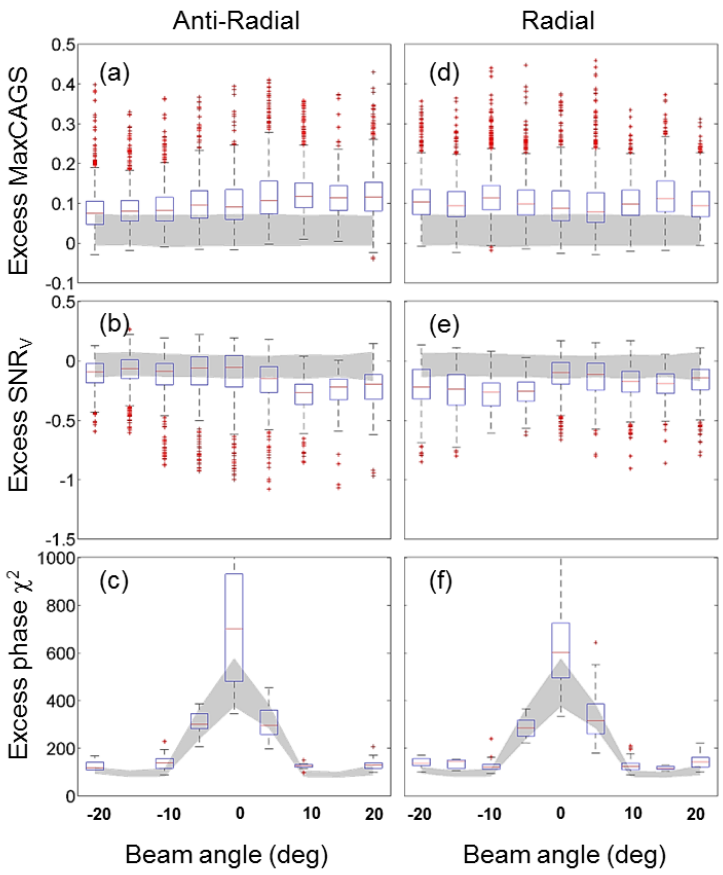

Figure 5.10 Box plots showing the parameters' excess values from the lesion-fitted ROI in Fibroadenoma 5 as a function of the beam steering angle. Left column: Anti-Radial view, right column: Radial view. Top row: Excess of the maximum value of the collapsed-average of the generalized spectrum (MaxCAGS); center row: excess of the echo amplitude SNR (SNR_V); bottom row: excess of the phase χ^2 measure. The gray band indicates the 25-75 percentile range measured in a diffuse-scattering phantom.

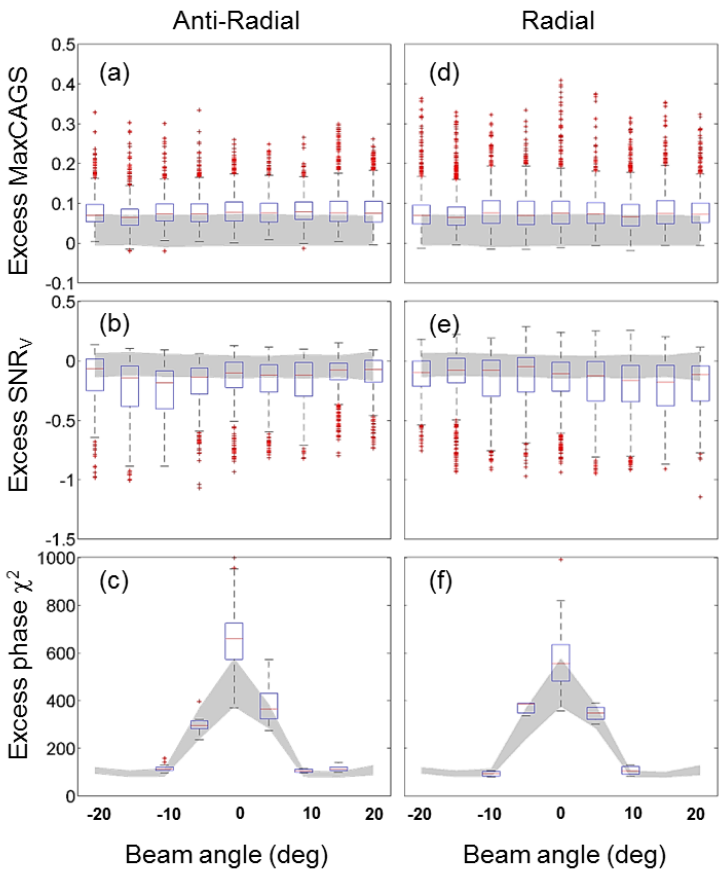

Figure 5.11 Box plots showing the parameters' excess values from the lesion-fitted ROI in Invasive Ductal Carcinoma 1 as a function of the beam steering angle. Left column: Anti-Radial view, right column: Radial view. Top row: Excess of the maximum value of the collapsed-average of the generalized spectrum (MaxCAGS); center row: excess of the echo amplitude SNR (SNR_V); bottom row: excess of the phase χ^2 measure. The gray band indicates the 25-75 percentile range measured in a diffuse-scattering phantom.

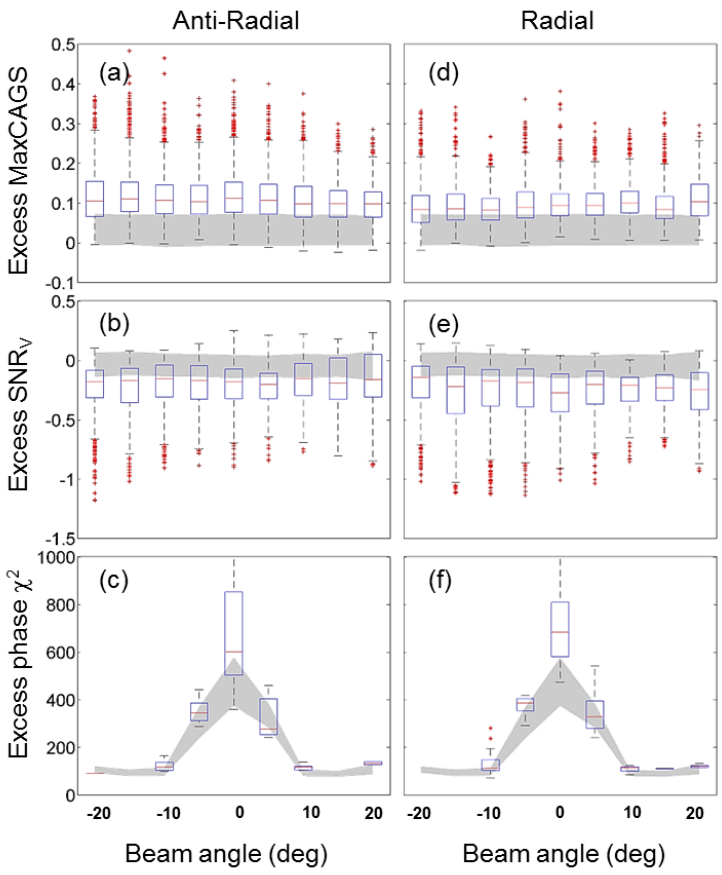

Figure 5.12 Box plots showing the parameters' excess values the lesion-fitted ROI in Invasive Ductal Carcinoma 2 as a function of the beam steering angle. Left column: Anti-Radial view, right column: Radial view. Top row: Excess of the maximum value of the collapsed-average of the generalized spectrum (MaxCAGS); center row: excess of the echo amplitude SNR (SNR_V); bottom row: excess of the phase χ^2 measure. The gray band indicates the 25-75 percentile range measured in a diffuse-scattering phantom.

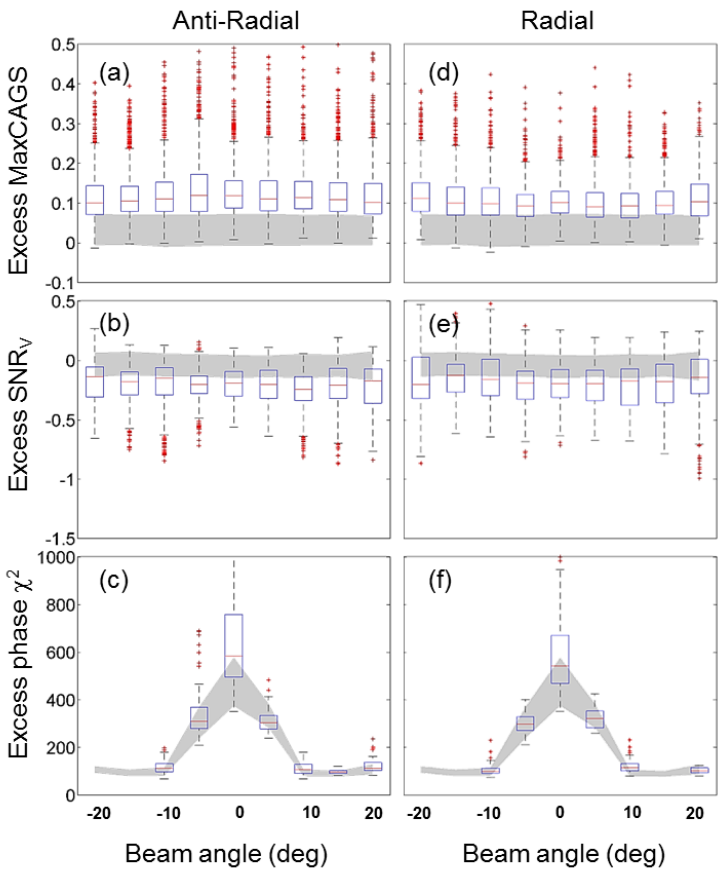

Figure 5.13 Box plots showing the parameters' excess values from the lesion-fitted ROI in Invasive Ductal Carcinoma 3 as a function of the beam steering angle. Left column: Anti-Radial view, right column: Radial view. Top row: Excess of the maximum value of the collapsed-average of the generalized spectrum (MaxCAGS); center row: excess of the echo amplitude SNR (SNR_V); bottom row: excess of the phase χ^2 measure. The gray band indicates the 25-75 percentile range measured in a diffuse-scattering phantom.

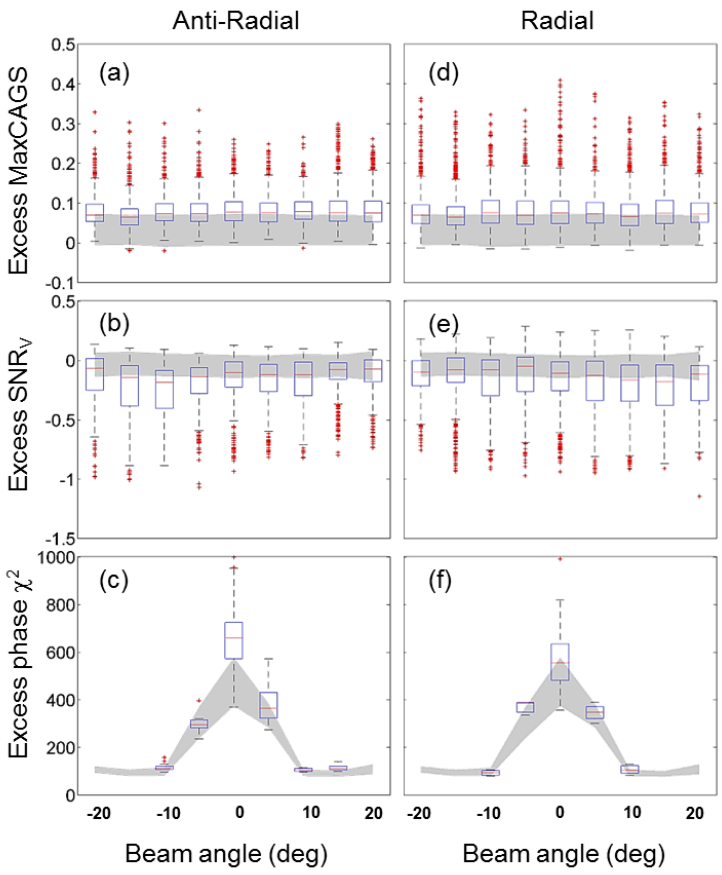

Figure 5.14 Box plots showing the parameters' excess values from the lesion-fitted ROI in Invasive Ductal Carcinoma 4 as a function of the beam steering angle. Left column: Anti-Radial view, right column: Radial view. Top row: Excess of the maximum value of the collapsed-average of the generalized spectrum (MaxCAGS); center row: excess of the echo amplitude SNR (SNR$_V$); bottom row: excess of the phase χ^2 measure. The gray band indicates the 25-75 percentile range measured in a diffuse-scattering phantom.

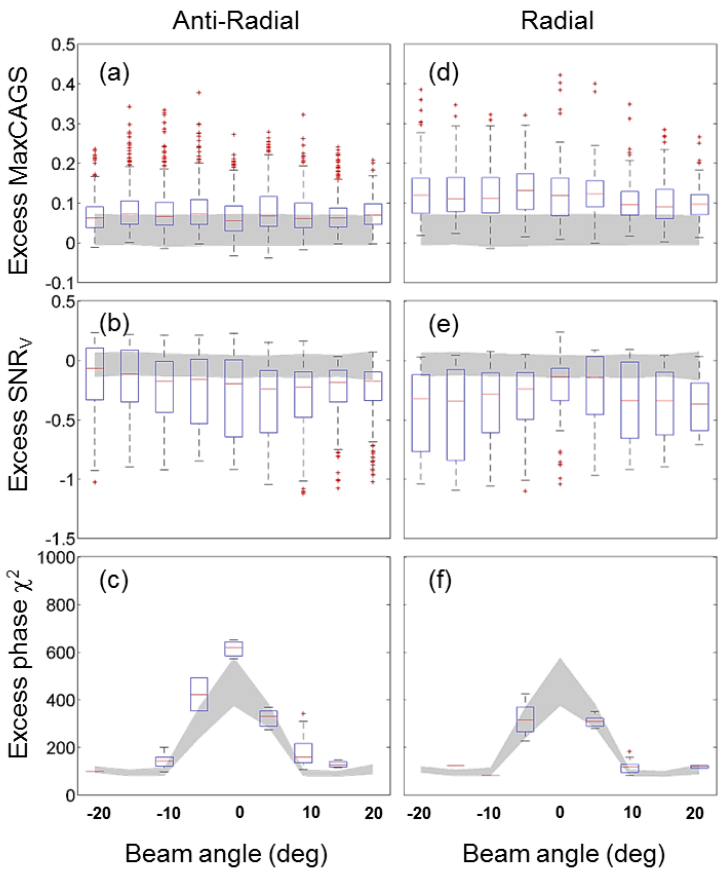

Figure 5.15 Box plots showing the parameters' excess values from the lesion-fitted ROI in Invasive Ductal Carcinoma 5 as a function of the beam steering angle. Left column: Anti-Radial view, right column: Radial view. Top row: Excess of the maximum value of the collapsed-average of the generalized spectrum (MaxCAGS); center row: excess of the echo amplitude SNR (SNR$_V$); bottom row: excess of the phase χ^2 measure. The gray band indicates the 25-75 percentile range measured in a diffuse-scattering phantom.

Figures 5.16-5.25 show the fraction of the lesion area classified as containing signals with (a) stationary echo signals, (b) specular reflectors, (c) stationary signals with Rayleigh statistics, and (d) uniform phase statistics as a function of the beam steering angle for the five fibroadenomas and the five invasive ductal carcinomas. Each subfigure contains three curves, a red curve for the anti-radial plane, a blue curve for the radial plane, and a black curve indicating the results from the diffuse scattering phantom. Note that the black curve is close to the expected limits: full stationary features, no specular reflectors, Rayleigh statistics, and uniform distribution of phases. Comparing Figs. 5.16(a)-5.25(a), the invasive ductal carcinomas tend to have a larger area with stationary features than the fibroadenomas. In some cases, such as in Figs 5.18(a) and 5.20(a), the lesion area fraction that is classified as stationary shows smaller values as the beam steering angle approaches 0^o. This is seen in both the anti-radial and the radial planes. In other cases, trends appear only in one of the planes, such as the anti-radial plane of Fig. 5.17(a) and Fig 5.19(a), or the radial plane Fig. 5.24(a).

Figures 5.16(b)-5.25(b) show the lesion area fraction classified as containing specular reflectors for the five fibroadenomas and the five invasive ductal carcinomas. In general, both lesion types show similar area fractions classified as specular reflectors. No consistent trends were observed as a function of the beam steering angle. This indicates the lack of directionality of the scattering sources, such as would be the case for a strong dominant scatterer, generally appearing as a bright spot within the lesion or possibly disorganized rod-like structures such as collagen fibers (see Discussion).

It is important to note that most of the areas classified as specular reflectors corresponded to boundaries between regions of different scattering properties, such as the lesion border. This structure, which is highly directional in its reflection properties, was not included in the lesion-fitted ROI. Thus, its effect is not shown in Figs 5.16(b)-5.25(b). As described in Chapter 4, a parameter sensitive to the presence of specular reflectors is the main-lobe width of the CAGS.

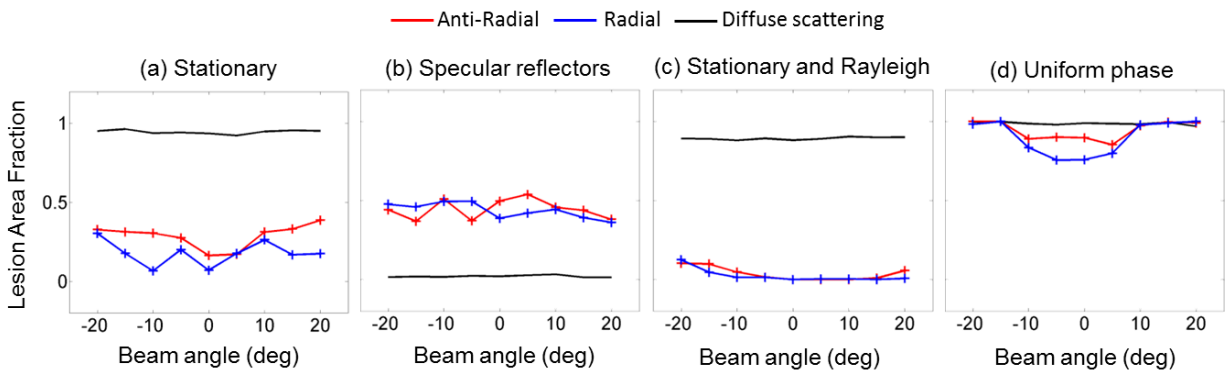

Figure 5.16 Lesion area fraction of Fibroadenoma 1 classified as containing (a) stationary echo signals, (b) specular reflectors, (c) stationary signals and Rayleigh statistics, and (d) uniform phase, as a function of the beam steering angle. Red: anti-radial view, blue: radial view, black: result from diffuse-scattering phantom.

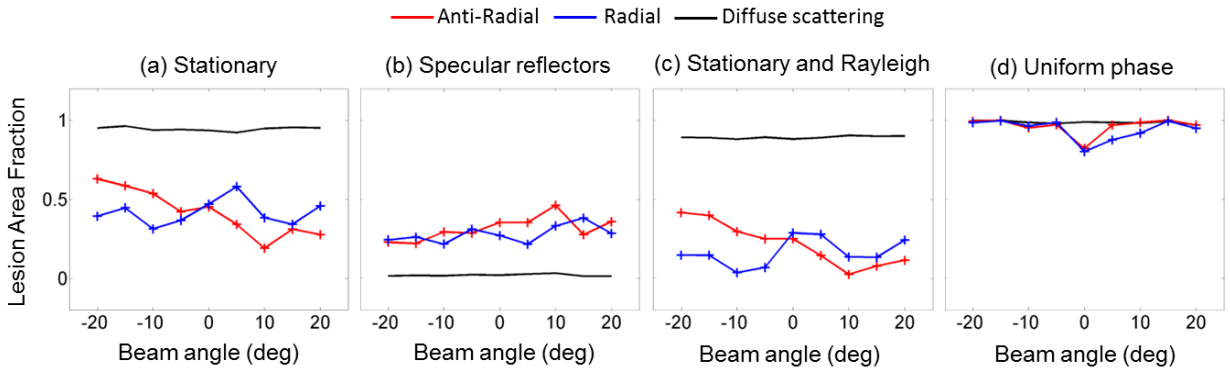

Figure 5.17 Lesion area fraction of Fibroadenoma 2 classified as containing (a) stationary echo signals, (b) specular reflectors, (c) stationary signals and Rayleigh statistics, and (d) uniform phase, as a function of the beam steering angle. Red: anti-radial view, blue: radial view, black: result from diffuse-scattering phantom.

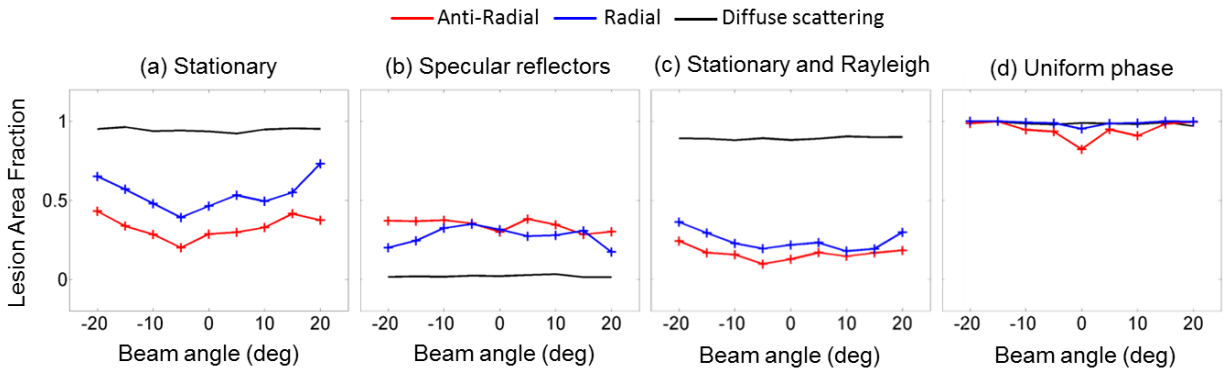

Figure 5.18 Lesion area fraction of Fibroadenoma 3 classified as containing (a) stationary echo signals, (b) specular reflectors, (c) stationary signals and Rayleigh statistics, and (d) uniform phase, as a function of the beam steering angle. Red: anti-radial view, blue: radial view, black: result from diffuse-scattering phantom.

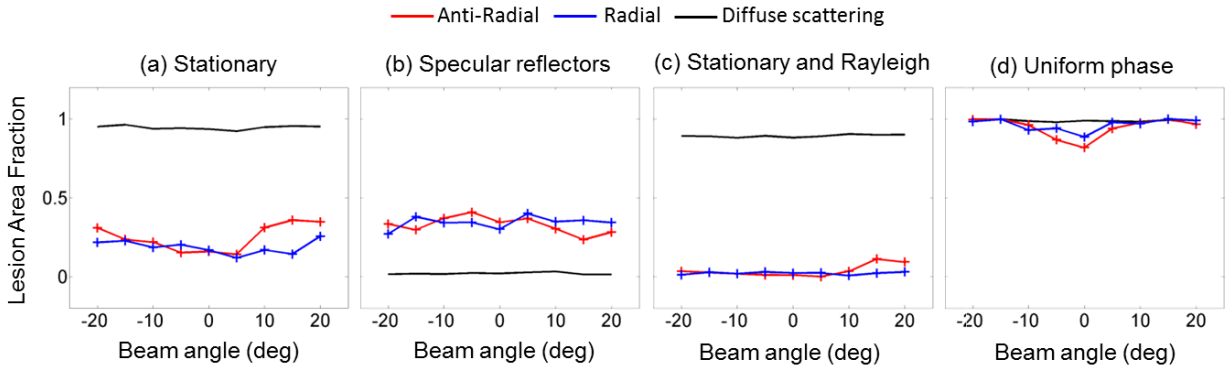

Figure 5.19 Lesion area fraction of Fibroadenoma 4 classified as containing (a) stationary echo signals, (b) specular reflectors, (c) stationary signals and Rayleigh statistics, and (d) uniform phase, as a function of the beam steering angle. Red: anti-radial view, blue: radial view, black: result from diffuse-scattering phantom.

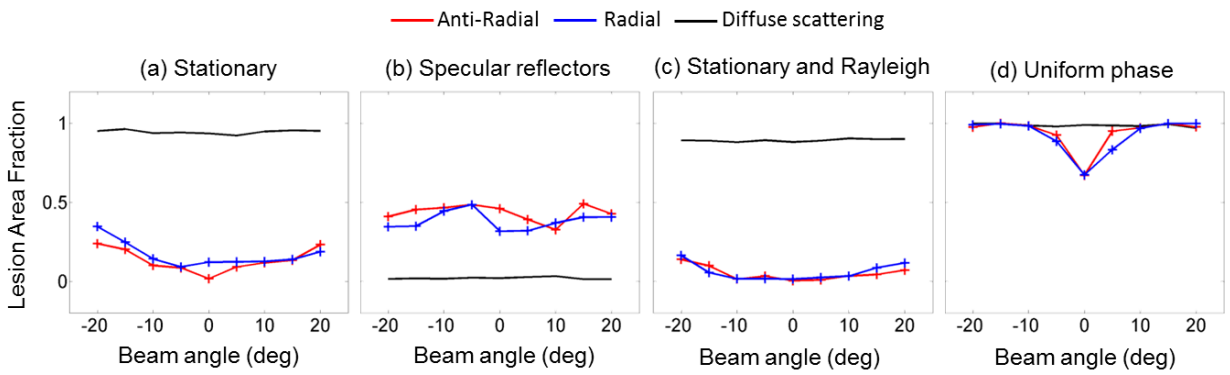

Figure 5.20 Lesion area fraction of Fibroadenoma 5 classified as containing (a) stationary echo signals, (b) specular reflectors, (c) stationary signals and Rayleigh statistics, and (d) uniform phase, as a function of the beam steering angle. Red: anti-radial view, blue: radial view, black: result from diffuse-scattering phantom.

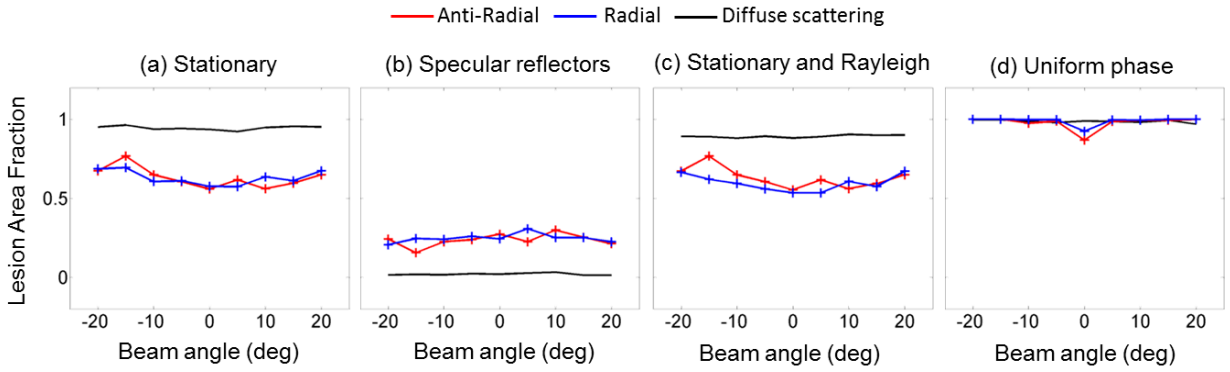

Figure 5.21 Lesion area fraction of Invasive Ductal Carcinoma 1 classified as containing (a) stationary echo signals, (b) specular reflectors, (c) stationary signals and Rayleigh statistics, and (d) uniform phase, as a function of the beam steering angle. Red: anti-radial view, blue: radial view, black: result from diffuse-scattering phantom.

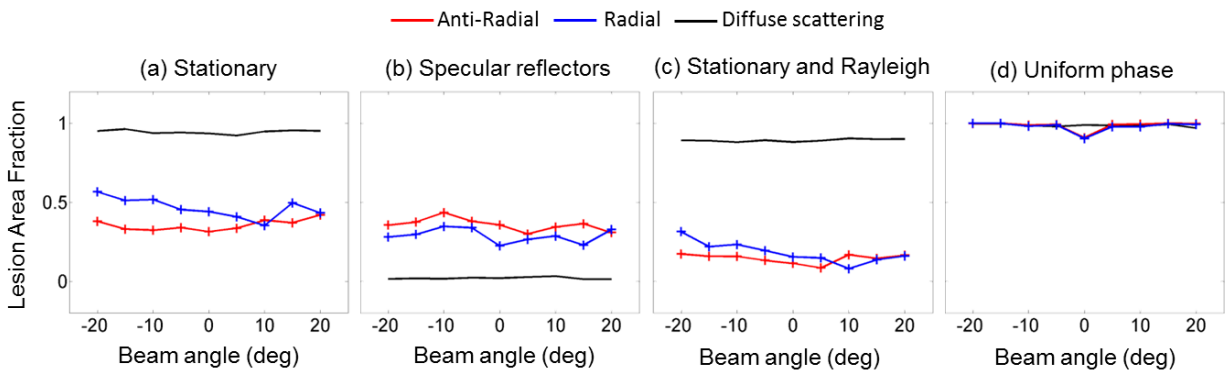

Figure 5.22 Lesion area fraction of Invasive Ductal Carcinoma 2 classified as containing (a) stationary echo signals, (b) specular reflectors, (c) stationary signals and Rayleigh statistics, and (d) uniform phase, as a function of the beam steering angle. Red: anti-radial view, blue: radial view, black: result from diffuse-scattering phantom.

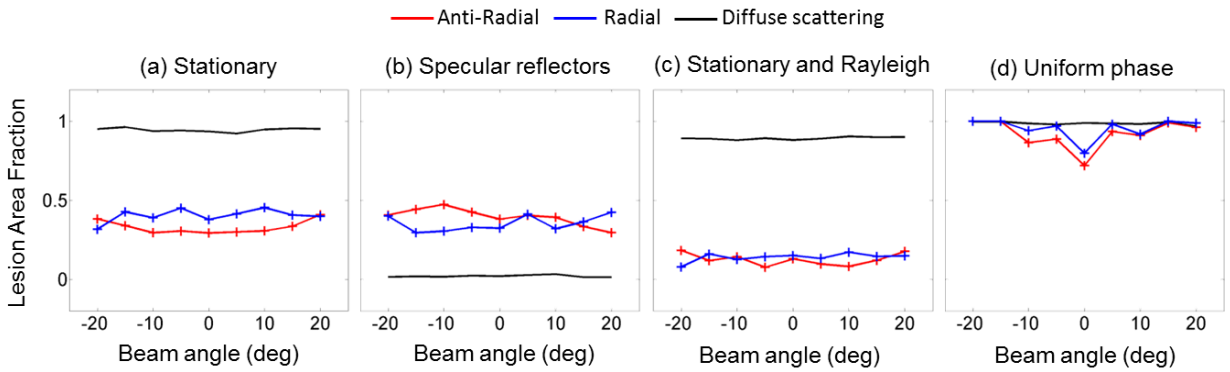

Figure 5.23 Lesion area fraction of Invasive Ductal Carcinoma 3 classified as containing (a) stationary echo signals, (b) specular reflectors, (c) stationary signals and Rayleigh statistics, and (d) uniform phase, as a function of the beam steering angle. Red: anti-radial view, blue: radial view, black: result from diffuse-scattering phantom.

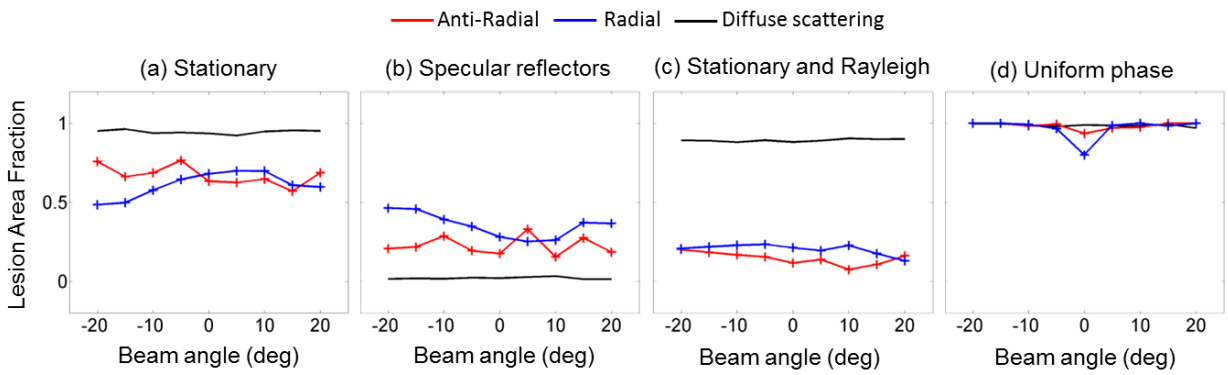

Figure 5.24 Lesion area fraction of Invasive Ductal Carcinoma 4 classified as containing (a) stationary echo signals, (b) specular reflectors, (c) stationary signals and Rayleigh statistics, and (d) uniform phase, as a function of the beam steering angle. Red: anti-radial view, blue: radial view, black: result from diffuse-scattering phantom.

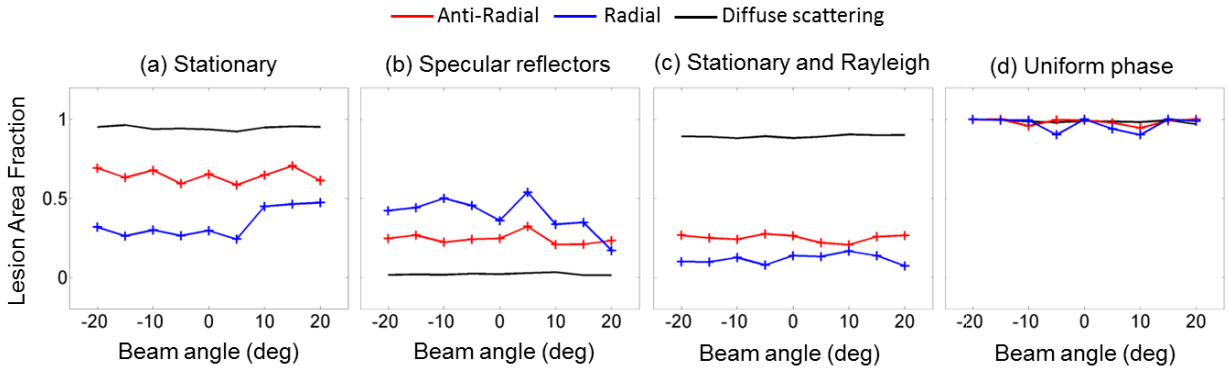

Figure 5.25 Lesion area fraction of Invasive Ductal Carcinoma 5 classified as containing (a) stationary echo signals, (b) specular reflectors, (c) stationary signals and Rayleigh statistics, and (d) uniform phase, as a function of the beam steering angle. Red: anti-radial view, blue: radial view, black: result from diffuse-scattering phantom.

Figure 5.26 shows B-mode (top), and parametric images of the main lobe width of the CAGS (center) and the excess MaxCAGS in regions not deemed as containing specular reflectors (bottom) for the anti-radial plane of Fibroadenoma 3. Three different beam steering angles are shown: (a) -20^{o}, (b) 0^{o}, and (c) 20^{o}. As can be observed in the center row, the regions with large values of the main lobe width of the CAGS lay on top of the tissue interfaces and lesion boundaries. Furthermore, these regions change with beam steer angle as expected from the relative degree of perpendicularity between the acoustic beam and the reflecting structures. Interesting features are indicated by the white arrows. These areas show visible periodic structures that are not detected by the CAGS main lobe width decision test, but show large MaxCAGS values in regions of non-specular reflectors. This example shows how both parameters based on the CAGS provide complementary information.

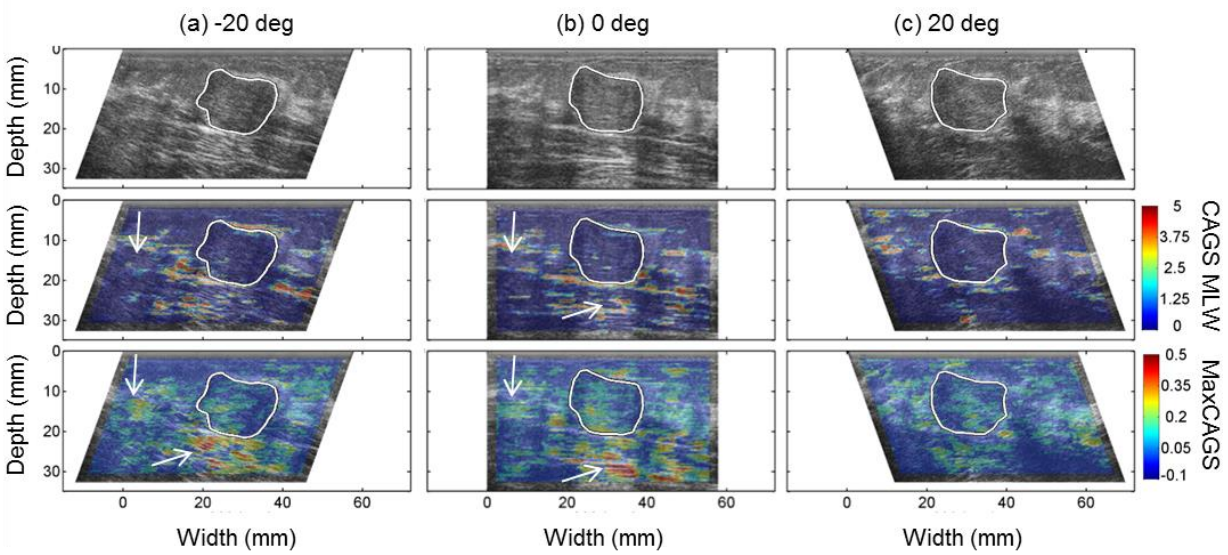

Figure 5.26 B-mode (Top row) and excess parametric images based on the main lobe width (MLW, center row) and the maximum value of the collapsed average of the generalized spectrum (MaxCAGS) for the anti-radial view of Fibroadenoma 3 scanned at (a) -20^{o}, (b) 0^{o}, and (c) 20^{o}. The MaxCAGS parametric images were assigned zero values in PERs where a specular reflector was detected.

Figures 5.16(c)-5.25(c) show the lesion area fraction classified as containing stationary echo signals and Rayleigh scattering. When looking at these figures, it is important to remember that they combine two

detection processes: a first one based on the MaxCAGS value, and a second one based on SNR_V. Thus, some of the trends observed in the SNR_V excess parameter figures are not readily observed in Figs. 5.16(c)-5.25(c). In general, the invasive ductal carcinomas tend to have larger areas classified in this category compared to the fibroadenoma. Figures 5.16(d)-5.25(d) show the lesion area fraction classified as having a uniform distribution of phases in the echo signals. Note that in all of the cases, most of the detection of non-uniform phase distribution occurs at smaller beam steer angles. This can be associated with the larger χ^2 values observed in Figs. 5.6(c)-5.15(c) and 5.6(f)-5.15(f). In general, these figures suggest that the fibroadenomas tend to show larger areas with non-uniform phase than the invasive ductal carcinomas.

In order to summarize the results presented in Figs. 5.16-5.25, the following two quantities are computed:

1. Angle-average of the lesion area fraction: This quantity expresses the overall fraction of the lesion area classified as one of the various categories described in Chapter 4. It is quantified as the average of the lesion area fraction corresponding to each category over the nine beam steering angles for each view and each subject.
2. Angle-range of the lesion area fraction: This quantity is measured as a first approach to quantify the anisotropy of the classification results. It is computed as the difference between the largest and the smallest values of the lesion area fraction corresponding to each of the categories described in Chapter 4 over all the beam steering angles for each plane and each subject. It is important to note that this quantity does not consider trends in the data.

Before continuing it is important to state that, because of the small number of cases included in this study, the comparison among different quantities in the analysis that ensues does not aim at making conclusive statements that are statistically significant. The character of the following analysis is merely exploratory. Figure 5.27 shows the angle average (a) and the angle range (b) of the fraction of the lesion area classified as containing stationary echo signals. Squares correspond to the five fibroadenomas (FA) and triangles to the five invasive ductal carcinomas (IDC). Black markers indicate the anti-radial (AR) plane and gray markers indicate the radial plane (R). The angle-average of the fraction of the invasive ductal carcinoma

classified as containing stationary features was about 74% larger in the invasive ductal carcinomas than in the fibroadenomas. Furthermore, the angle range of the stationary area fraction in the invasive ductal carcinoma was, on average, 36% smaller than in the fibroadenomas. This hints to a more isotropic scattering process occurring in the invasive ductal carcinomas.

Figure 5.28 shows the angle average (a) and the angle range (b) of the fraction of the lesion area classified as containing specular reflectors. Data are arranged in the same fashion as in Fig. 5.27. Although the angle-average values for the invasive ductal carcinomas were 14% smaller than the values of the fibroadenoma, the difference in the angle-range was only 3% of an overall specular area fraction angle-range of 0.16. This suggests a low directionality of the scattering process occurring at the specular reflectors, as previously discussed.

Figure 5.29 shows the angle average (a) and the angular range (b) of the fraction of the lesion area classified as containing Rayleigh statistics. Data are arranged in the same fashion as in Figs. 5.27 and 5.28. It is important to note that this is part of the area classified as containing stationary features. As explained in Chapter 2, to be able to estimate a first-order statistical parameter within a parameter estimation region, the statistics of the scattering process have to be the same over the PER, i.e., the echo signals need to be stationary. Due to the combined classifications, the angle-average area classified as containing Rayleigh statistics were, on average, rather small: 0.1 in the case of the fibroadenoma, and 0.16 in the case of the invasive ductal carcinoma. The angle average fraction corresponding to the Rayleigh statistics category was 61% larger in the invasive ductal carcinomas than in the fibroadenomas. These values do not consider Invasive Ductal Carcinoma 1, which had a significantly larger fraction of the lesion following Rayleigh statistics. In addition, the angle-range of this category was 30% smaller in the invasive ductal carcinoma than in the fibroadenoma.

Figure 5.30 shows the angle average (a) and the angle range (b) of the fraction of the lesion area classified as containing uniform phase statistics. Data are arranged in the same fashion as in Figs. 5.27-5.29. As described in previous figures, a large fraction of the lesions were classified as containing uniform phase statistics, all angle-average values being practically above 90%. Furthermore, the difference in angle-

average values between fibroadenomas and invasive ductal carcinomas was only about 2%. However, the angle-range value corresponding to this category was 30% smaller in the invasive ductal carcinomas (0.14) than in the fibroadenomas (0.19), suggesting more isotropic phase statistics in the former lesion type.

Finally, Fig. 5.31 shows the results for the diffuse scattering classification. It shows the angle average (a) and the angle range (b) of the fraction of the lesion area classified as containing diffuse scattering statistics. Data are arranged in the same fashion as in Figs. 5.27-5.30. On average, 15% of the areas of the fibroadenomas and 20% of the areas of the invasive ductal carcinomas were classified as containing diffuse scattering statistics. Note that these areas are slightly larger than the ones obtained for the stationary/Rayleigh statistics classification. This is because the diffuse scattering classification included not only the ideal stationary/Rayleigh statistics/uniform phase case, but also other secondary categories that improved the classification of the computational contrast phantom in Chapter 4 (categories c, i, j, and k). Excluding IDC1, this represents a difference of 34% in the area classification between invasive ductal carcinomas and fibroadenomas. The angle-range of the area classified as diffuse scattering was 27% smaller in the invasive ductal carcinoma cases than in the fibroadenomas. Again, this suggests a more incoherent and isotropic scattering process in the invasive ductal carcinomas.

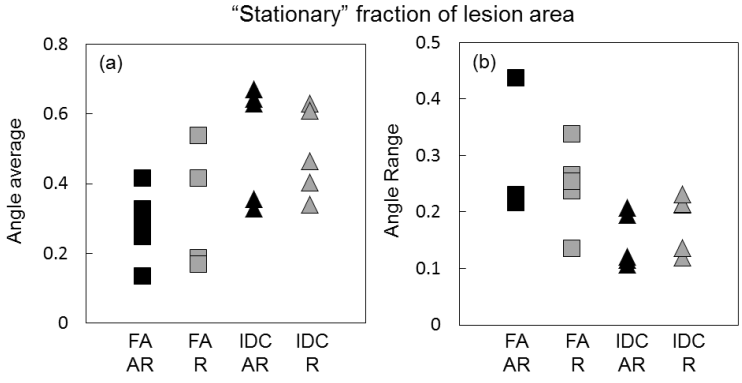

Figure 5.27 (a) Angle average and (b) range of the fraction of the lesion area determined by the lesion-fitted ROI classified as containing stationary echo signals. Squares: fibroadenomas (FA), triangles: invasive ductal carcinomas (IDC). Black: anti-radial view (AR), gray: radial view (R).

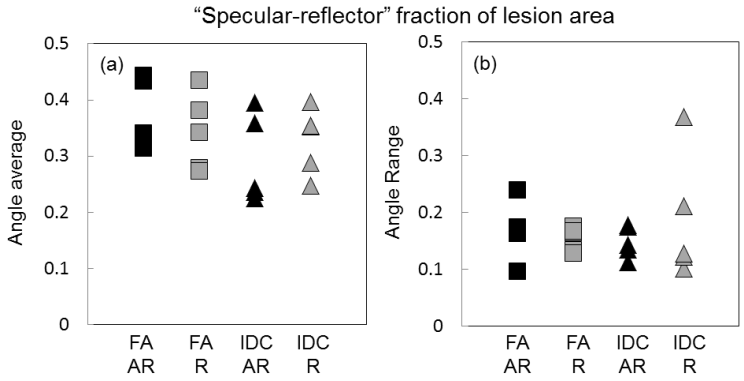

Figure 5.28 (a) Angle average and (b) range of the fraction of the lesion area determined by the lesion-fitted ROI classified as containing specular reflectors. Squares: fibroadenomas (FA), triangles: invasive ductal carcinomas (IDC). Black: anti-radial view (AR), gray: radial view (R).

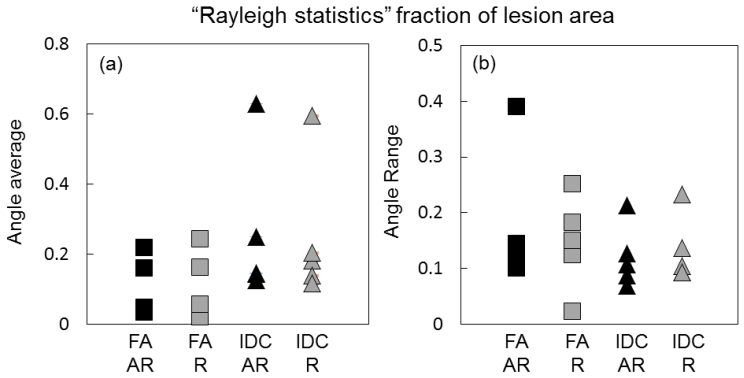

Figure 5.29 (a) Angle average and (b) range of the fraction of the lesion area determined by the lesion-fitted ROI classified as containing stationary echo signals with Rayleigh statistics. Squares: fibroadenomas (FA), triangles: invasive ductal carcinomas (IDC). Black: anti-radial view (AR), gray: radial view (R).

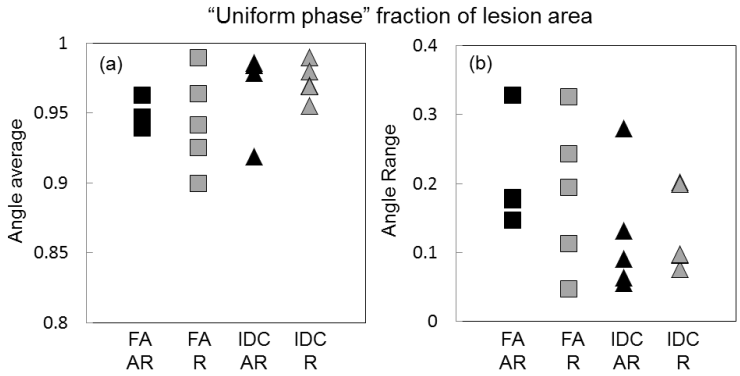

Figure 5.30 (a) Angle average and (b) range of the fraction of the lesion area determined by the lesion-fitted ROI classified as containing uniform phase statistics. Squares: fibroadenomas (FA), triangles: invasive ductal carcinomas (IDC). Black: anti-radial view (AR), gray: radial view (R).

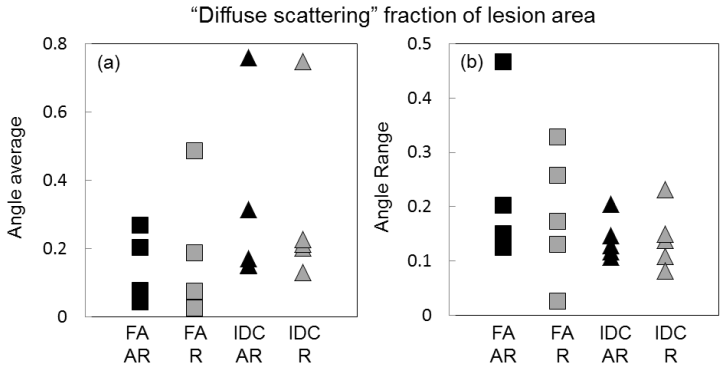

Figure 5.31 (a) Angle average and (b) range of the fraction of the lesion area determined by the lesion-fitted ROI classified as containing diffuse scattering. Squares: fibroadenomas (FA), triangles: invasive ductal carcinomas (IDC). Black: anti-radial view (AR), gray: radial view (R).

5.4 Discussion

This chapter has presented an initial *in vivo* application of the parameters studied and the tools derived in this dissertation for the distinction between two specific breast lesion types: fibroadenomas and invasive ductal carcinomas. The present analysis was merely preliminary in nature, and no statistically significant conclusions can be drawn from the limited data sample. In spite of these restrictions, some general trends that were observed are the following:

I. Backscatter echo signals obtained from *in vivo* invasive ductal carcinoma presented larger areas with backscatter echo signals possessing features closer to stationary conditions than fibroadenomas.

II. When backscattered echo signals were deemed stationary, most PERs presented Pre-Rayleigh statistics, leading to lower SNR_V values than in the diffuse scattering condition.

III. In general, the phase χ^2 excess values in both the diffuse scattering phantom and the *in vivo* data have larger values and larger statistical variation at smaller beam steering angles. However, after the classification test was performed, larger areas of the fibroadenomas contained non-uniform phase statistics than the invasive ducal carcinomas.

IV. In general, both lesion types show similar area fractions classified as specular reflectors. No consistent trends were observed as a function of the beam steering angle. This indicates the lack of directionality of the scattering sources.

V. In general, the results from the different classification tests tend to show less variation with beam-steering angle in the case of the invasive ductal carcinomas than in the case of the fibroadenomas.

In those cases where non-specular, non-stationary features were detected, we can look at the estimates of the mean scatterers spacing to gain more information about the structural properties of tissue. Figure 32 shows the angle average of (a) the median and (b) the range (computed as the difference between the 25 and 75 percentiles) of the mean scatterer spacing in those PERs within the lesion-fitted ROI that were classified as non-stationary and not corresponding to a specular reflector for the ten lesions studied here. Although the angle-average values tend to be similar, about 0.9mm, among different lesion types and planes as indicated by Fig. 5.32(a), the variability of the MSS estimates shown in Fig. 5.32(b) was as large as those median values. Thus, at this point, the large variability in the estimates does not allow us to make a conclusive statement about the nature of the scattering source based on the mean scatterer spacing.

Granting the large variability of the results, it is possible to observe that the backscattered echo signals from fibroadenomas tend to show features associated with a larger spatial heterogeneity than invasive ductal carcinomas: tissue interfaces leading to non-stationary features, large variance in the echo amplitude leading to pre-Rayleigh conditions, and less uniformity in the phase from the backscattered echoes. In contrast, results suggest that carcinomas are composed of more "homogenously random" distributions of scatterers. Thus, although obtained from a limited number of samples, these results can shed insight into the nature of the scattering sources in the breast fibroadenomas and invasive ductal carcinomas.

Before discussing the morphology of the tissue microstructure of fibroadenomas and invasive ductal carcinomas, it is pertinent to present a brief review of the anatomy of the breast to put these features in context. The breast tissue is highly complex. The main components of the breast are the glandular tissue, the lactiferous ducts, adipose tissue, and connective tissue. [155] The structural units of the mammary gland are the 15 to 20 mammary lobes. Each one of these lobes is associated to a lactiferous duct. Each duct reaches to and opens at the nipple. Within the lobe, the lactiferous duct branches into secretory lobules. The secretory lobules are linked to the main lactiferous duct by the interlobular ducts. Within each lobule the interlobule ducts divide into the terminal intralobular ducts, at the end of which a group of approximately 100 small sacs known as the alveoli are found. Together, the terminal ducts and the alveoli form the functional secretory unit of the breast gland known as the terminal ducto-lobular unit. The space around the lobules and the ducts is filled with adipose tissue and connective tissue. In particular, bands of connective tissue known as Cooper's ligaments surround the ducts. The net-like structure of these ligaments offers support to the breast.[155]

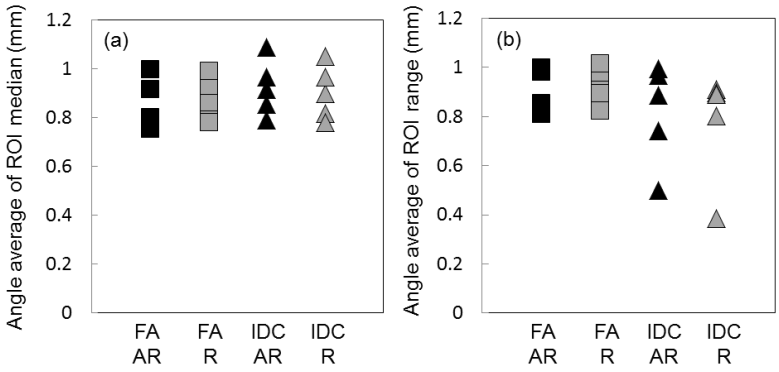

Figure 5.32 Angle average of the (a) median and (b) range, computed as the difference between the 25 and the 75 percentiles, of the Mean Scatterer Spacing (MSS) values obtained from PERs within the lesion fitted ROIs that were classified as containing non-stationary echo signals and not corresponding to specular reflectors.

The fibroadenomas and the infiltrating ductal carcinomas have characteristic histopathological morphologies that facilitate their diagnosis. Fibroadenomas grow from the terminal ducto-lobular unit. In fibroadenomas, both the fibrous stroma and epithelial elements (ducts and lobules) proliferate in varying proportions.[156] In general, they are composed mainly of proliferative fibrous stroma (80%) and epithelial tissue (20%).[157,158] The proliferation of the stroma can be pericanalicular (around tubular glands), intracanalicular (around compressed, slit-like ducts), or a combination of both.[151,159] They also show expanded and stretched ducts and acini which may present hyperplasia. Due to the presence of both stromal and epithelial components, they are usually referred to as "biphasic" lesions.[160] Also, between 40% and 50% of fibroadenomas are reported as "complex" because they possess one or many of the following elements: epithelial calcifications, apocrine metaplasia, sclerosing adenosis or cysts.[151,160] The invasive ductal carcinoma grows from the terminal intralobular ducts and consist of an abnormal proliferation of epithelial cells that break through the basement membrane and invade adjacent stroma.[161,162] The fibroadenoma possesses a more heterogeneous and structured organization than the invasive ductal carcinoma.

Once the basic features of the microstructure of both lesion types are known, the questions to address are whether we can relate QUS parameters to their structural properties and whether we can hypothesize what

the source of scattering is. Significant contributions in this line were the works by Oelze *et al.*,[39,163] who used rodent models of breast fibroadenoma, carcinoma, and sarcoma to perform a comparison of QUS parameters based on incoherent scattering and estimated from backscatter echo data obtained *in vivo* to structures observed in histological sections of the tumors stained with hematoxylin and eosin. In the case of the carcinomas, the authors succeeded at obtaining estimates of the effective scatterer diameter (ESD~30μm) that were comparable to structural features in the histopathological sections. Also, the authors were able to confirm that individual cells were the main scattering agent *in vivo*. This was done by estimating ESD from cell pellets grown in culture in which no stroma was present. ESD estimates from the cell pellets agreed with those estimated from *in vivo* echo signals. We attribute this success to the homogeneous, isotropic distribution of the cells within the carcinomas, which comply with the assumptions behind the ESD estimation methods. Furthermore, this observation agrees with our results that suggest that invasive ductal carcinomas have a more homogenously random distribution of scatterers. Therefore, we hypothesize that individual epithelial cells might be the source of scattering in the carcinomas that were analyzed in this dissertation. This also agrees with results from Liao *et al.*[164] who found that malignant breast tumors tend to have values of the Nakagami shape parameter closer to unity (closer to diffuse scattering conditions).

Comparing our results from the *in vivo* analysis of fibroadenomas with those from Oelze *et al.*[39] is not as easy a task as in the case of the carcinomas. Microscopic analysis of histopathological samples revealed that common to both fibroadenomas and sarcomas were clusters of cells that had an average size of 100μm surrounded by a large stromal component. This rises an important point: the scale of the heterogeneities (~100μm) was close to the size of the duration of the acoustic pulse used by the authors during the acquisition of the backscatter echo data (approx. 181μm assuming a Gaussian-shaped pulse with center frequency of 8.5 MHz and -6dB bandwidth of 7MHz). Thus, non-stationary features can be expected in the backscatter echo signals. This clearly violates the assumptions of stationary echo signals required in the ESD estimation algorithm. Nevertheless, in the case of the fibroadenomas, the authors

obtained ESD estimates that were comparable to the size of the epithelial cell clusters, and therefore concluded that the ESD was sensitive to the structural differences between the carcinomas and the fibroadenomas. In the case of the sarcomas, the ESD estimates were similar to those from the carcinomas and concluded that the ESD parameter was not sensitive to the structural differences between carcinomas and sarcomas. Only in the case of the sarcomas the authors attributed the lack of sensitivity to spatial heterogeneity. Interestingly, this was not considered to be a source of bias in the ESD estimates of the fibroadenomas. We believe that the observed spatial heterogeneity of tissue observed in these two lesion types and the bias that it can introduce in the estimates of the ESD makes it difficult to establish a correspondence between parameters based on incoherent scattering to tissue microstructure.

In an independent study, Donohue *et al.*[110] observed increased levels of coherent scattering when using parameters derived from the collapsed average of the generalized spectrum. Similarly to Oelze *et al.*,[39] the authors attributed the coherent scattering to the presence of a structured epithelial component. The authors reported a characteristic peak in the collapsed average of the generalized spectrum obtained from backscattered echoes from human breast fibroadenomas at a frequency corresponding to a mean scatterer spacing (MSS) of 1.8mm.[130] In another study, Huang *et al.*,[119] suggested that breast ducts were the most likely structure contributing to this source of coherence. Comparing with the results from Chapter 4, we observe that similar estimates where obtained when applying the algorithm developed in this dissertation to the tissue mimicking phantom containing nylon fibers. This can be seen in the histogram of mean scatterer spacing estimates shown in Fig. 4.27. Based on the fact that these high spacing values were the result of the transition from the region of diffuse scattering to the region with periodically arranged reflectors, it is possible that the large MSS values obtained from Donohue *et al.*[110] were the result of the transition from the stroma to the epithelial component in the fibroadenomas.

In another study, Donohue *et al.*[130] quantified the fraction of the area of breast lesions containing coherent scattering to the area containing diffuse scattering, using a Kolmogorov-Smirnov test to rule on the presence of diffuse scattering. The authors results showed that about 80% of lesions' areas were classified as diffuse scattering. Furthermore, they did not detect significant differences of the value of this

parameter between benign and malignant lesions. In contrast, our preliminary results showed significantly smaller fractional areas classified as diffuse scattering and showed differences between fibroadenomas and carcinomas. A possible explanation for the difference in results can be that Donohue *et al.*'s classification considered only two categories (Rayleigh statistics vs. coherent scattering) based on using the Kolmogorov-Smirnov test. We have expanded the number of scattering scenarios in our approach by considering not only coherent scattering detected by the generalized spectrum but also pre-Rayleigh and post-Rayleigh statistics when echo signals are stationary. By further dividing the stationary scenarios, our preliminary results showed larger values of the fractional area of diffuse scattering in carcinomas compared to fibroadenomas, which agrees with the expected tissue structure. In addition we have provided a first assessment of the anisotropy of this classification, which was shown to be of value for diagnostic purposes.

Following a different approach, we suggest to look at the "negative" of the picture: the stroma, instead of the epithelium. Findings from other research fields suggest that it is the stroma the structure that could provide valuable information to distinguish between benign and malignant breast lesions. In this sense, it is important to consider that the presence of the stroma can also introduce important sources of scattering, such as collagen. Collagen is the most abundant protein in the human body and one of the principal components of the stroma.[165,166] It is also considered to be the principal contributor to scattering in most tissues.[166-172] Its basic structural unit is the tropocollagen, which is composed of three polypeptides arranged in a 300nm-long, three-helix structure. Tropocollagen helices form fibrils with diameters between 50 to 200nm, which then form bundles and fibers and more complex structures.[173] Sehgal *et al.*[166] suggested that, when studying the interactions with an acoustic pulse, tissue could be modeled as an array of many small volume elements. Some volumes are composed of collagen fibers, which form heterogeneities large enough to produce a significant amount of scattering. The other volume elements are assumed to be composed of a "water-like" fluid containing all other proteins and lipids with size significantly smaller than the wavelength of the acoustic pulse and behaving as Rayleigh scatterers. This simplified model reflects the important role of collagen in ultrasound. For example, when highly

organized within a breast lesion, collagen has been associated with increased attenuation or shadowing in the corresponding B-mode images.[174]

Collagen is also one of the largest components of the fibrous connective tissue in the breast and is associated with increased mammographic density, which is an important independent risk factor of breast cancer.[175-180] From the various types of collagen, type I is the principal component of the stromal extracellular matrix, although type III and V can also be present in smaller amounts.[181]

To learn more about how the collagenous composition of breast tissue and tumors change depending on the tumor histotype, we can look at results from different spectroscopy or microscopy modalities sensitive to the submicron composition of breast tissue. One of these modalities is Raman spectroscopy, which relies on inelastic light scattering to provide information about the vibrational modes of molecules. Most importantly, because each molecule has a specific pattern of vibration, the Raman spectrum can serve as its molecular finger print.[182,183] Haka *et al.*[184] evaluated the feasibility of improving the diagnosis of breast cancer using Raman spectroscopy on *ex vivo* samples of human breast lesions. To overcome the difficulty of analyzing the complex Raman spectrum from the complicated molecular composition of breast tissue, the authors developed a set of "basis" spectra representing the most important components of the breast. These components were assumed to contribute linearly to the total Raman spectrum. Details of the decomposition can be seen Ref. 185. Results showed that the main difference between normal breast tissue and all breast lesions was an increased presence of collagen. Comparing between fibroadenomas and carcinomas, the main difference was that the contribution of fat to the Raman spectrum from fibroadenomas was 26% of the contribution to the spectrum from invasive carcinomas. The increase in fat content in malignant lesions agrees with other studies using Raman spectroscopy.[182,183] The authors also found that the collagen contribution in the invasive carcinomas was 41% of the collagen contribution to fibroadenomas. Furthermore, the contribution of collagen in the fibroadenoma was 40% larger than the contribution from the cell nucleus and the cell cytoplasm combined. In the case of the carcinoma, the contribution from collagen was 60% smaller than the contribution from the cell nucleus and cytoplasm. These findings, i.e., the larger collagen contribution and smaller cellular contribution to

the Raman spectrum from fibroadenomas, suggest that collagen could be acting as an important source of scattering in this lesion type. Furthermore, they support the hypothesis that the increased epithelial cellularity in carcinomas is the main contributor to scattering. However, these results do not provide information about the structural properties of the increased collagen concentration.

Information about the structural properties of collagen in different breast tumors has been a research topic of increasing interest. This information has been studied using second harmonic generation (SHG) microscopy. SHG is a modality of multiphoton laser-scanning microscopy that relies on very high photon densities to stimulate an elastic, nonlinear interaction of two photons with the non-centrosymmetric structure of collagen fibers to generate a photon of twice the energy of each of the incident ones but half their wavelength.[162,177,186-188] The contrast of the image resulting from the detection of these second harmonic photons depends solely on the structural properties of collagen fibers such as their thickness, cross liking, or alignment. This microscopy modality achieves resolution in the submicron scale and allows the visualization of individual collagen fibers, making possible to visualize the morphology of collagen fibers in the breast tissue stroma.[189] Using SHG, Falzon *et al.*[186] studied the shape of collagen fibers in *ex vivo* samples of healthy breast tissue as well as from benign lesions (fibroadenomas and sclerosing adenosis) and invasive ductal carcinoma. A quantitative analysis was achieved by parameterizing the shape of the collagen fibers through the "elliptical Fourier transform".[186] The authors obtained the dominant shape in each of the three tissue types by performing principal component analysis of the coefficients of the elliptical Fourier transform. The authors concluded that coefficients related to the presence of inflections between sections with positive curvature and negative curvature in collagen fibers are one of the main features to discern benign lesions from malignant lesions, which showed more straight fibers. In other words, collagen fibers in benign lesions tend to be wavier than collagen fibers in invasive ductal carcinoma. In a different study, Zheng *et al.*[190] used SHG images to compare the collagen structure in the stroma of fibroadenomas to the collagen structure in the stroma of normal tissue. The authors observed that collagen fibers in normal tissue and in fibroadenomas tend to align with the surface of the epithelial components of the fibroadenoma.[190] Similar observations were made by Provenzano *et*

al.[189] and Burnke *et al.*[162] However, the collagen fibers in the stroma of the fibroadenoma had a denser concentration.[190]

In summary, the information just presented leads to three ideas: (1) collagen is a main component of the large stromal portion of the fibroadenomas, (2) the amount of collagen in the stroma of fibroadenomas is larger than in the invasive carcinomas (which are dominated by a cellular component), and (3) there are important morphological differences in the collagen content in fibroadenomas compared to normal tissues and invasive carcinomas. From these ideas, we hypothesize that the bands of wavy collagen fibers in the stroma of fibroadenomas could have acted as the main sources of scattering. The spatial heterogeneity of these structures led to the detection of non-stationary features in the echo signal and a large variability of the mean scatterer spacing estimates. Furthermore, although the analyzed parameters and the classification results tend to vary with angle, no generalized trends were observed as a function of the beam steered angle. This observation could also be a result of the spatial heterogeneity of the collagen bands surrounding the epithelial components. In cases where the spatial heterogeneity was not large enough to produce positive tests for non-stationary features, the increased variance of the echo amplitude led to lower values of SNR_V. Thus, we hypothesize that the homogenously randomly distributed cancerous cells in invasive carcinomas led to the formation of backscatter echo signals with conditions that were closer to diffuse scattering. In contrast, the heterogeneously structured collagen fibers in the stroma of the fibroadenomas led to coherent scattering conditions. This hypothesis, however, can only be proved by extending the analysis presented here to a larger number of subjects to be able to distinguish between the true structural differences of the various lesion histotypes from the inherent biological variability. Furthermore, it will be necessary to correlate the findings with the microscopic analysis of either biopsy or surgical samples of the analyzed lesions. Only in this way a better knowledge about the Physics linking tissue microstructure with the parameters obtained from backscattered echo signals from ultrasound scanning will be at hand. These ideas are extended in Chapter 6 which discusses future work.

At this point, the performance of the classification algorithm has been only evaluated in simulations that considered only discrete scatterers with frequency-independent scattering amplitudes. However, the finite

size, shape, orientation, and elastic properties of the scatterers will also affect the spectral content of the backscatter echo signals.[191] Furthermore, as discussed before, scattering sources *in vivo* tend to originate from continuous variations of acoustic impedance, rather than from discrete scatterers. Thus, in order to achieve a better understanding of the results from the *in vivo* application of the algorithm, further tests are needed. These tests should involve simulations and phantom-based experiments with more complex scattering sources that are better representations of breast tissue. In this sense, the results presented here can be used as an orientation for the design of such phantoms considering the hypothesized sources of scattering in the case of the fibroadenomas and the carcinomas.

This dissertation have stated the need of finding zones where a low random scatterer number density may reduce the accuracy and precision of the QUS estimates based in incoherent scattering. This need has to be considered in the context of parametric image formation in which the number of samples of the resolution cell is limited by the spatial resolution constraints. In an ampler sense, the sole presence of a sparse distribution of random scatterers does not itself represent a limitation for QUS estimation when a large number of samples of the resolution cell is at hand, i.e., when performing bulk parameter estimation (see Chapter 1). For example, Insana *et al.*[30] estimated the effective scatterer size of polystyrene microspheres within tissue mimicking phantoms with scatterer number densities as low as 0.15 to 0.73 scatterers/mm^3 within 20% of the true sphere diameter. Similarly, King *et al.*[46] reported good estimates of the effective scatterer diameter of weakly scattering spheres with concentrations between 1.8 and 3.6 scatterers/mm^3. Common to these studies is the use of large amounts of data for the estimation. In the first study, the authors used 25 independent pulse echo waveforms and echo signal segments spanning 20.5μs (~15mm). In the second study, estimates were obtained from 100 independent pulse echo waveforms and 10μs echo signals (~8mm). Recently, Rubert and Varghese[192] analyzed the bias and variance of estimates of the slope of the attenuation coefficient as a function of frequency for various numerical and experimental phantoms with different scatterer number densities. The authors observed that the variance of the attenuation coefficient increased more than twice when the scatterer number density was reduced

below 2 scatterers/mm^3. In this analysis, the PER included 10 independent acoustic scan lines and a total echo segment longer than ~ 14mm (10mm for the slope estimation length plus 4 mm from the spectral estimation window length).[192] This increase in variance was reduced by increasing the total signal length used for the estimation of the attenuation coefficient. The authors' conclusion agrees with the statement at the beginning of this paragraph: it is not the low scatterer number density but rather its combination with constraints in the amount of data available for the estimation what imposes a limitation in parameter estimation. Evidently, this problem is ubiquitous in parametric image formation.[192]

To the best of our knowledge this work is the first of its kind in looking at the anisotropy of coherent scattering parameters in *in vivo* human breast lesions. The preliminary analysis of excess parameters and the classification results suggests that invasive ductal carcinomas tend to have scattering conditions that are more isotropic than those of fibroadenomas. This is based on looking only at the variation of the different parameters with beam steering angle. Further studies should also look at trends as a function of the beam steering angle, like some of those discussed in the Results section. It is important to note that the parameter selection and the classification process developed in previous chapters was optimized assuming a single beam steering view. The preliminary results of this chapter, which includes a seminal comparison of the variation of the parameters and classification results as the acoustic beam is angled, motivates deeper studies of the observed trends.

In conclusion, the preliminary application of the classification algorithm to echo data from breast lesions acquired *in vivo* agrees with previous independent observations that suggested that tissue microstructure of invasive ductal carcinomas produces conditions closer to diffuse scattering than fibroadenomas. Our results support the notion that individual epithelial cells are the main source of scattering in carcinomas. In the case of fibroadenomas our results, when analyzed in the context of results from other microscopy and spectroscopic techniques, led us to suggest that the collagen-rich stromal component in these lesions can be acting as the source of scattering. Theoretical and experimental verification of this hypothesis remains a topic of future work.

6. Conclusions and Future work

6.1 Summary and contributions

The general goal of this dissertation has been to improve the value of parametric images of scattering-based QUS parameters to be used in the diagnosis of breast lesions. This goal was achieved by designing an automated algorithm that identifies areas of the backscattered echo field in an RF data frame for which the estimation of either the power spectral density or related QUS parameters based on incoherent scattering would be problematic because of the presence of coherent scattering. When such areas are identified, the algorithm computes QUS parameters describing the most likely coherent scattering conditions present.

The automated algorithm incorporates metrics that were optimized to classify echo signals as arising from either coherent or incoherent scattering. It then classifies these signals as either stationary or non-stationary based on these metrics. These metrics include the spectral correlation quantified from the echo-signal generalized spectrum, and the signal-to-noise ratio of the echo-signal amplitude. Optimization processes were centered on the task of creating parametric images, where compromise must be made between spatial resolution and detection performance. Our work differs from previous uses of these or similar metrics as explicit diagnostic tools for different pathologies, such as described in the series of papers by Donohue *et al.*,[50,51,93,110,114-116,119,128,130] dealing with non-stationary features, or the papers of Shankar *et al.*[59,71,72,75,77,79,94] *and* Tsui *et al.*[63,76,164] dealing with stationary features.

An analysis of stationary features was presented in Chapter 2. There we evaluated the performance of a Generalized Likelihood Ratio Test for detecting echo signals arising from sources other than diffuse scatterers. The Likelihood Ratio Test is based on the Nakagami distribution, a theoretical model of the probability density function of the backscattered echo signal amplitude. Particular interest was paid to the scenario where organized scatterers are present, with a characteristic spacing smaller than the resolution cell, yet producing stationary echo signals. The performance of this test was compared to more conventional, model-based and model-free metrics used in previous studies for diagnostic purposes.

Additional applications of these metrics were suggested, including estimation of the speed of sound in tissue where the analysis is applied to echo signal data that are derived using different "trial" speeds of sound in the system beamformer.

The detection of non-stationary echo signals was presented in Chapter 3. We presented a theoretical and experimental analysis of the conspicuity of features related to coherent scattering in the generalized spectrum of backscattered echo signals. This analysis advanced the use of the generalized spectrum in Quantitative Ultrasound by comparing advanced estimators of the generalized spectrum, i.e., the multitaper estimator, to the singular spectrum analysis method for the task of creating parametric images based on coherent scattering. Particular interest was paid to the case where organized scatterers are present within the resolution cell, with a characteristic spacing (organization scale) larger than the resolution cell.

In Chapter 4, the analyses of stationary and non-stationary features in the echo signals were combined into a novel algorithm designed to distinguish parameter estimation regions with diffuse scattering conditions from those with coherent scattering conditions. The algorithm was able to distinguish different scattering conditions by empirically evaluating the statistical significance of the difference between the optimized metrics and their values estimated from a reference material designed to satisfy conditions of diffuse scattering. Furthermore, the connection of the analyses of the stationary and the non-stationary features provided a way to estimate descriptors of the tissue organization scales below and above the resolution limit imposed by the size of the acoustic pulse. The incorporation of the empirical decision method permitted an automatic selection of the estimator most adequate for the corresponding periodic spacing domain (not-resolved versus resolved spacing). This led to improvements in the accuracy and precision of estimates of the mean scatterer spacing.

The metrics studied in Chapters 2 and 3 were inadequate for discriminating between coherent scattering caused by organized tissue structures and a condition referred to as "false coherence" caused by a low concentration of randomly distributed scatterers. To address this ambiguity, we analyzed the phase non-uniformity of the backscattered echo signals, as proposed by Narayanan *et al.*,[65] and Molthen *et al*.[54]

Using this analysis we were able to improve the discrimination power of the algorithm between zones with organized scatterers and zones with a low number density of random scatterers. Also, the combination of the analysis of phase non-uniformity with the decision tests developed in this dissertation, provided an accurate method for the estimation of the mean scatterer spacing under stationary conditions.

Finally, Chapter 5 presented a preliminary application of the classification algorithm to the analysis of backscattered echo data from human breast tumors. RF echo signals from patients scanned prior to biopsies of suspicious masses were analyzed to evaluate the ability of the algorithm to discriminate between fibroadenomas and invasive ductal carcinomas. Although the limited number of subjects included in this preliminary application forbids making conclusive statements, the results showed that invasive ductal carcinomas tend to have larger areas complying with the assumptions of diffuse scattering than fibroadenomas. This suggests that invasive ductal carcinomas tend to have a more homogenously random distribution of subresolution scatterers than the fibroadenomas, and agrees with other studies that looked at parameters from incoherent and coherent scattering. This was also supported by the analysis of beam-steered echo signals, acquiring RF data during spatial compounding. Here it was shown that the studied parameters tend to be more isotropic in invasive ductal carcinomas than in fibroadenomas. In the case of fibroadenomas, results were more difficult to interpret. To help in the interpretation, a review of the results of studies of the tissue microstructure within fibroadenomas with other microscopic and imaging modalities suggested that the collagen fibers within the stromal component of this lesion type may act as the main source of scattering. Testing this hypothesis will be a topic of future research.

In summary, the most important contributions of the research presented in this dissertation to the field of Quantitative Ultrasound are the following:

- We have presented an automatic algorithm that identifies parameter estimation regions where the common assumptions of stationary echo signals and diffuse scattering are not met, thus alerting the user of possible bias in estimates of the power spectral density, as well as in the QUS parameters derived from the echo signal power spectrum. This algorithm was optimized for the

task of creating parametric images, so attention was paid to the compromise between spatial resolution and detection performance.

- By combining the analyses of both stationary and non-stationary features with the evaluation of the statistical significance of these features, the proposed algorithm offers a general approach to search for tissue organization over a wide range of scales, transitioning from subresolution features (smaller than the acoustic pulse) to resolved features (larger than the acoustic pulse). Thus, this algorithm provides a more comprehensive analysis than other approaches targeted at specific structures or body parts, such as ducts in the breast or portal triads in the liver.[110,131,134,139]
- Findings from the application of the algorithm to *in vivo* breast lesions have introduced the possible importance of anisotropy of the scattering process in breast masses, particularly to distinguish between different lesion types. The preliminary analysis presented here is one of the first studies addressing this problem *in vivo.* Results encourage its further exploration.

6.2 Significance

The contributions of this dissertation to the field of Quantitative Ultrasound are significant because they constitute a novel approach to the task of creating parametric images based on estimates of acoustic properties of tissue microstructure derived from the echo signal power spectral density. This approach goes beyond the conventional assumptions of stationary echo signals and incoherent scattering, conditions that are commonly assumed in QUS, and offers a new starting point in the analysis of backscattered echo signals. This new starting point is centered on choosing an analysis that is appropriate for the scattering source regardless of the validity or invalidity of these assumptions.

Unlike similar approaches,[126,130,145,146] the method proposed here was designed to be comprehensive in the sense that it considers a wide range of situations that could potentially lead to flawed estimations of conventional QUS parameters. These situations involve resolved and not-resolved periodic scatterers, low concentrations of random scatterers, and specular reflectors. Moreover, the selection of the metrics that

this new approach is based on was done considering the stationary or non-stationary nature of the echo signals.

In addition, given the algorithm considers the estimation of parameters related to either incoherent scattering or coherent scattering to be mutually exclusive, the parameters estimated from each scenario can now be used as independent variables for the purpose of lesion diagnosis. We expect that this will ultimately contribute to improving the specificity of medical ultrasound as a diagnostic tool for breast cancer.

6.3 Future work

The idea of collagen being an important source of scattering and the hypothesis that the techniques studied in this dissertation are sensitive to its structural properties serve as a basis for new exciting lines of research to develop in the future. From this idea, two important topics to investigate are (1) the corroboration of the link between collagen morphology and the coherent-scattering based QUS parameters and classification tasks proposed in this dissertation, and (2) the use of these parameters and the classification algorithm as an indirect method to monitor changes in the morphological features of collagen. In the context of the first topic, our group has been active at investigating the link between the morphology of collagen in tissue with QUS parameters. This investigation has been part of a protocol evaluating the feasibility of using QUS to monitor structural changes in the human cervix to predict spontaneous preterm birth. Some of the most important results of this protocol are presented in Reusch *et al.*[187] In this work, the authors compared QUS parameters based on coherent scattering (excess backscatter power loss and the integrated collapsed average of the generalized spectrum) to results from the "curvelet analysis"[193] of second harmonic generation (SHG) microscopy images obtained from *ex vivo* samples of human cervices. By performing a co-registration of QUS parametric images with SHG images the authors concluded that SHG images corroborated features observed in the QUS parametric images. In particular, zones of greater collagen alignment observed in SHG images corresponded to zones of high

backscatter power loss. Furthermore, high values of the frequency-integrated CAGS were observed at interfaces between regions with different collagen alignment, regions with periodic structures, and regions with isolated scatterers. Thus, the integrated CAGS was ambiguous for distinguishing among these structures. The work presented in this dissertation would be a useful tool to solve this ambiguity.[187]

Also, Reusch *et al.*[187] discussed the difficulty of using QUS parameters based on incoherent scattering for collagen-rich tissues such as the cervix (or the fibroadenoma in our case), because the spatial heterogeneity of collagen morphology limits the validity of the assumptions of stationary, isotropic echo signals. In order to gain understanding on the physical meaning of QUS parameters based on incoherent scattering computed in these cases, the authors suggested a comparison between the collagen-based spatial autocorrelation functions estimated from SHG images and spatial autocorrelation functions derived from ultrasound backscatter echo signals. This is motivated by the fact that the backscatter coefficient involved in the estimation of the effective scatterer diameter is proportional to the Fourier transform of the spatial correlation of the acoustic impedance function.[20] This analysis will help in the interpretation of results from the *in vivo* analysis presented and discussed in the previous chapter. This is also an area under investigation in our group.[194,195]

The second topic is based on the important role that collagen plays in the presence of malignancy. A known process associated with the development of tumors is the condensation of pre-existing collagen in regions around the tumors. This process, known as desmoplasia, has been demonstrated to play an important role in metastasis.[181,186] The stroma has been described as a "dynamic microenvironment" in which the collagenous component transmits mechanical stimuli to epithelial cells.[179] It has been demonstrated that the presence of collagen-rich stroma is necessary for the onset of the metastatic cascade, a chain of processes in which the basement membrane ruptures and tumor cells go through local invasion, intravasation, extravasation, and growth in a distant tissue.[196] In particular, it has been demonstrated that the process of local invasion occurs when cells "make use" of collagen fibers as pathways to reach blood vessels involved in intravasation.[196,197] Furthermore, collagen around tumors

undergoes significant structural changes to be able to serve as a migration pathway for the malignant cells.

The use of SHG microscopy for the study of collagen morphology in the extracellular matrix of breast tumors has been the subject of a collaborative work between the Laboratory for Optical and Computational Instrumentation and the Laboratory for Cell and Molecular Biology, both part of the University of Wisconsin. This collaboration has led to very interesting findings. First, patterns of collagen alignment observed in SHG images were linked to the progression of invasion of breast tumors.[177-179] This was done by establishing a classification system for different collagen morphologies known as the Tumor-Associated Collagen Signature (TACS). This classification consists of three categories: TACS-1 corresponds to zones of collagen concentration that occur around early tumors and which are composed of curved, relaxed collagen fibers. TACS-2 corresponds to straightened fibers aligned around the boundary of the tumor and is associated with later stages in tumor development. Finally, TACS-3 corresponds to a reorientation of the straight collagen fibers to penetrate the basement membrane and radiate from the center of the tumor.[177,178] This morphology has been observed in metastatic tumors, which agrees with the observation that tumor cells need collagen fibers to "crawl" from the tumor to the nearby blood vessels.[162,188] The transition from TACS-1 to TACS-3 is gradual.[196] It has been also demonstrated that TACS-3 is an independent prognostic marker for disease-free and disease specific survival. In a another study,[177] the TACS-3 pattern was not detected around the entire tumor, but only in localized zones in which cell invasion occurs. However, the presence of even a small TACS-3 region was associated with relapse and poor prognosis.[177] More recently, J. Bredfeldt, a fellow Medical Physics student, proposed in his dissertation quantitative methods to automatize the assessment of the TACS classification from SHG images.[193]

At this moment, the use of second harmonic generation as a method for routine biopsy is impractical due to its cost and the time needed to scan the tissue.[188] Thus, if these prospective lines of investigation result in a successful correlation between coherent-scattering based QUS parameters and morphological properties of collagen in breast lesions, particularly the TACS classification, these parameters could be

used as a method for the indirect assessment of tumor progression and, possibly, as a tool to evaluate prognosis. Parametric images of coherent-scattering based QUS parameters could then be of interest for this task, since they allow simultaneous analysis of the tumor interior, its border, and its surrounding region. Furthermore, the spatial information provided by parametric images can also exploit tools from "texture analysis" in order to obtain new parameters of diagnostic value related to the spatial heterogeneity of the collagen morphology.[19] Along this line, Sadeghi-Naini *et al*.,[198] applied tools of texture analysis to parametric images based on incoherent scattering parameters to monitor neo-adjuvant chemotherapy of patients with advanced breast cancer. The incorporation of parameters based on coherent-scattering and texture analysis can increase the sensitivity and specificity of the tools derived in this dissertation.[164]

All these ideas encourage further collaborations among our laboratory, the Laboratory for Optical and Computational Instrumentation, and the Laboratory for Cell and Molecular Biology, to bring together the strength of each imaging and microscopy modality to shed insight into the relationships between QUS parameters and tissue microstructure. A deeper knowledge about the relationship between breast tissue microstructure and QUS parameters based on incoherent and coherent scattering could be further used in the selection of appropriate parameters that could be incorporated in a multi-variable lesion classifier aimed at improving the diagnostic performance of ultrasound. Currently, our group is working on the development of a Bayesian classifier based on three incoherent-scattering QUS parameters: the attenuation coefficient, the effective scatterer diameter, and an inhomogeneity index obtained from the spatial variability of the scatterer diameter estimates.[26] We foresee that the inclusion of coherent-scattering based parameters, as well as the reduction of bias in the estimates of incoherent-scattering parameters resulting from their estimation under correct assumptions, will eventually lead to improvements in the performance of the classifier. Furthermore, to our knowledge, the results presented here constitute the first attempt at assessing the anisotropy of coherent-scattering based parameters for the analysis of human breast lesions *in vivo*. Based on the observed difference in the variation of the parameters among steering angles between the fibroadenomas and carcinomas, we predict that the

incorporation of parameters related to the anisotropy of coherent scattering will contribute to the improvement of the diagnostic power of the Bayesian classifier.

6.4 Conclusion

The structural complexity of breast tissue introduces difficulties in the quantification of conventional quantitative ultrasound parameters based on the estimation of the power spectral density and describing the scattering of the acoustic pulse. The algorithm developed in this dissertation provides a way to deal with some of these difficulties, particularly when they are the result of a coherent scattering process. This algorithm was designed under the philosophy that when these difficulties are present, the analysis of the echo signals should not circumvent them but provide information that describes the underlying scattering process. In this way, the backscattered echo data and the valuable information it carries is fully exploited. Although initially conceived for applications in the breast, this algorithm could be of potential interest to analyze other tissues in which some level of microstructural organization could be present, such as muscle, tendons, or cervix. This more comprehensive approach to the problem of quantifying parameters describing structural and acoustic properties of tissue will hopefully contribute to a better understanding of the these properties and how they are affected by different pathologies. This knowledge will certainly advance the diagnostic applications of Quantitative Ultrasound. Future work will further refine the tools developed here and explore the connections between the scattering features they are sensitive to and tissue microstructure studied through microscopy.

References

1 American Cancer Society. Cancer Facts & Figures 2014. Atlanta, (GA): American Cancer Society; c2014

2 American Cancer Society. Breast Cancer Facts & Figures 2013-2014 (GA). Atlanta: American Cancer Society, Inc. c2013

3 Bushberg JT, Siebert JA, Leidholdt EM, and Boone JM, The Essential Physics of Medical Imaging. Philadelphia (PA): Lippincott, Williams & Wilkins; c2002

4 Park JM, Franken EA, Garg M, Fajardo LL, and Niklason LT, Breast tomosynthesis: present considerations and future applications, *Radiographics*, 2007; 27 (1), S231-S240

5 Bick U and Diekmann F, "Digital mammography: What do we and what don't we know?," European *Radiology*, 2007; 17 (8), 1931-1942

6 Gartlehner G, Thaler K, Chapman A, et al., Mammography in combination with breast ultrasonography versus mammography for breast cancer screening in women at average risk, *Cochrane Database of Systematic* Reviews 4, 2013; 4. DOI: 10.1002/14751868.CD009632.pub2

7 Nothacker M, Duda V, M. Hahn M, et al., Early detection of breast cancer: benefits and risks of supplemental breast ultrasound in asymptomatic women with mammographically dense breast tissue. A systematic review, *BMC Cancer*, 2009; 9 (1), 335-343

8 Zagzebski JA, Lu ZF, and Yao LX, Quantitative ultrasound imaging: in vivo results in normal liver, *Ultrasonic Imaging*, 1993; 15 (4), 335-351

9 Mendelson EB, Berg WA, and Merrit CRB, Toward a standardized breast ultrasound lexicon, BI-RADS: Ultrasound, *Seminars in Roentgenology*, 2001; 36 (3), 217-225

10 American College of Radiology, BI-RADS: ultrasound. 1st ed. In: Breast imaging reporting and data system: BI-RADS atlas, 4th ed. Reston, VA. *American College of Radiology*, 2003

11 Levy L, Suissa M, Chiche JF, Teman G, Martin B, BIRADS ultrasonography, European Journal of *Radiology* 2007, 61 (2): 202-211

12 Hong AS, Rosen EL, Soo MS, and Baker JA, BI-RADS for sonography: Positive and negative predictive values of sonographic features, *Am. J. Roentgenol*., 2005; 184 (4), 1260-1265

13 Abdullah N, Mesuroelle B, El-Khoury M, and Kao E, Breast Imaging Reporting and Data System Lexicon for US: Interobserver agreement for assessment of breast masses, *Radiology*, 2009; 252 (3), 665-672

14 Calas MJG, Almeida RMVR, Gutfilen B, and Pereira WCA, Interobserver concordance in the BI-RADS classification of breast ultrasound exams, *Clinics*, 2012; 67 (2), 186-189

15 Lee HJ, Kim EK, Kim MJ, Youk JH, Lee JY, Kang DR, and Oh KK, Observer variability of breast imaging reporting and data system (BI-RADS) for breast ultrasound, *Eur. J. of Radiology*, 2008; 65 (2), 293-298

16 Calas MJG, Almeida RMVR, Gutfilen B, and Pereira WCA, Interobserver concordance in the BI-RADS classification of breast ultrasound exams, *Clinics*, 2012; 67 (2), 186-189

17 Oelze ML, Quantitative ultrasound techniques and improvements to diagnostic ultrasonic imaging, Ultrasonics Symposium (IUS),IEEE International 2012, 232-239

18 Nam K, Zagzebski JA, and Hall TJ, Quantitative assessment of in vivo breast masses using ultrasound attenuation and backscatter, *Ultrason. Imaging*, 2013; 35 (2), 147-162

19 Thijssen JM, Ultrasonic speckle formation, analysis and processing applied to tissue characterization, *Pattern Recognition Letters*, 2003; 24 (4), 659-675

20 Insana MF and Brown DG, Acoustic scattering theory applied to soft biological tissues, in Ultrasonic Scattering in Biological Tissues, Eds. KK Shung and GA Thieme, Boca Raton (FL): CRC Press, c1993

21 Wild JJ and Reid JM, Further pilot echographic studies on the histologic structure of tumors of the living intact human breast, *Am. J. Pathol*., 1952; 28 (5), 839-861

22 Lizzi FL, Alam K, Mikaelian S, Lee P, and Feleppa EJ, On the statistics of ultrasonic spectral parameters, *Ultrasound Med. Biol*., 2006; 32 (11), 1681-1695

23 D'Astous FT and Foster FS, Frequency dependence of ultrasound attenuation and backscatter in breast tissue, *Ultrasound Med. Biol*., 1986; 12 (10), 795-808

24 Rosado-Mendez IM, Nam K, Hall TJ, and Zagzebski JA, Task-oriented comparison of power spectral density estimation methods for quantifying acoustic attenuation in diagnostic ultrasound using a reference phantom method, *Ultrason. Imaging*, 2013; 35 (3), 214-234

25 Kaffas AE, Giles A, and Czarnota GJ, High-frequency 3D ultrasound for characterizing overall response to vascular targeting strategies, Ultrasonic Imaging and Tissue Characterization Symposium, Arlington, VA. 2013

26 Gerges-Nasief H, Rosado-Mendez IM, Kohn S, Zagzebski JA, and Hall TJ, A Bayesian classifier for differentiating between fibroadenomas and malignant breast tumors, *J. Ultrasound Med*., submitted 2013

27 Fink MA and Cardoso JF, Diffraction effects in pulse-echo measurements, *IEEE Trans. Son. Ultrason*. 1984; 31 (4): 313-329

28 Wagner RF, Smith SW, Sandrik JM, and Lopez H, Statistics of speckle in ultrasound B-scans, *IEEE Trans. Sonics Ultrason*., 1983; 30 (3), 157-164

29 Wagner RF, Insana MF, and Brown DG, Statistical properties of radio-frequency and envelope-detected signals with applications to medical ultrasound, *J. Opt. Soc. Am*., 1987; 4 (5), 910-922

30 Insana MF, Wagner RF, Brown DG, and Hall TJ, Describing small-scale structure in random media using pulse echo ultrasound, *J. Acoust. Soc. Am*., 1990; 87 (1), 179-192

31 Anderson ME, Soo MSC, and Trahey GE, In vivo breast tissue backscatter measurements with 7.5 and 10-MHz transducers, *Ultrasound Med. Biol*., 2001; 27 (1), 75-81

32 Lu ZF, Zagzebski JA, and Lee FT, Ultrasound backscatter and attenuation in human liver with diffuse disease, Ultrasound Med. Biol., 1999; 25 (7): 1047-1054

33 Wilson T, Chen Q, Zagzebski JA, Varghese T, and VanMiddlesworth L, Initial clinical experience imaging scatterer size and strain in thyroid nodules, *J. Ultrasound Med*., 2006; 25 (8): 1021-1029

34 Wear KA, Frequency dependence of ultrasonic backscatter from human trabecular bone: theory and experiments, *J. Acoust. Soc. Am.*, 1999; 106 (6), 3659-3664

35 Madsen EL, Dong F, Frank GR, et al., Interlaboratory comparison of ultrasonic backscatter, attenuation, and speed measurements, *J. Ultrasound Med*., 1999; 18 (9), 615-631

36 Wear KA, Stiles TA, Frank GR, et al., Interlaboratory comparison of ultrasonic backscatter coefficient measurements: image formation and interpretation, *J. Ultrasound Med*., 2005; 24 (9), 1245-1260

37 Wirtzfeld LA, Goshal G, Hafez ZT, et al. Cross-imaging platform comparison of ultrasonic backscatter coefficient measurement of live rat tumors, *J. Ultrasound Med*., 2010; 29 (7), 1118-1124

38 Nam K, Rosado-Mendez IM, Wirtzfeld LA, et al., Ultrasonic attenuation and backscatter coefficient estimates of rodent-tumor-mimicking structures: Comparison of results among clinical scanners, *Ultrason. Imaging*, 2011; 33 (4), 233-250

39 Oelze ML, O'Brien, Jr WD, Blue JP, and Zachary JF, Differentiation and characterization of rat mammary fibroadenomas and 4T1 mouse carcinomas using quantitative ultrasound imaging, *IEEE Trans. Med. Imaging*, 2004; 23 (6), 764-771

40 Yao LX, Zagzebski JA, and Madsen EL, Backscatter coefficient measurements using a reference phantom to extract depth-dependent instrumentation factors, *Ultrason. Imaging*, 1990; 12 (1), 58-70

41 Wagner RF, Insana MF, Brown DG, Unified approach to the detection and classification of speckle texture in diagnostic ultrasound, *Optical Engineering*, 1986; 25 (6), 738-742

42 Myers KJ, Kyprianou LS, and Park S., Wagner's unified theory of image quality: Three decades later, *Advances in Medical Physics*, 2010; 144-158

43 Vautard R and Ghil M, Singular spectrum analysis in nonlinear dynamics, with applications to paleoclimatic time series, Physica D, 1989; 35 (3), 395-424

44 Bozzo E, Carniel R, and Fasino D, Relationship between singular spectrum analysis and Fourier Analysis. Theory and application to the monitoring of volcanic activity, *Computers and Mathematics with applications*, 2010; 60 (3), 812-820

45 Chaturvedi P and Insana MF, Error bounds on ultrasonic scatterer size estimates, *J. Acoust. Soc. Am.*, 1996; 100 (1), 392-399

46 King MR, Anderson JJ, Herd MT, et al., Ultrasonic backscatter coefficients for weakly scattering, agar spheres in agar phantoms, *J. Acoust. Soc. Am.*, 2010; 129 (2), 903-908

47 Nam K, Rosado-Mendez IM, Wirtzfeld LA, Krumar V, Madsen EL, et al., Cross imaging system comparison of backscatter coefficient estimates from a tissue-mimicking material, *J. Acoust. Soc. Am.*, 2012; 133 (3): 1329-1334

48 Nam K, Rosado-Mendez IM, Wirtzfeld LA, Goshal G, Pawlicki AD, et al., Comparison of ultrasound attenuation and backscatter estimates in layered tissue-mimicking phantoms among three clinical scanner, *Ultrasonic Imaging*, 2012; 34 (4): 209-221

49 Wear KA, Wagner RF, Insana MF, and Hall TJ, Application of autoregressive spectral analysis to cepstral estimation of mean scatterer spacing, *IEEE Trans. Ultrason. Ferroelect. Freq. Control*, 1993; 40 (1), 50-58

50 Varghese T and Donohue KD, Mean-scatterer spacing estimates with spectral correlation, *J. Acoust. Soc. Am.*, 1994; 96 (6), 3504-3515

51 Donohue KD, Huang L, Burks T, Forsberg F, and Piccoli CW, Tissue classification with generalized spectrum parameters, *Ultrasound Med. Biol.*, 2001; 27 (11), 1515-1524

52 Insana MF, Wagner RF, Garra BS, Brown DG, and Shawker TH, Analysis of ultrasound image texture via generalized Rician statistics, *Optical Engineering*, 1986; 25 (6), 743-748

53 Pereira WCA and Maciel CD, Performance of ultrasound echo decomposition using singular spectrum analysis, *Ultrasound Med. Biol.*, 2001; 27 (9), 1231-1238

54 Molthen RC, Narayanan VM, Shankar PM, Reid JM, Genis V, Forsberg F, Halpern EJ, and Goldberg BB, Using phase information in ultrasonic backscatter for in vivo liver analysis, *Ultrasound Med. Biol.*, 1998; 24 (1),79-91

55 Dutt V and Greenleaf JF, Ultrasound echo envelope analysis using a homodyned K distribution signal model, *Ultrason. Imaging*, 1994; 16 (4), 265-287

56 Hruska DP and Oelze ML, Improved parameter estimates based on the homodyned K Distribution, *IEEE Trans. Ultrason. Ferroelect. Freq. Control*, 2009; 56 (11), 2471-2481

57 Madsen EL, Insana MF, and Zagzebski JA, Method of data reduction for accurate determination of acoustic backscatter coefficients, *J. Acoust. Soc. Am.*, 1984; 76 (3), 913-923

58 Destrempes F and Cloutier G, A critical review and uniformized representation of statistical distributions modeling the ultrasound echo envelope, *Ultrasound Med. Biol.*, 2010; 36 (7), 1037-1051

59 Shankar PM, A Model for ultrasonic scattering from tissues based on the K distribution, *Phys. Med. Biol.*, 1995; 40 (10), 1643-1659

60 Burckhardt CB, Speckle in ultrasound B-mode scans, *IEEE Trans. Sonics. Ultrason*. 1978; 25 (1), 1-6

61 Thuthill TA, Sperry RH, and Parker KJ, Deviations from Rayleigh statistics in ultrasonic speckle, *Ultrason. Imaging*, 1988; 10 (2), 81-89

62 Molthen RC, Shankar PM, and Reid JM, Characterization of ultrasonic B-scans using non-Rayleigh statistics, *Ultrasound Med. Biol*., 1995; 21 (2), 162-171

63 Tsui PH, and Wang SH, The effect of transducer characteristics on the estimation of Nakagami parameter as a function of scatterer concentration, *Ultrasound Med Biol*., 2004; 30 (10), 1355- 1363

64 Jakeman E and Pusey PN, Significance of K Distributions in Scattering Experiments, *Physical Review Letters*, 1978; 40 (9), 546-550

65 Narayanan VM, Shankar PM, and Reid JM, Non-Rayleigh Statistics of Ultrasonic Backscattered Signals, *IEEE Trans. Ultra. Ferroelec. Freq. Control*, 1994; 41 (6), 845-852

66 Jakeman E and Tough RJA, Generalized K distribution: a statistical model for weak scattering, *J. Opt. Soc. Am*. 1987; 4 (9), 1774-1782

67 Jakeman E, On the statistics of K-distributed noise, *J. Phys. A: Math. Gen*. 1980; 13 (1), 31-48

68 Destrempes F and Cloutier G, Review of envelope statistics model for quantitative ultrasound imaging and tissue characterization, in Quantitative Ultrasound in Soft Tissues, eds. Jonathan Mamou, and M. L. Oelze, Springer 2013; 219-274

69 Goodman JW, Statistical properties of laser speckle patterns, Laser Speckle and Related Phenomena, JC Dainty, ed., Springer-Verlag, Berlin, 1975

70 Jakeman E, Speckle statistics with a small number of scatterers, *Optical Engineering*, 1984; 23 (1), 453-461

71 Shankar PM, Reid JM, Ortega H, Piccoli CW, and Goldberg BB, Use of Non-Rayleigh statistics for the identification of tumors in ultrasonic B-scans of the breast, *IEEE Trans. Med. Imaging*, 1993; 12 (4), 687-692

72 Shankar PM, Molthen R, Narayanan VM, Reid JM, Genis V, Forsberg F, Piccoli CW, Lindenmayer AE, and Goldberg BB, Studies on the use of non-Rayleigh statistics for ultrasonic tissue characterization, *Ultrasound Med. Biol*., 1996; 22 (7): 873-882

73 Tadayon H., Homodyned-k probability density function. Available at http://www.mathworks. com/matlabcentral/fileexchange/36632-homodyned-k-probability-density-function.

74 Kay SM, Fundamentals of statistical signal processing: Estimation theory, Prentice Hall: Upper Saddle River, NJ. 1993

75 Shankar PM, The use of the compound probability density function in ultrasonic tissue characterization, *Phys. Med. Biol*., 2004; 49 (6), 1007-1015

76 Tsui PH and Chang CC, Imaging local scatterer concentrations by the Nakagami statistical model, *Ultrasound Med. Biol*., 2007; 33 (4), 608-619

77 Shankar PM, A general statistical model for ultrasonic backscattering from tissues, *IEEE Trans. Ultrason. Ferroelect. Freq. Control*, 2000; 47 (3), 727-736

78 Nakagami M, Statistical character of short-wave fading, J. Inst. Elec. Commun. Eng. Japan, 1943; 27, 146-150

79 Shankar PM, Ultrasonic tissue characterization using a generalized Nakagami model, *IEEE Trans. Ultrason. Ferroelec. Freq. Control*, 2001; 48 (6), 1716-1720

80 Nakagami M, The m distribution: A general formula of intensity distribution in rapid fading, in Statistical methods on radio wave propagation, ed. W. C. Hoffman, Pergamon Press: NY, 1960, pp. 3-36

81 Wilks SS, The large-sample distribution of the likelihood ratio for testing composite hypotheses, *The Annals of Mathematical Statistics*, 1938; 9 (1), 60-62

82 Nowak R, Lecture 11: The Generalized Likelihood Ratio, Lecture notes of ECE 830: Statistical Signal Processing, Available at http://nowak.ece.wisc.edu/ece830/

83 Lebanon L, Riemannian geometry and statistical machine learning, Ph. D. Thesis, School of Computer Science, Carnegie Mellon University, January 31, 2005. Available at http://www.lti.cs.cmu.edu/research/thesis/2005/guy_lebanon.pdf

84 Nam K, Rosado-Mendez IM, Rubert NC, Madsen EL, Zagzebski JA, and Hall TJ, Ultrasound attenuation measurements using a reference phantom with sound speed mismatch, *Ultrason. Imaging*, 2011; 33 (4), 251-263

85 Omari EA, Varghese T, Madsen EL, and Frank G, Evaluation of the impact of backscatter intensity variations on ultrasound attenuation estimation, *Med. Phys*., 2013, 40 (8), 082904

86 Ashfaq M, Brunke SS, Dahl JJ, Ermet H, Hansen C, and Insana MF, An ultrasound research interface for a clinical system, *IEEE Trans. Ultrason. Ferroelec. Freq. Control*, 2006; 53 (10), 1769-1781

87 Labyed Y, Bigelow TA. Estimating the total ultrasound attenuation along the propagation path by using a reference phantom. *J. Acoust. Soc. Am*., 2010; 129 (5), 3232–3238

88 Liu W and Zagzebski JA. Trade-offs in data acquisition and processing parameters for backscatter and scatterer size estimations, *IEEE Trans. Ultrason. Ferroelectr. Freq. Control*. 2010; 57 (2), 340–341

89 Hall TJ, Insana MF, Harrison LA, and Cox GG. Ultrasonic measurement of glomerular diameters in normal adult humans, *Ultrasound Med. Biol*. 1996; 22 (8), 987–997

90 O'Donnel M, Silverstein SD. Optimum displacement for compound image generation in medical ultrasound, *IEEE Trans. Ultrason. Ferroelectr. Freq. Control*, 1998; 35 (4), 470–476

91 Trahey GE, Smith SW, von Ramm OT, Speckle pattern correlation with lateral aperture translation: Experimental results and implications for spatial compounding, *IEEE Trans. Ultrason. Ferroelectr. Freq. Control*, 1986; 33 (3), 257–264

92 Herd MT, Hall TJ, Jiang J, Zagzebski JA, Improving the statistics of quantitative ultrasound techniques with deformation compounding: an experimental study. *Ultrasound Med. Biol*. 2011; 37 (12), 2066–2074

93 Varghese T and Donohue K, Estimating mean scatterer spacing with the frequency-smoothed spectral autocorrelation, *IEEE Trans. Ultrason. Ferroelectr. Freq. Control* 1995, 42 (3): 451-463

94 Shankar PM, A Compound scattering pdf for the ultrasonic echo envelope and its relationship to K and Nakagami distributions, *IEEE Trans. Ultrason. Ferroelect. Freq. Control*, 2003; 50 (3), 339-343

95 Larrue A and Noble JA, Modeling of errors in Nakagami imaging: Illustration of breast mass characterization, *Ultrasound Med. Bio*l., 2014; 40 (5), 917-930

96 Zagzebski JA, Essentials of Ultrasound Physics, St. Louis (MO): Mosby, c1996, 36-38 p.

97 Hayashi N, Tamaki N, Senda M, et al., A new method of measuring in vivo sound speed in the reflection mode, *J. Clin. Ultrasound*, 1988; 16 (2), 87-93

98 Anderson ME, McKeag MS, and Trahey GE, The impact of sound speed errors on medical ultrasound imaging, *J. Acoust. Soc. Am*., 2000; 107 (6), 3540-3548

99 Napolitano D, Chou CH, McLaughlin G, et al., Sound speed correction in ultrasound imaging, *Ultrasonics*, 2006; 44, e43-e46

100 McLaughlin GW, Practical aberration correction methods, *Ultrasound*, 2007; 15 (2), 99-104

101 Yoon C, Y. Lee Y, Chang JH, et al., In vitro estimation of mean sound speed based on minimum average phase variance in medical ultrasound imaging, *Ultrasonics*, 2011; 51 (7), 795-802

102 Cloostermans MJ, Verhoef WA, Thijssen JM. Generalized description and tracking estimation of the frequency dependent attenuation of ultrasound in biological tissues, *Ultrasonic Imaging*, 1985; 7 (2), 134–142

103 Rosado-Mendez IM, Nam K, Madsen E, Hall TJ, and Zagzebski JA, Pulse-echo sound speed estimation using second order speckle statistics, *AIP Conference Proceedings*, 2012; 1494 (1), 66-69

104 Robinson DE, Ophir J, Wilson LS, and Chen CF, Pulse-echo ultrasound speed measurements: progress and prospects, *Ultrasound Med. Biol*., 1991; 17 (6), 633-646

105 Thomson DJ, Spectrum Estimation and Harmonic Analysis, *Proceedings of the IEEE*, 1982; 70 (9), 1055-1096

106 Loeve M, Probability Theory, Princeton (NJ):Van Nostrand, 1963

107 Lu ZF, Zagzebski JA, and Lee FT, Ultrasound backscatter and attenuation in human liver with diffuse disease, *Ultrasound Med. Biol*.,1999; 25 (7), 1047-1054

108 Percival DB and Walden AT, Multitaper and Conventional Univariate Techniques, Cambridge University Press: Cambridge, UK, 1993

109 Haykin S, and Thomson DJ, Signal Detection in a nonstationary environment reformulated as an adaptive pattern classification problem, *Proceedings of the IEEE*, 1998; 86 (11), 2325-2344

110 Donohue KD, Fosberg F, Piccolli CW, and Goldberg BB, Analysis and classification of tissue with scatterer structure templates, *IEEE Trans. Ultrason. Ferroelect. Freq. Control*, 1999; 46 (2), 300-310

111 Mellors RJ, Vernon FL, and Thomson DJ, Detection of dispersive signals using multitaper –dual-frequency coherence, *Geophysical Journal International*, 1998; 135.1, 146-154

112 Gerr NL, and Allen JC, The generalized spectrum and spectral coherence of harmonizable time series, *Digital Signal Processing*, 1994; 4 (4), 222-238

113 Vernon FL, Mellors FJ, and Thomson DJ, Broadband signal enhancement of seismic array data: application to long period surface waves and high-frequency wave fields, at http://oai.dtic.mil/oai/oai?verb=getRecord&metadataPrefix=html&identifier=ADA343629. Consulted Feb. 26, 2014

114 Donohue KD, Bressler JM, Varghese T, and Bilgutay NM, Spectral correlation in ultrasonic pulse echo signal processing, *IEEE Trans. Ultrason. Ferroelect. Freq. Control*, 1993; 40 (4), 330-337

115 Donohue KD, Huang L, Genis V, and Forsberg F, Duct size detection and estimation in breast tissue, Ultrasonics Symposium, IEEE International 1999; 1363-1366

116 Donohue KD, Varghese T, and N. M. Bilgutay, Spectral redundancy in characterizing scatterer structures, *Review of Progress in Quantitative Nondestructive Evaluation*, 1994; 13, 779-786

117 Kuc R, Kiafar H, and O'Donnel M, Presence of cepstral peak in random reflected ultrasound signals, *Ultrasonic Imaging*, 1986; 8 (3): 196-212

118 Landini L and Verrazani L, Spectral characterization of tissues microstructure by ultrasounds: A stochastic approach, *IEEE Trans. Ultrason. Ferroelect. Freq. Control*, 1990; 37 (5), 448-456

119 Huang L, Donohue KD, Genis V, and Forsberg F, Duct detection and wall spacing estimation in breast tissue, *Ultrason. Imaging*, 2000; 22 (3), 138-153

120 Wear KA, Wagner RF, Garra BS, High resolution ultrasonic backscatter coefficient estimation based on autoregressive spectral estimation using Burg's algorithm, *IEEE. Trans. Med. Imag*., 1994; 13 (3): 500-507

121 Simon C, Shien J, Seip R, and Ebbini ES, A robust and computationally efficient algorithm for Mean Scatterer Spacing Estimation, *IEEE Trans. Ultrason. Ferroelectr. Freq. Control*, 1997; 44 (4), 882-894

122 Park J, Linberg CR, and Vernon FL, Multitaper Spectral Analysis of High-Frequency Seismograms, *Journal of Geophysical Research*, 1987; 92 (B12), 675-684

123 Harris FJ, On the use of windows for harmonic analysis with the discrete Fourier transform, *Proc. IEEE*, 1978; 66 (1), 51-83

124 Slepian D, Prolate spheroidal wave functions, Fourier analysis, and uncertainty – V. The Discrete Case, *Bell System Technical Journal*, 1978; 57 (5), 1381-1440

125 Lanzerotti LJ, Thomson DJ, Meloni A, Medford LV, and Maclennan CJ, Electromagnetic study of the Atlantic continental margin using a section of the transatlantic cable, *Journal of Geophysical Research*, 1986; 91 (B7), 7417-7427

126 Luchies AC, Goshal G, O'Brien WD, and Oelze ML, Quantitative ultrasonic characterization of diffuse scatterers in the presence of structures that produce coherent echoes, *IEEE Trans. Ultrason. Ferroelectr. Freq. Control*, 2012; 59 (5), 893-904

127 Welch PD, The use of fast Fourier transform for the estimation of power spectra: A method based on time averaging over short, modified periodograms, *IEEE Trans. Audio Electroacoust*., 1967; 15 (2), 70-73

128 Donohue KD, Ultrasonic scatterer structure classification with the generalized spectrum, Acoustics, Speech, and Signal Processing, 2001. Proceedings (ICASSP'01). 2001 IEEE International Conference on. 2001, 6; 3401-3404

129 Gefen S, Tretiak OJ, Piccoli CW, et al., ROC Analysis of ultrasound tissue characterization classifiers for breast cancer diagnosis, *IEEE Trans. Med. Imaging*, 2003; 22.2, 171-1787

130 Donohue KD, Huang L, Georgiou G, et al., Malignant and benign breast tissue classification performance using a scatterer structure preclassifier, *IEEE Trans. Ultrason. Ferroelectr. Freq. Control*, 2003; 50 (6), 724-729

131 Park J, D'Hondt SL, King JW, and Gibson C, Late cretaceous precessional cycles in double time: A warm-earth Milankovitch Response, *Science*, 1993; 261 (5127), 1431-1434

132 Hurd HL, and Gerr NL, Graphical methods for determining the presence of periodic correlation, *Journal of Time Series Analysis*, 1991; 12 (4), 337-350

133 Rubert N and Varghese T, Mean scatterer spacing estimation using multi-taper coherence, *IEEE Trans. Ultrason. Ferroelectr. Freq. Control*, 2013; 60 (6), 1061-1073

134 Machado CB, Pereira WCA, Meziri M, and Laugier P, Characterization of in vitro healthy and pathological human liver tissue periodicity using backscattered ultrasound signals, *Ultrasound Med. Biol.*, 2006; 32 (5), 649-657

135 Maciel CD and Pereira WCA, RF ultrasound echo decomposition using singular-spectrum analysis, *Acoustical Imaging*, 2000; 24, 107-112

136 Pereira WCA, Abdelwahab A, Bridal SL, and Laugier P, Singular spectrum anlaysis applied to 20MHz backscattered ultrasound signals from periodic and quasi-periodic phantoms, *Acoustical Imaging*, 2002; 26, 239-246

137 Pereira WCA, Bridal SL, Coron A, and Laugier P, Singular spectrum analysis applied to backscattered ultrasound signals from in vitro human cancellous bone specimens, *IEEE Trans. Ultrason. Ferroelect. Freq. Control, 2004*; 51 (3), 302-312

138 Machado CB, Pereira WCA, Meziri M and Laugier P, Characterization of in vitro healthy and pathological human liver tissue periodicity applying singular spectrum anlaysis to backscattered ultrasound, International Ultrasonics Symposium, 2005 Proceedings IEEE, 1679-1682

139 Machado CB, Padilla, F, Laugier P, Pereira, WCA, and Meziri M, Periodicity estimation under variations of scatterer spacings, thickness and pulse frequency: A 2D simulation study, International Ultrasonics Symposium (IUS), 2009 Proceedings IEEE .2240-2243

140 Ng J, Prager R, Kinsbury N, Treece G, and Gee A, Modeling ultrasound imaging as a linear shift-variant system, *IEEE Trans. Ultrason. Ferroelect. Freq. Control*, 2006; 53 (3), 549-563

141 Hassani H, Singular Spectrum Analysis: Methodology and Comparison, *Journal of Data Science*, 2007; 5 (2), 239-257

142 Oelze ML and O'Brien WD, Defining optimal axial and lateral resolution for estimating scatterer properties from volumes using ultrasound backscatter, *J. Acoust. Soc. Am.*, 2004; 115 (6), 3226-3234

143 Gubner JA. Probability and Random Processes for Electrical and Computer Engineers. Cambridge (UK): Cambridge University Press; 2006. 184p.

144 Scharf LL. Statistical Signal Processing. Reading, MA: Addison-Wesley; 1995, 105p.

145 Georgiou G and Cohen FS, Statistical characterization of diffuse scattering in ultrasound images, *IEEE Trans. Ultrason. Ferroelect. Freq. Control*, 1998; 45 (1), 57-64

146 Georgiou G and Cohen FS, Unsupervised segmentation of RF echo into regions with different scattering characteristics, *IEEE Trans. Ultrason. Ferroelect. Freq. Control*, 1998; 45 (3), 779-787

147 Cohen FS, Georgiou G, and Halpern EJ, WOLD decomposition of the backscatter echo in ultrasound images of soft tissue organs, *IEEE Trans. Ultrason. Ferroelect. Freq. Control*, 1997; 44 (2), 460-472

148 Georgiou G, and Cohen FS, Tissue characterization using the continuous wavelet transform, Part I: Decomposition method, *IEEE Trans. Ultrason. Ferroelect. Freq. Control*, 2001; 48 (2), 355-363

149 Georgiou G, and Cohen FS, Piccoli CW, Forsberg F, and Goldberg BB, Tissue characterization using the continuous wavelet transform, Part II: Application on breast RF data, *IEEE Trans. Ultrason. Ferroelect. Freq. Control*, 2001; 48 (2), 364-373

150 Madsen EL, Hobson AM, Shi H, Varghese T, Frank GR. Stability of heterogeneous elastography phantoms made from oil dispersions in aqueous gels, *Ultrasound Med. Biol*. 2006; 32 (2), 261–270

151 Guray M and Sahin AA, Benign breast diseases: Classification, diagnosis and management, *The Oncologist*, 2006; 11 (5), 435-449

152 Skaane P, and Knut E, Analysis of sonographic features in the differentiation of fibroadenoma and invasive ductal carcinoma, *Am J. Roentgenol*., 1998; 171 (1), 109-114

153 BreastCancer.Org, "IDC-Invasive Ductal Carcinoma", at http://www.breastcancer.org/symptoms /types/idc, consulted on Feb. 26, 2014

154 Mayer M and Batur P, Breast disorders and breast screening, at http://www.cleveland clinicmeded.com/medicalpubs/diseasemanagement/womens-health/breast-disorders-and-cancer-screening/ (Fig 1.)

155 Gray H, Anatomy, Descriptive and Surgical, TP Pick and R Howden, eds., New York (NY): Bounty, c1978

156 Iglesias A, Arias M, Santiago P, Rodriguez M, Mañas J, Saborido C, Benign breast lesions that simulate malignancy: Magnetic resonance imaging with radiologic-pathologic correlation, *Curr. Probl. Diagn. Radiol*., 2007; 36 (2), 66-82

157 157 Cole-Beuglet C, Soriano RZ, Kurtz AB, Goldberg BB, Fibroadenoma of the breast: Sonomammography correlated with pathology in 123 patients, *Am. J. Roentgenol*., 1983; 141 (2), 369-375

158 Gohering C and Moraiba A, Epidemiology of benign breast disease, with special attention to histologic types, *Epidemiol. Rev*., 1997; 19 (2), 310-327

159 Yang Y, Li F, Gao L, Wang Z, Thrall MJ, Shen SS, Wong KK, and Wong STC, Differential diagnosis of breast cancer using quantitative, label-free and molecular vibrational imaging, *Biomed. Opt. Express*, 2011; 2 (8), 2161-2175

160 Kuijper A, Mommers ECM, Van der Wall E, Van Diest PJ, Histopathology of fibroadenoma of the breast, *Am. J. Clin. Pathol*., 2001; 115(5), 736-742

161 Hirose M, Hashizume T, Seino N, Kubota H, Nobusawa H, Gokan T, Atlas of breast magnetic resonance imaging, *Curr. Probl. Diagn. Radiol*., 2007; 36 (2), 51-65

162 Burke K, Tang P, and Brown E, Second harmonic generation reveals matrix alterations during breast tumor progression, *J. Biomed. Opt*., 2013, 18 (3): 031106-031106

163 Oelze ML and Zachary JF, Examination of cancer in mouse models using high-frequency quantitative ultrasound, *Ultrasound Med. Biol*. 2006; 32 (11), 1649-1658

164 Liao YY, Tsui PH, Li CH, et al., Classification of scattering media within benign and malignant breast tumors based on ultrasound texture-feature-based and Nakagami-parameter images, *Med. Phys*. 2011; 38 (4), 2198-2207

165 Phlhammer J, and O'Brien, Jr. WD, Dependence of the ultrasonic scatter coefficient on collagen concentration in mammalian tissues, *J. Acoust. Soc. Am*., 1981; 69 (1), 283-285

166 Sehgal CM and Greenleaf JF, Scattering of ultrasound by tissues, *Ultrason. Imaging*, 1984; 6 (1), 60-80

167 Williams RM, Zipfel WR, and Webb WW, Interpreting second-harmonic generation images of collagen fibrils, *Biophys. J*., 2005; 88 (2), 1387-1396

168 Hall CS, Scott MJ, Lanza GM, Miller JG, and Wickline SA. The extracellular matrix is an important source of ultrasound backscatter from myocardium, *J. Acoust. Soc. Am.*, 2000; 107 (1), 612-619

169 Insana MF, Hall TJ, and Fishback JL, Identifying acoustic scattering sources in normal renal parenchyma from the anisotropy in acoustic properties, *Ultrasound Med. Biol*., 1991; 17 (6), 613–626

170 Sehgal CM, Quantitative relationship between tissue composition and scattering of ultrasound, *J. Acoust. Soc. Am*., 1993; 94 (4), 1944-1952

171 Rose JH, Kaufmann MR, Wickline SA, Hall CS, and Miller JG, A proposed microscopic elastic wave theory for ultrasonic backscatter from myocardial tissue, *J. Acoust. Soc. Am*., 1995; 97 (1), 656–668

172 Garcia T, Hornof WJ, and Insana MF, On the ultrasonic properties of tendon," *Ultrasound Med. Biol.*, 2003; 29 (12), 1797–1807

173 Lodish H, Berk A, Zipurski SL, et al., Molecular Cell Biology, 4th Ed. WH Freeman, New York: 2000. Information consulted at http://www.ncbi.nlm.nih.gov/books/NBK21592/

174 Gozzi G, Cressa C, Bazzocchi M, Stanta G, and Vidali C, Causes of attenuation of the sound waves in neoplasm of the breast: Histologic and echographic correlation study, *Radiol. Med*., 1986; 72 (4), 195–198

175 Lamb PM, Perry NM, Vinnicombe SJ, and Wells CA, Correlation between ultrasound characteristics, mammographic findings and histological grade in patients with invasive ductal carcinoma of the breast, *Clinical Radiology*, 2000; 55 (1), 40-44

176 Alowami S, Troup S, Al-Haddad S, Kirkpatrick I, Watson PH: Mammographic density is related to stroma and stromal proteoglycan expression, *Breast Cancer Res*., 2003; 5 (5), R130-R136

177 Conklin MW, Eickhoff JC, Riching KM, et al., Aligned collagen is a prognostic signature for survival in human breast carcinoma, *Am. J. Path*., 2011; 179 (3), 1231-1241

178 Provenzano PP, Eliceiri KW, Campbell JM, Inman DR, White JG, and Keely PJ, Collagen reorganization at the tumor-stromal interface facilitates local invasion, *BMC Medicine*, 2006; 4 (1), 38-53

179 Provenzano PP, Inman DR, Eliceiri KW, Knittel JG, Yan L, Rueden CT, White JG, and Keely PJ, Collagen density promotes mammary tumor initiation and progression, *BMC Medicine*, 2008; 6 (1), 11-25

180 Boyd N, Dite G, Stone J, Gunasekara A, et al., Heritability of mammographic density, a risk factor for breast cancer, *N. Engl. J. Med*., 2002; 347 (12), 886–894

181 Barsky SH, Rao CN, Grotendorst GR, and Liotta LA, Increased content of type V collagen in desmoplasia of human breast carcinoma, *Am. J. Pathol*., 1982; 108 (3), 276-283

182 Abramczyk H, Surmacki J, Brozen-Pluska B, Morawiec Z, and Tazbir M, The hallmarks of breast cancer by Raman spectroscopy, *Journal of Molecular Structure*, 2009; 924, 176-183

183 Abramczyk H, Brozek-Pluska B, Surmacki J, Jablonska J, Kordek R, The label-free Raman imaging of human breast cancer, *Journal of Molecular Liquids*, 2011; 165 (1-2), 124-132

184 Haka A, Shafer-Peltier KE, Fitzmaurice M, Crow J, Dasari RR, and Feld MS, Diagnosing breast cancer by using Raman spectroscopy, *Proc. Nat. Acad. Sci*., 2005; 102 (35), 12471-12476

185 Shafer-Peltier KE, Haka AS, Fitzmaurice M, Dasari RR, and Feld MS, Raman microspectroscopic model of human breast tissue: implications for breast cancer diagnosis in vivo, *J. Raman Spect*., 2002; 33 (7): 552-263

186 Falzon G, Pearson S, and Murison R, Analysis of collagen fiber shape changes in breast cancer, *Phys. Med. Biol*., 2008; 53 (23), 6641-6652

187 Reusch LM, Feltovich H, Carlson LC, Hall G, Campagnola PJ, Eliceiri KW, and Hall TJ, Nonlinear optical microscopy and ultrasound imaging of human cervical structure, *J. Biomed. Opt*., 2013; 18 (3), 031110

188 Locker J and Segall JE, Breast Cancer: The Matrix is the message, *Am. J. Path*., 2011; 179 (3), 966-968

189 Provenzano PP, Elicieri KW, and Keely PJ, Shining new light on 3D cell motility and the metastatic process, *Trends Cell Biol*., 2009; 19 (11), 638-648

190 Zheng L, Zhuo S, Chen G, Zhu X, Jiang X, Yan J, Chen J, and Xie S, Label-free discrimination of normal and fibroadenomal breast tissues using second harmonic generation imaging, *Scanning* 2011; 33 (4), 208-210

191 Hall TJ, Madsen EL, Zagzebski JA, Boote EJ, Accurate depth-independent determination of acoustic backscatter coefficients with focused transducers, *J. Acoust. Soc. Am*., 1989; 85 (6), 2410-2416

192 Rubert N and Varghese T, Scatterer number density considerations in reference phantom-based attenuation estimation, *Ultrasound Med. Biol*., 2014; 40 (7), 1680-1696

193 Bredfledt JS, Collagen Alignment Imaging and Analysis for Breast Cancer Classification, Ph.D. Dissertation, UW Madison, *Medical Physics*, 2014

194 Nordberg EP and Hall TJ, Correspondence between pulse-echo ultrasound and second-harmonic generation imaging autocorrelation functions of scattering structures: I, Work in progress

195 Nordberg EP and Hall TJ, Correspondence between pulse-echo ultrasound and second-harmonic generation imaging autocorrelation functions of scattering structures: II, Work in progress

196 Provenzano PP, Eliceiri KW, and Keely PJ, Shining new light on 3D cell motility and the metastatic process, *Imaging Cell Biology*, 2009; 19 (11), 638-648

197 Condeelis J, Singer RH, and Segall JE, The great escape: when cancer cells hijack the genes for chemotaxis and motility, *Annu. Rev. Cell Dev. Biol.*, 2005; 21,695-718

198 Sadeghi-Naini A, Falou O, Tadayyon H, et al., Conventional frequency ultrasonic biomarkers of cancer in vivo, *Translational Oncology*, 2013; 6 (3), 234-243